Structural and Kinetic Study of Low-temperature Oxidation Reactions on Noble Metal Single Atoms and Subnanometer Clusters

Yubing Lu

Dissertation submitted to the faculty of the Virginia Polytechnic Institute and State University in partial fulfillment of the requirements for the degree of

Doctor of Philosophy
In
Chemical Engineering

Ayman M. Karim

Hongliang Xin

John R. Morris

David F. Cox

March 26th, 2019

Blacksburg, VA

Keywords: Single-atom catalysts, Subnanometer clusters, CO oxidation, Kinetic study, Operando characterization, Diffuse reflectance infrared spectroscopy (DRIFTS), X-ray absorption fine structure (XAFS), Calorimetry

Structural and Kinetic Study of Low-temperature Oxidation Reactions on Noble Metal Single Atoms and Subnanometer Clusters

Yubing Lu

Abstract

Supported noble metal catalysts make the best utilization of noble metal atoms. Recent advances in nanotechnology have brought many attentions into the rational design of catalysts in the nanometer and subnanometer region. Recent studies showed that catalysts in the subnanometer regime could have extraordinary activity and selectivity. However, the structural performance relationships behind their unique catalytic performances are still unclear. To understand the effect of particle size and shape of noble metals, it is essential to understand the fundamental reaction mechanism. Single atoms catalysts and subnanometer clusters provide a unique opportunity for designing heterogeneous catalysts because of their unique geometric and electronic properties.

CO oxidation is one of the important probe reactions. However, the reaction mechanism of noble single atoms is still unclear. Additionally, there is no agreement on whether the activity of supported single atoms is higher or lower than supported nanoparticles. In this study, we applied different operando techniques including x-ray absorption fine structure (XAFS), diffuse reflectance infrared spectroscopy (DRIFTS), with other characterization techniques including calorimetry and high-resolution scanning transmission electron microscopy (STEM) to investigate

the active and stable structure of $Ir/MgAl_2O_4$ and Pt/CeO_2 single-atom catalysts during CO oxidation. With all these characterization techniques, we also performed a kinetic study and first principle calculations to understand the reaction mechanism of single atoms for CO oxidation. For Ir single atoms catalysts, our results indicate that instead of poisoning by CO on Ir nanoparticles, Ir single atoms could adsorb more than one ligand, and the Ir(CO)(O) structure was identified as the most stable structure under reaction condition. Though one CO was strongly adsorbed during the entire reaction cycle, another CO could react with the surface adsorbed O* through an Eley-Rideal reaction mechanism. Ir single atoms also provide an interfacial site for the facile O_2 activation between Ir and Al with a low barrier, and therefore O_2 activation step is feasible even at room temperature. For Pt single-atom catalysts, our results showed that $Pt(O)_3(CO)$ structure is stable in O_2 and N_2 at 150 °C. However, when dosing CO at 150 °C, one surface O* in $Pt(O)_3(CO)$ could react with CO to form CO_2, and the reacted O* can be refilled when flowing O_2 again at 150 °C. This suggests that an adsorbed CO is present in the entire reaction cycle as a ligand, and another gas phase CO could react with surface O* to form CO_2 during low-temperature CO oxidation.

Supported single atoms synthesized with conventional methods usually consist of a mixture of single atoms and nanoparticles. It is important to quantify the surface site fraction of single atoms and nanoparticles when studying catalytic performances. Because of the unique reaction mechanism of Ir single atoms and Ir nanoparticles, we showed that kinetic measurements could be applied as a simple and direct method of quantifying surface site fractions. Our kinetic methods could also potentially be applied to quantifying other surface species when their kinetic behaviors

are significantly different. We also benchmarked other in-situ and ex-situ methods of quantifying surface site fraction of single atoms and nanoparticles.

To bridge the gap between single atoms and nanoparticles and have a better understanding of the effect of nuclearity on CO oxidation, we also studied supported Ir subnanometer clusters with the average size less than 0.7 nm (< 13 atoms) prepared by both inorganic precursor and organometallic complex $Ir_4(CO)_{12}$. Low-temperature CO adsorption indicates that CO and O_2/O could co-adsorb on Ir subnanometer clusters, however on larger nanoparticle the particle surface is covered by CO only. Additional co-adsorption of CO and O_2 was studied by CO and O_2 calorimetry at room temperature. CO oxidation results showed that Ir subnanometer clusters are more active than Ir single atoms and Ir nanoparticles at all conditions, and this could be explained by the competitive adsorption of CO and O_2 on subnanometer clusters.

Structural and Kinetic Study of Low-temperature Oxidation Reactions on Noble Metal Single Atoms and Subnanometer Clusters

Yubing Lu

General Audience Abstract

CO oxidation is one of the important reactions in catalytic converters. Three-way catalysts, typically supported noble metals, are very efficient at high temperature but could be poisoned by CO at cold start. Better designed catalysts are required to improve the performance of the catalytic converter to lower the emissions of gasoline engines. To reach this goal, more efficient use of the noble metal is required. Single-atom catalysts consist of isolated noble metal atoms supported on different supports, which provide the best utilization of noble metal atoms and provides a new opportunity for a better design of heterogeneous catalysts. The unique electronic and geometric properties of metal single atoms catalysts could lead to a better activity and selectivity. Subnanometer clusters have also been shown to have unique electronic properties. With a better understanding of the structure of supported single atoms and subnanometer clusters, their catalytic performance can be optimized for better catalysts in the catalytic converter and other applications.

In this work, we applied in-situ and operando characterization, kinetic studies and first principle calculations aiming to understand the active and stable structure of noble metal single atoms and

subnanometer clusters under reaction condition, and their reaction mechanisms during CO oxidations. For $MgAl_2O_4$ supported Ir single atoms, our results suggest that CO could be co-adsorbed with O_2/O under reaction conditions. These multiple ligands adsorption leads to a unique reaction mechanism during CO oxidation. Though one CO was adsorbed during the whole reaction cycle, another gas phase CO could react with the O* species co-adsorbed with CO through an Eley-Rideal mechanism. This suggests that Ir single atoms are no longer poisoned by CO, and on the other hand the O_2 can be activated on an interfacial site with a low reaction barrier. Ir subnanometer clusters showed higher activities than Ir single atoms and nanoparticles. In-situ IR and high energy resolution fluorescence detected – X-ray absorption near edge spectroscopy (HERFD-XANES) showed that CO could co-adsorb with O_2 at room temperature, and this competitive adsorption could explain the high activity during CO oxidation. Supported Ir single atoms and subnanometer clusters are not poisoned by CO and O_2 could be co-adsorbed, this could be potentially applied to solve the poisoning of catalyst in the catalytic converter at cold start temperature. We also performed kinetic study on CeO_2 supported Pt single atoms. Similar behavior was observed, and we showed that the CO and O co-adsorbed complex is stable in O_2 and N_2, but could react in CO. With the understanding of the active structure of noble metal single atoms and the origin of activities, better-designed catalysts can be synthesized to improve the activity and selectivity of low-temperature oxidation reactions.

Acknowledgments

I would like to thank my advisor Prof. Ayman Karim for his guidance, help, and support throughout my Ph.D. study. His valuable and continuous guidance and ideas in experimental details, data analysis, writing, and oral presentation helped me gain the knowledge and skills not only for research but also how to become a successful and professional researcher, which will greatly benefit my future career. He also gave me many freedoms to study different areas and trained me with many fundamental skills. This work would not be possible without him. I would like also to thank Prof. Hongliang Xin who gave me many insights on my research and also taught me many skills of first-principle calculations.

I would like to thank all my committee members: Prof. David Cox, Prof. John Morris for their guidance and help during my study. I would also like to acknowledge my collaborators Dr. Simon Bare, Dr. Adam Hoffman, Dr. Alexey Boubnov, Dr. Alessandro Gallo at SSRL, Dr. Libor Kovaric at PNNL, Jiamin Wang and Dr. Liang Yu at Virginia Tech for their kindly help and training on my research. Thanks to all my colleagues for their help during my study here: Chun-Te Kuo, Xiwen Zhang, Wenhui Li, Saeed Mozzaffari, Malik Abrahim, Dr. Wendi Guo, Coogan Thompson, Eric Husman, Adrian Clark, Hunter Maixner, Andrew Wenzel, Rachael McCarthy, Tony Rogers. I also would like to thank Kevin Holshouser for his kindly help during setting up the lab.

Finally, I would like to thank my parents Fanglan Li, Zhengquan Lu and my wife Yuqing Zhao for their love and continuous support during my Ph.D.; and my son Aiden Lu for bringing happiness and new meaning to my life.

Table of Contents

Chapter 1. Background and literature review

1.1. Influence of metal-support interaction and particle size on CO oxidation reactions

The interaction of metal and the support was recognized as strong metal support interaction (SMSI) in 1978 by Tauster et al.[1-3]. The author observed the strong binding between the noble metal and the titanium cations and the formation of an intermetallic compounds[1]. Since then, metal-support interaction was studied on different metals and supports[4-13], especially on single crystal model catalysts under UHV conditions. This metal-support interaction could affect the electron transfer between metal/support interface to the adsorbate[14]. Relationship between the SMSI states and their catalytic properties contributes to their structure sensitivity. Usually, the structure-sensitive reactions will be strongly inhibited when catalysts are in SMSI states, such as during hydrogenation of CO and hydrolysis of hydrocarbon [15]. When the reaction is structure insensitive, such as the hydrogenation and dehydrogenation of hydrocarbons, the catalytic activities are mildly suppressed by SMSI. For CO oxidation, several studies showed that it could be influenced by SMSI and the extent could be different depends on the atmosphere around the noble metal and the reaction conditions[13, 16]. For example, SMSI plays an important role in Au activation on Au/TiO_2 catalysts[16]. Interaction of noble metal and the support includes the electron transfer between the metal species and the support and the surface O transfer[17]. For the Pt/CeO_2 catalyst[17], O reverse spillover was characterized as a purely nanoscale phenomenon, i.e. it only exists on nanostructured ceria only. These charge and O transfer could strongly affect the structure-activity dependence of

supported catalysts. Charge transfer between the metal and support can be influenced by the particle size of the supported noble metal. Subramanian et al.[18] reported a charge equilibrium between Au nanoparticles and the TiO_2 support. Fermi level of the TiO_2-Au complex system was determined by a C_{60}/C_{60}^- redox couple. The apparent Fermi level was shown to be size dependent in this study (20 mV for 8 nm diameter, 40 mV for 5 nm diameter and 60 mV for 3 nm diameter) and therefore indicates the metal support charge transfer has strong size dependence. Cargnello et al. [19] found that for ceria-supported group VIII metal catalysts, CO oxidation is greatly enhanced at the metal-ceria interface, thus the normalized reaction rate increase with the decreasing of nanoparticle size. However, for Al_2O_3 based group VIII metal catalysts, the normalized reaction rate of CO oxidation is almost independent of the particle size. Overbarry et al.[20] showed that for Au nanoparticles supported on TiO_2 in the range of 2-10 nm, the turn over frequency (TOF) decreased with particle size, and the author concluded that this activity decrease with decrease in the particle size is not due to the overall size-dependence on electronic properties but the change in the relative ratio of unsaturated sites when particle size decreases. Lopez-Acevedo et al.[21] showed that on well-characterized ligand-protected Au clusters between 1.2-2.4 nm, the quantum size effect (magnitude of the HOMO-LUMO gap) has a dominant role in the binding and activation of oxygen.

1.2. Single-atom catalysts

1.2.1. Introduction of single-atom catalysts

For a heterogeneous catalyst, the reaction proceeds at the surface of a supported noble metal or non-noble metal surface. Unlike a homogenous catalyst which could reach ~100% utilization of

the metal atoms, the heterogeneous catalyst could agglomerate into particles where only a small fraction of the metal atoms could be involved in the catalytic reactions. For instance, for Pt nanoparticles formed as a completely shelled polyhedron, 3 nm particle has 45% of the Pt atoms on the surface and 5.1 nm particle has 28%[22]. Increasing the percentage of the surface atom is important for the noble metal catalyst in industry, and this brought growing research interest in atomically dispersed noble metal catalysts[23]. In 1979, Yates and co-worker supported atomically dispersed Rh on Al_2O_3 and studied the structure of the CO adsorption and O_2 activation on these catalysts with infrared spectroscopy and NMR[24-25]. Gates and co-worker synthesized mononuclear Ir, Rh, Au and Os on different supports such as MgO, Al_2O_3 and zeolite[26-32]. Tao Zhang and co-works in 2011 showed that atomically dispersed Pt/FeO_x single-atom catalysts are more active than their nanoparticles counterparts[33]. With the advancement of characterization techniques such as high-angle annular dark-field scanning transmission electron microscopy (HAADF-STEM or STEM)[34-40] and the X-ray absorption spectroscopy (XAS)[41-43], more detailed structural and catalytic performance information of single-atom catalyst can be obtained.

1.2.2. Geometric and electronic properties of single-atom catalysts

Supported single atoms are usually anchored in specific sites of the support. Different types of sites were reported in the literature. The first type of site is where single atoms are replacing one of the specific atoms of the support. For Pt/FeO_x single-atom catalysts[33], HAADF-STEM and DFT calculation revealed that Pt located at the exact position of the original Fe atom on the surface. For the high loading Pt/MoS_2 single-atom catalysts, Pt single atoms replaced the original position of

Mo. Well-defined supports such as metal organic frameworks (MOFs)[44] and graphene[45] have also been shown to be ideal support to make high loading structural-defined single atoms catalysts where single atoms serve as metal nodes in MOF[44]. The second type of site is where single atoms are anchored on top of the support surface. Pd single atoms could be stabilized on top of the graphene support[46] and Ir catalysts could be supported on top of 3 or 4 surface O on $MgAl_2O_4$ support[47]. The third type of single atoms is the single atom alloy, where isolated metal single atoms are coordinated with a different type of metal atoms. Pd-Cu single atoms alloy[48] and Pt-Cu[49] was prepared and well characterized by scanning tunneling microscopy.

With the decreasing of particle size, the coordination number of metal atoms decreases and the electronic properties also dramatically change when the particle size is below 1 nm. In the quantum regime of metal nanoparticles, addition and subtraction of one single atom will dramatically change their structural, electronic and chemical properties. As shown in Figure 1, when the particle size decreases from 5 nm to 1 nm, the continuous metal band will be replaced by discrete molecular orbitals, and atomic orbitals dominate on a single atom. The smaller the nanoparticle, the larger the Kubo gap[50]. The metallic properties are replaced by the strong metal-support interaction with the decreasing of particle size as discussed earlier. For supported single atoms, the support serves as a ligand[51] that could tune the electronic properties of the metal center. At the same time, the electronic properties are also more sensitive to the adsorbates around for the single-atom catalysts as characterized by operando spectroscopy [41].

.

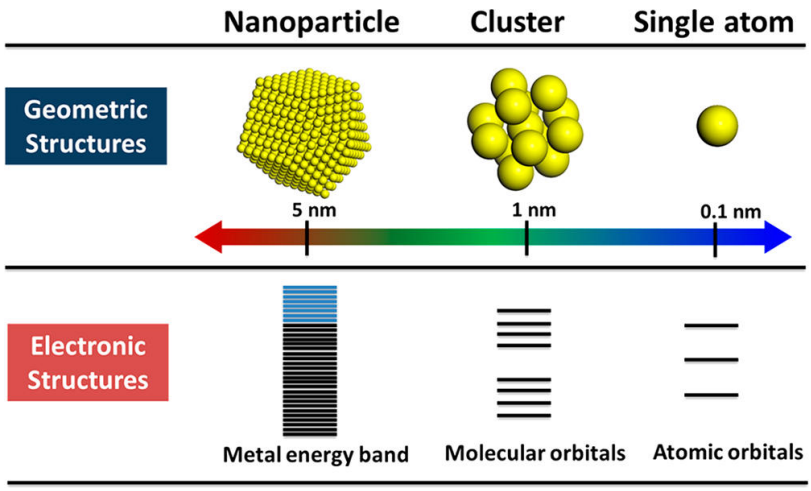

Figure 1. Geometric and electronic properties of nanoparticle, cluster and single atoms[52]. Copyright 2019 American Chemical Society.

1.2.3. Catalytic Applications of single-atom catalysts

Single-atom catalysts have been applied to different reactions aiming to improve the activity and selectivity. There are many examples in the last few years to show how single atoms can make an influence on designing better catalysts.

For oxidation reactions, CO oxidation[33, 43, 47, 53-59], preferential oxidation (PROX) of CO[36, 60], methane oxidation[61-62], selective oxidation of alcohols[63-64] and other reactions were studied on supported single atoms. Among those reactions, CO oxidation was studied the most because of its characteristic as a probe reaction.

For hydrogenation reactions, selective hydrogenation of 1-3 butadiene[65-67], selective hydrogenation acetylene[68-73], CO_2 hydrogenation[74-75], selective hydrogenation of acrolein[76], formaldehyde hydrogenation[77]etc. were studied in the past decade. Single-atom catalysts have been used for tuning the selectivity of hydrogenation reactions.

Water gas shift (WGS) reaction is also one of the reactions that have been studied with single-atom catalysts. FeO_x single-atom catalysts were shown to have one order of magnitude higher activity than cluster and nanoparticle counterpart for WGS reactions[78]. Pt and Au single-atom metal catalysts were also prepared with different support and the active sites were identified[79-80].

1.3. CO oxidation reactions

1.3.1. Introduction

CO oxidation is one of the most important prototypical reaction in heterogeneous catalysis and has excellent application in emission control[81-82] and removing the trace amount of CO in polymer electrolyte membrane fuel cell (PEMFC) since CO poisoning of the catalysts remains a problem[83-85]. Supported noble metal catalysts for low-temperature CO oxidation are the focus of this study.

1.3.2. Effect of particle size and support

Cargnello et al.[19] tailored the particle size of the Ni, Pd metal particles and therefore the length of the metal-support interface. For the Al_2O_3 supported particles, there is no size dependency; for CeO_2 support, smaller sized particle and therefore more significant metal-support interaction enhanced the activity of CO oxidation.

Au nanoparticles were proved to be active for CO oxidation by Haruta et al. in 1993[86]. Lopez et al.[87] reported the size dependence of CO oxidation activity on the Au particle size on different supports. As shown in Figure 2a, the CO oxidation activity dramatically increases with the decreasing of particle size from 10 nm to 1 nm. The effect of particle size proved to be more important than the interaction with support at this size regime since different supports showed

similar trends as shown in Figure 2. The activity increased by two orders of magnitude when the particle size decreased from 20-30 nm to 2-4 nm[87]. This can be explained by the increase of CO and O binding energy as the particles get smaller as shown in Figure 2b.

For the effect of support, Fampiou et al.[88] reported the influence of support on the CO oxidation kinetics and showed that the strong support-metal interaction could lower the reaction barrier of Pt_{13}/graphene catalyst by 0.5 eV. Comotti el al.[89] studied the effect of support on gold catalysts . Au nanoparticles were deposited on TiO_2, Al_2O_3, ZnO, and ZrO_2 with colloidal deposition method and the particle sizes are almost identical on all supports. The catalytic activities are very different on different supports. TiO_2 and Al_2O_3 are the most active catalysts and ZnO and ZrO_2 are much less active. This demonstrated that the metal support interaction will strongly influence the catalytic properties.

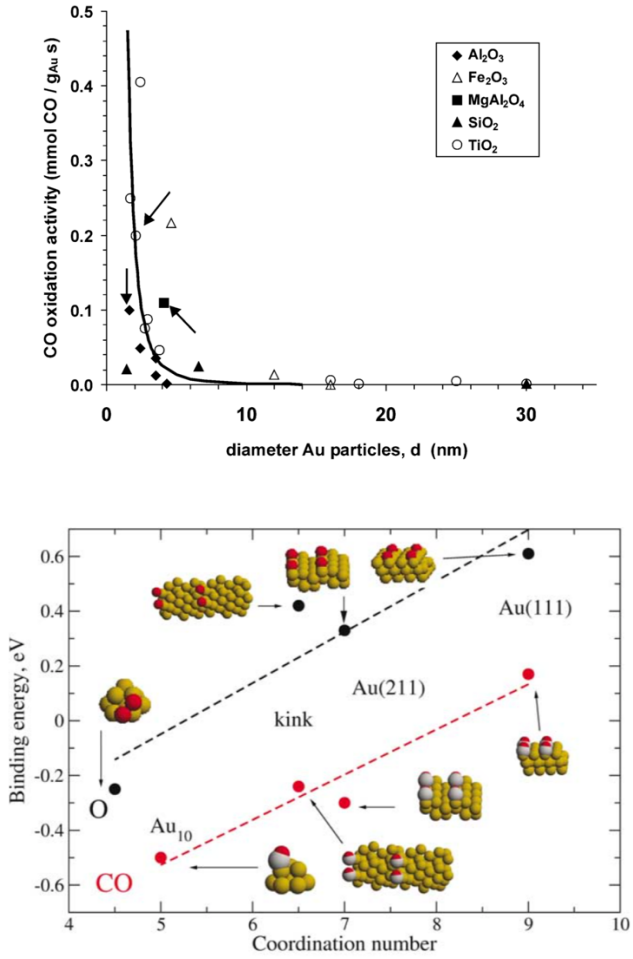

Figure 2. Measured activities of CO oxidation at 273 K for different Au-based catalysts (top) and the correlation between the binding energy of CO, O_2 with the coordination number of Au particles[87]. Copyright 2004 Elsevier.

With a further decrease of particle size below 1 nm, Lee et al.[90] showed the opposite trend for the correlation between particle size and CO oxidation activity. Au_1 to Au_7 were prepared by mass selected methods on a TiO_2 substrate, and the CO oxidation study results (Figure 3a) showed that Au single atoms (Au_1) are inactive and an activity increase with particle size was observed. Applying the DFT method, Liu et al. [91] calculated the reaction profile on Au_{1-4} and Au_7 (Figure

3b). The reaction barrier decreases with the increase of particle size, which is consistent with the experimentally measured size dependency by Lee et al.[90]. Size and shape dependency was also studied on larger Au clusters (Au_{16-20})[91], and the result showed the activity increased with particle size up to Au_{18}. For Au_{18}, the shape of the particle of plays an essential role as hollow-cage Au_{18} isomers showed much higher CO oxidation activity than the pyramidal Au_{18}. Liu et al.[92] systematically studied the behavior with a size range of 0.3-0.8 nm using density functional theory (DFT) calculation. A tri-molecular L-H mechanism was reported to be the most favorable mechanism where O_2 activation can be promoted by a co-adsorbed CO structure.

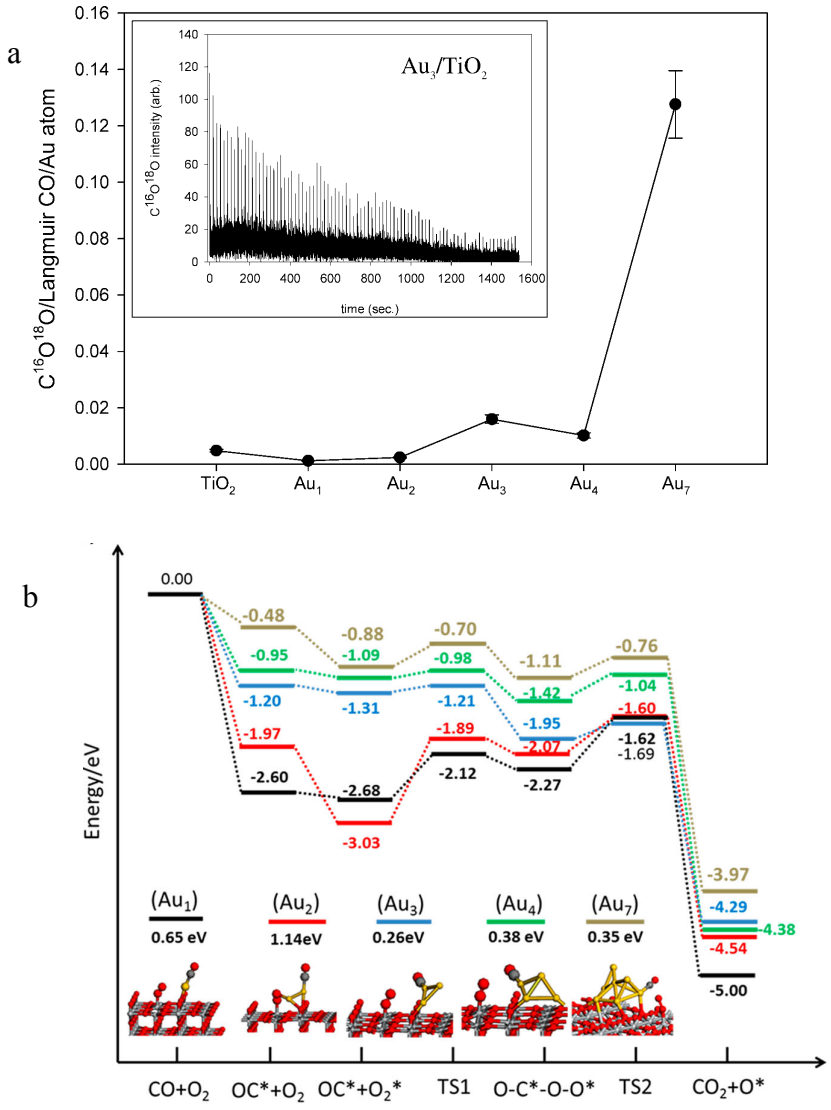

Figure 3. a) Size dependence of CO oxidation activity on Au-based catalyst. The number of atoms in clusters: 1-7.[90] **b)** Energy profile on TiO_2 supported Au_{1-4} and Au_7. Copyright 2004, 2013 American Chemical Society.

1.3.3. CO oxidation on Single-atom catalysts

CO oxidation has been reported on single-atom catalysts with different metals. For Pt single atoms, Qiao et al. reported Pt single atoms can be prepared with FeO_x support, and Pt single atoms showed

higher activity than the Pt nanoparticle counterpart (TOF × 10^2: 13.6 s^{-1} for Pt single atoms and 8.01 for Pt nanoparticles). Moses-DeBusk et al.[93] also showed that Al_2O_3 supported Pt single atoms are active for CO oxidation. DeRita et al.[55] reported that Pt/TiO_2 could be active for CO oxidation where Pt single atoms showed much weaker adsorption energy compared with the Pt particles and the oxidized Pt. Pt single atoms were 4-6 time more active than the nanoparticle when considering the normalized activity per Pt. Also sintering of Pt single atoms during reaction condition was observed. Ding et al.[94] showed synthesized Pt single atoms with different supports (HZSM-5, SiO_2, TiO_2, Al_2O_3, and ZrO_2). When doing temperature programming oxidation on the CO covered Pt single-atom catalysts, the bands in DRIFTS assigned to Pt single atoms came off at a much higher temperature than the peaks assigned to nanoparticles. This suggests that single atoms are not active for CO oxidation. Jones et al.[95] also showed that single atoms supported on CeO_2 have activity orders of magnitude lower than the Pt nanoparticles. There are still discrepancies on whether single-atom catalysts are active or not for CO oxidation. Operando characterization and detailed kinetic measurements are required to further understand the reaction mechanism of CO oxidation on single-atom catalysts[58, 96-99].

1.4. Reaction kinetics of CO oxidation

1.4.1. CO oxidation kinetics on extended surfaces and noble metal nanoparticles

For low-temperature CO oxidation, CO oxidation proceeds on the extended surface which is saturated with CO, and has been shown to have a kinetic rate dependence of $r = k[O_2]^1[CO]^{-1}$ on

Pd, Pt and Ir single crystal surfaces[100-101]. The reaction follows the Langmuir-Hinshelwood mechanism, and the reaction steps can be written as[100]

$$CO(g) \leftrightarrow CO* \quad 1\text{-}1$$

$$O_2(g) \rightarrow 2O* \quad 1\text{-}2$$

$$CO* + O* \rightarrow CO_2(g) \quad 1\text{-}3$$

CO is the dominant species on the surface and the rate equation can be simplified as[100]:

$$\frac{d[CO_2]}{dt} = k\exp\left(-E_{des,CO}/RT\right)P_{O_2}/P_{CO} \quad 1\text{-}4$$

Where the reaction rate is first order in O_2 and negative first order in CO, and the reaction limiting step is the desorption of CO.

Using kinetic, isotopic, infrared spectroscopy and first-principle calculation, Allian et al.[102] identified the reaction mechanism for the low-temperature CO oxidation on Pt particles size between 1-20 nm. CO assisted O_2 activation to form the O*-O-C*=O intermediates which lowered the reaction barrier for O_2 dissociation. The reaction elementary steps for the CO-assisted Langmuir-Hinshelwood route are:

$$CO + \overset{K_1}{\leftrightarrow} CO* \quad 1\text{-}5$$

$$O_2 + \overset{K_2}{\leftrightarrow} O_2* \quad 1\text{-}6$$

$$O_2 * + CO * \xrightarrow{k_3} CO_2 * + O * \quad 1\text{-}7$$

$$O * + CO * \xrightarrow{k_4} CO_2 * + * \quad 1\text{-}8$$

$$CO_2 * + \xrightarrow{k_5} CO_2 + * \quad 1\text{-}9$$

Then the rate equation at near CO* saturation coverage is:

$$r = \frac{k_2[O_2]}{K_1[CO]} \quad 1\text{-}10$$

Au extended surfaces are usually considered as inert; however, when particle size was smaller than 5 nm, gold nanoparticles become active for multiple catalytic reactions. Similar size effect was reported for silver nanoparticles. For CO oxidation reaction on Au nanoparticles, DFT calculation showed that Langmuir-Hinshelwood kinetic is competing with the Eley-Rideal mechanism on Au_{29} particles[103]. Norskov and co-worker[104] reported that Au_{10} nanoparticles are much more active than the extended surface because 1) its very low coordination and ability to have a strong interaction with adsorbates and 2) its geometry is well suited for reactions that need bond breaking of small molecules. When the Au particle size is even smaller, Au_3, a trimolecular Langmuir Hinshelwood kinetic was reported where co-adsorbed CO at Au_3 could promote the breaking of O-O bond through an OCOO* intermediate[92].

1.4.2. CO oxidation kinetics on single-atom catalysts

Unlike nanoparticles, single atoms do not provide two adjacent sites for CO and O_2 to adsorb and react. Several studies have reported the CO oxidation reaction mechanism on different noble metal

single atoms with different supports. In 2011, Qiao et al.[33] proposed a two steps Langmuir-Hinshelwood reaction mechanism for the CO oxidation on Pt/FeO_x single-atom catalyst and calculated the reaction barrier using DFT. A similar reaction mechanism was later reported by Liang et al.[56] on Ir/FeO_x single-atom catalyst with a higher reaction barrier. Moses-Debusk et al.[93] proposed a reaction mechanism of the CO oxidation reaction on a single atom $Pt/\theta\text{-}Al_2O_3$ catalyst using DRIFTS and DFT. This study showed that single atom $Pt/\theta\text{-}Al_2O_3$ catalyst follows a Langmuir-Hinshelwood kinetic where adsorbed CO and O_2 form a $Pt(CO_3)$ intermediate on one Pt single atom. After CO_2 desorption, Pt(O) react with one adsorbed CO to finish the reaction cycle. Nie et al. [105]showed that though Pt_1/CeO_2 single-atom catalysts can be activated through treatment in steam at high temperature, and DFT theoretical study showed that steam-pretreatment creates an $O_{lattice}[H]$ site coordinated with the Pt^{2+} single atom (Figure 4, intermediate I). This $O_{lattice}[H]$ site could react with an adsorbed CO to create a surface vacancy (Figure 4, intermediate III) with a reaction barrier of 53 kJ/mol. O_2 could then adsorb and fill the vacancy and a CO_2 is formed and then desorbed. After that, the OO[H] species (Figure 4, intermediate V) react with a second adsorbed CO to form CO_2 with an activation barrier of 38 kJ/mol. As a comparison, without steam treatment, the reaction will follow a similar step (Figure 4, insect, red line) with a higher reaction barrier of 122 kJ/mol. This work showed that single atoms could be activated by the H species from the support, and their electronic properties can be easily changed by a small change of their coordinated environment.

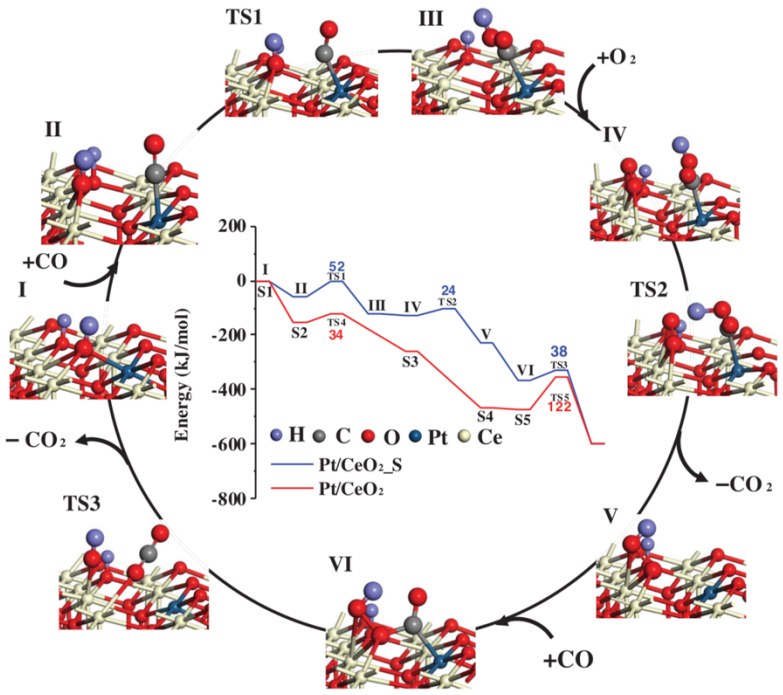

Figure 4. The proposed reaction mechanism for CO oxidation on steam-treated and non-steam-treated Pt/CeO_2 single-atom catalysts[105]. Copyright 2017 Science.

Using DFT calculation, Ghosh et al.[107] studied the reaction mechanism of CO oxidation on Rh/Al_2O_3 single-atom catalysts. The results showed that Rh single atom could bind with multiple adsorbates (Figure 5). O_2 can be activated at the interface of the Rh single atom and the surface. One (path A) or two (path B) CO could co-adsorbed with the activated O_2 for the first step of the reaction cycle depend on the gas phase CO concentration. The second step between the CO and the surface activated O was calculated as the rate-limiting step with a reaction barrier of 0.97 eV. Abbet et al.[106] studied the reaction mechanism of CO oxidation on Pd_1/MgO single-atom catalyst. Their experimental and DFT results suggest that two possible reactions intermediate exit under reaction condition: $Pd(CO)_2O_2$ and $Pd(CO_3)CO$.

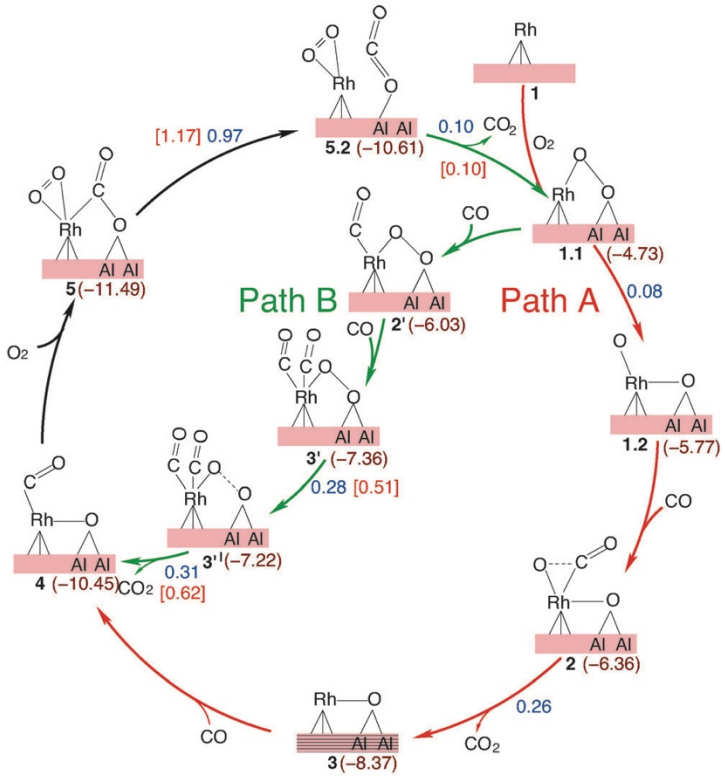

Figure 5. Schematic view of the proposed mechanism for CO oxidation on the Rh/g-Al_2O_3 surface[107]. Copyright 2013 ChemPubSoc Europe.

Mao et al.[57] reported a CO-promoted O_2 activation mechanism for CO oxidation on Au/h-BN single-atom catalysts. Applying DFT calculation, they showed that a tri-molecular Eley-Rideal (E-R) mechanism (reaction barrier 0.47 eV) is more favorable than bimolecular Langmuir-Hinshelwood mechanism (0.72 eV). The O_2 is activated between two adsorbed CO species ($Au(CO)_2$) through an (OOC)Au(COO) intermediate, with a low barrier of 0.09 eV.

1.5. Objectives of this work

Catalytic properties of low-temperature CO oxidation reactions on supported noble metal catalysts are affected by their particle size and metal-support interaction. Single-atom catalysts showed unique catalytic behaviors during low-temperature CO oxidation, however, their reaction mechanisms are no fully understood yet. The objectives of this work are:

I. Control the synthesis to achieve atomically dispersed Ir catalysts. During the controlled synthesis, understand the important steps that could affect the ratio of the single atom and nanoparticles.

II. Understand the structure of Ir single atom on the $MgAl_2O_4$ surface and understand how the metal support interaction could be enhanced to improve the stability of supported metal single stoms.

III. Understand the adsorption behavior of different adsorbates especially CO and O_2.

IV. Identify the stable intermediate on Ir single atoms during the CO oxidation reaction. Understand how could these stable intermediates be affected by the metal nuclearity under the subnanometer regime.

V. Understand the reaction mechanism of low-temperature oxidation reaction supported Ir single atoms and supported Ir subnanometer clusters. Understand the effect of adsorbates during the reaction conditions by combining the in-situ characterization techniques and the computational ab-initio modeling.

VI. Understand the reaction mechanism of low-temperature oxidation on CeO_2 supported Pt single atoms and investigate the general reaction mechanism and differences between noble metal single atoms for low-temperature oxidation reactions.

1.6. Approaches to this work

In this work, to stabilize Ir single atoms, we chose the $MgAl_2O_4$ spinel as support based on previous work which showed the strong ability of $MgAl_2O_4$ spinel to stabilize noble metal nanoparticles[108-110]. The $MgAl_2O_4$ spinel (111) facet was attributed to have a strong interaction with the Pt/Ir/Rh (111) facet with surface oxygen. Ir and Rh particles are the two metals to have the strongest interaction with the spinel among all the studied noble metals[109]. In this work, we are trying to utilize this strong metal support interaction, and further minimize the particle size to achieve the goal of making atomically dispersed Ir single atoms.

Incipient wetness and wet impregnation methods were applied for the synthesis. Both methods are simple and do not require specialized equipment. Thus, it has a high potential to be applied in industry to produce commercialized single atoms in the future. With the incipient wetness impregnation method, all the metal precursor will be loaded on the support regardless of the metal-support interaction. However, the uniformity of the metal during the synthesis is very difficult to control. The wet impregnation method could improve the uniformity of noble metal significantly. However, the amount of metal adsorbed and the uniformity of the metal is strongly dependent on the metal-support interaction and the metal precursor. Our approach is to maximize the interaction between the Ir precursor and the MAl_2O_4 by choosing proper metal precursor, optimizing the precursor pH and adjusting the metal loading during the synthesis. After the metal precursor is anchored on the MAl_2O_4 surface, we will optimize pretreatment conditions to enhance the metal support interaction further.

To understand the reaction mechanism of low-temperature oxidation reactions, it is very important to study the adsorption behavior of different adsorbates on Ir single atoms. Our approach is to combine in-situ characterization and computational ab-initio calculations to understand the adsorption of different adsorbates (CO, O_2) on Ir single atoms under room temperature and reaction conditions. High angle annular dark-field-scanning electron microscopy (HAADF-STEM) will also be applied to assist the in-situ characterization in understanding the structure of the catalysts. Detailed kinetic measurement will be combined with the in-situ characterization to understand the reaction mechanism.

The effect of nuclearity will also be studied on Ir catalysts in the subnanometer regime. Ir clusters with different cluster size from isolated atom to nanoparticles will be synthesized and the effect of nuclearity on low-temperature oxidation will be studied systemically.

References

1. Tauster, S. J.; Fung, S. C.; Garten, R. L., Strong metal-support interactions - group-8 noble-metals supported on TiO_2. *Journal of the American Chemical Society* **1978,** *100* (1), 170-175.

2. Tauster, S. J.; Fung, S. C., Strong metal-support interactions - occurrence among binary oxides of groups IIA-VB. *Journal of Catalysis* **1978,** *55* (1), 29-35.

3. Fung, S. C.; Tauster, S. J.; Baker, R. T. K.; Garten, R. L., Strong metal-support interactions - group-VIII noble-metals supported on transition-metal oxides. *Abstracts of Papers of the American Chemical Society* **1979,** (Apr), 174-174.

4. Praliaud, H.; Martin, G. A., Evidence of a strong metal-support interaction and of Ni-Si alloy formation in silica-supported nickel-catalysts. *Journal of Catalysis* **1981,** *72* (2), 394-396.

5. Fung, S. C., XPS studies of strong metal-support interactions (Smsi) - Pt-TiO_2. *Journal of Catalysis* **1982,** *76* (1), 225-230.

6. Turlier, P.; Martin, G. A., Evidence of a strong metal-support interaction in zirconia-supported nickel-catalysts. *React. Kinet. Catal. Lett.* **1982,** *21* (3), 387-390.

7. Burch, R., The Current status of strong metal-support interactions. *Appl Catal* **1984,** *12* (2), 285-286.

8. Tang, R. Y.; Wu, R. A.; Lin, L. W., Evidence of strong metal-support interaction in alumina-supported platinum catalysts. *Appl Catal* **1984,** *10* (2), 163-172.

9. Narayanan, S., Strong metal support interaction. *J Sci Ind Res India* **1985,** *44* (11), 580-587.

10. Tauster, S. J., Strong Metal-Support Interactions - Facts and uncertainties. *Abstracts of Papers of the American Chemical Society* **1985,** *189* (Apr-), 1-Petr.

11. Kalinkin, A. V.; Pashis, A. V., Studies of the effect of strong metal-support interaction (SMSI) over model catalyst Rh/TiO_2. *React. Kinet. Catal. Lett.* **1992,** *46* (1), 33-38.

12. Mendes, F. M. T.; Uhl, A.; Starr, D. E.; Guimond, S.; Schmal, M.; Kuhlenbeck, H.; Shaikhutdinov, S. K.; Freund, H. J., Strong metal support interaction on Co/niobia model catalysts. *Catalysis Letters* **2006,** *111* (1-2), 35-41.

13. d'Alnoncourt, R. N.; Friedrich, M.; Kunkes, E.; Rosenthal, D.; Girgsdies, F.; Zhang, B. S.; Shao, L. D.; Schuster, M.; Behrens, M.; Schlogl, R., Strong metal-support interactions between palladium and iron oxide and their effect on CO oxidation. *Journal of Catalysis* **2014,** *317*, 220-228.

14. Sun, Y. N.; Giordano, L.; Goniakowski, J.; Lewandowski, M.; Qin, Z. H.; Noguera, C.; Shaikhutdinov, S.; Pacchioni, G.; Freund, H. J., The interplay between structure and CO oxidation catalysis on metal-supported ultrathin oxide films. *Angewandte Chemie-International Edition* **2010,** *49* (26), 4418-4421.

15. Uchijima, T., SMSI effect in some reducible oxides including niobia. *Catalysis Today* **1996,** *28* (1-2), 105-117.

16. Klyushin, A. Y.; Jones, T. E.; Lunkenbein, T.; Kube, P.; Li, X.; Havecker, M.; Knop-Gericke, A.; Schlogl, R., Strong metal support interaction as a key factor of Au activation in CO Oxidation. *Chemcatchem* **2018,** *10* (18), 3985-3989.

17. Vayssilov, G. N.; Lykhach, Y.; Migani, A.; Staudt, T.; Petrova, G. P.; Tsud, N.; Skala, T.; Bruix, A.; Illas, F.; Prince, K. C.; Matolin, V.; Neyman, K. M.; Libuda, J., Support nanostructure boosts oxygen transfer to catalytically active platinum nanoparticles. *Nature materials* **2011,** *10* (4), 310-315.

18. Subramanian, V.; Wolf, E. E.; Kamat, P. V., Catalysis with TiO_2/gold nanocomposites. Effect of metal particle size on the Fermi level equilibration. *Journal of the American Chemical Society* **2004,** *126* (15), 4943-4950.

19. Cargnello, M.; Doan-Nguyen, V. V. T.; Gordon, T. R.; Diaz, R. E.; Stach, E. A.; Gorte, R. J.; Fornasiero, P.; Murray, C. B., Control of metal nanocrystal size reveals metal-support interface role for ceria catalysts. *Science* **2013,** *341* (6147), 771-773.

20. Overbury, S. H.; Schwartz, V.; Mullim, D. R.; Yan, W. F.; Dai, S., Evaluation of the Au size effect: CO oxidation catalyzed by Au/TiO_2. *Journal of Catalysis* **2006,** *241* (1), 56-65.

21. Lopez-Acevedo, O.; Kacprzak, K. A.; Akola, J.; Hakkinen, H., Quantum size effects in ambient CO oxidation catalysed by ligand-protected gold clusters. *Nature Chemistry* **2010,** *2* (4), 329-334.

22. An, K.; Somorjai, G. A., Size and shape control of metal nanoparticles for reaction selectivity in catalysis. *Chemcatchem* **2012,** *4* (10), 1512-1524.

23. Wang, A. Q.; Li, J.; Zhang, T., Heterogeneous single-atom catalysis. *Nat Rev Chem* **2018,** *2* (6), 65-81.

24. Yates, J. T.; Duncan, T. M.; Worley, S. D.; Vaughan, R. W., Infrared spectra of chemisorbed CO on Rh. *The Journal of Chemical Physics* **1979,** *70* (3), 1219.

25. Duncan, T. M.; Yates, J. T.; Vaughan, R. W., A 13C NMR study of the adsorbed states of CO on Rh dispersed on Al_2O_3. *The Journal of Chemical Physics* **1980,** *73* (2), 975.

26. Lu, J.; Aydin, C.; Browning, N. D.; Gates, B. C., Oxide- and Zeolite-Supported Isostructural $Ir(C_2H_4)_2$ Complexes: Molecular-level observations of electronic effects of supports as ligands. *Langmuir* **2012,** *28* (35), 12806-12815.

27. Flytzani-Stephanopoulos, M.; Gates, B. C., Atomically dispersed supported metal catalysts. *Annual review of chemical and biomolecular engineering* **2012,** *3*, 545-74.

28. Lu, J.; Aydin, C.; Liang, A. J.; Chen, C. Y.; Browning, N. D.; Gates, B. C., Molecular iridium catalysts in 1D channels of zeolite SSZ-53: Probing support and ligand effects in catalysis of ethylene hydrogenation and H-D exchange in the conversion of H_2 + D_2. *Abstracts of Papers of the American Chemical Society* **2012,** *243*.

29. Aydin, C.; Kulkarni, A.; Chi, M. F.; Browning, N. D.; Gates, B. C., Atomically resolved site-isolated catalyst on MgO: Mononuclear osmium dicarbonyls formed from $Os_3(CO)_{12}$. *J Phys Chem Lett* **2012,** *3* (14), 1865-1871.

30. Uzun, A.; Ortalan, V.; Browning, N. D.; Gates, B. C., Site-isolated iridium complexes on MgO powder: individual Ir atoms imaged by scanning transmission electron microscopy. *Chemical Communications* **2009,** (31), 4657-4659.

31. Uzun, A.; Ortalan, V.; Hao, Y. L.; Browning, N. D.; Gates, B. C., Imaging gold atoms in site-isolated MgO-Supported mononuclear gold complexes. *Journal of Physical Chemistry C* **2009,** *113* (39), 16847-16849.

32. Lei, Y.; Uhl, A.; Becker, C.; Wandelt, K.; Gates, B. C.; Meyer, R.; Trenary, M., Adsorption and reaction of $Rh(CO)_2(acac)$ on $Al_2O_3/Ni_3Al(111)$. *Physical Chemistry Chemical Physics* **2010,** *12* (6), 1264-1270.

33. Qiao, B. T.; Wang, A. Q.; Yang, X. F.; Allard, L. F.; Jiang, Z.; Cui, Y. T.; Liu, J. Y.; Li, J.; Zhang, T., Single-atom catalysis of CO oxidation using Pt-1/FeOx. *Nature Chemistry* **2011,** *3* (8), 634-641.

34. Chang, T. Y.; Tanaka, Y.; Ishikawa, R.; Toyoura, K.; Matsunaga, K.; Ikuhara, Y.; Shibata, N., Direct imaging of Pt single atoms adsorbed on TiO_2 (110) surfaces. *Nano Letters* **2014,** *14* (1), 134-138.

35. Han, C. W.; Iddir, H.; Uzun, A.; Curtiss, L. A.; Browning, N. D.; Gates, B. C.; Ortalan, V., Migration of Single Iridium Atoms and Tri-iridium Clusters on MgO Surfaces: Aberration-corrected STEM imaging and ab initio calculations. *J Phys Chem Lett* **2015,** *6* (23), 4675-4679.

36. Qiao, B. T.; Liu, J. X.; Wang, Y. G.; Lin, Q. Q.; Liu, X. Y.; Wang, A. Q.; Li, J.; Zhang, T.; Liu, J. Y., Highly efficient catalysis of preferential oxidation of CO in H_2-rich stream by gold single-atom catalysts. *ACS Catalysis* **2015,** *5* (11), 6249-6254.

37. Allen, J. E.; Hemesath, E. R.; Perea, D. E.; Lensch-Falk, J. L.; Li, Z. Y.; Yin, F.; Gass, M. H.; Wang, P.; Bleloch, A. L.; Palmer, R. E.; Lauhon, L. J., High-resolution detection of Au catalyst atoms in Si nanowires. *Nature Nanotechnology* **2008,** *3* (3), 168-173.

38. Yin, P. Q.; Yao, T.; Wu, Y.; Zheng, L. R.; Lin, Y.; Liu, W.; Ju, H. X.; Zhu, J. F.; Hong, X.; Deng, Z. X.; Zhou, G.; Wei, S. Q.; Li, Y. D., Single cobalt atoms with precise n-coordination as superior oxygen reduction reaction catalysts. *Angewandte Chemie-International Edition* **2016,** *55* (36), 10800-10805.

39. Yang, M.; Li, S.; Wang, Y.; Herron, J. A.; Xu, Y.; Allard, L. F.; Lee, S.; Huang, J.; Mavrikakis, M.; Flytzani-Stephanopoulos, M., Catalytically active Au-$O(OH)_x$-species stabilized by alkali ions on zeolites and mesoporous oxides. *Science* **2014,** *346* (6216), 1498-1501.

40. Xu, P. H.; Lu, J.; Aydin, C.; Debefve, L. M.; Browning, N. D.; Chen, C. Y.; Gates, B. C., Imaging individual lanthanum atoms in zeolite Y by scanning transmission electron microscopy: Evidence of lanthanum pair sites. *Microporous and Mesoporous Materials* **2015,** *213*, 95-99.

41. Hoffman, A. S.; Sokaras, D.; Zhang, S. J.; Debefve, L. M.; Fang, C. Y.; Gallo, A.; Kroll, T.; Dixon, D. A.; Bare, S. R.; Gates, B. C., High-energy-resolution X-ray absorption spectroscopy for identification of reactive surface species on supported single-site iridium catalysts. *Chemistry-a European Journal* **2017,** *23* (59), 14760-14768.

42. van Bokhoven, J. A.; Louis, C.; T Miller, J.; Tromp, M.; Safonova, O. V.; Glatzel, P., Activation of oxygen on gold/alumina catalysts: In situ high-energy-resolution fluorescence and time-resolved X-ray spectroscopy. *Angewandte Chemie-International Edition* **2006,** *45* (28), 4651-4654.

43. Kistler, J. D.; Chotigkrai, N.; Xu, P.; Enderle, B.; Praserthdam, P.; Chen, C. Y.; Browning, N. D.; Gates, B. C., A single-site platinum CO oxidation catalyst in zeolite KLTL: microscopic and spectroscopic determination of the locations of the platinum atoms. *Angew Chem Int Ed Engl* **2014,** *53* (34), 8904-7.

44. Wang, J.; Li, Z.; Wu, Y.; Li, Y., Fabrication of single-atom catalysts with precise structure and high metal loading. *Adv. Mater.* **2018,** *0* (0), 1801649.

45. Fei, H.; Dong, J.; Feng, Y.; Allen, C. S.; Wan, C.; Volosskiy, B.; Li, M.; Zhao, Z.; Wang, Y.; Sun, H.; An, P.; Chen, W.; Guo, Z.; Lee, C.; Chen, D.; Shakir, I.; Liu, M.; Hu, T.; Li, Y.; Kirkland, A. I.; Duan, X.; Huang, Y., General synthesis and definitive structural identification of MN_4C_4 single-atom catalysts with tunable electrocatalytic activities. *Nature Catalysis* **2018,** *1* (1), 63-72.

46. Yan, H.; Cheng, H.; Yi, H.; Lin, Y.; Yao, T.; Wang, C.; Li, J.; Wei, S.; Lu, J., Single-atom Pd/graphene catalyst achieved by atomic layer deposition: remarkable performance in selective hydrogenation of 1,3-butadiene. *J Am Chem Soc* **2015**.

47. Lu, Y.; Wang, J.; Yu, L.; Kovarik, L.; Zhang, X.; Hoffman, A. S.; Gallo, A.; Bare, S. R.; Sokaras, D.; Kroll, T.; Dagle, V.; Xin, H.; Karim, A. M., Identification of the active complex for CO oxidation over single-atom Ir-on-$MgAl_2O_4$ catalysts. *Nature Catalysis* **2019,** *2* (2), 149-156.

48. Kyriakou, G.; Boucher, M. B.; Jewell, A. D.; Lewis, E. A.; Lawton, T. J.; Baber, A. E.; Tierney, H. L.; Flytzani-Stephanopoulos, M.; Sykes, E. C. H., Isolated metal atom geometries as a strategy for selective heterogeneous hydrogenations. *Science* **2012,** *335* (6073), 1209-1212.

49. Liu, J. L.; Lucci, F. R.; Yang, M.; Lee, S.; Marcinkowski, M. D.; Therrien, A. J.; Williams, C. T.; Sykes, E. C. H.; Flytzani-Stephanopoulos, M., Tackling co poisoning with single-atom alloy catalysts. *Journal of the American Chemical Society* **2016,** *138* (20), 6396-6399.

50. Roldan Cuenya, B.; Behafarid, F., Nanocatalysis: size- and shape-dependent chemisorption and catalytic reactivity. *Surface Science Reports* **2015,** *70* (2), 135-187.

51. Lu, J.; Serna, P.; Gates, B. C., Zeolite- and MgO-supported molecular iridium complexes: support and ligand effects in catalysis of ethene hydrogenation and H-D Exchange in the conversion of H_2+D_2. *ACS Catalysis* **2011,** *1* (11), 1549-1561.

52. Liu, L. C.; Corma, A., Metal Catalysts for heterogeneous catalysis: from single atoms to nanoclusters and nanoparticles. *Chem. Rev.* **2018,** *118* (10), 4981-5079.

53. Zhang, Z.; Zhu, Y.; Asakura, H.; Zhang, B.; Zhang, J.; Zhou, M.; Han, Y.; Tanaka, T.; Wang, A.; Zhang, T.; Yan, N., Thermally stable single atom Pt/m-Al_2O_3 for selective hydrogenation and CO oxidation. *Nature communications* **2017,** *8*, 16100.

54. Moses-DeBusk, M.; Allard, L. F.; Blom, D. A.; Narula, C. K., Oxidation-induced structural changes in sub-nanometer platinum supported on alumina. *Chemcatchem* **2015,** *7* (15), 2391-2396.

55. DeRita, L.; Dai, S.; Lopez-Zepeda, K.; Pham, N.; Graham, G. W.; Pan, X. Q.; Christopher, P., Catalyst Architecture for stable single atom dispersion enables site-specific spectroscopic and reactivity measurements of CO Adsorbed to Pt atoms, oxidized Pt clusters, and metallic Pt clusters on TiO_2. *Journal of the American Chemical Society* **2017,** *139* (40), 14150-14165.

56. Liang, J. X.; Lin, J.; Yang, X. F.; Wang, A. Q.; Qiao, B. T.; Liu, J. Y.; Zhang, T.; Li, J., Theoretical and experimental investigations on single-atom catalysis: Ir_1/FeO_x for CO oxidation. *Journal of Physical Chemistry C* **2014,** *118* (38), 21945-21951.

57. Mao, K. K.; Li, L.; Zhang, W. H.; Pei, Y.; Zeng, X. C.; Wu, X. J.; Yang, J. L., A Theoretical study of single-atom catalysis of CO Oxidation using Au embedded 2D h-BN monolayer: A CO-promoted O_2 activation. *Scientific Reports* **2014,** *4*.

58. Lu, Y. B.; Kuo, C. T.; Zhang, X. W.; Wang, J. M.; Xin, H. L.; Karim, A., CO oxidation on supported Ir and Pt single atoms: Structural and kinetic study. *Abstracts of Papers of the American Chemical Society* **2018,** *255*.

59. Duan, S. B.; Wang, R. M.; Liu, J. Y., High-load Pt_1 single-atom catalysts for CO oxidation. *Abstracts of Papers of the American Chemical Society* **2016,** *251*.

60. Cao, L.; Liu, W.; Luo, Q.; Yin, R.; Wang, B.; Weissenrieder, J.; Soldemo, M.; Yan, H.; Lin, Y.; Sun, Z.; Ma, C.; Zhang, W.; Chen, S.; Wang, H.; Guan, Q.; Yao, T.; Wei, S.; Yang,

J.; Lu, J., Atomically dispersed iron hydroxide anchored on Pt for preferential oxidation of CO in H2. *Nature* **2019,** *565* (7741), 631-635.

61. Shan, J.; Li, M.; Allard, L. F.; Lee, S.; Flytzani-Stephanopoulos, M., Mild oxidation of methane to methanol or acetic acid on supported isolated rhodium catalysts. *Nature* **2017,** *551* (7682), 605-608.

62. Tang, Y.; Li, Y. T.; Fung, V.; Jiang, D. E.; Huang, W. X.; Zhang, S. R.; Iwasawa, Y.; Sakata, T.; Nguyen, L.; Zhang, X. Y.; Frenkel, A. I.; Tao, F., Single rhodium atoms anchored in micropores for efficient transformation of methane under mild conditions. *Nature communications* **2018,** *9*.

63. Li, T. B.; Liu, F.; Tang, Y.; Li, L.; Miao, S.; Su, Y.; Zhang, J. Y.; Huang, J. H.; Sun, H.; Haruta, M.; Wang, A. Q.; Qiao, B. T.; Li, J.; Zhang, T., Maximizing the number of interfacial sites in single-atom catalysts for the highly selective, solvent-free oxidation of primary alcohols. *Angewandte Chemie-International Edition* **2018,** *57* (26), 7795-7799.

64. Otake, K. I.; Cui, Y. X.; Buru, C. T.; Li, Z. Y.; Hupp, J. T.; Farha, O. K., Single-atom-based vanadium oxide catalysts supported on metal organic frameworks: selective alcohol oxidation and structure activity relationship. *Journal of the American Chemical Society* **2018,** *140* (28), 8652-8656.

65. Zhang, Z. L.; Zhu, Y. H.; Asakura, H.; Zhang, B.; Zhang, J. G.; Zhou, M. X.; Han, Y.; Tanaka, T.; Wang, A. Q.; Zhang, T.; Yan, N., Thermally stable single atom Pt/m-Al_2O_3 for selective hydrogenation and CO oxidation. *Nature communications* **2017,** *8*.

66. Lucci, F.; Liu, J. L.; Stephanopoulos, M.; Sykes, E. C., Selective hydrogenation of butadiene by Pt/Cu at the single atom limit. *Abstracts of Papers of the American Chemical Society* **2015,** *250*.

67. Lucci, F. R.; Liu, J. L.; Marcinkowski, M. D.; Yang, M.; Allard, L. F.; Flytzani-Stephanopoulos, M.; Sykes, E. C. H., Selective hydrogenation of 1,3-butadiene on platinum-copper alloys at the single-atom limit. *Nature communications* **2015,** *6*.

68. Zhuo, H. Y.; Zhang, X.; Li, J., Selective hydrogenation of acetylene on graphene supported single-atom Pt catalyst. *Abstracts of Papers of the American Chemical Society* **2017,** *254*.

69. Huang, X. H.; Xia, Y. J.; Cao, Y. J.; Zheng, X. S.; Pan, H. B.; Zhu, J. F.; Ma, C.; Wang, H. W.; Li, J. J.; You, R.; Wei, S. Q.; Huang, W. X.; Lu, J. L., Enhancing both selectivity and coking-resistance of a single-atom Pd_1/C_3N_4 catalyst for acetylene hydrogenation. *Nano Res* **2017,** *10* (4), 1302-1312.

70. Pei, G. X.; Liu, X. Y.; Wang, A. Q.; Lee, A. F.; Isaacs, M. A.; Li, L.; Pan, X. L.; Yang, X. F.; Wang, X. D.; Tai, Z. J.; Wilson, K.; Zhang, T., Ag alloyed pd single-atom catalysts for efficient selective hydrogenation of acetylene to ethylene in excess ethylene. *ACS Catalysis* **2015,** *5* (6), 3717-3725.

71. Pei, G. X.; Liu, X. Y.; Wang, A. Q.; Li, L.; Huang, Y. Q.; Zhang, T.; Lee, J. W.; Jang, B. W. L.; Mou, C. Y., Promotional effect of Pd single atoms on Au nanoparticles supported on silica for the selective hydrogenation of acetylene in excess ethylene. *New Journal of Chemistry* **2014,** *38* (5), 2043-2051.

72. Zhang, Q.; Guo, L.; Hao, Z. J., CO hydrogenation on M-1/W6S8 (M = Co and Ni) single-atom catalysts: Competition between C-2 hydrocarbons and methanol synthesis pathways. *Mol Catal* **2019,** *464*, 10-21.

73. Cao, X. X.; Mirjalili, A.; Xie, W. T.; Jang, B., Investigation of Pd-Cu single atom alloy catalysts for selective hydrogenation of acetylene in ethylene. *Abstracts of Papers of the American Chemical Society* **2015,** *249*.

74. Zhang, Q.; Guo, L.; Hao, Z. J., Computational investigation of M-1/W6S8 (M=Fe, Ru, and Os) single-atom catalysts for CO_2 hydrogenation. *Catal Surv Asia* **2018,** *22* (4), 195-207.

75. Caparros, F. J.; Soler, L.; Rossell, M. D.; Angurell, I.; Piccolo, L.; Rossell, O.; Llorca, J., Remarkable carbon dioxide hydrogenation to ethanol on a palladium/iron oxide single-atom catalyst. *Chemcatchem* **2018,** *10* (11), 2365-2369.

76. Aich, P.; Wei, H. J.; Basan, B.; Kropf, A. J.; Schweitzer, N. M.; Marshall, C. L.; Miller, J. T.; Meyer, R., Single-atom alloy Pd-Ag catalyst for selective hydrogenation of acrolein. *Journal of Physical Chemistry C* **2015,** *119* (32), 18140-18148.

77. Baker, L. R.; Kennedy, G.; Van Spronsen, M.; Hervier, A.; Cai, X. J.; Chen, S. Y.; Wang, L. W.; Somorjai, G. A., Furfuraldehyde hydrogenation on titanium oxide-supported platinum nanoparticles studied by sum frequency generation vibrational spectroscopy: acid-base catalysis explains the molecular origin of strong metal-support interactions. *Journal of the American Chemical Society* **2012,** *134* (34), 14208-14216.

78. Lin, J.; Wang, A. Q.; Qiao, B. T.; Liu, X. Y.; Yang, X. F.; Wang, X. D.; Liang, J. X.; Li, J. X.; Liu, J. Y.; Zhang, T., Remarkable performance of Ir_1/FeO_x Single-atom catalyst in

water gas shift reaction. *Journal of the American Chemical Society* **2013,** *135* (41), 15314-15317.

79. Yang, M.; Flytzani-Stephanopoulos, M., Design of single-atom metal catalysts on various supports for the low-temperature water-gas shift reaction. *Catalysis Today* **2017,** *298*, 216-225.

80. Yang, M.; Liu, J. L.; Lee, S.; Zugic, B.; Huang, J.; Allard, L. F.; Flytzani-Stephanopoulos, M., A common single-site Pt(II)-O(OH)$^{x-}$ Species stabilized by sodium on "active" and "inert" supports catalyzes the water-gas shift reaction. *Journal of the American Chemical Society* **2015,** *137* (10), 3470-3473.

81. Song, Y. Y.; Grabow, L. C., Activity trends for catalytic CO and NO co-oxidation at low temperature diesel emission conditions. *Industrial & Engineering Chemistry Research* **2018,** *57* (38), 12715-12725.

82. Kummer, J. T., Catalysts for automobile emission control. *Prog. Energy Combust. Sci.* **1980,** *6* (2), 177-199.

83. Lin, J.; Qiao, B.; Li, L.; Guan, H.; Ruan, C.; Wang, A.; Zhang, W.; Wang, X.; Zhang, T., Remarkable effects of hydroxyl species on low-temperature CO (preferential) oxidation over Ir/Fe(OH)$_x$ catalyst. *Journal of Catalysis* **2014,** *319*, 142-149.

84. Baschuk, J. J.; Li, X. G., Carbon monoxide poisoning of proton exchange membrane fuel cells. *Int J Energ Res* **2001,** *25* (8), 695-713.

85. Rodrigues, A.; Amphlett, J. C.; Mann, R. F.; Peppley, B. A.; Roberge, P. R., Carbon monoxide poisoning of proton-exchange membrane fuel cells. *Iecec-97 - Proceedings of*

the Thirty-Second Intersociety Energy Conversion Engineering Conference, Vols 1-4 **1997**, 768-773.

86. Haruta, M.; Tsubota, S.; Kobayashi, T.; Kageyama, H.; Genet, M. J.; Delmon, B., Low-temperature oxidation of Co over gold supported on TiO_2, alpha-$Fe2O_3$, and Co_3O_4. *Journal of Catalysis* **1993,** *144* (1), 175-192.

87. Lopez, N.; Janssens, T. V. W.; Clausen, B. S.; Xu, Y.; Mavrikakis, M.; Bligaard, T.; Norskov, J. K., On the origin of the catalytic activity of gold nanoparticles for low-temperature CO oxidation. *Journal of Catalysis* **2004,** *223* (1), 232-235.

88. Fampiou, I.; Ramasubramaniam, A., Influence of support effects on CO Oxidation kinetics on CO-saturated graphene-supported Pt_{13} nanoclusters. *The Journal of Physical Chemistry C* **2015,** *119* (16), 8703-8710.

89. Comotti, M.; Li, W.-C.; Spliethoff, B.; Schüth, F., Support effect in high activity gold catalysts for CO oxidation. *Journal of the American Chemical Society* **2006,** *128* (3), 917-924.

90. Lee, S.; Fan, C.; Wu, T.; Anderson, S. L., CO Oxidation on Au_n/TiO_2 catalysts produced by size-selected cluster deposition. *Journal of the American Chemical Society* **2004,** *126* (18), 5682-5683.

91. Li, L.; Gao, Y.; Li, H.; Zhao, Y.; Pei, Y.; Chen, Z. F.; Zeng, X. C., CO oxidation on TiO_2 (110) supported subnanometer gold clusters: size and shape effects. *Journal of the American Chemical Society* **2013,** *135* (51), 19336-19346.

92. Liu, C. Y.; Tan, Y. Z.; Lin, S. S.; Li, H.; Wu, X. J.; Li, L.; Pei, Y.; Zeng, X. C., CO self-promoting oxidation on nanosized gold clusters: triangular Au_3 active site and CO induced O-O scission. *Journal of the American Chemical Society* **2013,** *135* (7), 2583-2595.

93. Moses-DeBusk, M.; Yoon, M.; Allard, L. F.; Mullins, D. R.; Wu, Z. L.; Yang, X. F.; Veith, G.; Stocks, G. M.; Narula, C. K., CO Oxidation on supported single Pt atoms: experimental and ab initio density functional studies of CO interaction with Pt atom on theta-Al_2O_3(010) surface. *Journal of the American Chemical Society* **2013,** *135* (34), 12634-12645.

94. Ding, K.; Gulec, A.; Johnson, A. M.; Schweitzer, N. M.; Stucky, G. D.; Marks, L. D.; Stair, P. C., Identification of active sites in CO oxidation and water-gas shift over supported Pt catalysts. *Science* **2015,** *350* (6257), 189-192.

95. Jones, J.; Xiong, H. F.; Delariva, A. T.; Peterson, E. J.; Pham, H.; Challa, S. R.; Qi, G. S.; Oh, S.; Wiebenga, M. H.; Hernandez, X. I. P.; Wang, Y.; Datye, A. K., Thermally stable single-atom platinum-on-ceria catalysts via atom trapping. *Science* **2016,** *353* (6295), 150-154.

96. Lu, Y. B.; Ma, X. F.; Xin, H. L.; Karim, A., Supported Ir single atoms, subnanometer clusters and nanoparticles for CO oxidation. *Abstracts of Papers of the American Chemical Society* **2016,** *251*.

97. Lu, Y. B.; Kuo, C. T.; Ma, X. F.; Xin, H. L.; Karim, A., Mechanism of CO oxidation on supported Ir and Pt single atoms. *Abstracts of Papers of the American Chemical Society* **2017,** *253*.

98. Lu, Y. B.; Ma, X. F.; Kovarik, L.; Xin, H. L.; Karim, A., Origin of low temperature CO oxidation activity on Ir single atoms - Experimental and computational study. *Abstracts of Papers of the American Chemical Society* **2017,** *253*.

99. Lu, Y. B.; Hoffman, A.; Boubnov, A.; Bare, S.; Karim, A., In-situ/operando characterization of supported Ir single atoms. *Abstracts of Papers of the American Chemical Society* **2018,** *255*.

100. Berlowitz, P. J.; Peden, C. H. F.; Goodman, D. W., Kinetics of CO Oxidation on single-crystal Pd, Pt, and Ir. *Journal of Physical Chemistry* **1988,** *92* (18), 5213-5221.

101. Gao, F.; Wang, Y. L.; Goodman, D. W., CO Oxidation over AuPd(100) from ultrahigh vacuum to near-atmospheric pressures: CO adsorption-induced surface segregation and reaction kinetics. *Journal of Physical Chemistry C* **2009,** *113* (33), 14993-15000.

102. Allian, A. D.; Takanabe, K.; Fujdala, K. L.; Hao, X.; Truex, T. J.; Cai, J.; Buda, C.; Neurock, M.; Iglesia, E., Chemisorption of CO and mechanism of CO oxidation on supported platinum nanoclusters. *J Am Chem Soc* **2011,** *133* (12), 4498-517.

103. Chen, H. T.; Chang, J. G.; Ju, S. P.; Chen, H. L., First-principle calculations on CO oxidation catalyzed by a gold nanoparticle. *J. Comput. Chem.* **2010,** *31* (2), 258-265.

104. Lopez, N.; Norskov, J. K., Catalytic CO oxidation by a gold nanoparticle: A density functional study. *Journal of the American Chemical Society* **2002,** *124* (38), 11262-11263.

105. Nie, L.; Mei, D. H.; Xiong, H. F.; Peng, B.; Ken, Z. B.; Hernandez, X. I. P.; DeLariva, A.; Wang, M.; Engelhard, M. H.; Kovarik, L.; Datye, A. K.; Wang, Y., Activation of surface

lattice oxygen in single-atom Pt/CeO_2 for low-temperature CO oxidation. *Science* **2017,** *358* (6369), 1419-+.

106. Abbet, S.; Heiz, U.; Hakkinen, H.; Landman, U., CO oxidation on a single Pd atom supported on magnesia. *Physical Review Letters* **2001,** *86* (26), 5950-5953.

107. Ghosh, T. K.; Nair, N. N., Rh1/-Al2O3 Single-Atom Catalysis of O_2 Activation and CO Oxidation: mechanism, effects of hydration, oxidation state, and cluster size. *Chemcatchem* **2013,** *5* (7), 1811-1821.

108. Li, W. Z.; Kovarik, L.; Mei, D.; Liu, J.; Wang, Y.; Peden, C. H., Stable platinum nanoparticles on specific $MgAl_2O_4$ spinel facets at high temperatures in oxidizing atmospheres. *Nature communications* **2013,** *4*, 2481.

109. Li, W.-Z.; Kovarik, L.; Mei, D.; Engelhard, M. H.; Gao, F.; Liu, J.; Wang, Y.; Peden, C. H. F., A General mechanism for stabilizing the small sizes of precious metal nanoparticles on oxide supports. *Chemistry of Materials* **2014,** *26* (19), 5475-5481.

110. Mei, D.; Glezakou, V.-A.; Lebarbier, V.; Kovarik, L.; Wan, H.; Albrecht, K. O.; Gerber, M.; Rousseau, R.; Dagle, R. A., Highly active and stable $MgAl_2O_4$-supported Rh and Ir catalysts for methane steam reforming: A combined experimental and theoretical study. *Journal of Catalysis* **2014,** *316*, 11-23.

Chapter 2. Identification of the Active Complex for CO Oxidation over Single Atom Ir-on-$MgAl_2O_4$ Catalysts

This work has been published in *Nature Catalysis* and is available online. Reprinted (adapted) with permission from Lu, Y.; Wang, J.; Yu, L.; Kovarik, L.; Zhang, X.; Hoffman, A. S.; Gallo, A.; Bare, S. R.; Sokaras, D.; Kroll, T.; Dagle, V.; Xin, H.; Karim, A. M., Identification of the active complex for CO oxidation over single-atom Ir-on-$MgAl_2O_4$ catalysts. *Nature Catalysis* **2019,** *2* (2), 149-156.

This published article was co-authored by: Jiamin Wang,[1] Liang Yu,[1] Libor Kovarik,[2] Xiwen Zhang,[1] Adam Hoffman,[3] Alessandro Gallo,[4,5] Simon R. Bare,[3] Dimosthenis Sokaras,[3] Thomas Kroll,[3] Vanessa Dagle,[2] Hongliang Xin,[1*] Ayman M. Karim[1*]

Author Affiliation:

[1]Department of Chemical Engineering, Virginia Polytechnic Institute and State University, Blacksburg, VA 24060, USA.

[2]Pacific Northwest National Laboratory, Richland, WA 99352, USA.

[3]Stanford Synchrotron Radiation Lightsource, SLAC National Accelerator Laboratory, Menlo Park, CA 94025, USA.

[4]Department of Chemical Engineering, Stanford University, Stanford, CA 94305, USA.

[5]SUNCAT Center for Interface Science and Catalysis, SLAC National Accelerator Laboratory, Menlo Park, CA 94025, USA.

Attribution:

Yubing Lu performed the synthesis of all catalysts, characterizations (DRIFTS, helping with HERFD), catalytic tests, data analysis, reaction mechanism analysis and wrote the first draft of the paper. Jiamin Wang performed the DFT calculations for the reaction barriers and IR frequencies. Liang Yu performed the XANES DFT calculations. Libor Kovarik conducted the STEM analysis and contributed to the writing of the STEM section. Xiwen Zhang performed synthesis and catalytic reproducibility tests. Adam Hoffman, Alessandro Gallo, and Simon R. Bare designed and performed the HERFD experiments and data analysis and contributed to writing the XAS section. Dimosthenis Sokaras and Thomas Kroll were responsible for optimizing the crystal optics, developing the scripts to allow the HERFD data to be collected and monitoring the initial data quality. Vanessa Dagle synthesized and characterized the 1% $Ir/MgAl_2O_4$ catalyst. Hongliang Xin designed and directed the computational part of the study and the writing of the DFT results. Ayman M. Karim conceived the idea and planned and directed the project. Yubing Lu, Hongliang Xin and Ayman M. Karim co-wrote the paper. All the authors discussed the results and commented on the paper.

*Correspondence to: Hongliang Xin hxin@vt.edu and Ayman M. Karim amkarim@vt.edu.

2.1. Abstract

Supported single atoms provide an opportunity to design new heterogeneous catalysts while optimizing the utilization of noble metals. However, identification of the active single-atom structure is required for understanding the reaction mechanism and guiding catalyst design. Here, we use in-situ infrared spectroscopy, operando x-ray adsorption spectroscopy and quantum chemical calculations to identify the active single-atom complex as well as the resting state of the $Ir/MgAl_2O_4$ catalysts during the low-temperature CO oxidation. In contrast to poisoning of iridium nanoparticles by CO, here we show that the formation of Ir(CO) on single atoms results in a different reaction mechanism and high activity for low-temperature CO oxidation. This is due to the ability of single atoms to coordinate with multiple ligands, where Ir(CO) provides an interfacial site for facile O_2 activation between Ir and Al and lowers the reaction barrier between gas phase CO(g) and *O in Ir(CO)(O) through an Eley-Rideal mechanism.

2.2. Introduction

The catalytic oxidation of carbon monoxide (CO) to carbon dioxide (CO_2) is an important reaction for several processes, including removal of CO from H_2 for fuel cell applications[1, 2], and automotive emission control[3, 4]. Supported single atoms make the best utilization of noble metals [5], offer unique electronic properties[6-9] and also provide an ideal system to understand the reaction mechanisms on a molecular level and guide the development of optimized catalysts[10]. Additionally, single-atom catalysts (SAC) provide valuable information to bridge homogeneous and heterogeneous catalysis[7, 9, 11]. Currently, the reaction mechanism for low-temperature CO oxidation on supported metal single atoms is highly debated and there is no agreement in the literature on whether single atoms exhibit higher intrinsic activity than their larger nanoparticles

(NP) counterparts, especially on non-reducible metal oxide supports. For instance, Pt single atoms supported on FeO_x[12] and Al_2O_3[13, 14] catalysts were reported to be active for low-temperature CO oxidation. Additionally, mononuclear Pt (and Au) coordinated with $O(OH)_x$-(Na or K) ensembles were found to be active for low-temperature water gas shift[15, 16]. On the other hand, other reports indicated that isolated Pt sites on Al_2O_3 and CeO_2 were not active for low-temperature CO oxidation[17-19] or water gas shift[17]. Recently, steam treatment of Pt_1/CeO_2 (at 750 °C) led to a much higher activity for CO oxidation by activating the CeO_2 surface lattice oxygen. However, using infrared spectroscopy, a CO band at 2096 cm^{-1} was observed during CO oxidation and in O_2 flow at 180 °C [20] indicating strong CO adsorption on Pt single atoms. To resolve some of these discrepancies, identification of the active structure (ligand configuration) under reaction conditions is required. Therefore, detailed kinetic studies coupled with in situ/operando spectroscopy and quantum chemical calculations are critical for understanding the reaction mechanism and identifying the relationship between catalytic activity and ligand configuration on supported single atoms to help design catalysts on a molecular level.

In this work, we used in-situ and operando infrared and x-ray absorption spectroscopies and quantum chemical calculations to identify the Ir single-atom complex formed during CO oxidation and probed its reactivity towards CO, O_2, and $CO+O_2$, thereby providing insights on the individual reaction steps. Additionally, we benchmarked the low-temperature CO oxidation kinetics on supported Ir single atoms and Ir nanoparticles to elucidate the differences in reaction mechanisms. $MgAl_2O_4$ was used as a support because it has been shown to stabilize noble metal clusters and single atoms against sintering[21-23]. Ir was chosen for this study since Ir nanoparticles have similar

catalytic properties to Pt for CO oxidation and Ir single atoms have been more widely characterized using x-ray absorption spectroscopy and infrared spectroscopy of adsorbed CO[5, 24-26].

2.3. Methods

Synthesis and pretreatment. The 0.0025% single-atom catalyst (SAC) was prepared by wet impregnation. The $MgAl_2O_4$ support (Puralox MG 28, Sasol) was calcined at 500 °C for 4 hr before impregnation. 200 mL DI water was added to a Pyrex bottle and the pH was adjusted with nitric acid to 2.8. The Ir nitrate precursor (8.7 wt. % Ir, Furuya Metal CO. Ltd.) was added into the pH adjusted solution. The $MgAl_2O_4$ support was then added into the solution while stirring. The final pH of the solution was 9.5. The nominal Ir weight loading was 0.0025%. After 12 hr of stirring, the solution was filtered out and the solid sample was dried in air for 24 hr at room temperature. The sample was then dried at 80 ℃ and 100 °C before calcination at 500 °C for 4 hr. The Ir in the solution after filtration was measured by inductively coupled plasma atomic emission spectroscopy and no Ir was detected. The 1% Ir/$MgAl_2O_4$ samples were synthesized by incipient impregnation. The proper amount of Ir nitrate precursor was added to the $MgAl_2O_4$ support (Puralox MG30, Sasol) drop by drop, and the sample was then dried at 80 °C and 100 °C (at 0.5 °C/min) for 4 hr respectively. The dried sample was then calcined at 500 °C in air for 4 hr. The 0.2 % Ir/MgA_2O_4 nanoparticle sample was prepared by wet impregnation. Proper amount $Ir(CO)_2(acac)$ (Sigma Aldrich) precursor was dissolved in 8 mL of toluene (Sigma Aldrich) in a 20 ml vial while flowing N_2 at room temperature. Then the dissolved $Ir(CO)_2(acac)$ toluene solution was injected into another vial containing 5g $MgAl_2O_4$ (Puralox MG 28, Sasol) under N_2 flow. The sample was then dried under N_2 flow at room temperature overnight to evaporate the toluene. No calcination was

performed on this catalyst. The CO and acac ligands were removed in-situ by treatment in H_2 at 500 °C which led to the formation of 1 nm nanoparticles as detailed below.

All the in-situ characterizations and the CO oxidation reaction followed the same pretreatment procedure. For the Ir single-atom catalyst, the sample was calcined in 5 kPa O_2 (certified grade, Airgas) at 100 °C for 30 min (1 °C/min ramp rate) and 400 °C for 30 min (5 °C/min ramp rate). The calcined sample was then pretreated in He (99.999% Airgas) at 650 °C for 30 min with 15 °C/min ramp rate. The temperature was then cooled in He to 110 °C and purged for 10 min before switching to 20 kPa H_2 (balance He). The sample was then reduced in H_2 (99.999% Airgas) at 500 °C (15 °C/min ramp rate) for 2 hr. After reduction, He was used to flush the H_2 at 650 °C for 30 min then cooled down in He to 35 °C. For the 1% Ir catalyst, after calcination at 500°C, the catalyst was reduced in 20 kPa H_2 at 800 °C (15 °C /min) for 2 hours followed by flushing with He for 30 min at the same temperature then cooling down in He to 35 °C. The 0.2% Ir/MgA_2O_4 nanoparticle sample (prepared with $Ir(CO)_2$(acac) precursor) was pretreated with 20 kPa H_2 at 500 °C (10 °C/min ramp rate) for 2 hours to remove the CO and acac ligands and then cooled down in 20% H_2 to room temperature and then purged with He for 10 min.

DRIFTS. DRIFTS was used to characterize the interaction of the supported Ir catalysts with CO. The in-situ DRIFTS experiments were performed using a Thermo Scientific IS-50R FT-IR equipped with an MCT/A detector. Spectral resolution of 4 cm^{-1} was used to collect spectra which are reported in the Kubelka-Munk (KM) units. Approximately 50 mg sample (25-90 microns) was loaded in the Harrick Praying Mantis high-temperature DRIFTS reaction chamber. The chamber was sealed and connected to a flow system with temperature control, and gases were flown through

the sample at atmospheric pressure. Each reported spectrum is an average of 32 scans. The supported Ir samples were pretreated in-situ in the DRITS cell before collecting the spectra. The gas pretreatment procedure was the same as previously mentioned. The composition of the effluent gases was measured by an online quadrupole mass spectrometer (Pfeiffer Omni Star, QMG220). A secondary electron multiplier detector was used to monitor signals for CO_2 (m/z = 44 and m/z=28), CO (m/z = 28), O_2 (m/z = 32) and He (m/z = 4). The CO line connected to the IR and the flow reactor for kinetic measurements was equipped with a metal carbonyl purifier (Matheson, NanoChem Metal-X) to remove the trace amount of metal carbonyl as well as the molecular sieve 3A (8-12 mesh) trap to remove trace (ppm) levels of CO_2. No CO_2 was detected in the mass spectrometer with the CO or O_2 flowing during a blank test. The CO adsorption measurement was conducted at 35 °C unless otherwise stated. The samples were exposed to CO doses by varying the time and also increasing the partial pressure of CO (5% CO certified grade, Airgas). As a reference experiment, the $MgAl_2O_4$ support was pretreated with the same procedure as the 0.0025% Ir/$MgAl_2O_4$ (SAC), and no IR band was detected in the ν_{CO} region.

HERFD-XANES. HERFD-XANES measurements were collected at Beamline 6-2 at the Stanford Synchrotron Radiation Light Source (SSRL) [41]. A liquid-nitrogen-cooled double-crystal Si(311) monochromator was equipped to select the energy of the incident beam with a flux of 3 x 10^{12} photons × s^{-1}. A Rowland circle spectrometer (radius 1 m) equipped with three spherically bent Si (800) analyzers and a silicon drift detector was used to select the Ir L_α (9175 eV) emission line with a measured resolution of 1.3 eV. An iridium foil was scanned in the transmission mode for initial energy calibration.

Each sample (120 mg in mass, 25-90 microns) was loaded into a packed bed flow reactor. The in-situ packed bed reactor consists of a Be tube (Materion; PF-60 Grade) (OD 5 mm and ID 3.8 mm) connected to the gas line using graphite ferrules and heated by a stainless steel heating block equipped with four 100 W heating cartridges (Watlow). The in-situ reactor assembly was protected from oxidation by an air-free box with polyimide film X-rays windows and continuous He or N_2 flow. Two type-K thermocouples were used to monitor and control the heating block and the catalytic bed temperature. A portable gas delivery system equipped with 5 MFCs (Brooks - SLA5800) was used to control the gas flow. The composition of effluent gases was measured by an online quadrupole mass spectrometer (Hiden HPR20). The 0.0025% $Ir/MgAl_2O_4$ (SAC) was first heated in a flow of 10 kPa O_2, balance He (Certified grade Airgas) to 400 °C at 10 °C/min followed by a dwell of 20 min. Then the sample was pretreated with He (99.999% Airgas) at 650 °C for 30 min and cooled down to room temperature, and then H_2 (99.999% Airgas) 500 °C and He 650 °C steps as described in the previous synthesis and pretreatment section. The pretreated sample was then cooled down in He to room temperature. At room temperature, 5 kPa CO (Certified grade Airgas) was introduced into the reactor and HERFD-XANES spectra were collected during CO flow. After CO flow the reactor was purged with He. 5 kPa O_2 was then introduced into the reactor and HERFD-XANES spectra were collected during O_2 flow. The sample was then heated in 0.4 kPa CO + 2 kPa O_2 to 155 °C. After CO oxidation with 1 kPa CO + 8 kPa O_2 at 155 °C for 1 hr the reactor was cooled down to 100 °C under He flow. At 100 °C 2 kPa CO was pulsed into the reactor chamber multiple times. After HERFD XANES spectra were stabilized, 1 kPa CO + 8 kPa O_2 were flowed through the sample. HERFD-XANES spectra were

collected the entire time at 155 and 100 °C. The total flow rate was kept at 50 sccm during pretreatment and measurement.

All HERFD-XANES spectra were measured within 2 min and three to six scans were averaged to improve signal-to-noise ratio. The analysis of the HERFD XANES data was carried out with the software ATHENA of the IFEFFIT package [42, 43]. The edge, determined by the first inflection point of the absorption edge of the Ir foil, was calibrated to the reported Ir L_3 energy, 11215 eV. This calibration was used to calibrate a known glitch in the monochromator observed in the I_0 signal of each scan. A least-squares Gaussian fit of the glitch, determined the error in the energy calibration of the samples to be 0.022 eV. Energy calibration was achieved by aligning the glitch in each scan to the glitch in the Ir foil reference scans. Three to six scans per sample were averaged with the averaged spectra being used for deglitching and normalization. The averaged spectrum was processed by fitting a second-order polynomial to the pre-edge region and subtracting this from the entire spectrum. Edge energy was determined by the first derivative of the normalized absorbance. The data were normalized by dividing the absorption intensity by the height of the absorption edge.

Volumetric chemisorption. Volumetric O_2/CO chemisorption was performed with a Mircromeritics 3Flex. 0.6 g of catalyst was packed in a quartz sample holder and pretreated with the same procedure described in the synthesis section. The total flow rate for each step was 80 sccm. The sample with pellet size between 425 – 710 microns was evacuated at 35 °C for 1 h before the O_2/CO (99.999%, Airgas) chemisorption analysis. Two O_2/CO chemisorption isotherms were performed between 5 mmHg and 450 mm Hg at 35 °C with an evacuation step between the two isotherms to remove the physically adsorbed O_2/CO. The 1st isotherm represents both the

chemisorbed and the physisorbed O_2/CO. The 2nd isotherm indicates the amount of physisorbed O_2/CO. The difference between the two O_2/CO isotherms is reported as the amount of chemisorbed O_2/CO. The dispersion of 1% Ir/$MgAl_2O_4$ catalyst (calcined at 500 °C and reduced at 800 °C) was measured as 90% with a stoichiometry of 1CO:1Ir. The stoichiometry of 1 CO:Ir was used to calculate the dispersion of Ir nanoparticle catalyst (0.2% Ir/$MgAl_2O_4$) (Supplementary Table 5) [44] and 100% dispersion was used for calculating TOF on the 0.0025% Ir/$MgAl_2O_4$ (SAC) considering the low weight loading of Ir.

BET surface area. The BET surface area was measured by multiple-point N_2 adsorption and desorption cycles in a Micromeritics 3Flex at 77.35 K. All samples were degassed at 200 °C with N_2 flow overnight before measurement.

CO oxidation kinetic measurements. CO oxidation kinetic measurements were performed under differential conditions in a conventional laboratory tubular plug flow reactor (7 mm inner diameter quartz tube). Dilution experiments were performed according to Koros-Nowak test to determine the necessary dilution ratio for measurements under strict kinetic control without mass and heat transfer effects [45-47]. The catalysts (after intraparticle dilution) were pressed into 106-250 microns pellets. The dilution ratio test to eliminate transport limitations was performed on 2% Pt/γ-Al_2O_3 catalyst using γ-Al_2O_3 as the diluent. Intraparticle dilutions ratio of 1:200 and 1:1000 showed no difference in activity under different CO and O_2 conditions between 145 °C and 170 °C, which indicates the measured catalytic activity were evaluated under kinetic control without any transport artifacts. Based on the dilution test, the 0.2% Ir/$MgAl_2O_4$ was diluted with silica at a 1:40 ratio and the 1% Ir/$MgAl_2O_4$ was diluted with silica at a 1:200 ratio, and the 0.0025% Ir/$MgAl_2O_4$ (SAC) required no dilution because of the low Ir loading. Negligible activity was measured on the

$MgAl_2O_4$ support compared with all the catalysts. Each catalyst pretreatment was the same as mentioned above, and the total flow rate during pretreatment was kept at 80 sccm. After pretreatment, 5% CO (certified grade Airgas) was mixed with 100% O_2 (99.999% Airgas) and He (99.999% Airgas) at 35 °C. The catalyst temperature was measured by a K-type thermocouple (OMEGA) attached at the center of the catalyst bed on the outside of the tube. The reactor was heated from room temperature to the reaction temperature at 3 °C/min in 0.1 kPa CO and 2 kPa O_2 balanced with He. During the steady-state kinetic measurements, the conversion of CO was always below 3% by varying the total flow rate between 50-100 sccm. To investigate the effect of CO partial pressure on reaction rate, the partial pressure of O_2 was held constant at 10 kPa (Fig. 2a, c) and the partial pressure of CO was varied between 0.1 – 1 kPa. To investigate the effect of O_2 partial pressure, the CO partial pressure was held constant at 1 kPa (Fig. 2b) and the partial pressure of O_2 was varied between 2 – 14 kPa, then the measurements were repeated at 0.2 kPa CO partial pressure (Supplementary Fig. 3). The kinetic measurements for each catalyst took between 12 to 18 hours for each experiment. The 0.2% $Ir/MgAl_2O_4$ (NP) catalyst stability was not affected by the higher CO partial pressures during the CO or O_2 reaction order measurements. The kinetic experiments were reproduced using two different aliquots from the same batch and also reproduced using two different batches. Error bars of the kinetic measurements were calculated based on multiple points on the same catalyst at different times during one experiment and from experiments using different catalyst aliquots/batches.

The composition of the effluent gases was measured by a gas chromatograph (Inficon Micro GC Fusion). Turn over frequencies (TOFs) were calculated by normalizing the reaction rate

(mol/g_{cat}/s) to the number of Ir sites per gram of catalyst (mol_{Ir}/g_{cat}) measured by using CO chemisorption as discussed in the volumetric chemisorption section.

We should note that we rigorously monitored the catalyst stability by re-measuring the catalyst periodically throughout the experiment under the first condition measured and the catalyst activity was very stable (±5%) during the entire kinetic measurement. HAADF-STEM images of the catalysts after CO oxidation (Supplementary Fig. 1) indicate Ir remains atomically dispersed during the reaction.

Scanning transmission electron microscopy. Aberration-corrected electron microscopy images for Ir/$MgAl_2O_4$ samples were taken on FEI TITAN 80-300 in STEM mode using a high angle annular dark field (HAADF) detector. The resolution is 0.1 nm, with the CEOS GmbH double-hexapole aberration corrector. To calculate the atomic percentage of each catalyst from multiple STEM images, the number of atoms per particle (N) was estimated with a spherical model[48]:

$$N = \frac{\pi D^3 \rho N_A}{6 M_w} \quad (1)$$

where D is the nanoparticle diameter, ρ is the bulk metal density, N_A is Avogadro's number, and Mw is the metal molecular weight.

DFT calculations of reaction pathways. All DFT calculations were performed by QUICKSTEP in CP2K package [49]. The exchange-correlation potential was treated with the generalized gradient approximation parameterized by the spin-polarized Perdew-Burke-Ernzerh functional[50]. The wave functions were expanded in molecular optimized double-ζ valence polarized Gaussian basis sets (DZVP-MOLOPT-SR-GTH) for Al, Mg and Ir elements, triple-ζ valence basis sets (TZV2P-MOLOPT-GTH) for O and C elements, with an auxiliary plane-wave basis set with a cutoff energy

of 480 Rydberg. Brillouin zone integration is performed with a reciprocal space mesh consisting of only the gamma point. The DFT-D3 van der Waals correction by Grimme[51] was applied. Core electrons have been modeled by the scalar relativistic norm-conserving Goedecker-Teter-Hutter (GTH) potentials with 10, 3, 6, 4 and 17 valence electrons for Mg, Al, O, C and Ir, respectively. The spinel $MgAl_2O_4$ bulk structure has a face-centered cubic Bravais lattice with space group Fd3m. Optimized lattice constant with a = 8.146 Å is close to experimental value a = 8.086 Å[37]. The O_2(Al)-termination was shown to be the most stable for $MgAl_2O_4$[37]. Therefore, the model system used for the DFT calculations is an O_2(Al)-terminated $MgAl_2O_4$ (111) and (211) surfaces with periodic boundary condition along x, y and z-direction. Ir single atoms were adsorbed at different sites (Supplementary Table 3). Vacuum of 15 Å distance was added along z direction to avoid interactions with the adjacent cell. In cell and geometry optimizations, the maximum forces were converged to 4.5×10^{-4} Hartree/Bohr. The zero-point energy and entropy correction were obtained from the quasi-harmonic approximation. For molecules, the translational and rotational contributions to internal energy and entropy are taken into account using statistical thermodynamics. To locate the transition state, we use climbing image nudged-elastic-band method (CI-NEB)[52]. Vibrational analysis was used to further verify transition states, only one imaginary frequency mode indicates that the transition states are the true saddle points.

XANES Simulations. XANES spectra calculations are performed using the plane-wave based PWSCF (Quantum-ESPRESSO) code. The ultrasoft Vanderbilt pseudopotential method with Perdew-Burke-Ernzerhof (PBE) exchange-correlation functional is adopted. A cutoff energy of 700 eV for the wave functions is used. The Monkhorst-Pack scheme is used for sampling the Brillouin zone. To determine Ir L3-edge spectra, we create a special pseudopotential for the Ir

atom, which contains an Ir 2p core hole. In the SCF calculation to obtain the converged wave function and charge density, spin-polarization is not considered and the total charge of the system is specified as +1 in order to compensate the extra electron in the empty states, i.e., the excited-state core-hole (XCH) approximation. The spectrum is calculated using the XSpectra program which gives the X-ray absorption cross section as a function of excitation energy relative to the LUMO energy. A Lorentzian broadening factor of 1.5 eV related to the core-hole lifetime is chosen for all spectrum calculations. Since the absorbing Ir atoms with different ligands are nonequivalent, we need to obtain the absolute energy scale. To properly align spectra of different structures, the delta Kohn-Sham energy is calculated to represent the transition energy by lifting a core electron from the ground state to the first core excited state the LUMO[53] using the GPAW program. To have a spin up core hole and an electron in the lowest unoccupied spin up state, the magnetic moment of the Ir atom with the hole is set to one and the total magnetic moment is fixed in spin-polarized calculations. The absolute energy of calculated spectra is corrected using the measured edge energy of $Ir(CO)_2$(Al-v) system where 2CO ligands are adsorbed at $Ir/MgAl_2O_4$ with a surface oxygen vacancy near the active site.

2.4. Results

2.4.1. Atomic resolution characterization

Fig. 1 shows an aberration corrected high angle annular dark field scanning transmission electron microscopy (HAADF-STEM) images of 1% $Ir/MgAl_2O_4$ after calcination at 500 °C before (a) and after reduction in H_2 at 800 °C (b). It can be seen that Ir is predominantly atomically dispersed after calcination but agglomeration occurs during reduction and the relative amount of single atoms

compared with nanoparticles decreases at higher reduction temperature. Despite the high reduction temperature, the size of Ir nanoparticles was limited to less than 2 nm which was also observed when MgO was used as the support[27]. By lowering the loading (0.0025 wt.%) only atomically dispersed Ir was detected after pretreatment and a representative image after reduction in H_2 at 500 °C is shown in Fig. 1c and no nanoparticles were detected (Supplementary Fig. 1). $MgAl_2O_4$ resulted in the stabilization of significant fraction of Ir single atoms when iridium nitrate was used for the synthesis even at high Ir weight loadings and after high reduction temperatures as shown in Fig. 1a, b. Therefore, to obtain a reference sample without single atoms, we also synthesized a 0.2% $Ir/MgAl_2O_4$ using $Ir(CO)_2(acac)$ as the precursor, which after removal of the ligands in H_2 at 500 °C resulted in the formation of almost exclusively ~ 1nm nanoparticles as shown in the HAADF-STEM image and the histogram in Fig. 1d and Supplementary Fig. 2.

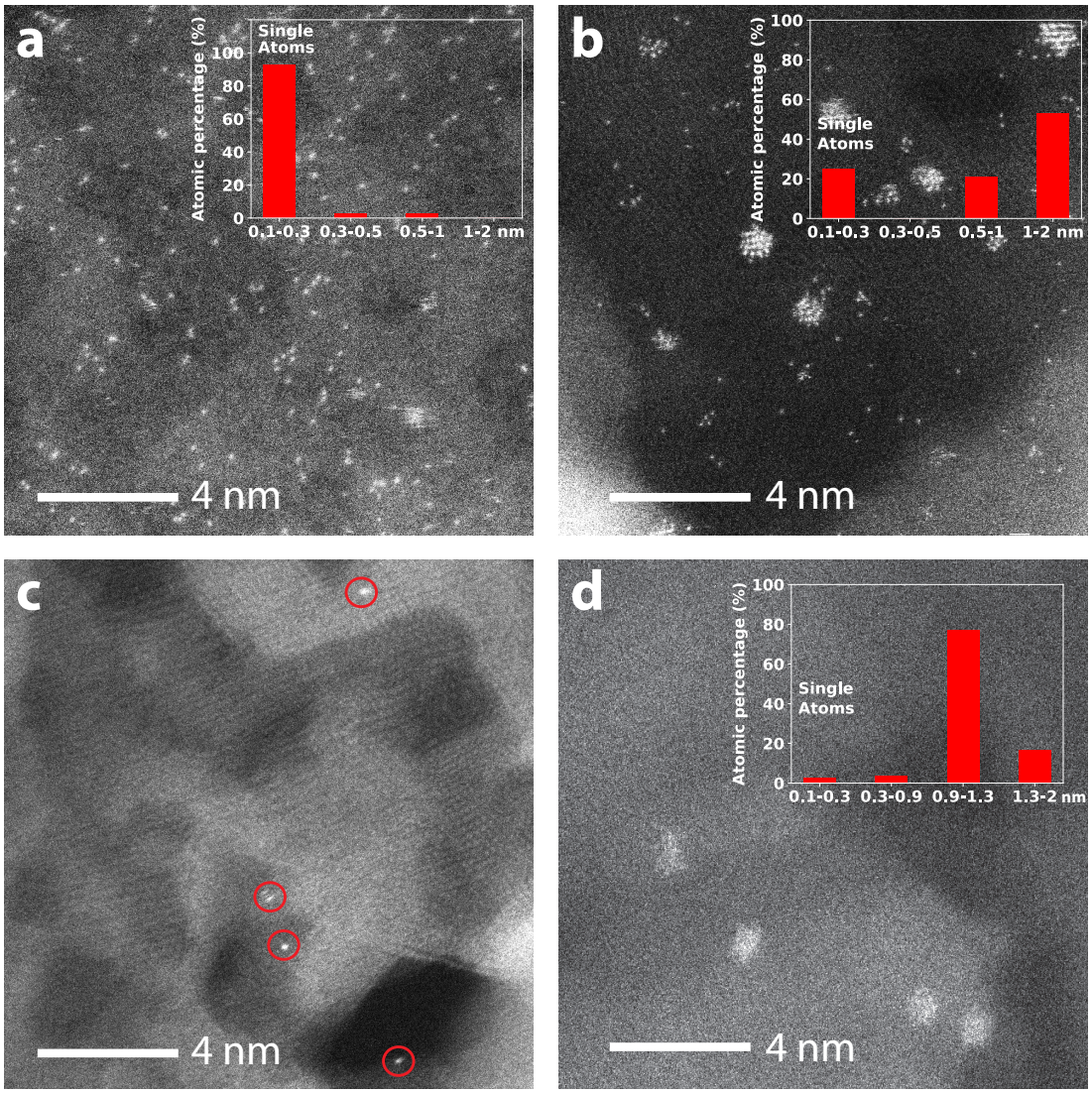

Figure 1. High angle annular dark field – scanning transmission electron microscopy (HAADF-STEM) images of different Ir SAC and NP samples. The inset shows the size distribution of Ir species from multiple STEM images. Representative HAADF-STEM images of 1% Ir/$MgAl_2O_4$ calcined at 500 °C, before (a) and after (b) H_2 reduction at 800 °C. c, 0.0025% Ir/$MgAl_2O_4$ catalyst (SAC) after reduction at 500 °C, the single atoms are identified by red circles, no nanoparticles were detected in lower magnification images for the 0.0025% Ir/$MgAl_2O_4$, see Supplementary Fig.

1. d, 0.2% Ir/$MgAl_2O_4$ (NP) prepared with $Ir(CO)_2$(acac) precursor with average particle size ~ 1nm.

2.4.2. CO oxidation kinetics

The catalytic activity for the 0.0025% $Ir_1/MgAl_2O_4$ single-atom catalyst (SAC) and 0.2% Ir/$MgAl_2O_4$ nanoparticles catalyst (NP) was evaluated for CO oxidation under strict kinetic control, and no deactivation or sintering was observed for the single-atom catalyst (see Supplementary Fig. 1 and other details in supplementary information). The effect of CO (P_{CO}) and O_2 (P_{O_2}) partial pressures on turnover frequency (TOF) was measured at 155 °C and the results are reported in Fig. 2 and Supplementary Fig. 3. On Ir nanoparticles (~ 1 nm), the measured CO and O_2 reaction orders were -1.0 ± 0.1 and 0.9 ± 0.1, respectively. The reaction orders are consistent with the widely accepted CO oxidation mechanism on noble metals (Ir, Pt, Pd, and Rh) where, at low reaction temperatures, the reaction is limited by O_2 activation on a CO-saturated surface[3, 28, 29]. On Ir single atoms, the measured CO and O_2 reactions orders under the same conditions were 0.9 ± 0.1 and 0.1 ± 0.05 respectively, indicating a different mechanism than on nanoparticles (Fig. 2 and Supplementary Fig. 3). In contrast to nanoparticles, the positive CO order of ~1 indicates that Ir single atoms are not poisoned by CO during CO oxidation and the O_2 order of ~0 suggests a facile O_2 activation. More importantly, Ir single atoms are much more active at high CO partial pressure (~7x higher than nanoparticles) while nanoparticles are slightly more active at low CO partial pressure. The different CO reaction orders can be clearly seen for the CO oxidation activity of the catalyst containing a mixture of single atoms and nanoparticles (1% catalyst reduced at 800 °C, STEM image in Fig. 1c and Supplementary Fig 4) which displayed a CO reaction order that

changed from negative to positive as the CO partial pressure increased (Fig. 2c). The differences in reaction orders of CO and O_2 on Ir SAC and NP show that kinetic measurements provide a sensitive probe for the detection of single atoms due to different reaction mechanism. Additionally, these results could help explain some of the disagreements in the literature on whether single atoms are more active than nanoparticles since the catalysts activities were reported at different reaction conditions.

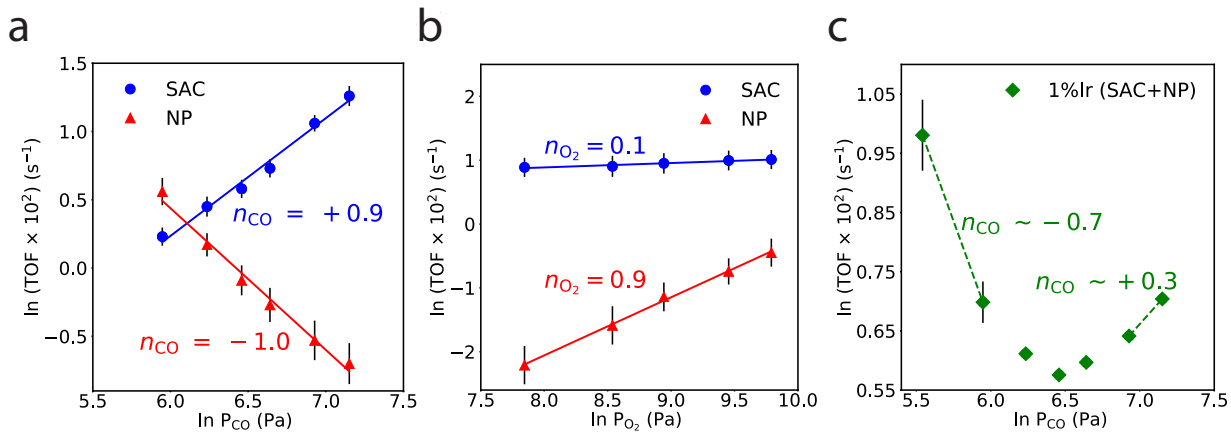

Figure 2. CO oxidation kinetic measurements on Ir SAC, Ir NP, and SAC+NP mixture. Effect of CO **(a)** and O_2 **(b)** partial pressure on turnover frequency (TOF) respectively on supported 0.0025% Ir/$MgAl_2O_4$ (single-atom catalyst, SAC) and 0.2% Ir/ $MgAl_2O_4$ prepared with $Ir(CO)_2$(acac) precursor (nanoparticles, NP) (the $MgAl_2O_4$ support activity was negligible under the conditions tested). P_{O_2}= 10 kPa, P_{CO}= 0.3-1 kPa in A; P_{CO} = 1 kPa, P_{O_2} = 2-14 kPa in B. All measured at 155 °C. **c,** Effect of CO partial pressure on turnover frequency (TOF) on the catalyst containing a mixture of Ir single atoms and nanoparticles, 1% Ir/$MgAl_2O_4$ calcined at 500 °C, and reduced at 800 °C. In panel **c**, estimates of the CO reaction order based on two points at each of the low and high P_{CO} are listed to show the change in order from negative to positive resulting

from the NPs and SAC, respectively. Error bars were calculated based on multiple measurements on the same catalyst at different times during one experiment and from experiments using different catalyst aliquots/batches.

2.4.3. In-situ characterization at room temperature

In-situ diffuse reflectance infrared Fourier transform spectroscopy (DRIFTS) and high-energy resolution fluorescence detected (HERFD) XAS experiments provide important structural and chemical details to better understand the unique CO and O_2 reaction orders on Ir single atoms. Fig. 3a shows the DRIFTS spectrum after adsorption of CO on the 0.0025% Ir/$MgAl_2O_4$ catalyst (SAC) at -60 °C where two bands (2070, 1989 cm^{-1}) can be seen in the C−O vibrational frequency region. These two bands are assigned to the symmetric (ν_s) and the anti-symmetric vibrational modes (ν_{as}) of the Ir gem-dicarbonyl, $Ir(CO)_2$, respectively based on reports of atomically dispersed $Ir(CO)_2$ gem-dicarbonyl supported on MgO and γ-Al_2O_3 [25]. The intensity of the anti-symmetric vibrational band (I_{as}) is slightly higher than the symmetric vibrational (I_s) band and the bond angle between the two CO (θ) can be estimated as 98 ° based on $\frac{I_{as}}{I_s} = \tan^2\left(\frac{\theta}{2}\right)$ [30]. Upon flowing O_2 (0.1 kPa) at -20 °C over the $Ir(CO)_2$, a new single band was observed at a higher frequency (2092 cm^{-1}, a shift of 22 cm^{-1} from the ν_s of $Ir(CO)_2$) suggesting partial oxidation of the Ir single atoms, likely forming Ir(CO)(O). This assignment is made according to a study on Al_2O_3 supported Rh single atoms where O_2 (activated by UV irradiation at -100 °C) reacted with $Rh(CO)_2$ to form Rh(CO)(O) and the observed shift between the Rh(CO)(O) and the symmetric band of $Rh(CO)_2$ was 22 cm^{-1} (from 2100 (symmetric band) to 2122 cm^{-1}) [31, 32]. As a reference, almost no shift of ν_{CO} was

observed when flowing O_2 on Ir nanoparticles (0.2% Ir/$MgAl_2O_4$) as shown in Supplementary Fig. 5.

To complement the DRIFTS results and directly probe the Ir electronic structure, a similar experiment was performed using in-situ high-energy resolution fluorescence detected- x-ray absorption near edge spectroscopy (HERFD-XANES) at the Ir L_3-edge (Fig. 3b). HERFD-XANES has been used to identify the interaction of CO with single metal atoms and nanoparticles and has proved to be a sensitive probe for the detection of ligands bound to metal centers [26, 33-36], e.g. the detection of ethylene and CO ligands adsorbed on catalytically active iridium centers isolated on zeolite HY and on MgO support [26]. After pretreating the sample in a similar manner to the DRIFTS experiment, and flowing CO at room temperature, the resulting spectrum (Fig. 3b red) is assigned to $Ir(CO)_2$ [26]. After flowing O_2 on the carbonylated Ir single atoms ($Ir(CO)_2$), part of the carbonylated feature was replaced by a higher energy feature (blue), suggesting partial oxidation of the Ir which is consistent with the DRIFTS results in Fig. 3a (facile O_2 activation and partial oxidation of Ir). Additionally, CO_2 was detected in the reactor effluent by mass spectrometry (Supplementary Fig. 6). Notably, a similar, but not as significant higher energy feature was also observed (Supplementary Fig. 7) on the 1% Ir sample containing a mixture of single atoms and nanoparticles (STEM.in Fig. 1b) when flowing O_2 on the CO adsorbed saturated catalyst at room temperature.

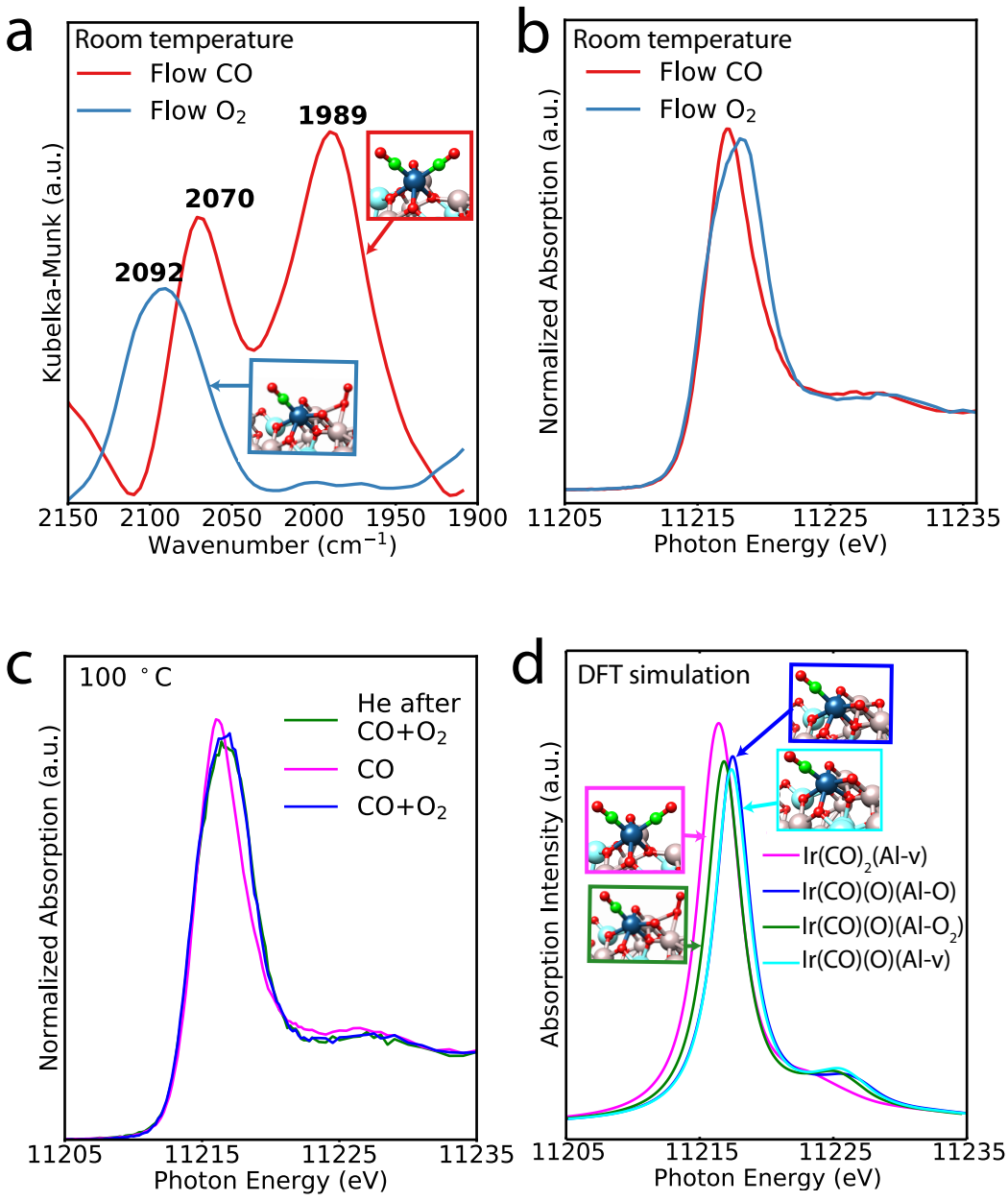

Figure 3. In-situ IR and operando HERFD-XANES spectra (Experimental and DFT) of Ir single atoms. a, In-situ IR spectra in the ν_{CO} region characterizing 0.0025% Ir/$MgAl_2O_4$ (single-atom catalyst, SAC) with CO adsorbed at -60 °C and atmosphere pressure (red), after flowing 5 kPa O_2 on CO adsorbed surfaces at -20 °C and cooled down to -60 °C in He (blue). **b**, HERFD-

XANES spectra of supported Ir SAC after dosing 1 kPa CO at room temperature and atmospheric pressure (red) and then after flowing 5 kPa O_2 at room temperature (blue). **c**, Ir L_3-edge spectra of 0.0025% Ir/$MgAl_2O_4$ (single-atom catalyst, SAC) under He after CO reaction conditions (1 kPa CO and 8 kPa O_2) at 100 °C (green), followed by flowing 2kPa CO at the same temperature (magenta), and then flowing 1 kPa CO and 8 kPa O_2 again at 100 °C (blue). **d**, DFT simulation of Ir L_3-edge spectra of the Ir single atoms with two CO ligands and a surface oxygen vacancy (magenta, Ir$(CO)_2$-(Al-v)), and with a (CO)(O) (blue, Ir(CO)(O)), and with (CO)(O) and adsorbed O_2 on the vacancy on nearest two Al atoms (green, Ir(CO)(O)-(Al-O_2)), and with (CO)(O) and a vacancy on nearest two Al atoms (light blue, Ir(CO)(O)-(Al-v)). The structures in panel D are provided in Supplementary Fig 10.

2.4.4. Mechanistic elucidation of the facile O_2 activation

To provide more details on the ligand (CO, O) configuration on Ir single atoms and the O_2 activation step at low temperature, we performed density functional theory (DFT) calculations of supported Ir single atoms at defect sites of the $MgAl_2O_4$ support. We have compared two model systems, including 1) Ir single atoms supported on $MgAl_2O_4$(111), and 2) Ir replacing the Al atom close to the step of $MgAl_2O_4$(211). The O_2(Al)-termination was used because of its high thermodynamic stability[37]. We found that the second model, i.e., Ir replacing the Al atom on $MgAl_2O_4$(211) step surface, is more plausible to represent the structure of the active site because 3CO ligand configuration is favorable on the (111) model, in contradiction with 2CO ligands observed in the experiments, see those two model structures with CO ligands in Supplementary Table 3. We used this as the $MgAl_2O_4$(211) model system in the following discussion (see

Supplementary Tables 3-6 for model systems, computational details can be found in the supplementary information). Our DFT calculations showed that Ir forms a dicarbonyl in a 6-coordinate structure with 4 oxygens from the support with the differential CO adsorption energy of -1.98 eV. Under CO gas stream, the $Ir(CO)_2$ structure will likely be surrounded by oxygen vacancies or carbonate, forming a locally stable structure. DFT calculations show that O_2 would adsorb on a nearby vacancy with an adsorption energy of -1.05 eV relative to a gas phase O_2. The adsorbed *CO can react with the $*O_2$ forming CO_2 with DFT-calculated kinetic barrier of ~0.58 eV. This pathway for O_2 adsorption and reaction between one *CO in $Ir(CO)_2$ and $*O_2$ to form Ir(CO)(O) (Supplementary Fig. 8) can explain the ability of Ir single atoms to activate O_2 in our low temperature DRIFTS experiments (Fig. 3a). On the other hand, the diffusion of one of the CO ligands in $Ir(CO)_2$ to a slightly further surface oxygen forming CO_2 is associated with a high barrier of ~2 eV (Supplementary Fig. 8). We note that if the vacancy site is occupied by atomic *O instead of $*O_2$, the CO ligand (in $Ir(CO)_2$) diffusion to this surface oxygen forming CO_2 has a low barrier of ~0.45 eV. This locally stable $Ir(CO)_2$ structure suggests that under CO gas stream it will be surrounded by some oxygen vacancies. The bond angle between the two CO from DFT ($\theta = 90°$) is similar to the experimentally estimated angle of 98°. We also note that the Bader charges of the $Ir(CO)_2$ and Ir(CO)(O) complexes calculated by DFT (+0.8 vs. +1.4, Supplementary Table 7) are consistent with the partial oxidation of Ir observed in DRIFTS (Fig. 3a). Therefore, both in-situ techniques (DRIFTS and HERFD-XANES) and DFT calculations indicate that upon CO adsorption at low temperature on the reduced catalyst, Ir single atoms form $Ir(CO)_2$, likely with surface oxygen vacancies. Additionally, the exposure of $Ir(CO)_2$ to O_2 results in facile O_2

activation and the formation of the stable complex Ir(CO)(O) through an incomplete CO oxidation reaction cycle, i.e. $Ir(CO)_2 + O_2 \rightarrow Ir(CO)(O) + CO_2$.

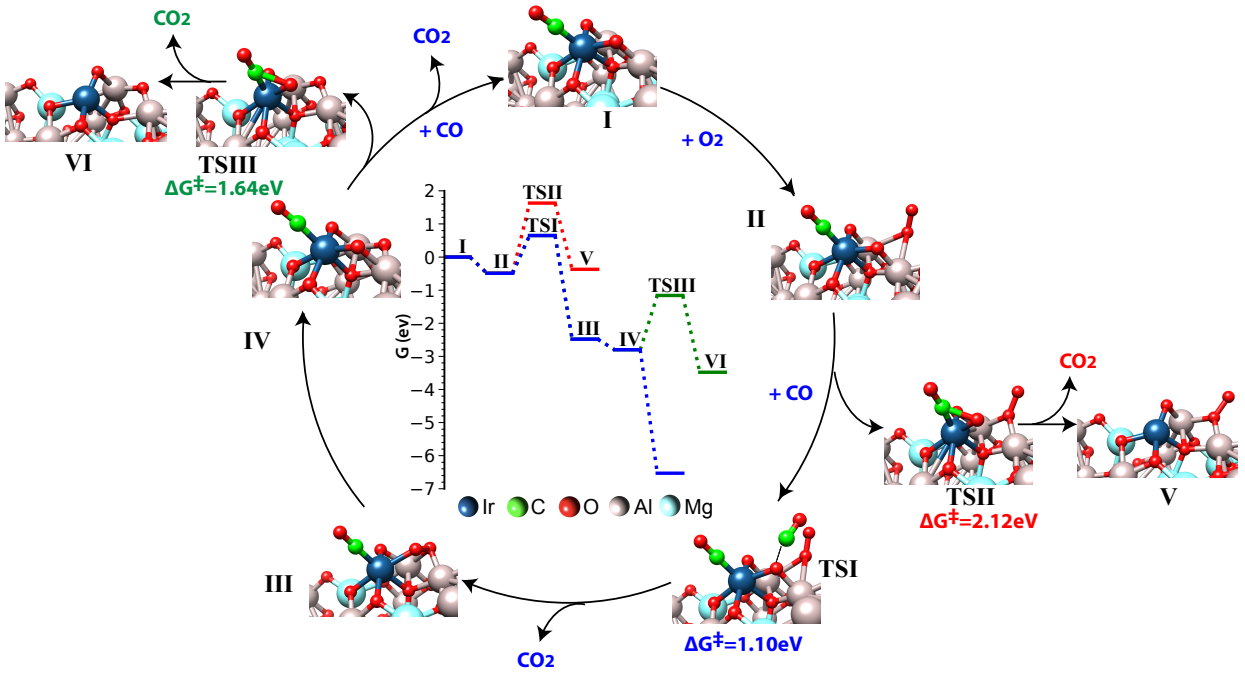

Figure 4. DFT calculated free energy diagram of CO oxidation on Ir single atoms supported on $MgAl_2O_4$. Adsorbed *CO and *O on Ir single atoms on O_2(Al)-terminated $MgAl_2O_4$ (211) surface with a nearby O-vacancy (structure I, Ir(CO)(O)). It is energetically favorable to adsorb oxygen forming $*O_2$ at the vacancy site (structure I→II). Gas phase CO then reacts with the adsorbed O in the Ir(CO)(O) (i.e. E-R pathway, structure II→III) with free energy barrier ~1.1 eV (TSI). In contrast, there is 2.1 eV (TSII) free energy barrier for the reaction between adsorbed *CO and *O in the Ir(CO)(O), i.e., the L-H pathway which is unfavorable. $*O_2$ can then readily dissociate to heal the vacancy (structure III to IV, no barrier). To complete the reaction cycle (structure IV to I), gas phase CO reacts with a surface oxygen (~0 eV free energy barrier), forming

a vacancy, while the L-H pathway through TSIII has a ~1.6 eV barrier. The reaction cycle is limited by the E-R step (gas phase CO reacts with the *O in Ir(CO)(O) (structure II to III).

2.4.5. Operando identification of resting state and active complex

To determine the stability of the Ir(CO)(O) complex and identify the active complex of Ir single atoms during CO oxidation, we performed an operando HERFD-XANES experiment at higher temperatures on the 0.0025% Ir/$MgAl_2O_4$ (SAC) (Fig. 3c). After CO oxidation at 155 °C the temperature was lowered in pure He to 100 °C, and the spectrum at 100 °C in He is shown as the blue spectrum in Fig. 3c. The spectra in pure He and in CO+O_2 at 100 and 155 °C were almost identical (Supplementary Fig. 9) and very similar to the spectrum obtained at room temperature after dosing O_2 on $Ir(CO)_2$ which we assigned to Ir(CO)(O) as discussed above. While Ir(CO)(O) is stable in He and in O_2 at 100 °C, dosing CO on this Ir(CO)(O) complex resulted in the removal of the partially oxidized Ir carbonyl feature in the blue spectrum (CO_2 was detected in the reactor effluent by the mass spectrometer, see Supplementary Fig. 6) and the resulting spectrum (pink spectrum in Fig 3c) was similar to that of $Ir(CO)_2$ obtained at room temperature (red spectrum in Fig. 3a). After dosing CO, we flowed CO and O_2 again at 100 °C, and the final spectrum (blue) shifted back and is almost identical to the original spectrum (green) before dosing CO. The changes in the spectra were reversible and indicate that Ir(CO)(O) is the most stable complex/intermediate under reaction conditions and that Ir(CO) is the active complex (i.e. CO is present as a ligand during the entire reaction cycle). We note that the most stable complex/intermediate for a single atom represents the resting state of the catalyst since this intermediate is involved in the rate

determining step. For nanoparticles, on the other hand, the most stable intermediate can often be a spectator species which blocks most of the surface sites.

2.4.6. DFT calculated CO oxidation mechanism

The stability of Ir(CO)(O) in He and O_2 while reacting with CO (Fig. 3c and Supplementary Fig. 9) suggests that the reaction follows an Eley-Rideal instead of Langmuir-Hinshelwood mechanism. To provide further insights on the reaction mechanism, we calculated the free energy diagram for the different possible pathways starting from Ir(CO)(O) with a surface oxygen vacancy (Fig. 4, Supplementary Table 8). Our DFT results show that it is energetically favorable to adsorb oxygen forming $*O_2$ at the vacancy site. In the following step, the reaction between gas phase CO and adsorbed O in the Ir(CO)(O) (i.e. Eley-Rideal pathway, E-R) has a free energy barrier ~1.1 eV (TSI), suggesting that this step is forbidden at room temperature and only kinetically accessible at higher temperatures. In contrast, there is a 2.1 eV (TSII) activation barrier between adsorbed *CO and *O in the Ir(CO)(O), i.e., the Langmuir-Hinshelwood (L-H) pathway (see Fig. 4). This is consistent with the stability of Ir(CO)(O) in He observed experimentally at 100 °C (Supplementary Fig. 9) while reacting with gas phase CO to form $Ir(CO)_2$ (Fig. 3). Our DFT calculations of the hypothetical pathway without CO adsorbed on Ir show that the reason for the E-R pathway being favorable is that the adsorption of CO weakens the O binding strength on Ir sites by ~3 eV. After the creation of an open coordination at Ir single atoms, the adsorbed O_2 ($*O_2$) can readily dissociate to heal the vacancy with a negligible barrier (structure III to IV). This step is more favorable than adsorption of a second CO from the gas phase which is typically associated with an entropic barrier, consistent with our operando HERFD-XANES where we did not observe $Ir(CO)_2$. In contrast, the

O_2 dissociation on the bare support with two adjacent vacancies has a barrier of ~1.78 eV, indicating the promoting role of Ir single atoms in O_2 activation (Supplementary Fig. 10). To complete the reaction cycle, gas phase CO can react with a nearby surface oxygen (~0 eV free energy barrier), forming a vacancy, while the L-H pathway through TSIII has a ~1.6 eV barrier. The full reaction is kinetically limited by the E-R step for creating an open Ir site in the Ir(CO)(O) structure for a facile O_2 activation. This reaction mechanism is consistent with the measured CO order of ~1 and O_2 order of ~0 on Ir single atoms (Fig. 2).

To further validate the structure of reaction intermediates, we calculated the Ir-L_3 edge XANES spectra of various Ir structures as shown in Fig. 3d and Supplementary Fig. 11 using DFT within the full core-hole approximation [38]. The calculated spectrum (Fig. 3d) for $Ir(CO)_2$ shows a sharp peak with a long tail, similar to the shape of the measured spectrum after dosing CO (Fig. 3b). The steady state spectra exhibit a shoulder at higher energies, which are assigned to a combination of reaction intermediates, Ir(CO)(O)-(Al-v), Ir(CO)(O) and Ir(CO)(O) with O_2 adsorbed on the vacancy (structures I, II and IV in Fig. 4, spectra for other possible structures along the reaction pathway are provided in Supplementary Fig. 11). We note that all the complexes/intermediates in the reaction cycle have a strongly bound CO (~ -2.0 eV binding energy, see Supplementary Table 6) which is consistent with our in-situ/operando experimental results showing that Ir(CO) is the active complex for CO oxidation. We also note that DFT calculations on Ir on $MgAl_2O_4$ (111) showed that the E-R pathway was more favorable than L-H (barrier lower by 0.6- 1 eV) and the XANES spectra for $Ir(CO)_2$ and Ir(CO)(O) on this site were also very similar to those measured experimentally (Fig 3B and 3C), suggesting that the electronic structure and catalytic properties of Ir single atoms is not sensitive to the chosen model.

2.5. Discussion

The in-situ and operando spectroscopy results supported with quantum chemical calculations provide remarkable molecular level details on the mechanism of CO oxidation on supported Ir single atoms. The low temperature in-situ DRIFTS and HERFD-XANES results (Fig. 3a, b, respectively) show that O_2 activation is a kinetically facile step (i.e. it does not affect the overall reaction rate) since it can proceed at and below room temperature, resulting in an incomplete reaction cycle $Ir(CO)_2 + O_2 \rightarrow Ir(CO)(O) + CO_2$. This is consistent with the ~0 reaction order measured for O_2 (Fig. 2) and negligible barrier for O_2 activation calculated by DFT. The HERFD-XANES spectra at higher temperatures confirm that Ir(CO)(O) is the most stable complex (resting state) during CO oxidation (Fig. 3c and Supplementary Fig. 9). Furthermore, the stability of Ir(CO)(O) in helium at the reaction temperature (Supplementary Fig. 9) indicates that the surface reaction between *CO and *O on Ir_1 is not favorable at the investigated temperatures. However, dosing CO on this structure resulted in the formation of $Ir(CO)_2$ (Fig. 3c, d) indicating that at 100 °C, gas phase CO reacts with the *O in Ir(CO)(O) to form CO_2 (Supplementary Fig. 6), followed by CO adsorption to form $Ir(CO)_2$. These experimental results are further supported by the DFT calculated reaction mechanism where O_2 activation has a negligible barrier and the rate-limiting step is the creation of an open coordination at Ir single atoms through an E-R pathway (barrier of 1.1 eV vs. 2.1 eV for L-H pathway). Furthermore, the apparent activation barrier estimated from DFT is ~0.6 eV = 58 kJ/mol (E-R intrinsic barrier of 1.1 eV corrected by the O_2 free energy of adsorption -0.49 eV while assuming the coverage of other intermediates is small) is in agreement with the apparent activation energy of 62 kJ/mol measured experimentally on Ir single atoms

(0.0025% Ir/$MgAl_2O_4$, SAC, Supplementary Fig. 12 and Supplementary Table 9). Therefore, our experimental and DFT results provide strong evidence for an Eley-Rideal mechanism for CO oxidation on Ir single atoms supported on $MgAl_2O_4$. More importantly, the results show that Ir(CO) is the active supported complex and Ir(CO)(O) is the most stable intermediate (resting state) during the reaction.

Supported metal single atoms present tremendous opportunities for designing catalysts at the atomic scale. A few research groups have shown that supports[7, 25, 39] and other ligands[10, 40] can be used to modify their electronic and catalytic properties analogous to modifying the ligands in a homogeneous catalyst[8, 27, 38]. For example, CO was reported to promote the selective hydrogenation of 1,3-butadiene on Rh single atoms and dimers supported on MgO[40] and promote the formation of methanol from methane oxidation on Rh_1/ZSM-5 (CO was required for methanol formation despite not being a reactant)[10]. In this work, using in-situ and operando FTIR, HERFD-XANES and DFT calculations we show that the active metal single-atom complex is formed under reaction conditions and contains one of the reactants as a ligand. Our results demonstrate that Ir(CO) is the active complex and the formation of this Ir single atom complex on $MgAl_2O_4$ promotes CO oxidation via an Eley-Rideal mechanism where Ir(CO)(O) is the resting state of the catalyst. More importantly, our results show that detection of adsorbed CO on metal single atoms by infrared spectroscopy under reaction conditions or under O_2 flow (both indicate strong CO adsorption)[17, 18, 20] does not necessarily indicate low activity for CO oxidation. More generally, the results show that due to the ability of single atoms to bind to more than one ligand, strong adsorption by a ligand (or one of the reactants, e.g. CO) does not necessarily lead to catalyst poisoning. Our DFT results indicate that Ir single atoms play a crucial role in facilitating O_2

activation, while the CO ligand lowers the barrier for the Eley-Rideal rate-limiting step. The results highlight the importance of combining in-situ/operando spectroscopy, together with quantum chemical calculations, and kinetic measurements to identify the active complex, most stable intermediate (resting state) and reaction mechanism. Additionally, we anticipate that due to the ability of supported single-atom catalysts to bind to multiple ligands, the work can be extended to other metals where a strongly adsorbed ligand (e.g. CO) can be an integral part of the active metal single-atom complex providing an avenue to promote specific reaction pathways and control the catalyst activity and selectivity.

2.6. Acknowledgments

This research was primarily sponsored by the Army Research Office and was accomplished under Grant Number W911NF-16-1-0400. The views and conclusions contained in this document are those of the authors and should not be interpreted as representing the official policies, either expressed or implied, of the Army Research Office or the U.S. Government. The U.S. Government is authorized to reproduce and distribute reprints for Government purposes notwithstanding any copyright notation herein. Additional support by SABIC (Saudi Basic Industries Corporation) and by the U.S. Department of Energy (DOE) Office of Basic Energy Sciences to the SUNCAT Center for Interface Science and Catalysis is acknowledged. Use of the Stanford Synchrotron Radiation Light Source (SSRL, beamlines 6-2, user proposal 4645), SLAC National Accelerator Laboratory is supported by the U.S. Department of Energy, office of Basic Energy Sciences under Contract No. DE-AC02-76SF00515. STEM imaging was performed at the William R. Wiley Environmental

Molecular Science Laboratory (EMSL) sponsored by the U.S. Department of Energy, office of Biological and Environmental Research located at Pacific Northwest National Laboratory (PNNL) under science theme proposal 49326. Computing time was awarded at EMSL under the same proposal. L.Y. and H.X acknowledge the partial financial support from the American Chemical Society Petroleum Research Fund (ACS PRF 55581-DNI5) and computational support from the advanced research computing at Virginia Polytechnic Institute and State University.

References

1. Oh, S.H. & Sinkevitch, R.M. Carbon monoxide removal from hydrogen-rich fuel cell feedstreams by selective catalytic oxidation. *J. Catal.* **142**, 254-262 (1993).

2. Alayoglu, S., Nilekar, A.U., Mavrikakis, M. & Eichhorn, B. Ru–Pt core–shell nanoparticles for preferential oxidation of carbon monoxide in hydrogen. *Nat. Mater.* **7**, 333 (2008).

3. Allian, A.D. et al. Chemisorption of CO and mechanism of CO oxidation on supported platinum nanoclusters. *J. Am. Chem. Soc.* **133**, 4498-4517 (2011).

4. Twigg, M.V. Progress and future challenges in controlling automotive exhaust gas emissions. *Appl. Catal., B* **70**, 2-15 (2007).

5. Lin, J. et al. Remarkable Performance of Ir_1/FeO_x single-atom catalyst in water gas shift reaction. *J. Am. Chem. Soc.* **135**, 15314-15317 (2013).

6. Yang, X.F. et al. Single-atom catalysts: a new frontier in heterogeneous catalysis. *Acc. Chem. Res.* **46**, 1740-1748 (2013).

7. Lu, J., Serna, P., Aydin, C., Browning, N.D. & Gates, B.C. Supported molecular iridium catalysts: resolving effects of metal nuclearity and supports as ligands. *J. Am. Chem. Soc.* **133**, 16186-16195 (2011).

8. Kyriakou, G. et al. Isolated metal atom geometries as a strategy for selective heterogeneous hydrogenations. *Science* **335**, 1209-1212 (2012).

9. Liu, J. Catalysis by supported single metal atoms. *ACS Catal.* **7**, 34-59 (2017).

10. Shan, J., Li, M., Allard, L.F., Lee, S. & Flytzani-Stephanopoulos, M. Mild oxidation of methane to methanol or acetic acid on supported isolated rhodium catalysts. *Nature* **551**, 605-608 (2017).

11. Cui, X., Li, W., Ryabchuk, P., Junge, K. & Beller, M. Bridging homogeneous and heterogeneous catalysis by heterogeneous single-metal-site catalysts. *Nat. Catal.* **1**, 385-397 (2018).

12. Qiao, B.T. et al. Single-atom catalysis of CO oxidation using Pt_1/FeO_x. *Nat. Chem.* **3**, 634-641 (2011).

13. Moses-DeBusk, M. et al. CO oxidation on supported single Pt atoms: experimental and ab initio density functional studies of CO interaction with Pt atom on theta-Al_2O_3(010) surface. *J. Am. Chem. Soc.* **135**, 12634-12645 (2013).

14. Kistler, J.D. et al. A single-site platinum CO oxidation catalyst in zeolite KLTL: microscopic and spectroscopic determination of the locations of the platinum atoms. *Angew. Chem. Int. Ed.* **53**, 8904-8907 (2014).

15. Yang, M. et al. Catalytically active Au-$O(OH)_x$-species stabilized by alkali ions on zeolites and mesoporous oxides. *Science* **346**, 1498-1501 (2014).

16. Yang, M. et al. A common single-site Pt(II)-$O(OH)_x$- Species stabilized by sodium on "active" and "inert" supports catalyzes the water-gas shift reaction. *J. Am. Chem. Soc.* **137**, 3470-3473 (2015).

17. Ding, K. et al. Identification of active sites in CO oxidation and water-gas shift over supported Pt catalysts. *Science* **350**, 189-192 (2015).

18. Jones, J. et al. Thermally stable single-atom platinum-on-ceria catalysts via atom trapping. *Science* **353**, 150-154 (2016).

19. Stephens, I.E.L., Elias, J.S. & Shao-Horn, Y. The importance of being together. *Science* **350**, 164-165 (2015).

20. Nie, L. et al. Activation of surface lattice oxygen in single-atom Pt/CeO_2 for low-temperature CO oxidation. *Science* **358**, 1419-1423 (2017).

21. Luo, J.Y. et al. Advantages of MgAlOx over gamma-Al_2O_3 as a Support material for potassium-based high-temperature lean NO_x traps. *ACS Catal.* **5**, 4680-4689 (2015).

22. Li, W.-Z. et al. A general mechanism for stabilizing the small sizes of precious metal nanoparticles on oxide supports. *Chem. Mater.* **26**, 5475-5481 (2014).

23. Li, W.-Z. et al. Stable platinum nanoparticles on specific $MgAl_2O_4$ spinel facets at high temperatures in oxidizing atmospheres. *Nat. Comm.* **4** (2013).

24. Lin, J. et al. Design of a highly active $Ir/Fe(OH)_x$ catalyst: versatile application of Pt-group metals for the preferential oxidation of carbon monoxide. *Angew. Chem. Int. Ed.* **51**, 2920-2924 (2012).

25. Lu, J., Aydin, C., Browning, N.D. & Gates, B.C. Oxide- and zeolite-supported isostructural $ir(C_2H_4)_2$ complexes: molecular-level observations of electronic effects of supports as ligands. *Langmuir* **28**, 12806-12815 (2012).

26. Hoffman, A.S. et al. High-energy-resolution x-ray absorption spectroscopy for identification of reactive surface species on supported single-site iridium catalysts. *Chem. Eur. J.* **23**, 14760-14768 (2017).

27. Aydin, C., Lu, J., Browning, N.D. & Gates, B.C. A "Smart" Catalyst: Sinter-resistant supported iridium clusters visualized with electron microscopy. *Angew. Chem. Int. Ed.* **51**, 5929-5934 (2012).

28. Berlowitz, P.J., Peden, C.H.F. & Goodman, D.W. kinetics of CO oxidation on single-crystal Pd, Pt, and I r. *J. Phys. Chem.* **92**, 5213-5221 (1988).

29. Cargnello, M. et al. Control of metal nanocrystal size reveals metal-support interface role for ceria catalysts. *Science* **341**, 771-773 (2013).

30. Mihaylov, M. et al. New types of nonclassical iridium carbonyls formed in Ir-ZSM-5: a fourier transform infrared spectroscopy investigation. *J. Phys. Chem. B* **110**, 10383-10389 (2006).

31. Wovchko, E.A. & Yates, J.T. Activation of O_2 on a photochemically generated Rh^I site on an Al_2O_3 surface: low-temperature O_2 dissociation and CO oxidation. *J. Am. Chem. Soc.* **120**, 10523-10527 (1998).

32. Abbet, S., Heiz, U., Hakkinen, H. & Landman, U. CO oxidation on a single Pd atom supported on magnesia. *Phys. Rev. Lett.* **86**, 5950-5953 (2001).

33. Atkins, A.J., Bauer, M. & Jacob, C.R. High-resolution x-ray absorption spectroscopy of iron carbonyl complexes. *Phys. Chem. Chem. Phys.* **17**, 13937-13948 (2015).

34. Boubnov, A. et al. Selective catalytic reduction of NO over Fe-ZSM-5: mechanistic insights by operando herfd-xanes and valence-to-core x-ray emission spectroscopy. *J. Am. Chem. Soc.* **136**, 13006-13015 (2014).

35. van Bokhoven, J.A. et al. Activation of oxygen on gold/alumina catalysts: in situ high-energy-resolution fluorescence and time-resolved x-ray spectroscopy. *Angew. Chem. Int. Ed.* **45**, 4651-4654 (2006).

36. Safonova, O.V. et al. Identification of CO adsorption sites in supported Pt catalysts using high-energy-resolution fluorescence detection x-ray spectroscopy. *J. Phys. Chem. B* **110**, 16162-16164 (2006).

37. Cai, Q.X., Wang, J.G., Wang, Y. & Mei, D.H. First-principles thermodynamics study of spinel $MgAl_2O_4$ surface stability. *J. Phys. Chem. C* **120**, 19087-19096 (2016).

38. Ljungberg, M.P., Mortensen, J.J. & Pettersson, L.G.M. An implementation of core level spectroscopies in a real space Projector Augmented Wave density functional theory code. *J. Electron. Spectrosc.* **184**, 427-439 (2011).

39. Lu, J., Serna, P. & Gates, B.C. Zeolite- and MgO-Supported Molecular Iridium Complexes: Support and Ligand Effects in Catalysis of Ethene Hydrogenation and H–D Exchange in the Conversion of $H_2 + D_2$. *ACS Catal.* **1**, 1549-1561 (2011).

40. Yardimci, D., Serna, P. & Gates, B.C. Tuning catalytic selectivity: zeolite- and magnesium oxide-supported molecular rhodium catalysts for hydrogenation of 1,3-butadiene. *ACS Catal.* **2**, 2100-2113 (2012).

41. Sokaras, D. et al. A seven-crystal Johann-type hard x-ray spectrometer at the Stanford Synchrotron Radiation Lightsource. *Review of Scientific Instruments* **84**, 053102 (2013).

42. Ravel, B. & Newville, M. ATHENA, ARTEMIS, HEPHAESTUS: data analysis for x-ray absorption spectroscopy using IFEFFIT. *J. Synchrotron Radiat.* **12**, 537-541 (2005).

43. Newville, M. IFEFFIT: interactive XAFS analysis and FEFF fitting. *J Synchrotron Radiat.* **8**, 322-324 (2001).

44. Brooks, C.S. Characterization of iridium catalyst surfaces by gas chemisorption. *J. of Colloid Interface Sci.* **34**, 419-427 (1970).

45. Bonet, F. et al. Kinetics of heterogeneous catlytic reactions. (Princeton University Press / Princeton, N.J., 1984).

46. Koros, R.M. & Nowak, E.J. A diagnostic test of the kinetic regime in a packed bed reactor. *Chemical Engineering Science* **22**, 470 (1967).

47. Madon, R.J. & Boudart, M. Experimental criterion for the absence of artifacts in the measurement of rates of heterogeneous catalytic reactions. *Ind. Eng. Chem. Fund.* **21**, 438-447 (1982).

48. Mozaffari, S. et al. Colloidal nanoparticle size control: experimental and kinetic modeling investigation of the ligand metal binding role in controlling the nucleation and growth kinetics. *Nanoscale* **9**, 13772-13785 (2017).

49. Hutter, J., Iannuzzi, M., Schiffmann, F. & VandeVondele, J. CP2K: atomistic simulations of condensed matter systems. *Wires Comput. Mol. Sci.* **4**, 15-25 (2014).

50. Paier, J., Hirschl, R., Marsman, M. & Kresse, G. The Perdew-Burke-Ernzerhof exchange-correlation functional applied to the G2-1 test set using a plane-wave basis set. *J. Chem. Phys.* **122** (2005).

51. Grimme, S., Antony, J., Ehrlich, S. & Krieg, H. A consistent and accurate ab initio parametrization of density functional dispersion correction (DFT-D) for the 94 elements H-Pu. *J. Chem. Phys.* **132** (2010).

52. Henkelman, G., Uberuaga, B.P. & Jónsson, H. A climbing image nudged elastic band method for finding saddle points and minimum energy paths. *J. Chem. Phys.* **113**, 9901 (2000).

53. M. P. Ljungberg, J. J. Mortensen, L. G. M. Pettersson, An implementation of core level spectroscopies in a real space Projector Augmented Wave density functional theory code. *J. Electron. Spectrosc.* **184**, 427-439 (2011).

Appendix A

The 1%Ir/$MgAl_2O_4$ sample was calcined at 500 °C and reduced at 800 °C, and a representative STEM image of this sample is shown in Supplementary Fig. 3. The STEM images for this sample suggest that it contains a mixture of Ir single atoms and nanoparticles.

In-situ IR characterization (Supplementary Fig. 13) of this 1% Ir sample (STEM in Supplementary Fig. 4) consisting of a mixture of Ir SAC and NP was performed at room temperature. DRIFTS of CO adsorption at room temperature showed one main band at 2058 cm^{-1} in the CO stretching region. Additionally, a weak band at ~1980 cm^{-1} was also detected which can be attributed to the ν_{as} of the gem-dicarbonyl on Ir single atoms. After dosing O_2, the 2058 cm^{-1} band decreased and a new shoulder appeared at 2090 cm^{-1}. This is consistent with what we observed on pure Ir single-atom catalyst as shown in Fig. 3a. This confirmed the existence of surface Ir single atoms as shown in the STEM images.

In-situ HERFD characterization of 1% Ir sample, which consists of a mixture of Ir SAC and NP, was also performed at room temperature (Supplementary Fig. 7). The sample was first in-situ pretreated with H_2 reduction at 800 XSpectra. After dosing O_2 at room temperature on the carbonylated Ir (red), the extra feature at the higher energy of the edge maxima of the Ir L_3-edge HERFD spectrum indicates a partial oxidation of the Ir. This oxidation state change can be attributed to O_2 co-adsorption with CO on Ir single atoms and possibly on small clusters. The extent of these changes was not as significant on this sample (mixture of SAC and NP) as the ~100% single-atom sample (Fig. 3b), which indicates that O adsorption with CO is mostly present on Ir single atoms.

The composition of effluent gases during the HERFD-XANES measurement of 0.0025% $Ir/MgAl_2O_4$ (SAC) was measured by a mass spectrometer as shown in Supplementary Fig. 6. The in-situ pretreated sample (pretreatment details in experimental methods of HERFD-XANES) was first exposed to a flow of 5% CO and the HERFD-XANES spectra of the carbonylated sample ($Ir(CO)_2$) was shown as red in Fig. 3b. After flowing O_2 at room temperature on the carbonylated sample, the carbonaylated feature in the HERFD-XANES spectrum was partially replaced by a higher energy feature (blue in Fig. 3b), and this spectrum was assigned to the Ir(CO)(O) structure. A significant spike of CO_2 composition was measured by mass spectroscopy during the O_2 flow as shown in Supplementary Fig. 6a. This suggests the O_2 was activated on the Ir single-atom catalyst at room temperature, and the activated O then reacted with one of the CO in $Ir(CO)_2$ structure to form CO_2. After stabilization, the CO_2 level was still higher than before introducing O_2, and this can be attributed to the decomposition of surface carbonate on $MgAl_2O_4$ support. After CO oxidation at 155 °C, the reactor was cooled down to 100 ℃ in He. The Ir SAC still maintained the Ir(CO)(O) structure in He as shown in Supplementary Fig. 9. At 100 ℃ when flowing CO on the Ir SAC sample without O_2, the Ir(CO)(O) reacted with gas phase CO and adsorbed another CO to form $Ir(CO)_2$ (as shown in Fig. 3c), at the same time the CO_2 level increased as detected by the mass spec (Supplementary Fig. 6b). This confirmed that the change in HERFD-XANES during CO flow was from the CO oxidation reaction. During the HERFD-XANES experiment, the reaction order of CO was measured as 1 ± 0.2 at 155 °C, which is consistent with the kinetic measurement results (Fig. 2).

In Supplementary Fig. 11, Ir L_3-edge spectra for Ir single atoms adsorbed on the O_2(Al)-terminated $MgAl_2O_4$ (211) surface with different ligand configurations was simulated using DFT-based

calculations (See Supplementary Table 4 for detailed structures). The shapes of $Ir(CO)_2$ and Ir(CO)(O) are consistent with the experimentally measured HERFD-XANES spectra (Fig. 3, b, c). The Ir(CO)(O) was calculated with 3 different nearby structures, where one of the nearest Al to Ir was adsorbed with an O_2 (Ir(CO)(O)-(Al-O_2), adsorbed with a O^* (Ir(CO)(O)-(Al-O) or have a vacancy (Ir(CO)(O)-(Al-v) respectively. All of these 3 Ir(CO)(O) complexes are possible during the experiment. Therefore, a combination of these three Ir(CO)(O) spectra is a better comparison with the experimentally measured spectrum after flowing O_2 at room temperature (Fig. 3b blue) and is in very good agreement with the experiment. We note that the $Ir(CO)_2$ with an O vacancy on the nearest Al ($Ir(CO)_2$-(Al-v)) was shifted to higher energy with a lower white line intensity compared with the $Ir(CO)_2$ with O_2 adsorbed on the vacancy. The $Ir(CO)_2$-(Al-v) is more consistent with the experiment since it was collected under CO flow and our DFT results showed low barrier for vacancy formation. especially in a flow of CO

The stability of the Ir(CO)(O) structure is shown in Supplementary Fig. 9. The spectrum in blue was collected under CO oxidation condition (1 kPa CO + 8 kPa O_2) at 155 °C. After CO oxidation at 155 °C the sample was cooled down to 100 °C in He. The red spectrum represents the sample at 100 °C in He. At 100 °C 1 kPa CO + 8 kPa O_2 was introduced to the reactor again and the spectrum under CO and O_2 was shown as green. HERFD-XANES spectra of Ir SAC under He (100 °C) and CO+O_2 (100 °C and 155 °C) are identical indicating the stability of Ir(CO)(O) and also confirming that it is a stable intermediate during low-temperature CO oxidation.

Apparent activation energy (E_{app}) of the 0.0025% Ir/$MgAl_2O_4$ (SAC) (Supplementary Fig. 12) was measured between 145 and 160 °C under two different CO partial pressures (P_{CO}= 0.2 kPa and 1

kPa), with the same O_2 partial pressure (P_{O_2}) kept at 10 kPa. E_{app} were measured as 62 kJ/mol at 0.2 kPa P_{CO} and 67 kJ/mol at 1 kPa P_{CO}. Similar apparent activation energies at these two conditions suggest that the reaction pathway is independent of the CO partial pressure.

The apparent activation energies of CO oxidation reactions of different samples were also summarized in Supplementary Table 9. E_{app} were measured at the same condition for these 3 samples, with 1 kPa CO and 10 kPa O_2, between 145 °C and 160 °C with 5 °C increment. E_{app} for the 0.0025% Ir/$MgAl_2O_4$ (SAC) was measured as 62 kJ/mol. E_{app} for the 0.2% Ir/$MgAl_2O_4$ (NP) was measured as 101 kJ/mol. This further supports our results that Ir SAC and Ir NP have different reaction mechanisms for low-temperature CO oxidation as shown in the manuscript. E_{app} of the 1% Ir/$MgAl_2O_4$ reduced at 800 °C sample (mixture of SAC and NP, see Supplementary Fig. 3 for STEM) was measured as 71 kJ/mol, which is between the E_{app} of the SAC and NP samples, which is consistent with the composition of the sample.

To test the effect of temperature on stability under reaction condition for the low loading single-atom catalyst we performed the kinetic measurement and tested the reaction order of CO at two different temperatures with the same catalysts (0.0025% Ir/$MgAl_2O_4$), as shown on Supplementary Fig. 14. The reaction order of CO was first measured at 155 °C. The reaction order of CO was measured as +0.8 (P_{O_2} = 10 kPa, P_{CO} =0.3-1 kPa). After this the kinetic measurement was performed at a higher temperature of 200 °C from higher P_{CO} (1 kPa) to lower P_{CO}. P_{CO} was kept at 10 kPa. The reaction order of CO was measured as +0.7, which is slightly lower than the reaction order measured at 155 °C. After the entire kinetic measurement, a stability test was performed at the very first condition at 200 °C (P_{O_2}= 10 kPa, P_{CO}=1 kPa). The activity was maintained very well

at the entire P_{CO} range and the deactivation is minimal (2%). The reaction order and the stability test at 200 °C suggest that the Ir single atom is stable for low temperature CO oxidation (less than 200 °C).

Due to facile O_2 activation on $MgAl_2O_4$ step surface, this CO promotion effect is different from the tri-molecular Eley-Rideal mechanism on Au/h-BN reported by Mao et al. [1] where O_2 from gas phase reacts with two adsorbed *CO. We calculated the reaction barrier for the tri-molecular Eley-Rideal mechanism for Ir single atom on $MgAl_2O_4$(211) step site (~1.2 eV, Supplementary Fig. 15), which is unlikely to occur at room temperature and also the barrier is much higher than the pathway involving O_2 adsorption on the vacancy and reaction with one CO from $Ir(CO)_2$ (~0.58 eV).

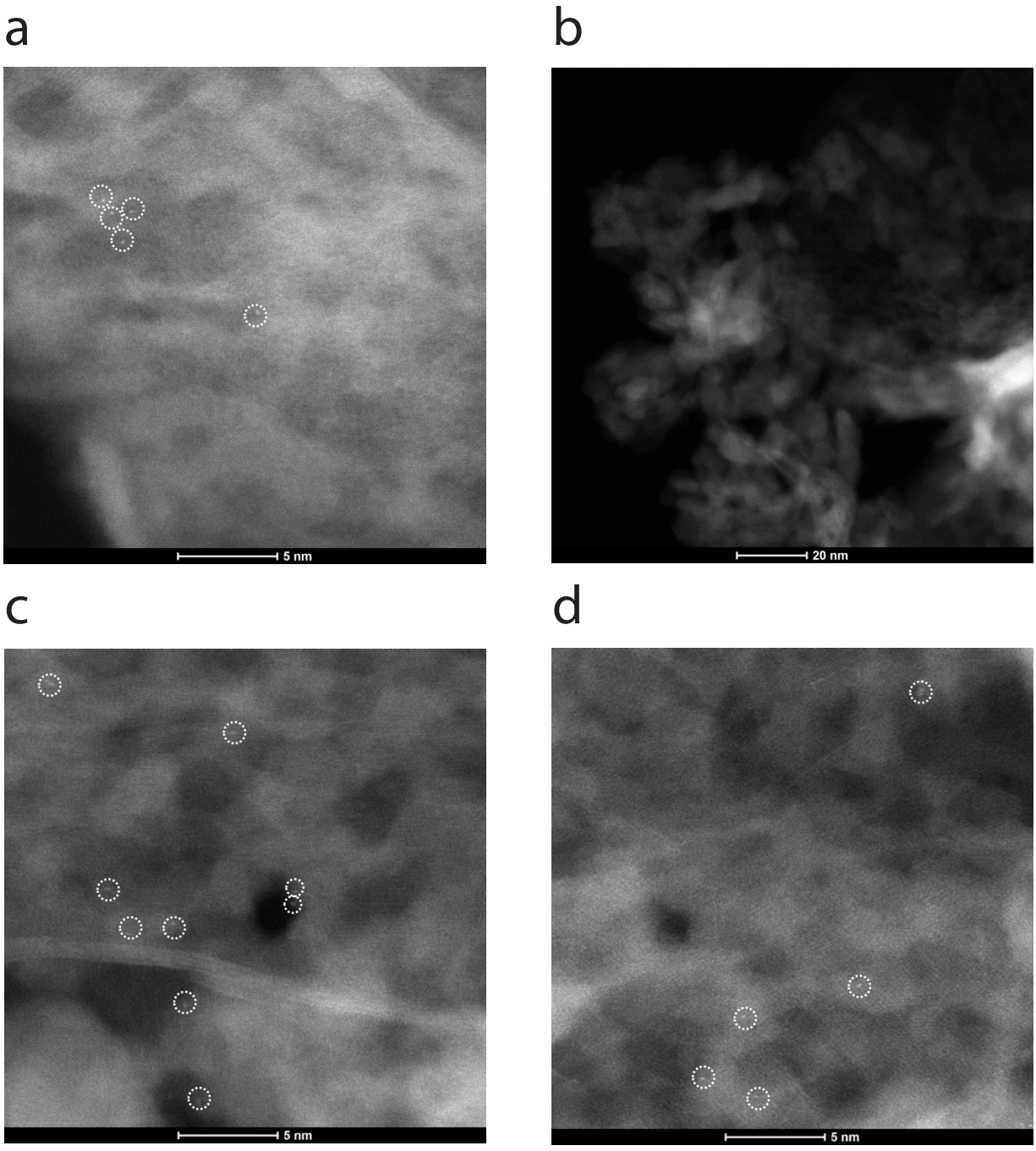

Supplementary Figure 1 | Representative STEM images of Ir SAC. STEM images of 0.0025% Ir/$MgAl_2O_4$ (SAC) after reduction at 500 °C (**a**) high magnification and (**b**) low magnification, (**c, d**) after CO oxidation. Single atoms are identified by white circles.

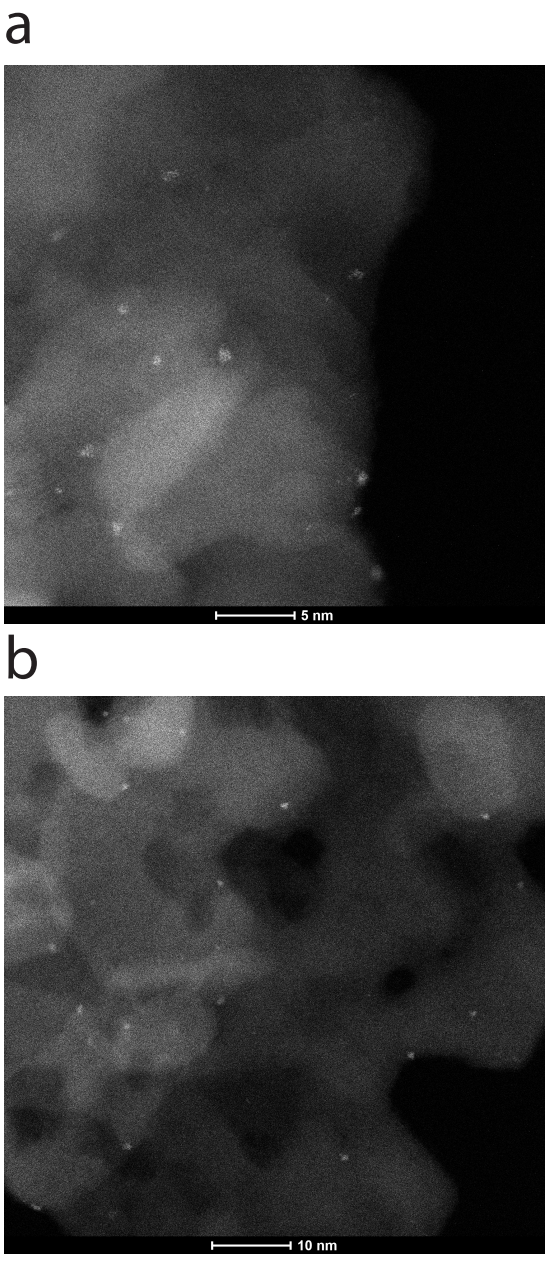

Supplementary Figure 2 | Representative STEM images of Ir NP. a, b, STEM images of the 0.2% Ir/$MgAl_2O_4$ sample prepared with $Ir(CO)_2(acac)$ precursor after pre-treatment in 20% H_2 at 500 °C for 2hr.

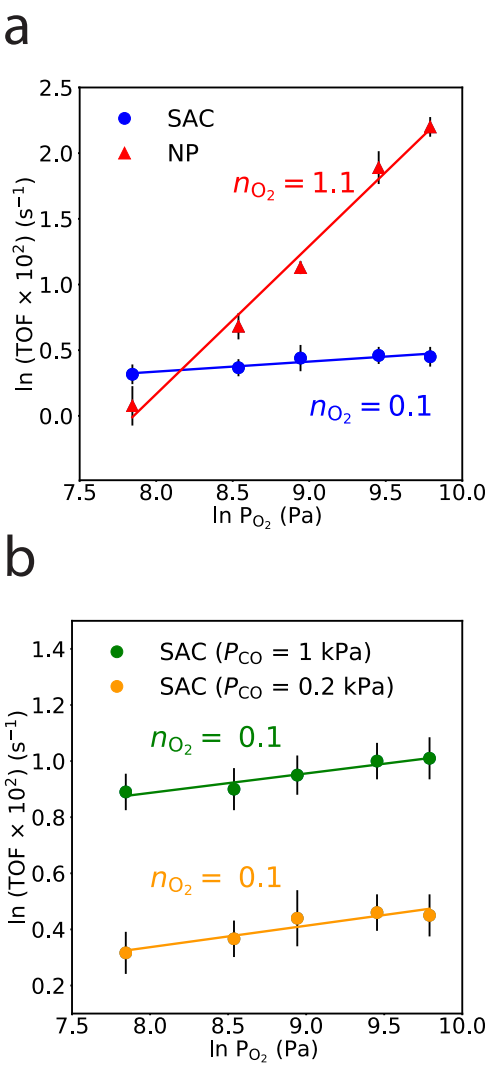

Supplementary Figure 3 | Effect of O_2 partial pressure on TOF on Ir SAC and NP. a, Effect of O_2 partial pressure on turnover frequency (TOF) on supported Ir single atoms and Ir nanoparticles. P_{CO} = 0.2 kPa, P_{O_2} = 2-14 kPa, T = 155 °C. **b**, Effect of O_2 partial pressure on turnover frequency (TOF) on Ir single atoms at two CO partial pressures, P_{CO} = 0.2 kPa and 1kPa respectively, P_{O_2} = 2-14 kPa, T = 155 °C. The difference between the two lines in **b** is due to the positive reaction order in CO. Error bars were calculated based on multiple measurements on the

same catalyst at different times during one experiment and from experiments using different catalyst aliquots/batches.

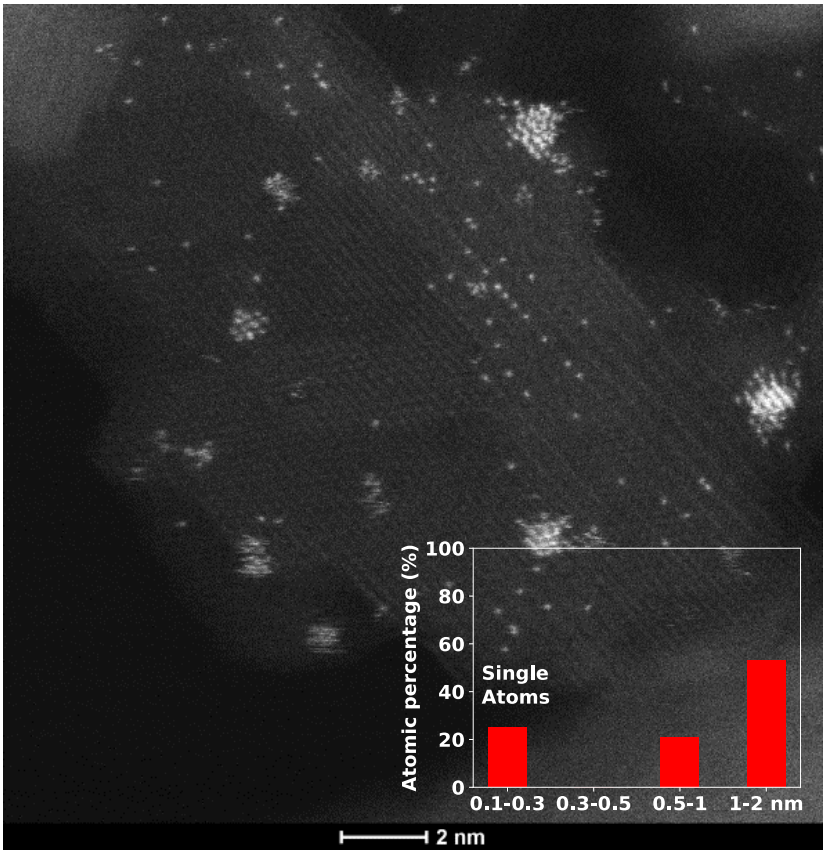

Supplementary Figure 4 | Representative STEM image of sample with a mixture of Ir SAC and Ir NP. 1% Ir/$MgAl_2O_4$ sample was calcined at 500 °C and reduced at 800 °C.

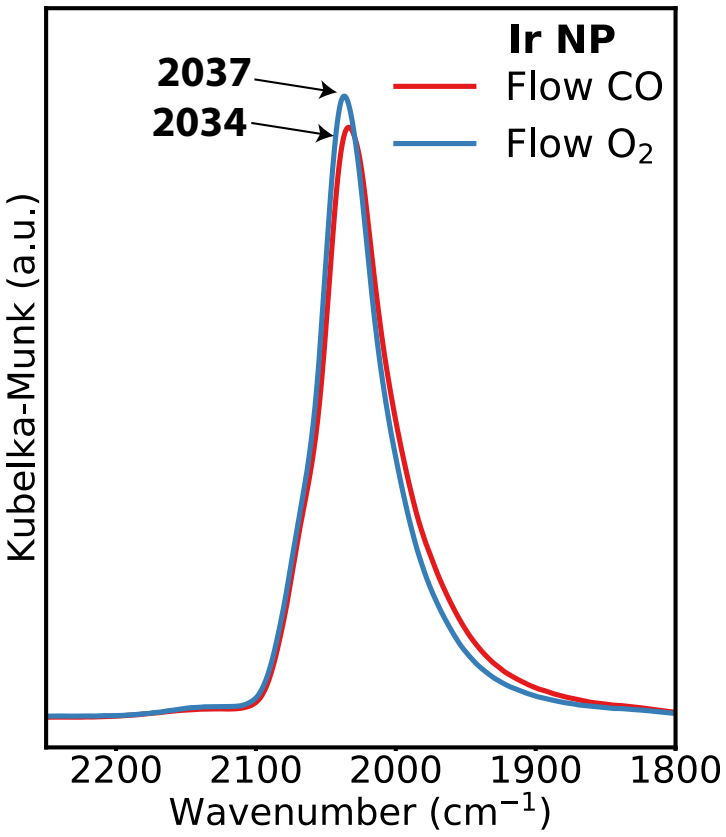

Supplementary Figure 5 | In-situ IR of Ir NP at room temperature. In-situ IR spectra in the ν_{CO} region characterizing samples of 0.2% Ir/$MgAl_2O_4$ (nanoparticles with average size ~ 1 nm) formed by CO adsorbed at room temperature (red), and flowed 5 kPa O_2 on CO adsorbed Ir at room temperature (blue).

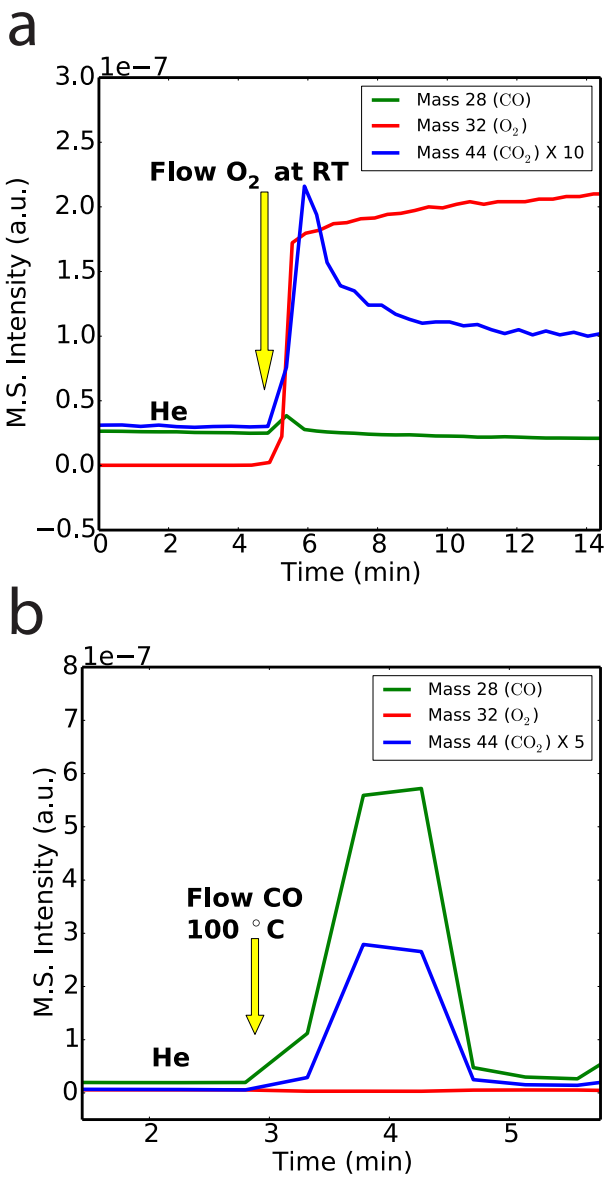

Supplementary Figure 6 | Mass spectrometry results during in-situ HERFD-XANES. Mass 28 (CO), Mass 32 (O_2) and Mass 44 (CO_2) response during HERFD-XANES experiment on Ir/$MgAl_2O_4$ SAC (0.0025 wt.%) (HERFD-XANES spectra are shown in Fig. 3 b, c). **a,** Dose 5% O_2 at room temperature on CO adsorbed Ir SAC. **b,** Dosing 2% CO at 100 ℃ after CO oxidation at 155 °C and cooling down in He.

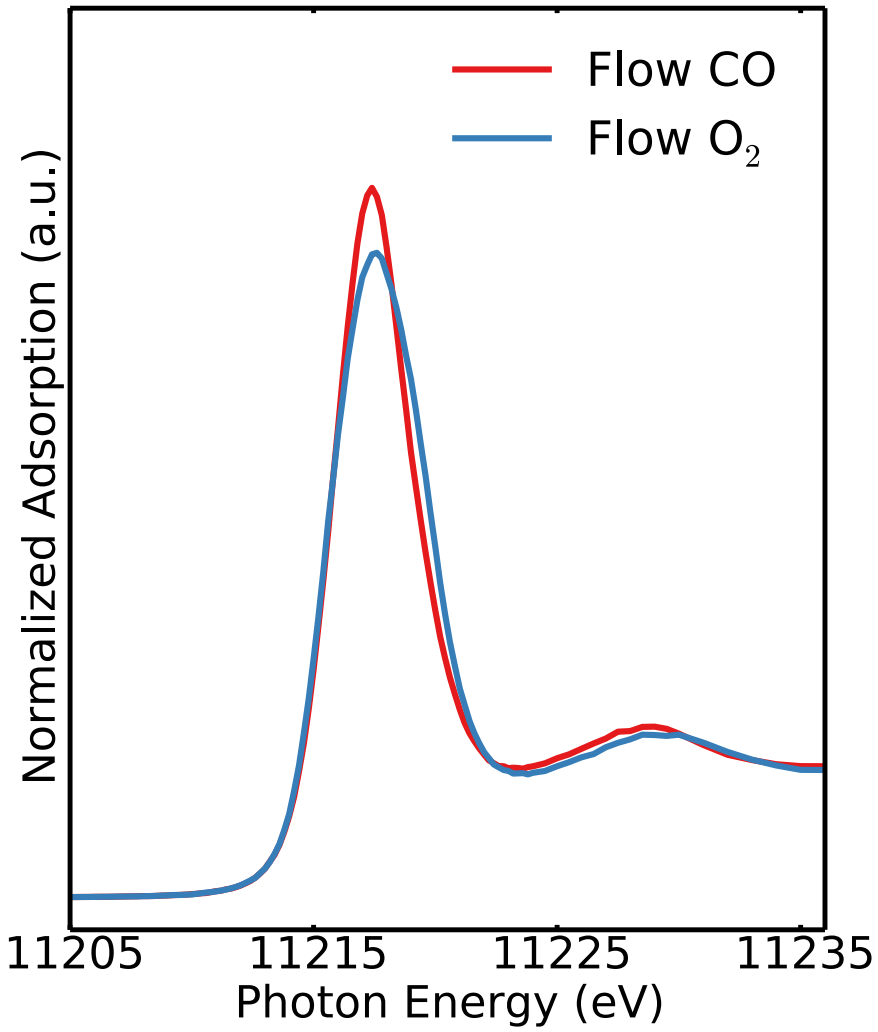

Supplementary Figure 7 | HERFD-XANES spectra at the Ir L_3-edge of Ir SAC+NP mixture. Supported 1% Ir/$MgAl_2O_4$ calcined at 500 °C and reduced at 800 °C after dosing 1 kPa CO (balance He) at room temperature (red) and then flow 5 kPa O_2 (balance He) at room temperature (blue).

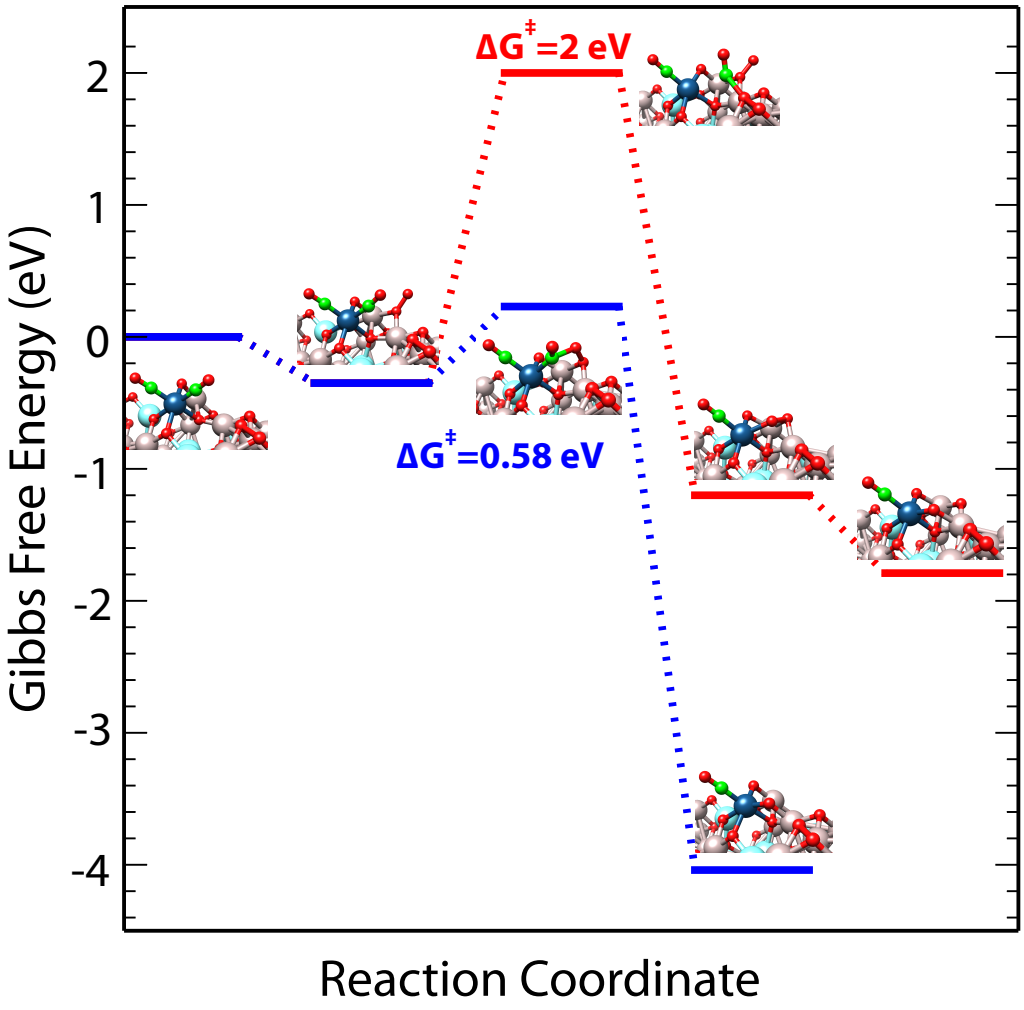

Supplementary Figure 8 | Proposed reaction mechanism for O_2 reaction with one *CO from $Ir(CO)_2$ at room temperature. On O_2(Al)-terminated $MgAl_2O_4$ (211) surface, *CO from $Ir(CO)_2$ reacts with the $*O_2$ forming CO_2 with DFT-calculated kinetic barrier of ~0.58 eV (blue). Diffusion of one of the CO ligands in $Ir(CO)_2$ to a slightly further surface oxygen to form CO_2 is associated with a high barrier of ~2 eV (red).

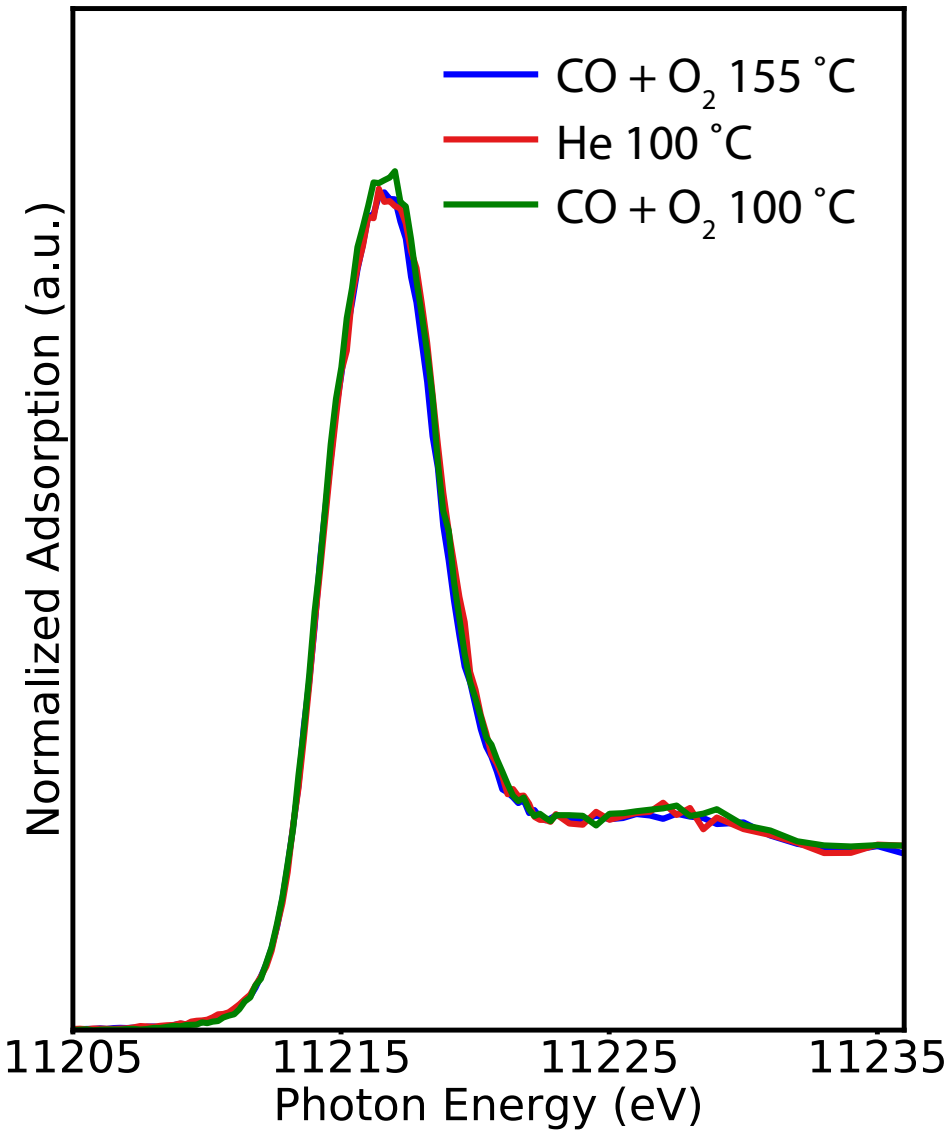

Supplementary Figure 9 | In-situ and operando HERFD-XANES of Ir SAC.

HERFD-XANES spectra of 0.0025% Ir/$MgAl_2O_4$ (SAC) when flowing CO (1 kPa) + O_2 (8 kPa) at 155 °C (blue), flowing He at 100 °C (red) and CO (1 kPa) + O_2 (8 kPa) at 100 °C (green).

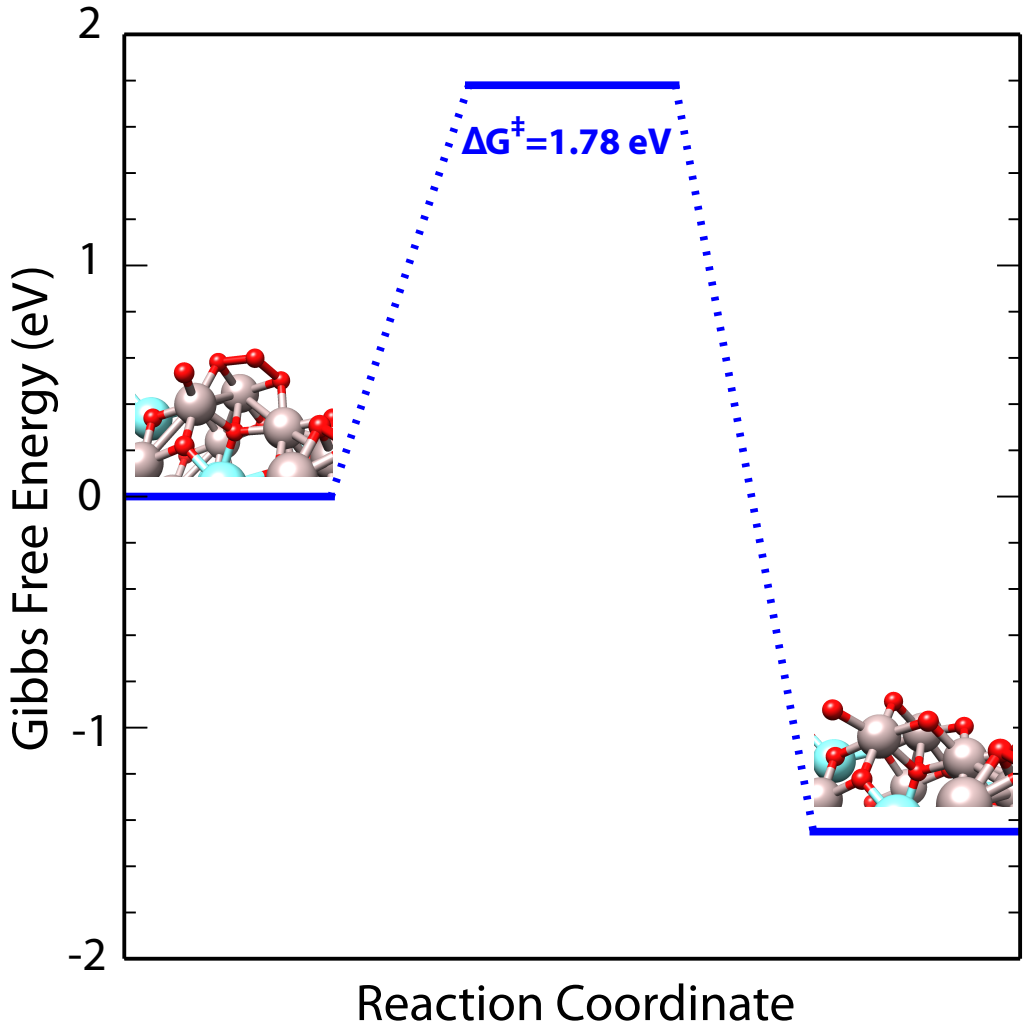

Supplementary Figure 10 | DFT calculated O_2 dissociation on $MgAl_2O_4$(211) surface. O_2 dissociation on the clean O_2(Al)-terminated $MgAl_2O_4$ (211) surface with two adjacent vacancies has an activation barrier of ~1.78 eV.

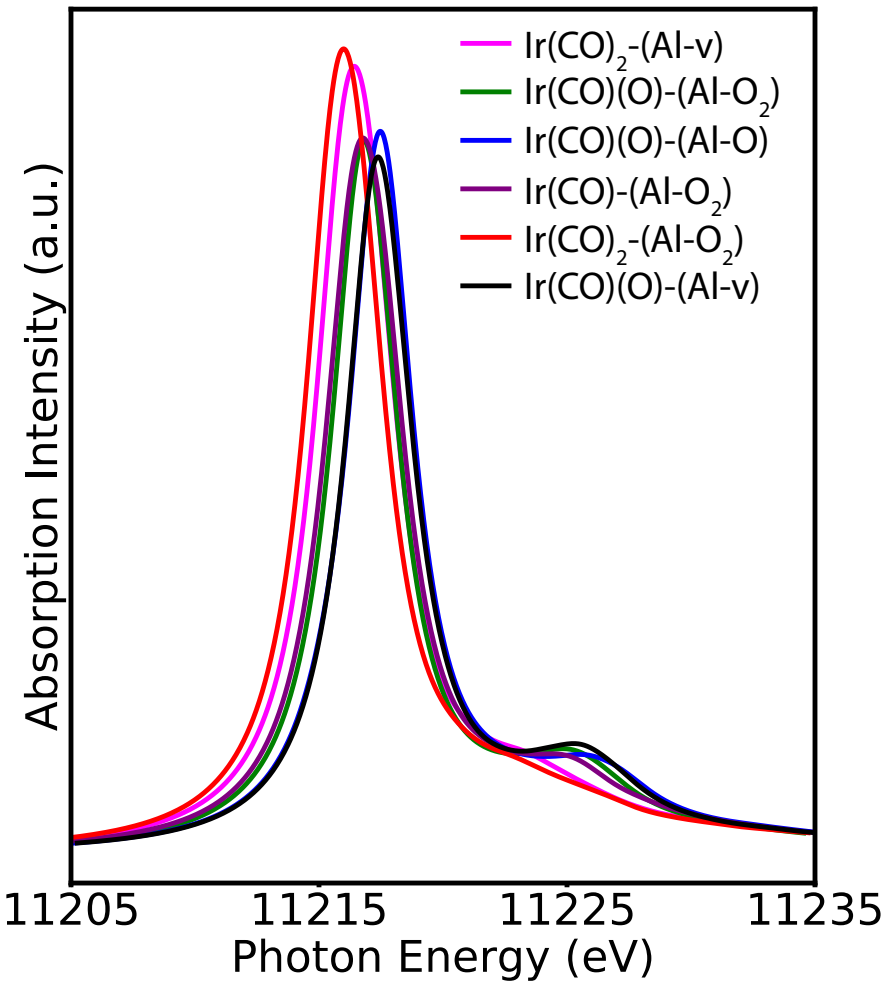

Supplementary Figure 11 | DFT simulated Ir L_3-edge XANES spectra. DFT simulated XANES spectra for Ir single atoms adsorbed on the O_2(Al)-terminated $MgAl_2O_4$ (211) surface with different ligand configurations. of $Ir(CO)_2$-(Al-v) (magenta), Ir(CO)(O)-(Al-O_2) (green), Ir(CO)(O)-(Al-O) (blue), Ir(CO)-(Al-O_2) (purple), $Ir(CO)_2$-(Al-O_2) (red), Ir(CO)-(Al-v) (black).

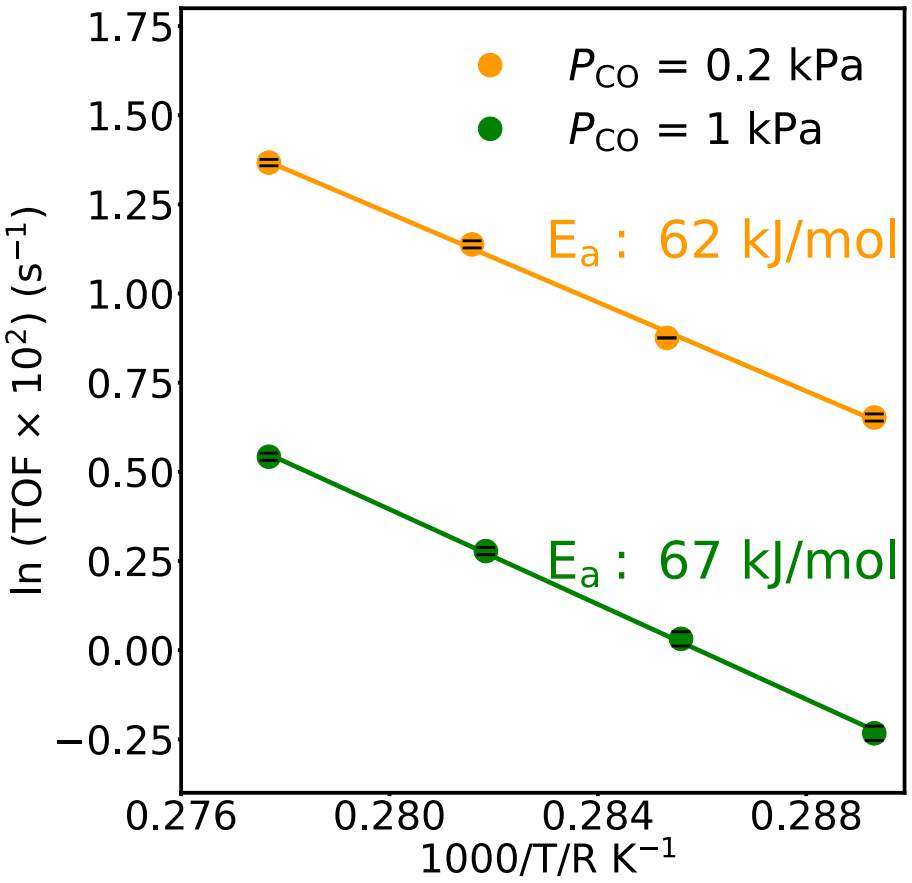

Supplementary Figure 12 | Apparent activation energy of Ir SAC. Apparent activation energy (E_{app}) of 0.0025% Ir/$MgAl_2O_4$ (SAC) measured between 145 and 160 ℃ with 5 °C temperature increment, P_{CO}= 1kPa and 0.2 kPa, P_{O_2} = 10 kPa. Error bars were calculated based on multiple measurements on the same catalyst at different times during one experiment and from experiments using two different catalyst batches.

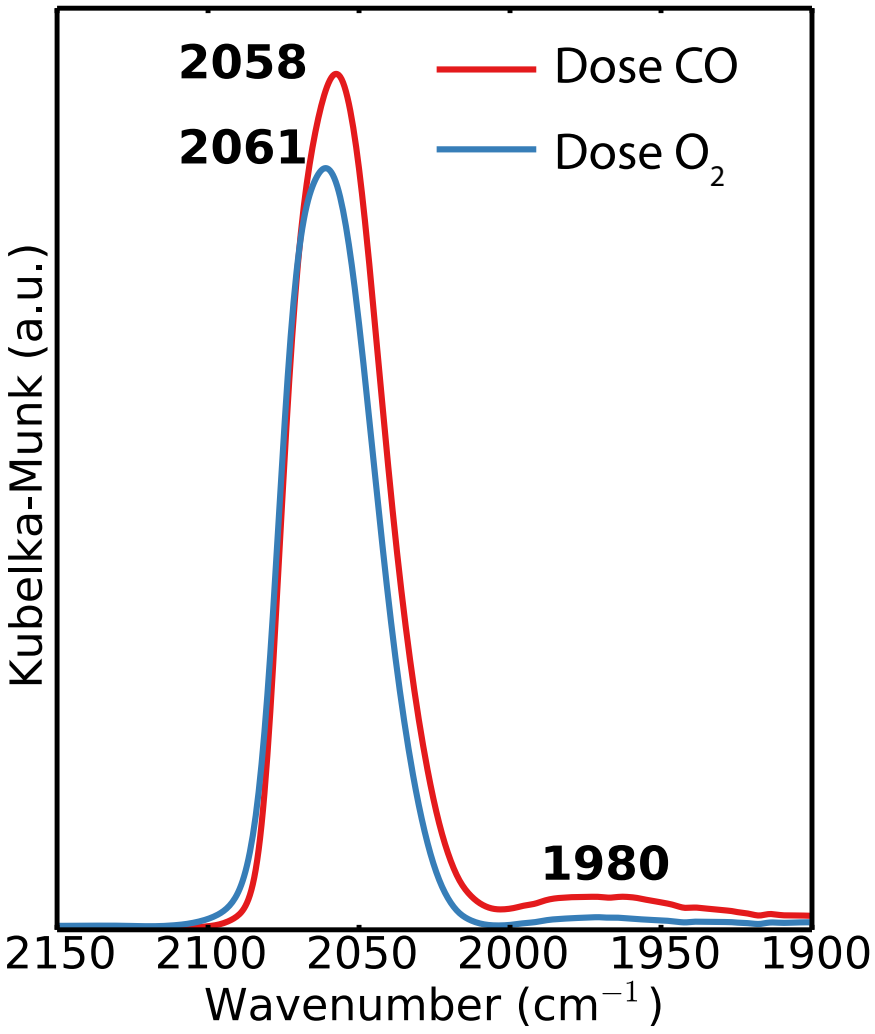

Supplementary Figure 13 | In-situ IR spectra of 1% Ir/$MgAl_2O_4$ sample with a mixture of Ir SAC and Ir NP. IR spectra in the ν_{CO} region characterizing sample of 1% Ir/$MgAl_2O_4$ calcined at 500 °C and reduced at 800 °C (mixture of SAC and NP) with CO adsorbed at room temperature (red), and dose 5 kPa O_2 on the CO adsorbed catalyst at room temperature (blue).

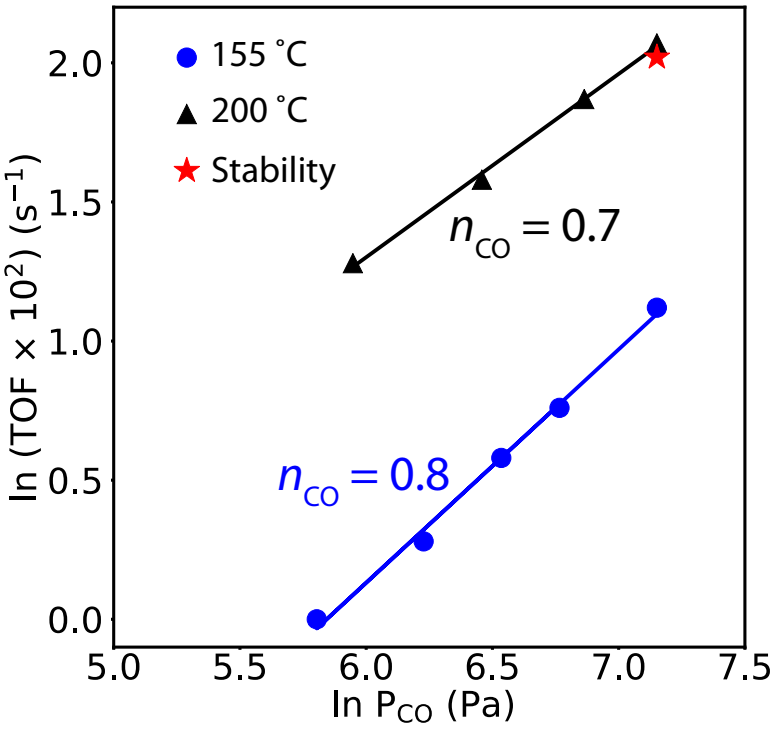

Supplementary Figure 14 | CO oxidation kinetic measurement of the CO reaction order and the stability test at 155 and 200 °C. Effect of CO partial pressure on turnover frequency (TOF) on supported 0.0025% Ir/$MgAl_2O_4$ was firstly measured at 155 °C. P_{O_2} = 10 kPa, P_{CO} = 0.26-1 kPa. The effect of CO partial pressure on turnover frequency (TOF) was performed at 200 °C, with P_{O_2} = 10 kPa. The P_{CO} was varied from 1 kPa to 0.3 kPa. After the kinetic measurement, a stability test was performed at the initial condition at 200 °C (P_{O_2} = 10 kPa, P_{CO} = 1 kPa) and the result shows the catalyst is very stable at the entire CO partial pressure range at 200 °C (2% deactivation compared with the initial measurement at the same condition). For the 0.0025% Ir/$MgAl_2O_4$ single-atom catalyst, due to the low weight loading and the low E_a of ~60 kJ/mol, the conversion was limited to ~3% at all the conditions in our study. However, higher conversions at higher

temperatures (200-220 °C) on the catalyst containing a mixture of single atoms and nanoparticles did not affect the catalyst stability and the activity and reaction orders were reproducible after cooling the reactor to 155 °C.

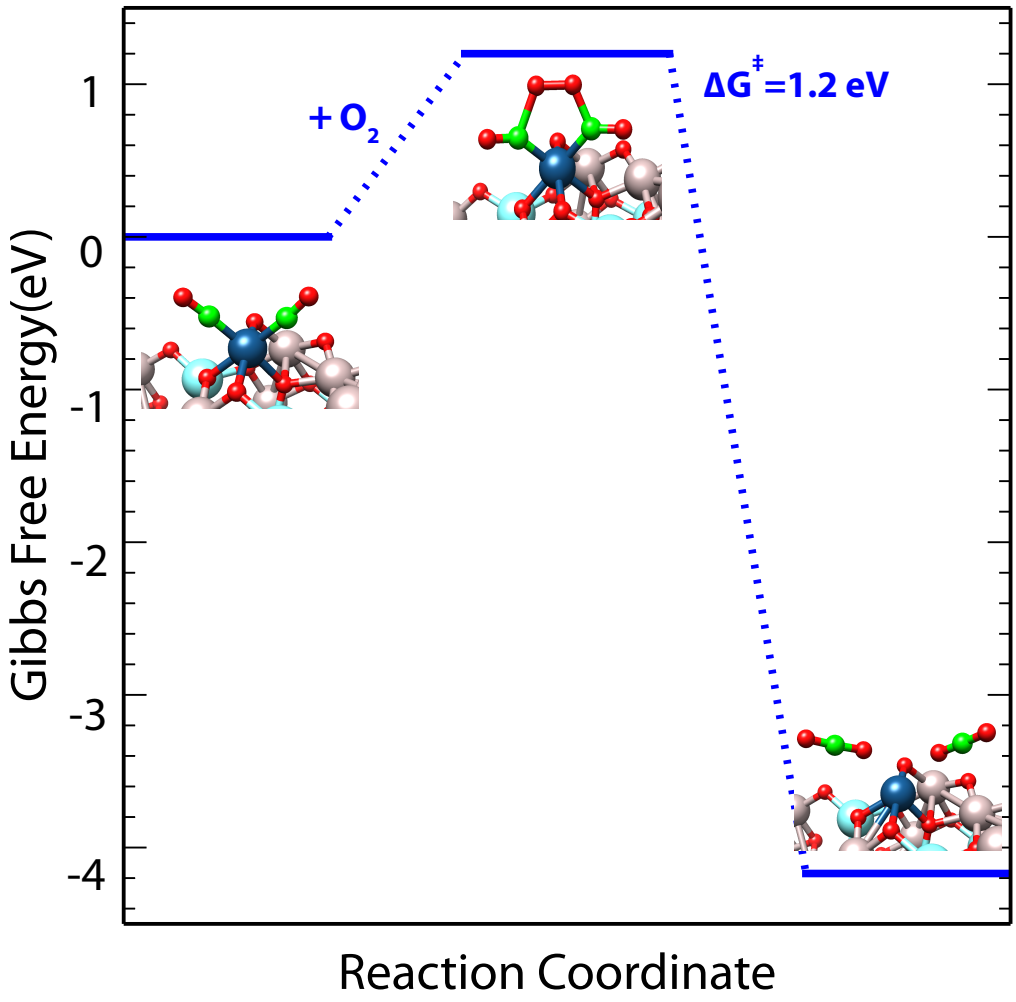

Supplementary Figure 15 | DFT calculated pathway of gas phase O_2 reacting with $Ir(CO)_2$. Gas phase O_2 react with $Ir(CO)_2$ adsorbed on O_2(Al)-terminated $MgAl_2O_4$ (211) surface forming 2 CO_2 through Eley-Rideal (E-R) mechanism similar to the pathway reported by Mao et al. [1]

Supplementary Table 1 | Pretreatment conditions and important physical properties of all samples.

Catalyst	STEM image	Preparation	Calcination	Reduction	BET surface area (m^2/g)
0.2% $Ir/MgAl_2O_4$	Fig. 1d Supplementary Fig. 2	wet impregnation	No calcination step	20% H_2 at 500 °C for 2 hr	101
1% $Ir/MgAl_2O_4$, calcined at 500 °C	Fig. 1a	Incipient wetness impregnation	Air calcination at 500 °C for 4 hr	No reduction	230
1% $Ir/MgAl_2O_4$, calcined at 500 °C, reduced at 800 °C	Fig. 1b Supplementary Fig. 4	Incipient wetness impregnation	Air calcination at 500 °C for 4 hr	20% H_2 at 800 °C for 2 hr	177
0.0025% $Ir/MgAl_2O_4$ (SAC)	Fig. 1c Supplementary Fig. 1	Wet impregnation with initial pH 2.8 and final pH 9.5	Air calcination at 500 °C for 4 hr	20% H_2 at 500 °C for 2 hr	100

Supplementary Table 2 | Volumetric chemisorption. CO/O_2 volumetric chemisorption on 0.2% $Ir/MgAl_2O_4$ nanoparticle only catalyst (NP) and the 1% $Ir/MgAl_2O_4$ calcined at 500 °C and reduced at 800 °C (mixture of SAC and NP).

Catalyst	Gas	Qty. adsorbed μmol/g	Qty. Adsorbed mol/mol Ir	Gas:Ir	Dispersion
0.2% $Ir/MgAl_2O_4$	CO	15.32	0.15	CO:Ir = 1:1	90 %
1% $Ir/MgAl_2O_4$	O_2	19.93	0.38	O:Ir = 1:1	77 %
1% $Ir/MgAl_2O_4$	CO	47.11	0.90	CO:Ir =1:1	90 %

Supplementary Table 3 | DFT optimized structures of Ir SAC on $MgAl_2O_4$ (111) and (211) surfaces. Side view of the of DFT optimized geometric structures of (a) three CO ligands on Ir single atoms supported on O_2(Al)-terminated $MgAl_2O_4$(111) surface, and (b) two CO ligands on Ir single atoms replacing Al on O_2(Al)-terminated $MgAl_2O_4$(211) surface.

Structure	Side view
$Ir_1(CO)_3$ adsorbed on $MgAl_2O_4$(111)	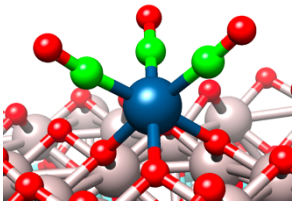
$Ir_1(CO)_2$ adsorbed on $MgAl_2O_4$(211)	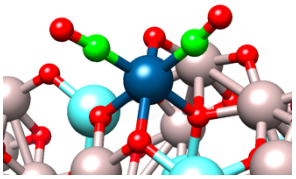

Supplementary Table 4 | Side view of the DFT optimized geometric structures for Ir single atoms on O_2(Al)-terminated $MgAl_2O_4$(211) surface with different ligand configurations.

Structure/ Step in Fig. 4	Side view	Structure	Side view
Ir(CO)(O)-(Al-v) (I)	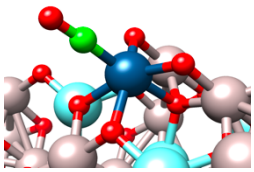	$Ir(CO)_2$-(Al-v)	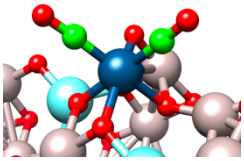
Ir(CO)(O)-(Al-O_2) (II)	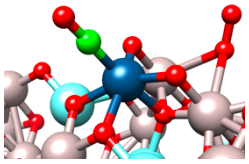	$Ir(CO)_2$-(Al-O)	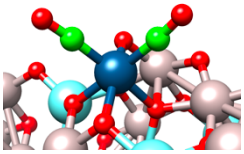
Ir(CO)-(Al-O_2) (III)	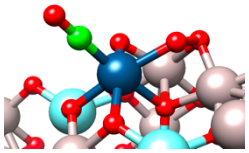	$Ir(CO)_2$-(Al-O_2)	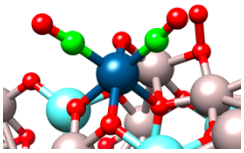
Ir(CO)(O)-(Al-O) (IV)	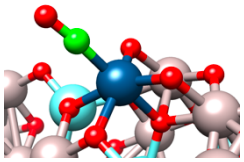	Ir(CO-O)-(Al-carbonate)	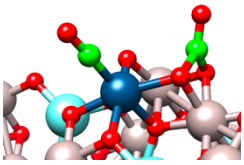
Ir(v)-(Al-O_2) (V)	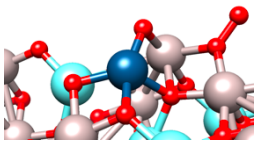	Ir_1 on $MgAl_2O_4$ (211) surface	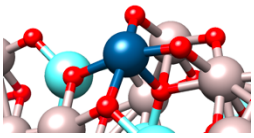
Ir(v)-(Al-O) (VI)	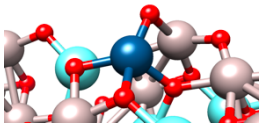	$MgAl_2O_4$ (211)	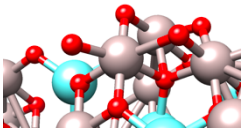

Supplementary Table 5 | DFT calculated energies for gas phase molecules, structures II and TSI with entropy (-TS) and zero-point energy corrections to the free energies.

Species	Entropy correction at 298.15 K (eV)	Entropy correction at 373 K (eV)	Zero-point energy correction (eV)
O_2 [a]	-0.62	-0.78	0.1
CO	-0.62	-0.77	0.14
CO_2	-0.69	-0.86	0.31
II	-0.04	-0.05	0.10
TSI	-0.26	-0.32	0.23

[a] Gas phase O_2 has a DFT functional correction +0.75 eV.

Supplementary Table 6 | Calculated CO and surface O_2 binding energies of Ir single atoms adsorbed on O_2(Al)-terminated $MgAl_2O_4$ (211) surface with different adsorbate configurations.

Structure	CO^* binding energy/eV	$O_2^{\#}$ binding energy/eV
Ir(CO)-(Al-O_2)	-2.11	-2.05
Ir(CO)(O)-(Al-O)	-2.12	/
Ir(CO)(O)-(Al-O_2)	-2.68	-1.18
Ir(CO)(O)-(Al-v)	-2.59	/
Ir$(CO)_2$-(Al-O)	-2.00	/
Ir$(CO)_2$-(Al-O_2)	-2.17	-1.05
Ir$(CO)_2$-(Al-v)	-2.15	/

* Average binding energy per CO is shown in the table

O_2 adsorb on a nearby vacancy of Ir single atom

Supplementary Table 7 | DFT calculated Bader charge on Ir single atoms adsorbed on O_2(Al)-terminated $MgAl_2O_4$ (211) surface with different adsorbate configurations.

Structure	Bader charge of Ir
Ir(CO)-(Al-O_2)	+1.2
Ir(CO)(O)-(Al-O)	+1.38
Ir(CO)(O)-(Al-O_2)	+1.39
Ir(CO)(O)-(Al-v)	+1.43
Ir$(CO)_2$-(Al-O)	+0.77
Ir$(CO)_2$-(Al-O_2)	+0.79
Ir$(CO)_2$-(Al-v)	+0.83

Supplementary Table 8 | DFT calculated Gibbs free energy changes for CO oxidation at 373.15 K over Ir single atoms supported on $MgAl_2O_4$ (211) surface. All energies are relative to the structure I.

Structure in Fig. 4	Gibbs free energy (eV)
I	0
II	-0.49
TSI	0.65
III	-2.48
IV	-2.80
TSII	1.63
V	-0.37
TSIII	-1.16
VI	-3.48

Supplementary Table 9 | Apparent activation energy (E_{app}) of samples with a different ratio of Ir SAC:NP.

Sample[a]	SAC:NP[b]	Apparent activation energy[c] kJ/mol
0.2%Ir/$MgAl_2O_4$ [d]	~ 0:100	101
1% Ir/$MgAl_2O_4$	mixture	71
0.0025% Ir/$MgAl_2O_4$ (SAC)	~ 100:0	62

[a] Pretreatment details in Materials and Methods

[b] From HAADF-STEM images, see Supplementary Fig. 2, Supplementary Fig. 4, and Supplementary Fig. 1 respectively.

[c] Measured at 1 kPa CO and 10 kPa O_2. Between 145 °C and 160 °C with 5 °C increment.

[d] Prepared with organometallic precursor $Ir(CO)_2(acac)$.

Supplementary Table 10 | DFT calculated CO vibration frequencies ($\boldsymbol{\nu_{CO}}$) of Ir single atoms on O_2(Al)-terminated $MgAl_2O_4$ (211) surface with different adsorbate configurations.

Structure	$\boldsymbol{\nu_{CO}}$ cm^{-1}
Ir(CO)(O)-(Al-O)	2094
Ir(CO)(O)-(Al-O_2)	2092
Ir(CO)(O)-(Al-v)	2097
Ir(CO)(O)-(Al-carbonate)	2087
Ir$(CO)_2$-(Al-O)	2104, 2052
Ir$(CO)_2$-(Al-O_2)	2103, 2034
Ir$(CO)_2$-(Al-v)	2102, 2033

Appendix References

1. Mao, K.K. et al. A theoretical study of single-atom catalysis of CO oxidation using Au embedded 2D h-BN monolayer: a CO-promoted O_2 activation. Scientific Reports 4 (2014).

Chapter 3. A Versatile Approach for Quantification of Surface Site Fractions using Reaction Kinetics: The Case of CO Oxidation on Supported Ir Single Atoms and Nanoparticles

This article has been submitted and currently under review. Reprinted (adapted) with permission from Lu, Y.; Kuo,C.; Kovarik, L.; Hoffman, A.S.; Boubnov, A.; Driscoll, D.M.; Morris, J.R.; Bare, S.R.; Karim, A. M.; Versatile Approach for Quantification of Surface Site Fractions using Reaction Kinetics: The Case of CO Oxidation on Supported Ir Single Atoms and Nanoparticles.

This article was co-authored by: Chun-Te Kuo,[†] Libor Kovarik,[‡] Adam S. Hoffman,[§] Alexey Boubnov,[§] Darren M. Driscoll,[||] John R. Morris,[||] Simon R. Bare[§], Ayman M. Karim*[†]

Author Affiliation:

† Department of Chemical Engineering, Virginia Polytechnic Institute and State University, Blacksburg, VA 24060, USA.

‡ Pacific Northwest National Laboratory, Richland, WA 99352, USA.

§ Stanford Synchrotron Radiation Light Source, SLAC National Accelerator Laboratory, Menlo Park, CA 94025, USA.

|| Department of Chemistry, Virginia Polytechnic Institute and State University, Blacksburg, VA 24060, USA.

*Correspondence to: Ayman M. Karim amkarim@vt.edu.

KEYWORDS Single-atom catalysts, Kinetics, CO oxidation, X-ray absorption spectroscopy, infrared spectroscopy, scanning transmission electron microscopy

Attribution:

Yubing Lu performed the synthesis, characterizations and catalytic tests, data analysis, and wrote the first draft of the paper. Adam S. Hoffman, Alexey Boubnov and Simon R. Bare helped design the EXAFS experiment and contributed to writing the XAS section. Adam S. Hoffman, Alexey Boubnov, Yubing Lu, Chun-Te Kuo performed the EXAFS experiments. Ayman M. Karim did the EXAFS analysis. Chun-Te Kuo, Darren M. Driscoll, and John R. Morris helped with the IR experiment. Ayman M. Karim conceived the idea and planned and directed the project. Yubing Lu and Ayman M. Karim co-wrote the paper. All the authors discussed the results and commented on the paper.

3.1. Abstract

Supported metal single-atom catalysts have shown unique activity and selectivity for several reactions. Investigating the reaction mechanism and unambiguous assignment of the activity and selectivity requires catalysts with exclusively single atoms. However, single-atom catalysts prepared with conventional impregnation methods typically consist of a mixture of single atoms and nanoparticles. Here, we show that owing to different reaction mechanisms on single atoms and nanoparticles, reaction kinetics can serve as a surface sensitive characterization technique for

quantifying their surface site fractions. As a case study, we use CO oxidation kinetics on $Ir/MgAl_2O_4$ to quantify the surface site fractions of single atoms and nanoparticles and the results are consistent with aberration-corrected scanning transmission electron microscopy, X-ray absorption fine structure, and infrared spectroscopies. Additionally, by varying the reaction conditions, we show that CO oxidation kinetics is sensitive for detecting a small fraction of single atoms which is difficult by other techniques. Moreover, by carefully choosing the reaction conditions, the activity of single atoms (or nanoparticles) can be made dominant, enabling a study of their reaction mechanism on a catalyst containing a mixture of single atoms and nanoparticles. These results are general and could be applied to other systems where two types of sites have different reaction mechanisms.

3.2. Introduction

Supported noble metals are important for many industrial applications and supported single-atom catalysts (SACs) have gained significant attention because they offer an efficient use of the noble metals[1-3]. Additionally, single-atom catalysts have unique electronic properties compared with nanoparticles and have exhibited excellent activity and selectivity for several reactions[3-7]. Some studies showed that high loading single atoms could be prepared (e.g. Pt/CeO_2[3, 8], Pt/MoS_2[9], Pt/zeolite-templated carbon[10] Pt/SiC[11] and Pd/TiO_2[12]). However, SACs prepared on oxide supports with traditional methods, such as wet impregnation, require calcination and reduction. While exclusively single atoms have been reported after calcination, the single atoms can become mobile and agglomerate into nanoparticles especially during reduction and/or reaction[13-18]. Additionally, due to strong metal-support interaction, the single metal atoms are also prone to diffuse into the

sub-surface layer or bulk phase of the support[19]. Therefore, to correlate the catalytic performance with the metal size, it is crucial to quantify the relative amounts of single atoms and nanoparticles under reaction conditions.

There are several methods that can be used to provide structural information on highly dispersed supported metal catalysts. Owing to the advancement of aberration-corrected electron optics[20-21], single atoms and sub-nanometer clusters can be readily visualized by high-angle annular dark-field scanning transmission electron microscopy (HAADF-STEM or STEM)[22-27]. However, it is difficult to differentiate single atoms on the surface from those in the sub-surface layer of the support. Spectroscopic methods provide a powerful insight into the structure of supported noble metal catalysts. Fourier-transform infrared spectroscopy (FTIR) has been used to characterize the surface species and identify single noble metal atoms but can be difficult to interpret for quantitative measurements when C-O vibrational bands for single atoms and nanoparticles are broad and overlap[8, 28-33]. X-ray absorption spectroscopy (XAS) complemented by STEM[1, 34-37] has been reported as a powerful tool to provide structural information (local structure and bonding with the support) of supported single atoms and sub-nanometer clusters. However, in a sample containing a mixture of single atoms and nanoparticles, multiple techniques are needed to provide sufficient information to quantify the fraction of surface single atom sites. Additionally, interpretation of the results from multiple techniques can be challenging due to the different, sometimes average, information (and bulk vs. surface as well as *in-situ* vs. *ex-situ*) provided by each technique.

Owing to their different structural and electronic properties and the ability to coordinate with more than one adsorbate, the reaction mechanism, and consequently the catalytic performance of single

atoms are often different compared with metal nanoparticles[28, 38-39]. For example, using density functional theory (DFT) and microkinetic modeling, Ammal et al.[40] showed that positively charged Pt single atoms supported on TiO_2 are more active for the water-gas shift reaction compared to Pt nanoparticles. Their microkinetic modeling results showed that the reaction order of CO and H_2O are different on Pt single atoms (CO: 1.00, H_2O: 0.04) than on nanoparticles, specifically on edge interface atoms on Pt_8 clusters (CO: 0.62, H_2O: 0.61) and on corner interface atoms in Pt_8 (CO: 0.01, H_2O: 0.01). Peterson et al.[41] synthesized stable Pd single atoms on γ-Al_2O_3 with the addition of La_2O_3. Reaction orders on the atomically dispersed Pd (Pd/La-alumina) were reported as 0.35 for CO and 0.15 for O_2, which are different from those measured on Pd nanoparticles (Pd/alumina-deactivated), -1.20 for CO and 0.84 for O_2. Recently we reported that CO oxidation proceeds by different mechanisms at low temperature (< 200 °C) on Ir single atoms and nanoparticles supported on $MgAl_2O_4$ which were reflected in CO and O_2 orders of 1 and 0, respectively, on single atoms and -1 and 1, respectively, on nanoparticles[42].

In this study, we exploit the difference in reaction mechanism (and reaction orders) for low-temperature CO oxidation on Ir single atoms[42] and Ir nanoparticles supported on $MgAl_2O_4$ and show that kinetic measurements can be used as both a facile and sensitive characterization tool for quantifying the number *and* fraction of surface sites of single atoms and nanoparticles. Using STEM, CO chemisorption, *in-situ* FTIR and XAS, we show that reaction kinetics provide a direct and accurate method for quantifying the surface composition of the catalyst under reaction conditions. Moreover, the reaction conditions can be chosen to make the activity of the single atoms dominant and enable investigating the reaction mechanism on catalysts with a mixture of single atoms and nanoparticles. The methodology can be extended to other catalysts and reactions

to quantify the surface composition of two different sites (e.g. single atoms and nanoparticles, or two different metals, metal 1 and metal 2), provided the reaction mechanism is different on the two types of sites.

3.3. Methods

Synthesis and pretreatment. The 0.2 wt.% Ir/MgA_2O_4 nanoparticle sample (sample 0) was prepared by wet impregnation. Under a N_2 flow at room temperature, an appropriate amount $Ir(CO)_2$(acac) (Sigma Aldrich) precursor was dissolved in 8 mL of toluene (Sigma Aldrich) in a 20 mL vial. Then the solution of $Ir(CO)_2$(acac) in toluene was injected into another vial containing 5 g $MgAl_2O_4$ (Puralox MG 28, Sasol) under N_2 flow. The sample was then dried under N_2 flow at room temperature overnight to evaporate the toluene. The CO and acetylacetonate (acac) ligands were removed *in-situ* by treatment in 20 kPa H_2 (balance He, 100 sccm total flow rate) at 500 °C for 2 h (10 °C/min) which led to the formation of ~1 nm diameter nanoparticles, as detailed below. The 1 wt.% Ir/$MgAl_2O_4$ samples (samples 1, 2 and 5) were synthesized by incipient-wetness impregnation. The proper amount of iridium nitrate precursor (8.7 wt.%, Furuya Metal Co. Ltd.) was added to the $MgAl_2O_4$ support (Puralox MG30, Sasol) drop–by-drop while mixing, and the sample was then dried at 80 °C for 4 h and 100 °C (at 0.5 °C/min) for 12 h. After impregnation and drying, sample 1 was reduced *in-situ* with 20 kPa H_2 (balance He, 80 sccm total flow rate) at 800 °C (at 10 °C/min) for 2 h. Sample 2 was calcined at 500 °C (at 5 °C/min) in air for 4 h before *in-situ* reduction in a flow of 20 kPa H_2 (balance He) at 800 °C (at 10 °C/min). Sample 4 was calcined at 500 °C (at 5 °C/min) in air for 4 h before *in-situ* reduction in a flow of 20 kPa H_2 (balance He) at 500 °C (at 10 °C/min) for 2 h. The 0.05 wt.% Ir/$MgAl_2O_4$ (sample 3) was prepared

by wet impregnation. The $MgAl_2O_4$ support (Puralox MG 28, Sasol) was calcined at 500 °C for 4 h before impregnation. 1 L deionized water was added to a Pyrex flask and the pH was adjusted with nitric acid to 2.8. The iridium nitrate precursor was added into the pH-adjusted solution. The $MgAl_2O_4$ support was then added into the solution while stirring. After 4 h of stirring, the final pH of the solution was 9.5. The nominal Ir weight loading was 0.05 wt.%. The solution was filtered out and the solid sample was dried in air overnight at room temperature. The sample was then dried at 80 ℃ and 100 °C before calcination in air at 500 °C for 4 h. After that, the sample was reduced *in-situ* in a flow of 20 kPa H_2 (balance He) at 500 °C (at 10 °C/min) for 2 h. The 0.0025 wt.% Ir/$MgAl_2O_4$ single-atom catalyst (SAC, sample 4) was prepared by wet impregnation. The same steps as sample 3 were applied except that 200 mL of deionized water was added to the Pyrex flask, and the nominal Ir loading was 0.0025 wt.%. The calcination and reduction temperatures were both 500 °C. All the *in-situ* characterization and the CO oxidation reaction followed the same pretreatment procedure as mentioned above. The actual weight loadings of samples 3 and 4 (prepared by wet impregnation method) were determined by measuring the Ir concentration of the solutions after wet impregnation, using inductively coupled plasma-atomic emission spectroscopy (ICP-AES) on a Spectro ARCOS II Multi-View ICP Model FHM22 with CETAC Autosampler instrument. Details about synthesis of samples 0-5 are summarized in Supporting Information Table S1.

Diffuse-reflectance infrared Fourier-transform spectroscopy (DRIFTS). DRIFTS was used to characterize the interaction of the supported Ir catalysts with CO. The *in-situ* DRIFTS experiments were performed using a Thermo Scientific IS-50R FT-IR equipped with an MCT/A detector. A spectral resolution of 4 cm^{-1} was used to collect spectra, which are reported in the Kubelka-Munk

(KM) units. Approximately 50 mg sample (25-90 μm diameter particles) was loaded in the Harrick Praying Mantis high-temperature DRIFTS reaction chamber. The chamber was sealed and connected to a flow system with temperature control, and gases were flown through the sample at atmospheric pressure. Each reported spectrum is an average of 32 scans. The supported Ir samples were pretreated *in-situ* in the DRITS cell before collecting the spectra. The gas pretreatment procedure was the same as mentioned above. For in-situ pretreated catalyst, a spectrum under N_2 after the pretreatment was collected as the background. For samples that required ex-situ pretreatment, a spectrum of the $MgAl_2O_4$ support was used as the background.

Scanning transmission electron microscopy (STEM). Aberration-corrected electron microscopy images for $Ir/MgAl_2O_4$ samples were taken on FEI TITAN 80-300 in STEM-mode using a high-angle annular dark-field (HAADF) detector. The resolution is 0.1 nm with the CEOS GmbH double-hexapole aberration corrector. To calculate the atomic percentage of single atoms and nanoparticles of different sizes in each catalyst, we measured the diameter of the nanoparticles (*D*), and counted the single atoms and particles from multiple STEM images using ImageJ[43]. To estimate the number of atoms per particle we setup a model for hemispherical nanoparticle shape, which is the most abundant particle shape observed by STEM (see Figure S1, Supporting Information). We modified a cuboctahedron model[44] to represent a hemispherical particle. For a cuboctahedron particle, the number of total atoms N_T, the number of atoms lying on an equivalent edge is defined as m (corner atoms included). N_T can be represented by m with the equation [44]: $N_T = 16m^3 - 33\ m^2 + 24m - 2$. The number of atoms on the central cross section of the cuboctahedron (N_C) can be calculated as: $N_C=(3m - 2) \times (m-1) + (2m - 1) \times m$. For a semi-cuboctahedron particle on a support (with the same radius as the cuboctahedron), the number of

atoms (N_{hemi}) can then be calculated as $N_{hemi} = \frac{N_T+N_C}{2}$. With the above equations, we can first calculate the number of atoms in a spherical particle as[45], $N_T=\frac{\pi D^3 \rho N_A}{6M_w}$, with a diameter *D* measured by STEM, then calculate N_{hemi} in each particle and the total number of atoms in all nanoparticles (N_{hemi_total}). The total atomic fraction of single atoms (i.e. bulk, volume fraction) was calculated using the number of single atoms (SA) measured by STEM (N_{SA}) and the total atoms in all the nanoparticles (N_{hemi_total}) as $N_{SA}/(N_{SA}+N_{hemi\_total})$. The total number of surface atoms in nanoparticles (N_{s_total}) was calculated from the total atoms in each particle using the dispersion for completely shelled polyhedron[46] for particles ≥ 0.7 nm, while smaller ones were assumed to have 100% dispersion. The surface fraction of single atoms can then be calculated as $N_{SA}/(N_{SA}+N_{s\_total})$.

For sample 0, 55 Ir single atoms and 59 nanoparticles were counted from 8 STEM images. For sample 1, 127 Ir single atoms and 60 Ir nanoparticles were counted from 5 STEM images. For sample 2, 1410 Ir single atoms and 102 Ir nanoparticles were counted from 5 STEM images. For sample 3, 1160 Ir single atoms and 36 Ir nanoparticles were counted from 15 STEM images. For sample 4, only single atoms were observed. For sample 5, 2310 Ir single atoms and 71 Ir nanoparticles were counted from 5 STEM images. See Supporting Information Table S1 for detailed size distribution.

X-ray absorption spectroscopy (XAS). The catalysts were characterized by *in-situ* XAS at the Ir L_3-edge (11215 eV) using an in-house built cell with a 4 mm ID glassy carbon tube[47]. The XAS measurements were performed at the Stanford Synchrotron Radiation Light Source (SSRL). The measurement for the high weight loading samples (1 wt.% Ir, samples 1, 2 and 5) was performed at bend-magnet beamline 2-2 in transmission mode using ion chambers (pure N_2 for all ion

chambers). The photon energy was selected using a water cooled, double-crystal, Si (220) $\phi = 90°$ monochromator. The measurements on the 0.05 wt.% Ir catalyst (sample 3) were performed at beamline 9-3 in fluorescence mode. Beamline 9-3 is a 16-pole, 2-Tesla wiggler side station with vertically collimating mirror for harmonic rejection and a cylindrically bend mirror for focusing. The photon energy was selected using a liquid-nitrogen-cooled, double-crystal Si (220) $\phi = 90°$ monochromator. Samples were scanned simultaneously in transmission and fluorescence detection modes using ion chambers (see above) and a 100-element solid-state Ge monolith detector (Canberra). An Ir standard (Ir black powder) was scanned simultaneously with each sample for energy calibration. Step-scanning X-ray absorption spectra were measured from 10965 eV to 12610 eV, corresponding to photoelectron wave number $k = 19$ Å^{-1}. The catalysts were pretreated similar to before the catalytic measurements, then cooled to room temperature in pure H_2 flow (50 sccm) and the EXAFS spectra were collected at room temperature under pure H_2 flow. XANES and EXAFS data processing and analysis were performed using Athena and Artemis programs of the Demeter data analysis package[48-49]. For each catalyst, four scans were collected and merged after alignment. χ(k) was obtained by subtracting smooth atomic background from the normalized absorption coefficient using the AUTOBK code. The theoretical EXAFS signal was constructed using the FEFF6 code[50] and fitted to the data in *R*-space using the Artemis program. For modeling the Ir, an *fcc* crystal structure with a lattice constant of 3.92 Å was used. The Ir-Al and Ir-Mg and Ir-O scattering paths were simulated from density functional theory calculated structures where an Ir atom was adsorbed on the three-fold hollow Al or Mg sites (for Ir-Al and Ir-Mg respectively) of O2(Al)-terminated $MgAl_2O_4(111)$[42]. The theoretical EXAFS scattering paths were fit to the data in *R*-space using the Artemis program of the Demeter package. The spectra were fit by varying the

coordination number of the single scattering Ir-Ir, Ir-O, and Ir-Al/Mg paths, the bond length disorder (σ^2), and the effective scattering lengths for each path and the correction to the threshold energy, ΔE_0. S_0^2 (the passive electron reduction factor) was obtained by first analyzing the spectrum for an Ir black, and the best fit value (0.83) was fixed during the fitting. The *k*-range used for Fourier-transform of the $\chi(k)$ was 2.5-16 $Å^{-1}$ for 1 wt.% Ir samples and 2.5-13 $Å^{-1}$ for 0.05 wt.% Ir sample and the *R*-range for fitting was 1.3-3.0 Å.

CO volumetric chemisorption. Volumetric CO chemisorption was performed with a Micromeritics 3Flex surface characterization analyzer. 0.3-1.0 g of catalyst (particle size between 425 – 710 μm) was packed in a quartz sample holder and pretreated with the same procedure described in the synthesis section. The total flow rate for each step was 80 sccm. The sample was evacuated at 35 °C for 1 h before the chemisorption analysis using CO (Airgas, 99.997%, semiconductor grade, in an aluminum cylinder, $Fe(CO)_5$ content <0.1 ppmw). Two CO chemisorption isotherms were performed between 5 mm Hg and 450 mm Hg at 35 °C with an evacuation step between the two isotherms to remove the physically adsorbed CO. The 1st isotherm represents both the chemisorbed and the physisorbed CO. The 2nd isotherm indicates the amount of physisorbed CO. The difference of the two CO isotherms is reported as the amount of chemisorbed CO.

CO oxidation kinetic measurements. CO oxidation kinetic measurements were performed under differential conditions (<3% conversion) in a conventional laboratory tubular plug flow reactor (7 mm ID quartz tube). Dilution experiments were performed according to Koros-Nowak test to determine the necessary dilution ratio for measurements under strict kinetic control without mass and heat transfer effects[51-53]. The catalysts (after intraparticle dilution) were pressed and sieved into a 106-250 μm diameter fraction. The dilution ratio test to eliminate transport limitations was

performed on 1 wt.% Ir/$MgAl_2O_4$ catalyst using SiO_2 as the diluent. Intraparticle dilutions ratio of 1:40, 1:200 and 1:1000 showed no difference in activity under different CO and O_2 conditions between 145 °C and 170 °C, which indicates the measured catalytic activity was evaluated under kinetic control without transport artifacts. Based on the dilution test, the 0.2 wt.% Ir/$MgAl_2O_4$ (sample 0) was diluted with silica at a 1:20 ratio, and the 1% Ir/$MgAl_2O_4$ (samples 1, 2, 5) were diluted with silica (Silica gel, for chromatography, 0.075-0.250 mm (150 Å pore size), calcined at 850 °C) at a 1:40 ratio, and the 0.0025 wt.% Ir/$MgAl_2O_4$ (SAC, sample 4) and the 0.05% Ir/$MgAl_2O_4$ (sample 3) required no dilution because of the low Ir loading. Negligible activity (~1/10 activity of the lowest loading catalyst, 0.0025 wt.%, sample 4) was measured on the $MgAl_2O_4$ support compared with that from all of the catalysts. Each catalyst pretreatment was the same as mentioned above, and the total flow rate during pretreatment was kept at 80 sccm. The catalyst temperature was measured by a K-type thermocouple (OMEGA) attached at the center of the catalyst bed on the outside of the tube. After pretreatment, CO (5%, balance N_2, certified grade Airgas) was mixed with pure O_2 (99.999% Airgas) and He (99.999% Airgas, equipped with moisture/O_2 trap, Agilent OT3-2) at 35 °C to control the partial pressures of CO and O_2 (by varying their flowrates using Brooks mass flow controllers SLA5800 series). The CO gas line was equipped with a metal carbonyl purifier (Matheson, NanoChem Metal-X) to remove the trace amount of metal carbonyl and a molecular sieve 3A (8–12 mesh) trap to remove trace (ppm) levels of CO_2. No CO_2 was detected in the mass spectrometer with the CO or O_2 flowing during a blank test. The reactor was heated from room temperature to the reaction temperature at 3 °C/min in 0.5 kPa CO and 10 kPa O_2 balanced with He. During the steady-state kinetic measurements, the conversion of CO was always below 3% by varying the total flow rate between 50-100 sccm. To

investigate the effect of CO partial pressure on reaction rate, the partial pressure of O_2 was held constant at 10 (or 2) kPa and the partial pressure of CO was varied between 0.2 – 1.0 kPa. To investigate the effect of O_2 partial pressure, the CO partial pressure was held constant at 1.0 kPa and the partial pressure of O_2 was varied between 2 – 14 kPa, then the measurements were repeated at 0.2 kPa CO partial pressure. The kinetic experiments were reproduced using two different aliquots from the same batch and also reproduced using two different batches of the catalyst. We note that we rigorously monitored the catalyst stability by re-measuring the catalyst activity periodically throughout the experiment under the first condition measured. The activity was stable (< 10% deactivation) for each catalyst tested during the entire kinetic measurement. The composition of the effluent gases was measured by a gas chromatograph (Inficon Micro GC Fusion with two modules each with a separate carrier gas, injector, column and thermal conductivity detector (TCD). Column A: Rt-Molsieve 5A, 0.25 mm ID (10m) using Ar as the carrier gas. Column B: Rt-Q-Bond 0.25 mm ID (12m) using He as the carrier gas. With the exception of sample 0, the reaction rates were normalized by the total moles of Ir, not the amount of adsorbed CO from chemisorption measurements. Normalizing the activity using CO chemisorption requires knowledge of the CO:Ir stoichiometry to calculate the number of Ir surface sites. For the catalysts containing a mixture of single atoms (CO:Ir = 2:1) and nanoparticles (CO:Ir = 1:1), the CO:Ir stoichiometry will be different depending on their composition (fraction of single atoms vs. nanoparticles). Moreover, measurements of the site fraction of single atoms and nanoparticles using a different technique (e.g. STEM, EXAFS or DRIFTS) is required to calculate the CO:Ir stoichiometry in each sample. Therefore, normalizing the activity using the calculated CO:Ir

stoichiometry will be biased by the technique used to estimate the fraction of single atoms and nanoparticles.

3.4. Results

3.4.1. Structural characterization using STEM and XAS

Five Ir/$MgAl_2O_4$ catalysts were synthesized (with different precursors, loadings and pretreatment, see Methods and Supporting Information Table S1 for details) to vary the percentage of single atoms and nanoparticles, denoted as SA and NP from herein, respectively. The catalysts were characterized by HAADF-STEM to determine the Ir cluster size distributions and the fraction of single atoms. The particle sizes were measured across multiple STEM images and for each particle, a semi-cuboctahedron model (see Methods section and Supporting Information Figure S1 for details) was used to calculate the number of atoms within each particle. The atomic percentage (based on total atoms) for single atoms and different size nanoparticles was then calculated to generate the size distribution for each sample. Representative STEM images, the size distributions and fraction of single atoms for samples 0-4 are shown in Figure 1. As shown in Figure 1f, the five catalysts have a different fraction of single atoms (total atom basis), namely, 2% (sample 0), 16% (sample 1), 35% (sample 2), 61% (sample 3) and ~ 100% (sample 4). Most nanoparticles were 0.7-2 nm in diameter (detailed size distributions and surface site fractions are shown in Supporting Information Table S2). We note that the fraction of single atoms obtained on total atoms basis was similar (only slightly lower) to that obtained on surface atoms basis (Supporting Information Table S2), due to the small nanoparticle size (high dispersion) in the three samples. Two more batches of sample 3, where one was after CO oxidation, were also measured to determine the variations

between batches of the same sample which was approximately ± 9% for the percentage of single atoms (Supporting Information Figure S2) indicating reproducibility and negligible agglomeration during the reaction.

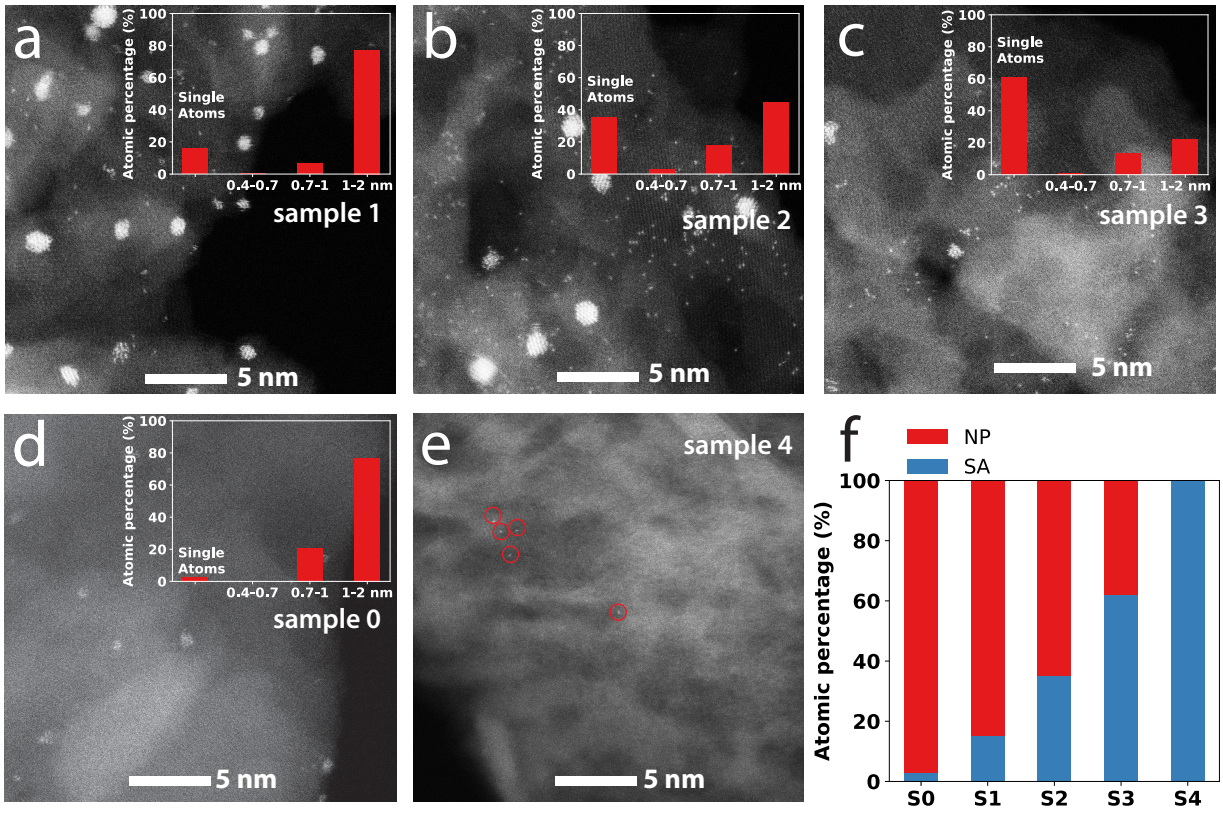

Figure 1. High angle annular dark field – scanning transmission electron microscopy images of Ir samples with different SA: NP ratios (sample 0-4). The insets (red bars) show the size distribution (atomic percentage on total atoms basis) of Ir species from multiple STEM images. Representative STEM images of (a) 1 wt.% Ir on $MgAl_2O_4$ without calcination and reduced at 800 °C in H_2 (sample 1). SA : NP = 15% : 85%. (b) 1 wt.% Ir on $MgAl_2O_4$ calcined at 500 °C in air and reduced at 800 °C in H_2 (sample 2). SA : NP = 35% : 65%. (c) 0.05 wt.% Ir on $MgAl_2O_4$ calcined at 500 °C in air and reduced at 500 °C in H_2 (sample 3). SA : NP = 61% : 39%. (d) 0.2 wt.% Ir on

$MgAl_2O_4$ prepared with $Ir(CO)_2(acac)$ precursor and reduced at 500 °C in H_2 (sample 0). SA : NP = 2% : 98%. (e) 0.0025 wt.% Ir on $MgAl_2O_4$ calcined at 500 °C in air and reduced at 500 °C in H_2 (sample 4) with Ir single atoms ~ 100 %. (f) Atomic percentage (total atoms basis) of single atoms (blue) and nanoparticles (red) of samples 0-4.

Figure 2a shows the XANES spectra at the Ir L_3-edge of samples 1-3 after pretreatment. Sample 3 (61% SA from STEM) has the highest white line intensity followed by sample 2 (35% SA from STEM) and sample 1 (16% SA from STEM). The white line intensity increased with an increase in the percentage of the single atoms in each sample. This is expected because Ir single atoms are bound to O from the support and therefore are more electron deficient compared with Ir atoms in nanoparticles[33]. The corresponding EXAFS spectra of samples 1-3 are shown in Figure 2b (spectra and fits are provided in the Supporting Information Figure S4-9) and modeling results of the catalysts are summarized in Table 1. The average first shell Ir-Ir coordination number decreased with the increase in SA% from STEM (6.6, 6.0 and 2.4 for samples 1-3). On the other hand, the Ir-O coordination number increased with the increase in SA% from STEM (0.2, 0.9, and 2.2). The decrease in Ir-Ir coordination and increase in Ir-O coordination is in agreement with the higher contribution from single atoms. It has been shown that the $MgAl_2O_4$ exposed mostly (111) facets[19, 42, 54-55]. On an O-terminated (highly stable thermodynamically)[56] $MgAl_2O_4$ (111) surface, an Ir single atom is bonded with 3 surface O, and on an O- terminated $MgAl_2O_4$ (211) surface, Ir is bonded with 4 surface O[42]. Based on these Ir-O coordination numbers, the percentage of Ir single atoms on samples 1-3 can be estimated as 5-7%, 23-30% and 55-73% which are in agreement with those estimated from STEM (total atoms basis, Figure 1f, Supporting Information Table S2).

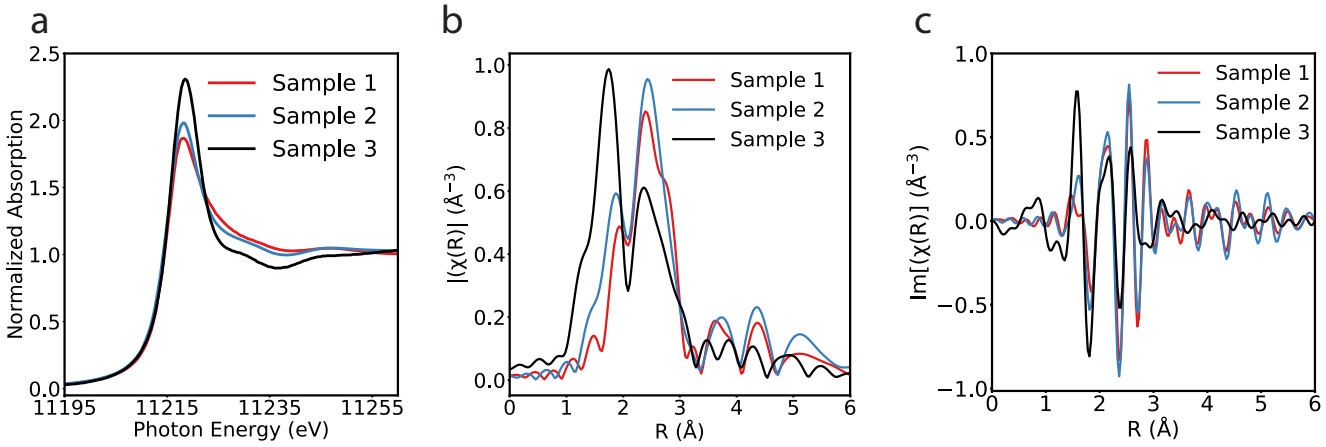

Figure 2. Ir L_3-edge X-ray absorption spectroscopy of samples 1-3. (a) XANES, and EXAFS magnitude (b) and (c) imaginary part of the of the Fourier transformed k^2-weighted $\chi(k)$ data, Δk = 2.7-13 $Å^{-1}$.

Table 1. Summary of EXAFS modeling of samples 1-3 after reduction.

Sample		Sample 1	Sample 2	Sample 3
Atomic (STEM)	SA%	16%	35%	61%
$N_{Ir\text{-}Ir}$		6.6±0.4	6.0±0.6	2.4±1.2
$N_{Ir\text{-}O}$		0.2±0.1	0.9±0.3	2.2±0.4
$N_{Ir\text{-}Al/Mg}$		0.2±0.1	1.0±0.3	2.3±0.4
$R_{Ir\text{-}Ir}$ (Å)		2.689±0.002	2.661±0.004	2.65±0.02
$R_{Ir\text{-}O}$ (Å)		2.06±0.04	2.070±0.015	2.040±0.010
$R_{Ir\text{-}Al/Mg}$ (Å)		2.93±0.04	2.974±0.020	2.973±0.018
$\sigma^2_{Ir\text{-}Ir} \times 10^3$ ($Å^2$)		5.8±0.3	5.2±0.3	3±2
$\sigma^2_{Ir\text{-}O} \times 10^3$ ($Å^2$)		1±7	3±3	1±1
$\sigma^2_{Ir\text{-}Al/Mg} \times 10^3$ ($Å^2$)		0±5	2±4	1±4
$\Delta E_{0\ Ir\text{-}Ir}$ (eV)		7.0±0.7	8.5±1.3	3±4

$\Delta E_{0\ Ir\text{-}O}$ (eV)	10±5	12±4	11+3
$\Delta E_{0\ Ir\text{-}Al/Mg}$ (eV)	10±5	12±4	10[a]
Reduced χ^2	16	154	122
R-factor	0.0003	0.0027	0.0064

[a] fixed during the fit

Notation: N, coordination number of absorber-backscatterer pair; R, radial absorber-backscatterer distance; σ^2, the mean square displacement of the half-path length and represents the stiffness of the bond for a single scattering path, ΔE_0, correction to the threshold energy.

3.4.2. Identification and quantification of surface SA and NP using DRIFTS

CO chemisorption in DRIFTS was used to characterize the surface Ir species. In the CO vibrational region, the bands at ~2061 cm^{-1} and 2000 cm^{-1} are assigned to the symmetric and anti-symmetric vibrational modes of the Ir gem-dicarbonyl ($Ir(CO)_2$) of Ir single atoms[57-58]. Vibrational bands for linearly adsorbed CO on Ir nanoparticles are located between 2030-2090 cm^{-1} depending on the particle size and support[59-60]. The linear band of sample 3 (0.05 wt.%, 61% SA from STEM) is centered at 2042 cm^{-1} while it was at a higher frequency, around 2050-2060 cm^{-1}, on samples 1 and 2 (1 wt.%) which is consistent with their larger average particle size. The relative intensity of the gem-dicarbonyl anti-symmetric band at 2000 cm^{-1} compared to the linear vibrational band increases from sample 1-3, which indicates an increase in the percentage of single atoms. This is consistent with the percentage of single atoms observed from STEM and EXAFS. Estimation of the percentage of surface single atoms and nanoparticles of a mixture sample using DRIFTS has

been performed when the extinction coefficients are known or can be measured as was shown for Rh and Pt [28, 61]. We estimated the extinction coefficients of the Ir single atoms and nanoparticles using the spectra for $MgAl_2O_4$ supported single atoms only catalyst (sample 4) and nanoparticles only catalyst (sample 0) [42]. The DRIFTS spectra of these two catalysts are shown in Supporting Information Figure S3. Kubelka-Munk (K-M) theory has been used for quantitative analysis of DRIFTS spectra, but we acknowledge that DRIFTS inherently could have error due to differences in powder particle size and packing density between samples [62-64]. Based on the integrated band area (K-M unit) and mol of Ir in each sample (30 mg of sample in the chamber), the extinction coefficients of the Ir single atoms (ε_{SA}) and Ir nanoparticles (ε_{NP}) were estimated as 24 ± 4 and 54 ± 11 ($\times 10^5$ cm^{-1}/mol, using spectra from 3 different measurements of each sample) respectively. For comparison, extinction coefficient for gem-dicarbonyl and linear CO on Rh for Rh/Al_2O_3 were reported as 74 and 26 ($\times$ 10^8 cm^{-1}/mol), respectively[28, 61]. The Ir single atoms site fraction X_{SA} can be calculated with the following equation[28]:

$$X_{SA}=\frac{A_{SA}/\left(\varepsilon_{SA}\times\left(\frac{CO}{Ir}\right)_{SA}\right)}{A_{SA}/\left(\varepsilon_{SA}\times\left(\frac{CO}{Ir}\right)_{SA}\right)+A_{NP}/\left(\varepsilon_{NP}\times\left(\frac{CO}{Ir}\right)_{NP}\right)} \quad (1)$$

where X_{SA} (and $X_{NP} = 1 - X_{SA}$) is calculated on the basis of the areas of the gem-dicarbonyl per CO (A_{SA}) and linear CO bands (A_{NP}), extinction coefficient (ε_{SA} and ε_{NP}) and the stoichiometry of CO adsorbed per Ir atoms (CO/Ir =1 for NP and 2 for SA). Deconvolution of the single atoms and nanoparticles IR bands for sample 3 is shown in Figure 3b. Bands centered at 2066 and 1997 cm^{-1} are assigned to the gem-dicarbonyl on Ir single atoms. The band centered at 2042 cm^{-1} is assigned to the linear stretching CO on Ir nanoparticles. The integrated band areas of the symmetric and

anti-symmetric CO stretching bands, and the linear CO stretching band, are determined to be 0.17, 0.15 and 0.26 cm^{-1}, respectively. Applying equation (1), the site fraction of single atoms (X_{SA}) was 58 ± 9%, which is slightly lower than the 66% surface single atoms observed from STEM (Supporting Information Table S2). We note that the actual surface SA% is expected to be lower than 58% estimated from DRIFTS since we used symmetric peaks for all the CO bands, including the linearly adsorbed CO on nanoparticles, which typically has asymmetry because nanoparticles contain a distribution of different adsorption sites[65]. This results in an overestimation of the areas for the gem-dicarbonyl bands. Deconvolution of the bands for samples 1 and 2 was not possible (attempted fitting resulted in non-singular results with large variation) due to the non-symmetric shape of the linear band and its overlap with the symmetric stretching CO band of the gem-dicarbonyl (on nanoparticles and single atoms, respectively). The results show that the estimatiotn of site fractions is challenging when the CO IR bands of single atoms and nanoparticles overlap. Additionally, the error in band deconvolution is expected to increase significantly for low percentage of single atoms or nanoparticles.

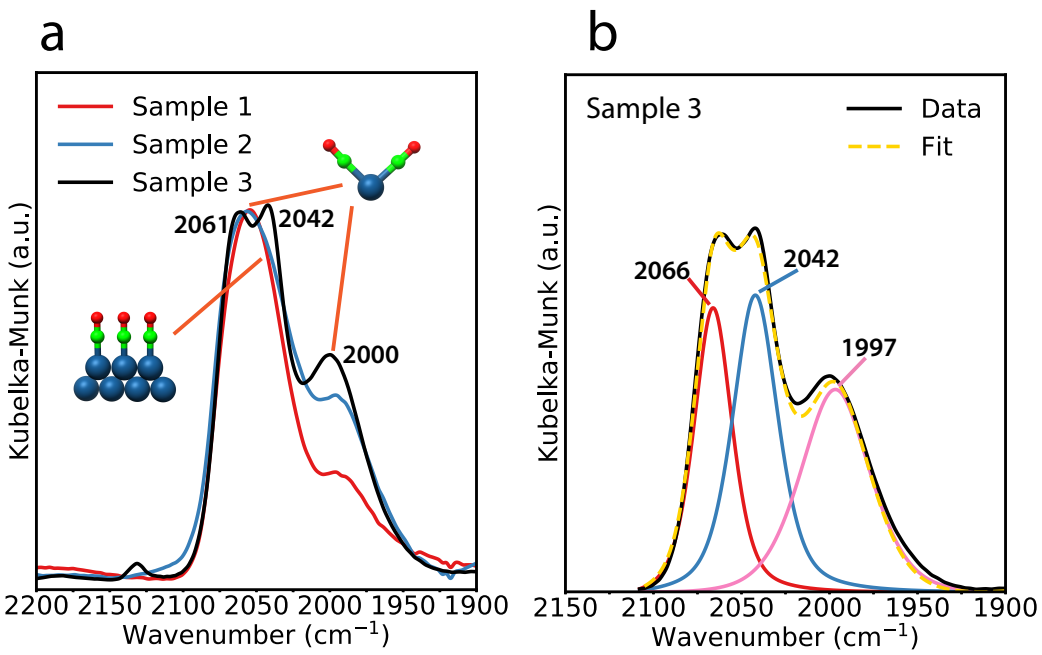

Figure 3. In-situ infrared spectroscopy (IR) spectra of CO adsorption in the ν_{CO} region characterizing samples 1-3 and the deconvolution of bands for sample 3. (a) IR spectra of sample 1-3. Spectra are normalized by the Ir weight loading. Samples 1 and 2 (1 wt.% Ir) were reduced ex-situ at 800 °C in H_2 and then covered with CO at room temperature. After that samples were transferred to the DRIFTS cell, reduced in-situ with CO at 80 °C and the IR spectra were collected at -40 °C. Sample 3 (0.05 wt.% Ir) was pretreated in-situ at 500 °C in H_2, saturated with CO at room temperature and the spectra were collected at -40 °C. (b) Deconvolution of bands representing single atoms ($Ir(CO)_2$) and nanoparticles (Ir(CO)) for the IR spectrum of sample 3.

In summary, the site fraction of single atoms estimated by STEM and XAS were similar (Table 2) and the DRIFTS results were in qualitative agreement in terms of ranking the samples based on the fraction of single atoms. However, the site fraction estimated using DRIFTS is reliable only when extinction coefficients are accurately measured and the dicarbonyl and linear bands do not significantly overlap.

Table 2. Percentage of single atoms estimated from EXAFS, STEM and CO oxidation kinetic measurements.

Sample	EXAFS	STEM (total atoms)	STEM (surface atoms)	CO oxidation
SA% in sample 1	5-7%	16%	19%	18 ± 5%
SA% in sample 2	23-30%	35%	39%	32 ± 2%
SA% in sample 3	55-73%	61%	66%	42 ± 5%

3.4.3. Quantification of the surface fraction of SA and NP using reaction kinetics

A previous study[42] in our group showed that supported Ir single atoms have a different reaction mechanism than Ir nanoparticles for low-temperature CO oxidation (100- 220 °C). Gas phase O_2 can be readily activated (even at room temperature) on the CO-adsorbed Ir single atoms. Additionally, Ir(CO)(O) was identified as the most stable complex (resting-state) and the rate-limiting step is the reaction of gas phase CO with O from Ir(CO)(O) through an Eley-Rideal

mechanism to complete the cycle. A consequence of this mechanism is different CO and O_2 reaction orders which were determined to be 1 and 0, respectively, i.e. $r(Ir_{SA}) \propto P_{CO}$. This is in contrast to CO and O_2 orders of -1 and 1 on Ir nanoparticles, i.e. $r(Ir_{NP}) \propto \frac{P_{O_2}}{P_{CO}}$. Therefore, as the reaction condition is varied (e.g. P_{CO} or P_{O_2}), single atoms and nanoparticles will contribute differently to the overall activity when they co-exist in the same catalyst. For example, as the CO partial pressure (P_{CO}) increases, the contribution from single atoms increases and that from nanoparticles decreases, resulting in a gradual increase in the local CO reaction order. The CO reaction order was measured on samples 1-3 at the same condition as the standard samples of pure single atoms and pure nanoparticles (Figure 4). The CO reaction orders changed from negative at lower P_{CO} to positive at higher P_{CO}, which is consistent with the contribution from both single atoms and nanoparticles as discussed above. Additionally, a more positive CO order indicates a higher contribution of single atoms. Therefore, the results in Figure 4 indicate that the percentage of single atoms increases in the following order, sample 1 < sample 2 < sample 3 which is consistent with the STEM, XAS and FTIR results.

To estimate the percentage of single atoms and nanoparticles, two assumptions were made: 1) on the support surface there is no interaction between single atoms and nanoparticles during CO oxidation (i.e. no synergistic effect between single atoms and nanoparticles) and 2) the activity of supported nanoparticles is structure insensitive (no dependence on size). Structure insensitivity is a reasonable assumption as the non-uniformity and reconstruction of cluster surfaces when the surface is saturated with CO was shown to result in only a small effect of on activity for Pt nanoparticles [66-67]. Using the reaction rate (per mol Ir) of pure Ir single atoms and pure nanoparticles (samples 0 and 4, respectively), the mixture sample (single atoms and nanoparticles)

can be estimated by a linear combination. The reaction rate of the mixture sample, $r_i(Ir_{mix})_{fit}$ ($mol \cdot mol_{Ir}^{-1} \cdot s^{-1}$) at each condition can be represented by equation (2):

$$r_i(Ir_{mix})_{fit} = r_i(Ir_{SA}) \times \frac{n_{SA}}{n_{Ir}} + r_i(Ir_{NP}) \times \frac{n_{NP}}{n_{Ir}} \quad (2)$$

where $r_i(Ir_{SA})$ and $r_i(Ir_{NP})$ represent the rate of Ir single atoms per mol and rate of Ir nanoparticles per mol at condition (i), respectively ($mol \cdot mol_{Ir}^{-1} \cdot s^{-1}$) and n_{SA}, n_{NP} and n_{Ir} denote the number of moles of single atoms, moles of nanoparticles, and total number of moles in the reactor, respectively. n_{Ir} is known for each experiment based on the amount of catalyst and Ir loading. The number of moles of single atoms (n_{SA}) and nanoparticles (n_{NP}) are two unknown variables which were fit by minimizing the normalized residual sum of squared errors (RSS) as defined in equation (3) where $r_i(Ir_{mix})_{exp}$ ($mol \cdot mol_{Ir}^{-1} \cdot s^{-1}$) denotes the experimentally measured reaction rate of the mixture sample. The fraction of single atoms and nanoparticles, X_{SA} and X_{SA} can then be calculated as $n_{SA}/(n_{SA} + n_{NP})$ and $n_{NP}/(n_{SA} + n_{NP})$, respectively.

$$RSS = \sum \left(\frac{r_i(Ir_{mix})_{fit} - r_i(Ir_{mix})_{exp}}{r_i(Ir_{mix})_{exp}} \right)^2 \quad (3)$$

The fitting results (dashed lines) along with the individual contributions from single atoms and nanoparticles (blue and red lines in bottom figures, respectively) are shown in Figure 4 (see Supporting Information Figures S11 and S12 for the quantification results using the O_2 order measurements). The fits are in excellent agreement with experimental data and the estimated X_{SA} in samples 1-3 from the fits were 18 ± 5%, 32 ± 2%, and 42 ± 5% respectively (errors were obtained from uncertainty analysis of the fit). The fitted percentages of SA and NP for the 1 wt.% Ir catalysts

(samples 1 and 2) are consistent with those estimated from STEM (Table 2). In contrast, the percentage of single atoms (42 ± 5%) for sample 3 was significantly lower than estimated from STEM (61% atomic and 66% surface), DRIFTS (58 ± 9%) and EXAFS (55-73%). While multiple factors can contribute to the lower single atoms site fraction for sample 3 estimated from CO oxidation compared with other techniques, we will show that it is most likely due to inaccessibility of a significant fraction of the single atoms (i.e. in the sub-surface). An important parameter generated from the fit, the total number of Ir moles ($n_{SA} + n_{NP}$), can be used to estimate the Ir loading and compare it to the nominal loading (see Supporting Information Table S3 for $n_{SA} + n_{NP}$ normalized per gram catalyst). The estimated Ir loading from the fit for samples 1 and 2 was similar but higher than the nominal loading of 1% (1.33% and 1.39%, respectively) while it was significantly lower than the nominal loading for sample 3 (0.035% vs. 0.05%). While a deviation between the fit and the nominal loading should be expected due to experimental errors and small variations in the activity of different size Ir nanoparticles, it is noteworthy that sample 3 showed a lower value while samples 1 and 2 showed a higher value than the nominal loading. Additionally, the measured (CO/total Ir) ratio from chemisorption for sample 3 (0.96, Supporting Information Table S3) was much lower than expected and lower than that calculated based on the percentage of single atoms from STEM (1.54, see calculation details below Supporting Information Table S3). On the other hand, the measured and calculated (CO/total Ir) ratios were consistent for samples 1 (1.0 vs. 1.03) and 2 (1.4 vs. 1.24). Therefore, the results suggest that some of the Ir single atoms in sample 3 are not accessible (i.e. in the sub-surface layer or bulk of $MgAl_2O_4$) and using the measured CO/Ir and loading, we estimate that 45-55% of the single atoms are in the sub-surface layer or bulk. From a structural perspective, Ir sits in an octahedral position in pure IrO_2 (rutile[68-

[69]) and we suspect that during calcination Ir single atoms can diffuse and fill Al vacancy sites (also octahedral) in the spinel and become stable in the sub-surface of $MgAl_2O_4$. A similar dissolution in the bulk was observed for Pt single atoms on $MgAl_2O_4$[19]. It is likely that Ir single atoms diffuse in the sub-surface/bulk of $MgAl_2O_4$ during calcination and only a fraction is pulled to the surface after reduction at 500 °C (sample 3), while the higher temperature reduction of 800 °C (samples 1 and 2) results in pulling all the Ir single atoms to the surface.

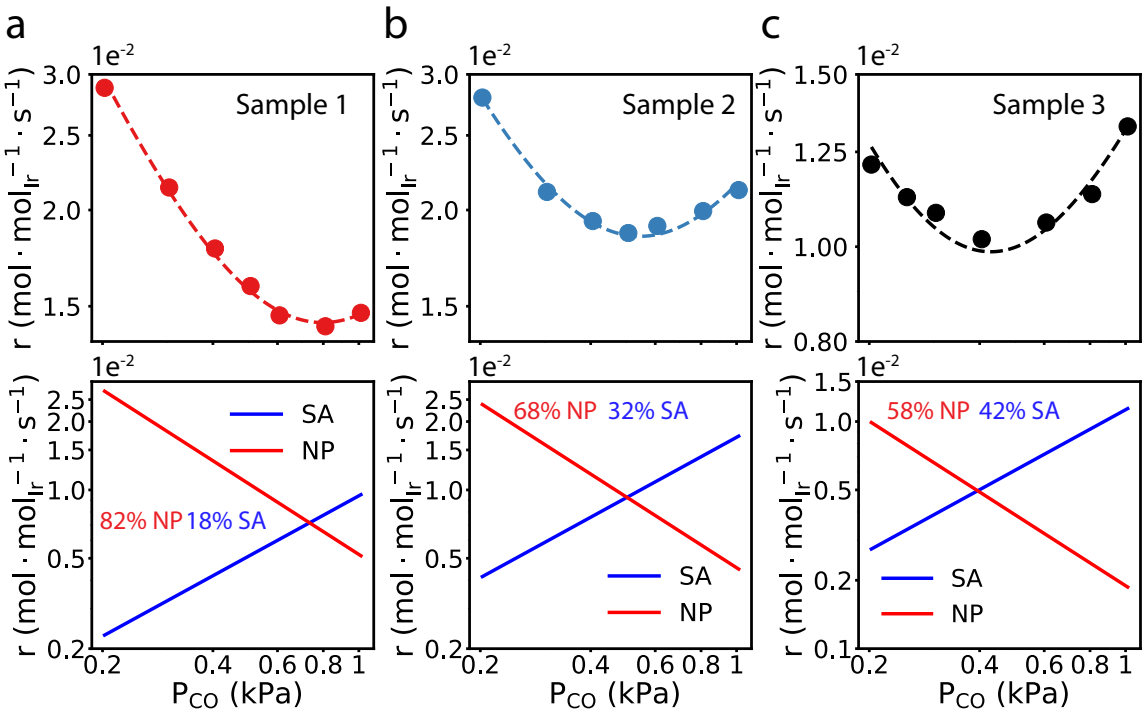

Figure 4. CO oxidation kinetic measurements (effect of CO partial pressure on reaction rate) on samples 1-3, which contain mixtures of Ir single atoms (SA) and nanoparticles (NP) and the results of fitting the reaction rate with a linear combination of single atoms and nanoparticles. All samples were measured at 155 °C with P_{CO} between 0.2-1 kPa and P_{O_2} at 10 kPa and T = 155 °C. The results were reproducible when the measurements were conducted from low to high P_{CO} or high

to low P_{CO} and the catalysts were stable during the entire experiment (<10% deactivation). Top figures are experiments (filled circles) and fits (dashed lines). Bottom figures are the individual contributions of SA and NP. (a) 1 wt.% Ir on $MgAl_2O_4$ without calcination and reduced at 800 °C in H_2 (sample 1); (b) 1 wt.% Ir on $MgAl_2O_4$ calcined at 500 °C and reduced at 800 °C (sample 2); (c) 0.05 wt.% Ir on $MgAl_2O_4$ calcined at 500 °C and reduced at 500 °C (sample 3). Reaction rates of samples 1-3 were normalized by the total moles of Ir in each sample. The percentage of SA and NP from fitting the reaction rates of samples 1-3 were (a) 18% SA + 82% NP, (b) 32% SA + 68% NP (c) 42% SA + 58% NP, respectively.

To test this hypothesis, we measured the 1 wt.% catalyst after reduction at 500 °C (sample 5, details in Methods) instead of 800 °C (sample 2) and a large discrepancy between STEM and CO oxidation results was observed. Figure 5 shows that sample 5 contains a large fraction of single atoms (65% from STEM based on total atoms), but the CO oxidation kinetics showed a constant -1 CO order indicating negligible contribution from single atoms to the catalyst activity. Consistent with the CO oxidation on sample 5, the CO chemisorption results also showed (CO/total Ir) was only 0.2 (Supporting Information Table S3) and the DRIFTS of adsorbed CO showed no identifiable dicarbonyl bands (Figure 5b), indicating that most of the single atoms are in the sub-surface. To estimate if a small fraction of Ir single atoms is on the surface, we measured the CO order at a lower O_2 partial pressure (2 kPa) where single atoms have a higher contribution to the activity ($r(Ir_{SA}) \propto P_{CO}$ while $r(Ir_{NP}) \propto \frac{P_{O_2}}{P_{CO}}$). A surface site fraction of 5% single atoms and 95% NPs was estimated at this condition. While these results confirm that most of the single atoms in sample 5 are in the sub-surface, they also indicate that a small fraction (<10%) of single atoms can

be detected with kinetic measurements by tailoring the reaction conditions to maximize their contribution.

The results show that using STEM or EXAFS to estimate /quantify the fraction of single atoms could be misleading since the surface and sub-surface single atoms cannot be readily differentiated. Kinetic measurements, and in this case reaction order of CO, can be a better and more sensitive surface method to quantify the number of surface metal single atoms and their fraction of the total surface sites. We note that due to the difference in both CO and O_2 reaction orders on SA and NP ($r(Ir_{SA}) \propto P_{CO}$ while $(Ir_{NP}) \propto \frac{P_{O_2}}{P_{CO}}$), one can choose conditions to have the kinetics either be dominated by one of the sites or have both contribute with similar extents. This can be used to extract the orders for each type of site separately or to estimate their site fraction even when their fraction is small. For example, by increasing the CO partial pressure while decreasing that of O_2, the contribution of single atoms to the catalyst activity will increase and can be dominant. Therefore, measuring the CO order at low (high) P_{O_2} and a high (low) range of P_{CO} would allow maximizing the contribution of single atoms (nanoparticles) in a sample containing a mixture of single atoms and nanoparticle (a similar argument can be made for O_2 order measurements). This effect is illustrated in the estimation of a small fraction of single atom sites for sample 5 by maximizing the contribution of the single atoms using low P_{O_2} (see Figure 5). Similarly, the reaction conditions can be chosen to extract the intrinsic kinetics on single atoms or nanoparticles when a catalyst containing exclusively one of them is not available. To illustrate this effect, we attempted to maximize the contribution of nanoparticles in a sample containing a significant fraction of single atoms (32% ± 2%, sample 2). We measured the reaction rate at P_{O_2}= 50 kPa (5

times higher than P_{O_2} in Figure 4) to maximize the activity of the nanoparticles and the results show a CO reaction order of -1 (Supporting Information Fig S13), indicating the activity is dominated by nanoparticles as we expected. The results show that the correct reaction orders can be measured for one type of sites by tailoring the reaction conditions. We note that the effect of temperature on kinetics could also be used to differentiate single atoms and nanoparticle if there is a large difference in apparent activation energy on each site.

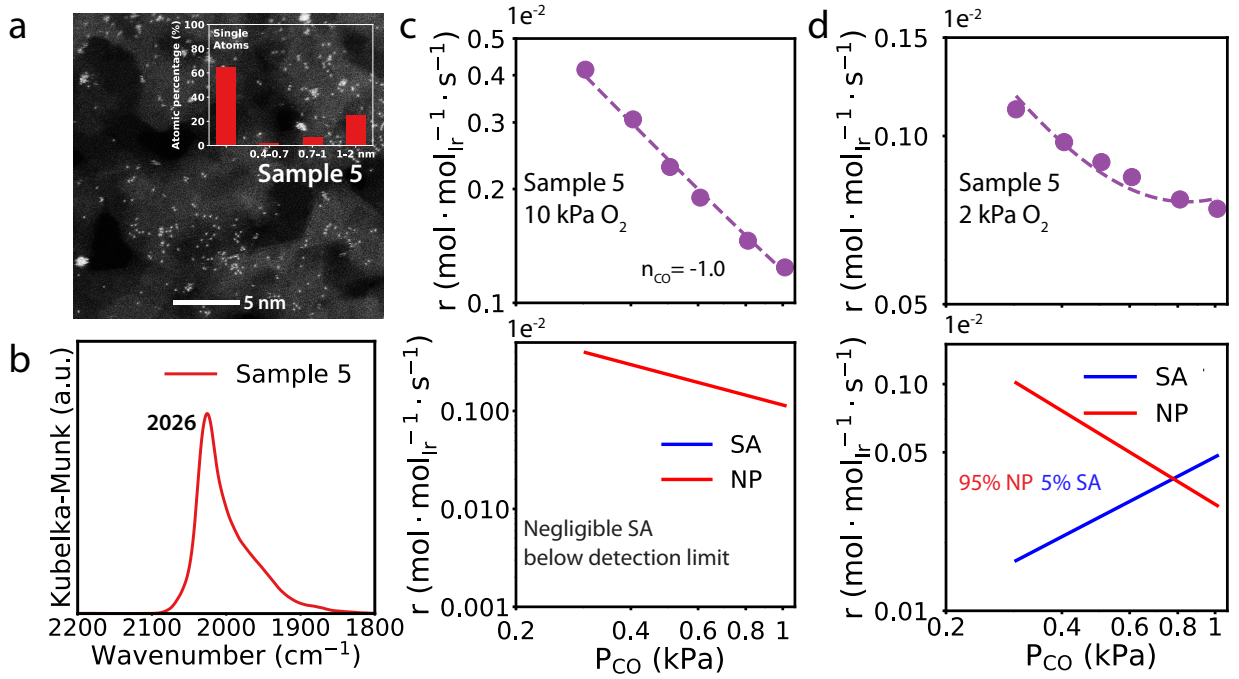

Figure 5. Representative HAADF-STEM image and size distribution (a), DRIFTS after CO adsorption (b), and the CO reaction order and fitting of the SA and NP site fractions (c-d) of sample 5, 1 wt.% Ir supported on $MgAl_2O_4$, calcined at 500 °C in air, and reduced at 500 °C in H_2. (a) The size distribution obtained from the STEM images showed that single atoms represent about 65% (total atoms basis) of the Ir in the sample, while the DRIFTS results (b) showed a negligible

contribution from single atoms as evidenced by the absence of CO bands corresponding to $Ir(CO)_2$. (c, d) CO oxidation measurements showing the effect of CO partial pressure on reaction rate on sample 5 (top figures) at P_{O_2} = 10 kPa (c) and 2 kPa (d) and T = 155 °C. Top figures in panels c-d are experiments (filled circles) and fits (dashed lines). Bottom figures are the individual contributions of SA and NP. Reaction order of CO was -1 at P_{O_2}= 10 kPa, panel (c), indicating a negligible contribution of single atoms at these conditions while the local CO order showed an increase with P_{CO} at P_{O_2} = 2 kPa, panel (d) and the fit show that 5% of the surface site are single atoms. The results indicate that less than 10% of the Ir single atoms detected by STEM are on the surface.

In this work, different *in-situ* and *ex-situ* techniques were used to quantify the fraction of single atoms and nanoparticles of multiple samples. Similar percentage of single atoms were obtained using STEM, XAS, FTIR and CO oxidation kinetic measurement (Table 2) except for samples having a significant fraction of single atoms in the sub-surface layer of the support. For such samples, FTIR and CO oxidation measurements, being surface techniques, were shown to be more accurate. Additionally, FTIR and CO oxidation measurements have the advantage of being low-cost and not requiring sophisticated facilities. However, FTIR spectroscopy is not sensitive to a small site fraction of single atoms or nanoparticles. We show that of all the techniques, CO oxidation is the most sensitive and versatile surface characterization tool for quantifying the single atom and nanoparticle site fractions. Specifically, by tailoring the reaction conditions, even a small site fraction (single atom or nanoparticle) can be measured and the results have the advantage of being performed under reaction conditions. The methodology of using kinetics as a characterization tool, while we developed it for Ir single atoms and nanoparticles, can also be

generalized to other metals or two types of sites, provided they have different reaction orders. Lastly, the methodology can also be used to extract the intrinsic kinetics of one of the sites using a sample containing a mixture.

3.5. Conclusions

We have combined the strengths of multiple techniques (STEM, XAS and FTIR) to characterize and compare the site fractions of iridium in catalyst samples containing a mixture of single atoms and nanoparticles. Because of the unique reaction mechanism of CO oxidation on supported Ir single atoms, we identified kinetic measurements as a unique, facile and effective method to quantify the site distribution of iridium as single atoms and nanoparticles under reaction conditions. STEM and XAS can provide structural information of the catalysts however, differentiation between single atoms on the surface and in the sub-surface is challenging especially for a mixture of single atoms and nanoparticles. Infrared spectroscopy, on the other hand, is surface-sensitive and can differentiate and estimate the site fractions of nanoparticles and single atoms based on the gem dicarbonyl and linearly bound CO bands. However, quantification becomes challenging when the peaks are overlapping, or the site fraction is small. We show that the site fractions estimated from kinetic measurements on different catalysts are consistent with STEM, XAS, and FTIR. More importantly, CO oxidation measurements directly measure the number of sites, allowing the determination of the catalyst dispersion and whether single atoms are on the surface or in the sub-surface. Additionally, the sensitivity of the kinetic measurements can be tailored by the reaction conditions to increase the contribution of single atoms or nanoparticles, making it very sensitive to small fraction of either site or to measure the intrinsic kinetics in a sample containing a mixture.

This methodology is not limited to iridium and can potentially be used as a facile and sensitive tool for other reactions/metal catalysts to differentiate between two types of sites, provided they have different reaction orders.

3.6. Acknowledgment

This research was primarily sponsored by the Army Research Office and was accomplished under Grant Number W911NF-16-1-0400. The views and conclusions contained in this document are those of the authors and should not be interpreted as representing the official policies, either expressed or implied, of the Army Research Office or the U.S. Government. The U.S. Government is authorized to reproduce and distribute reprints for Government purposes notwithstanding any copyright notation herein. Use of the Stanford Synchrotron Radiation Light Source (SSRL, beamlines 2-2 and 9-3, user proposal 4645), SLAC National Accelerator Laboratory is supported by the U.S. Department of Energy, office of Basic Energy Sciences under Contract No. DE-AC02-76SF00515 and by Synchrotron Catalysis Consortium, US Department of Energy Grant No. DE-SC0012335. Additional support by the Consortium for Operando and Advanced Catalyst Characterization via Electronic Spectroscopy and Structure (Co-ACCESS) at SLAC is acknowledged. Co-ACCESS, is supported by the U.S. Department of Energy, Office of Science, Office of Basic Energy Sciences, Chemical Sciences, Geosciences and Biosciences under Contract DE-AC02-76SF00515. STEM imaging was performed at the William R. Wiley Environmental Molecular Science Laboratory (EMSL) sponsored by the U.S. Department of Energy, office of Biological and Environmental Research located at Pacific Northwest National Laboratory (PNNL)

under science theme proposal 49326. We thank Athena Tilley at Virginia Tech Soil Testing Laboratory for conducting the ICP-ASE analysis.

References

1. Flytzani-Stephanopoulos, M.; Gates, B. C., Atomically dispersed supported metal catalysts. *Annual review of chemical and biomolecular engineering* **2012,** *3*, 545-74.

2. Zhang, C.; Liu, F.; Zhai, Y.; Ariga, H.; Yi, N.; Liu, Y.; Asakura, K.; Flytzani-Stephanopoulos, M.; He, H., Alkali-metal-promoted Pt/TiO_2 opens a more efficient pathway to formaldehyde oxidation at ambient temperatures. *Angew Chem Int Ed Engl* **2012,** *51* (38), 9628-32.

3. Nie, L.; Mei, D. H.; Xiong, H. F.; Peng, B.; Ken, Z. B.; Hernandez, X. I. P.; DeLariva, A.; Wang, M.; Engelhard, M. H.; Kovarik, L.; Datye, A. K.; Wang, Y., Activation of surface lattice oxygen in single-atom Pt/CeO_2 for low-temperature CO oxidation. *Science* **2017,** *358* (6369), 1419-+.

4. Yang, X. F.; Wang, A. Q.; Qiao, B. T.; Li, J.; Liu, J. Y.; Zhang, T., Single-atom catalysts: a new frontier in heterogeneous catalysis. *Accounts of Chemical Research* **2013,** *46* (8), 1740-1748.

5. Qiao, B. T.; Wang, A. Q.; Yang, X. F.; Allard, L. F.; Jiang, Z.; Cui, Y. T.; Liu, J. Y.; Li, J.; Zhang, T., Single-atom catalysis of CO oxidation using Pt_1/FeO_x. *Nature Chemistry* **2011,** *3* (8), 634-641.

6. Shan, J.; Li, M.; Allard, L. F.; Lee, S.; Flytzani-Stephanopoulos, M., Mild oxidation of methane to methanol or acetic acid on supported isolated rhodium catalysts. *Nature* **2017,** *551* (7682), 605-608.

7. Lin, J.; Wang, A. Q.; Qiao, B. T.; Liu, X. Y.; Yang, X. F.; Wang, X. D.; Liang, J. X.; Li, J. X.; Liu, J. Y.; Zhang, T., Remarkable Performance of Ir-1/FeOx Single-atom catalyst in water gas shift reaction. *Journal of the American Chemical Society* **2013,** *135* (41), 15314-15317.

8. Jones, J.; Xiong, H. F.; Delariva, A. T.; Peterson, E. J.; Pham, H.; Challa, S. R.; Qi, G. S.; Oh, S.; Wiebenga, M. H.; Hernandez, X. I. P.; Wang, Y.; Datye, A. K., Thermally stable single-atom platinum-on-ceria catalysts via atom trapping. *Science* **2016,** *353* (6295), 150-154.

9. Li, H. L.; Wang, L. B.; Dai, Y. Z.; Pu, Z. T.; Lao, Z. H.; Chen, Y. W.; Wang, M. L.; Zheng, X. S.; Zhu, J. F.; Zhang, W. H.; Si, R.; Ma, C.; Zeng, J., Synergetic interaction between neighbouring platinum monomers in CO_2 hydrogenation. *Nature Nanotechnology* **2018,** *13* (5), 411-+.

10. Choi, C. H.; Kim, M.; Kwon, H. C.; Cho, S. J.; Yun, S.; Kim, H. T.; Mayrhofer, K. J.; Kim, H.; Choi, M., Tuning selectivity of electrochemical reactions by atomically dispersed platinum catalyst. *Nature communications* **2016,** *7*, 10922.

11. Huang, D.; de Vera, G. A.; Chu, C.; Zhu, Q.; Stavitski, E.; Mao, J.; Xin, H.; Spies, J. A.; Schmuttenmaer, C. A.; Niu, J.; Haller, G. L.; Kim, J.-H., Single-atom Pt catalyst for effective C–F bond activation via hydrodefluorination. *ACS Catalysis* **2018,** *8* (10), 9353-9358.

12. Liu, P. X.; Zhao, Y.; Qin, R. X.; Mo, S. G.; Chen, G. X.; Gu, L.; Chevrier, D. M.; Zhang, P.; Guo, Q.; Zang, D. D.; Wu, B. H.; Fu, G.; Zheng, N. F., Photochemical route for synthesizing atomically dispersed palladium catalysts. *Science* **2016,** *352* (6287), 797-801.

13. Zhang, Z.; Zhu, Y.; Asakura, H.; Zhang, B.; Zhang, J.; Zhou, M.; Han, Y.; Tanaka, T.; Wang, A.; Zhang, T.; Yan, N., Thermally stable single atom Pt/m-Al_2O_3 for selective hydrogenation and CO oxidation. *Nature communications* **2017,** *8*, 16100.

14. Zhao, A.; Gates, B. C., Hexairidium Clusters Supported on γ-Al_2O_3: Synthesis, Structure, and Catalytic Activity for Toluene Hydrogenation. *Journal of the American Chemical Society* **1996,** *118* (10), 2458-2469.

15. Kawi, S.; Chang, J. R.; Gates, B. C., Tetrairidium clusters supported on gamma-alumina: formation from [$Ir_4(CO)_{12}$] and carbon monoxide-induced morphology changes. *The Journal of Physical Chemistry* **1993,** *97* (20), 5375-5383.

16. Moses-DeBusk, M.; Yoon, M.; Allard, L. F.; Mullins, D. R.; Wu, Z.; Yang, X.; Veith, G.; Stocks, G. M.; Narula, C. K., CO Oxidation on supported single pt atoms: experimental and ab initio density functional studies of CO interaction with Pt Atom on θ-Al_2O_3(010) Surface. *J. Am. Chem. Soc.* **2013,** *135* (34), 12634-12645.

17. Sasahara, A.; Pang, C. L.; Onishi, H., Probe microscope observation of platinum atoms deposited on the TiO_2(110)-(1x1) surface. *Journal of Physical Chemistry B* **2006,** *110* (27), 13453-13457.

18. Moses-DeBusk, M.; Allard, L. F.; Blom, D. A.; Narula, C. K., Oxidation-induced structural changes in sub-nanometer platinum supported on alumina. *ChemCatChem* **2015,** *7* (15), 2391-2396.

19. Luo, J.; Gao, F.; Karim, A. M.; Xu, P.; Browning, N. D.; Peden, C. H. F., Advantages of $MgAlO_x$ over γ-Al_2O_3 as a support material for potassium-based high-temperature lean NO_x traps. *ACS Catalysis* **2015,** *5* (8), 4680-4689.

20. Krivanek, O. L.; Chisholm, M. F.; Nicolosi, V.; Pennycook, T. J.; Corbin, G. J.; Dellby, N.; Murfitt, M. F.; Own, C. S.; Szilagyi, Z. S.; Oxley, M. P.; Pantelides, S. T.; Pennycook, S. J., Atom-by-atom structural and chemical analysis by annular dark-field electron microscopy. *Nature* **2010,** *464* (7288), 571-574.

21. Zhu, Y.; Inada, H.; Nakamura, K.; Wall, J., Imaging single atoms using secondary electrons with an aberration-corrected electron microscope. *Nature materials* **2009,** *8* (10), 808-812.

22. Chang, T. Y.; Tanaka, Y.; Ishikawa, R.; Toyoura, K.; Matsunaga, K.; Ikuhara, Y.; Shibata, N., Direct imaging of Pt single atoms adsorbed on TiO_2 (110) surfaces. *Nano Letters* **2014,** *14* (1), 134-138.

23. Han, C. W.; Iddir, H.; Uzun, A.; Curtiss, L. A.; Browning, N. D.; Gates, B. C.; Ortalan, V., Migration of single iridium atoms and tri-iridium clusters on MgO surfaces: Aberration-corrected STEM imaging and ab initio calculations. *J Phys Chem Lett* **2015,** *6* (23), 4675-4679.

24. Qiao, B. T.; Liu, J. X.; Wang, Y. G.; Lin, Q. Q.; Liu, X. Y.; Wang, A. Q.; Li, J.; Zhang, T.; Liu, J. Y., Highly efficient catalysis of preferential oxidation of CO in H_2-rich stream by gold single-atom catalysts. *ACS Catalysis* **2015,** *5* (11), 6249-6254.

25. Allen, J. E.; Hemesath, E. R.; Perea, D. E.; Lensch-Falk, J. L.; Li, Z. Y.; Yin, F.; Gass, M. H.; Wang, P.; Bleloch, A. L.; Palmer, R. E.; Lauhon, L. J., High-resolution detection of Au catalyst atoms in Si nanowires. *Nature Nanotechnology* **2008,** *3* (3), 168-173.

26. Yin, P. Q.; Yao, T.; Wu, Y.; Zheng, L. R.; Lin, Y.; Liu, W.; Ju, H. X.; Zhu, J. F.; Hong, X.; Deng, Z. X.; Zhou, G.; Wei, S. Q.; Li, Y. D., Single cobalt atoms with precise n-coordination as superior oxygen reduction reaction catalysts. *Angewandte Chemie-International Edition* **2016,** *55* (36), 10800-10805.

27. Yang, M.; Li, S.; Wang, Y.; Herron, J. A.; Xu, Y.; Allard, L. F.; Lee, S.; Huang, J.; Mavrikakis, M.; Flytzani-Stephanopoulos, M., Catalytically active Au-O(OH)(x)-species stabilized by alkali ions on zeolites and mesoporous oxides. *Science* **2014,** *346* (6216), 1498-1501.

28. Matsubu, J. C.; Yang, V. N.; Christopher, P., Isolated metal active site concentration and stability controls catalytic CO_2 reduction selectivity. *J Am Chem Soc* **2015**.

29. DeRita, L.; Dai, S.; Lopez-Zepeda, K.; Pham, N.; Graham, G. W.; Pan, X. Q.; Christopher, P., Catalyst architecture for stable single atom dispersion enables site-specific spectroscopic and reactivity measurements of CO adsorbed to Pt Atoms, oxidized Pt clusters, and metallic Pt Clusters on TiO_2. *Journal of the American Chemical Society* **2017,** *139* (40), 14150-14165.

30. Ding, K.; Gulec, A.; Johnson, A. M.; Schweitzer, N. M.; Stucky, G. D.; Marks, L. D.; Stair, P. C., Identification of active sites in CO oxidation and water-gas shift over supported Pt catalysts. *Science* **2015,** *350* (6257), 189-192.

31. Wang, C.; Gu, X.-K.; Yan, H.; Lin, Y.; Li, J.; Liu, D.; Li, W.-X.; Lu, J., Water-mediated Mars–Van Krevelen mechanism for CO oxidation on ceria-supported single-atom Pt_1 catalyst. *ACS Catalysis* **2017,** *7* (1), 887-891.

32. Piernavieja-Hermida, M.; Lu, Z.; White, A.; Low, K. B.; Wu, T. P.; Elam, J. W.; Wu, Z. L.; Lei, Y., Towards ALD thin film stabilized single-atom Pd-1 catalysts. *Nanoscale* **2016,** *8* (33), 15348-15356.

33. Lu, J.; Serna, P.; Gates, B. C., Zeolite- and MgO-supported molecular iridium complexes: support and ligand effects in catalysis of ethene hydrogenation and H-D exchange in the conversion of H_2+D_2. *ACS Catalysis* **2011,** *1* (11), 1549-1561.

34. Kistler, J. D.; Chotigkrai, N.; Xu, P.; Enderle, B.; Praserthdam, P.; Chen, C. Y.; Browning, N. D.; Gates, B. C., A single-site platinum CO oxidation catalyst in zeolite KLTL: microscopic and spectroscopic determination of the locations of the platinum atoms. *Angew Chem Int Ed Engl* **2014,** *53* (34), 8904-7.

35. Kistler, J. D.; Chotigkrai, N.; Xu, P. H.; Enderle, B.; Praserthdam, P.; Chen, C. Y.; Browning, N. D.; Gates, B. C., A Single-site platinum CO oxidation catalyst in zeolite KLTL: Microscopic and spectroscopic determination of the locations of the platinum atoms. *Angewandte Chemie-International Edition* **2014,** *53* (34), 8904-8907.

36. Zhang, H. B.; Liu, G. G.; Shi, L.; Ye, J. H., Single-Atom Catalysts: Emerging multifunctional materials in heterogeneous catalysis. *Adv Energy Mater* **2018,** *8* (1).

37. Wang, W. L.; Santos, E. J. G.; Jiang, B.; Cubuk, E. D.; Ophus, C.; Centeno, A.; Pesquera, A.; Zurutuza, A.; Ciston, J.; Westervelt, R.; Kaxiras, E., Direct observation of a long-lived single-atom catalyst chiseling atomic structures in graphene. *Nano Letters* **2014,** *14* (2), 450-455.

38. Tang, Y.; Li, Y. T.; Fung, V.; Jiang, D. E.; Huang, W. X.; Zhang, S. R.; Iwasawa, Y.; Sakata, T.; Nguyen, L.; Zhang, X. Y.; Frenkel, A. I.; Tao, F., Single rhodium atoms

anchored in micropores for efficient transformation of methane under mild conditions. *Nature communications* **2018,** *9*.

39. Lin, J.; Qiao, B.; Liu, J.; Huang, Y.; Wang, A.; Li, L.; Zhang, W.; Allard, L. F.; Wang, X.; Zhang, T., Design of a highly active Ir/Fe(OH)x catalyst: versatile application of Pt-group metals for the preferential oxidation of carbon monoxide. *Angew Chem Int Ed Engl* **2012,** *51* (12), 2920-4.

40. Ammal, S. C.; Heyden, A., Water-gas shift activity of atomically dispersed cationic platinum versus metallic platinum clusters on titania supports. *ACS Catalysis* **2017,** *7* (1), 301-309.

41. Peterson, E. J.; DeLaRiva, A. T.; Lin, S.; Johnson, R. S.; Guo, H.; Miller, J. T.; Hun Kwak, J.; Peden, C. H.; Kiefer, B.; Allard, L. F.; Ribeiro, F. H.; Datye, A. K., Low-temperature carbon monoxide oxidation catalysed by regenerable atomically dispersed palladium on alumina. *Nature communications* **2014,** *5*, 4885.

42. Lu, Y.; Wang, J.; Yu, L.; Kovarik, L.; Zhang, X.; Hoffman, A. S.; Gallo, A.; Bare, S. R.; Sokaras, D.; Kroll, T.; Dagle, V.; Xin, H.; Karim, A. M., Identification of the active complex for CO oxidation over single-atom Ir-on-$MgAl_2O_4$ catalysts. *Nature Catalysis* **2019,** *2* (2), 149-156.

43. Collins, T. J., ImageJ for microscopy. *Biotechniques* **2007,** *43* (1), 25-+.

44. Van Hardeveld, R.; Hartog, F., The statistics of surface atoms and surface sites on metal crystals. *Surface Science* **1969,** *15* (2), 189-230.

45. Mozaffari, S.; Li, W. H.; Thompson, C.; Ivanov, S.; Seifert, S.; Lee, B.; Kovarik, L.; Karim, A. M., Colloidal nanoparticle size control: experimental and kinetic modeling investigation of the ligand metal binding role in controlling the nucleation and growth kinetics. *Nanoscale* **2017,** *9* (36), 13772-13785.

46. An, K.; Somorjai, G. A., Size and shape control of metal nanoparticles for reaction selectivity in catalysis. *Chemcatchem* **2012,** *4* (10), 1512-1524.

47. Karim, A. M.; Howard, C.; Roberts, B.; Kovarik, L.; Zhang, L.; King, D. L.; Wang, Y., In Situ x-ray absorption fine structure studies on the effect of ph on pt electronic density during aqueous phase reforming of glycerol. *ACS Catalysis* **2012,** *2* (11), 2387-2394.

48. Ravel, B.; Newville, M., ATHENA, ARTEMIS, HEPHAESTUS: data analysis for X-ray absorption spectroscopy using IFEFFIT. *J Synchrotron Radiat* **2005,** *12*, 537-541.

49. Newville, M., IFEFFIT: interactive XAFS analysis and FEFF fitting. *J Synchrotron Radiat* **2001,** *8*, 322-324.

50. Zabinsky, S. I.; Rehr, J. J.; Ankudinov, A.; Albers, R. C.; Eller, M. J., Multiple-scattering calculations of x-ray-absorption spectra. *Physical Review B* **1995,** *52* (4), 2995-3009.

51. Bonet, F.; Grugeon, S.; Dupont, L.; Urbina, R. H.; Boudart, M.; Djega-Mariadassou, G., *Kinetics of heterogeneous catlytic reactions*. Princeton University Press / Princeton, N.J.: 1984.

52. Koros, R. M.; Nowak, E. J., A diagnostic test of the kinetic regime in a packed bed reactor. *Chem. Eng. Sci.* **1967,** *22* (3), 470.

53. Madon, R. J.; Boudart, M., Experimental criterion for the absence of artifacts in the measurement of rates of heterogeneous catalytic reactions. *Ind Eng Chem Fund* **1982,** *21* (4), 438-447.

54. Li, W.-Z.; Kovarik, L.; Mei, D.; Engelhard, M. H.; Gao, F.; Liu, J.; Wang, Y.; Peden, C. H. F., A General mechanism for stabilizing the small sizes of precious metal nanoparticles on oxide supports. *Chem. Mater.* **2014,** *26* (19), 5475-5481.

55. Li, W.-Z.; Kovarik, L.; Mei, D.; Liu, J.; Wang, Y.; Peden, C. H. F., Stable platinum nanoparticles on specific $MgAl_2O_4$ spinel facets at high temperatures in oxidizing atmospheres. *Nature Communications* **2013,** *4*.

56. Cai, Q. X.; Wang, J. G.; Wang, Y.; Mei, D. H., First-principles thermodynamics study of spinel $MgAl_2O_4$ surface stability. *Journal of Physical Chemistry C* **2016,** *120* (34), 19087-19096.

57. Lu, J.; Aydin, C.; Browning, N. D.; Gates, B. C., Oxide- and Zeolite-supported isostructural $Ir(C_2H_4)_2$ complexes: molecular-level observations of electronic effects of supports as ligands. *Langmuir* **2012,** *28* (35), 12806-12815.

58. Lu, J.; Serna, P.; Aydin, C.; Browning, N. D.; Gates, B. C., Supported molecular iridium catalysts: resolving effects of metal nuclearity and supports as ligands. *Journal of the American Chemical Society* **2011,** *133* (40), 16186-16195.

59. Frank, M.; Baumer, M.; Kuhnemuth, R.; Freund, H. J., Metal atoms and particles on oxide supports: Probing structure and charge by infrared spectroscopy. *Journal of Physical Chemistry B* **2001,** *105* (36), 8569-8576.

60. Toolenaar, F. J. C. M.; Bastein, A. G. T. M.; Ponec, V., The effect of particle-size in the adsorption of carbon-monoxide on iridium - an infrared investigation. *Journal of Catalysis* **1983,** *82* (1), 35-44.

61. Duncan, T. M.; Yates, J. T.; Vaughan, R. W., A ^{13}C NMR study of the adsorbed states of CO on Rh dispersed on Al_2O_3. *The Journal of Chemical Physics* **1980,** *73* (2), 975-985.

62. Murthy, R. S. S.; Leyden, D. E., Quantitative-determination of (3-aminopropyl) triethoxysilane on silica-gel surface using diffuse reflectance infrared fourier-transform spectrometry. *Anal Chem* **1986,** *58* (6), 1228-1233.

63. Kubelka, P., New contributions to the optics of intensely light-scattering materials. Part I. *J. Opt. Soc. Am.* **1948,** *38* (5), 448-457.

64. Fuller, M. P.; Griffiths, P. R., Diffuse reflectance measurements by infrared fourier-transform spectrometry. *Anal Chem* **1978,** *50* (13), 1906-1910.

65. Kappers, M. J.; Miller, J. T.; Koningsberger, D. C., Deconvolution and curve fitting of IR spectra for CO adsorbed on Pt/K-LTL: Potassium promoter effect and adsorption site distribution. *Journal of Physical Chemistry* **1996,** *100* (8), 3227-3236.

66. Vera, E.; Alcantar-Vazquez, B.; Pfeiffer, H., CO_2 chemisorption and evidence of the CO oxidation-chemisorption mechanisms on sodium cobaltate. *Chem. Eng. J.* **2015,** *271*, 106-113.

67. Kale, M. J.; Christopher, P., Utilizing quantitative in situ ftir spectroscopy to identify well-coordinated Pt atoms as the active site for CO oxidation on Al_2O_3-supported Pt catalysts. *ACS Catalysis* **2016,** *6* (8), 5599-5609.

68. Ping, Y.; Galli, G.; Goddard, W. A., Electronic structure of IrO_2: The role of the metal d orbitals. *J. Phys. Chem. C* **2015,** *119* (21), 11570-11577.

69. Ono, S.; Brodholt, J. P.; Price, G. D., Structural phase transitions in IrO_2 at high pressures. *J. Phys.: Condens. Matter* **2008,** *20* (4), 045202.

Appendix B

Table S1 Synthesis and pretreatment details of $Ir/MgAl_2O_4$ samples 0-5

Sample	Weight loading	Preparation method [a]	Precursor	Calcination temperature [b]	Reduction temperature [c]
0	0.2 %	Wet impregnation	$Ir(CO)_2(acac)$	Dried at room temperature	500 °C
1	1%	IWI	$Ir(NO_3)_2$	110 °C	800 °C
2	1%	IWI	$Ir(NO_3)_2$	500 °C	800 °C
3	0.05%	Wet impregnation	$Ir(NO_3)_2$	500 °C	500 °C
4	0.0025%	Wet impregnation	$Ir(NO_3)_2$	500 °C	500 °C
5	1%	IWI	$Ir(NO_3)_2$	500 °C	500 °C

a. IWI: incipient wetness impregnation.

b. Calcined in air for 4 h.

c. Reduced in 20 kPa H_2 (balance He, 100 sccm total flow rate) for 2 h.

Table S2 Size distribution (atomic percentage) of the $Ir/MgAl_2O_4$ catalysts obtained from multiple STEM images. See below for details on the calculations of surface and total atomic percentages.

Catalyst	Single atoms	0.5-0.7 nm	0.7-1.0 nm	1-1.5 nm	1.5-2 nm
Sample 0 (total atoms)	2%	0%	22%	62%	14%
Sample 1 (total atoms)	16 %	0%	7%	45%	32%
Sample 2 (total atoms)	35 %	3%	18%	37%	8%
Sample 3 (total atoms)	61 %	1%	14%	24%	0%
Sample 5 (total atoms)	65%	2%	7%	25%	1%
Sample 0 (surface atoms)	3%	0%	26%	61%	10%
Sample 1 (surface atoms)	19 %	0%	8%	47%	25%
Sample 2 (surface atoms)	39 %	3%	18%	33%	6%
Sample 3 (surface atoms)	66 %	1%	14%	19%	0%
Sample 5 (surface atoms)	71%	2%	7%	20%	1%

To estimate the number of atoms per particle we setup a model for hemispherical nanoparticle shape, which is the most abundant particle shape observed by STEM (see Figure S1, Supporting Information). We modified a cuboctahedron model[1] to represent a hemispherical particle. For a cuboctahedron particle, the number of total atoms N_T, the number of atoms lying on an equivalent edge is defined as m (corner atom included). N_T can be represented by m with the equation [1]: $N_T = 16m^3 - 33\ m^2 + 24m - 2$. The number of atoms on the central cross-section of the cuboctahedron (N_C) can be calculated as: $N_C=(3m - 2) \times (m - 1) + (2m - 1) \times m$. For a semi-cuboctahedron particle on a support (with the same radius as the cuboctahedron), the number of

atoms (N_{hemi}) can then be calculated as $N_{hemi}=\frac{N_T + N_C}{2}$. With the above equations, we can first calculate the number of atoms in a spherical particle as[2], $N_T=\frac{\pi D^3 \rho N_A}{6M_w}$, with a diameter *D* measured by STEM, then calculate N_{hemi} in each particle and the total number of atoms in all nanoparticles (N_{hemi_total}). The total atomic fraction of single atoms (i.e. bulk, volume fraction) was calculated using the number of single atoms (SA) measured by STEM (N_{SA}) and the total atoms in all the nanoparticles (N_{hemi_total}) as $N_{SA}/(N_{SA} + N_{hemi\_total})$. The total number of surface atoms in nanoparticles (N_{s_total}) was calculated from the total atoms in each particle using the dispersion for completely shelled polyhedron[3] for particles ≥ 0.7 nm, while smaller ones were assumed to have 100% dispersion. The surface fraction of single atoms can then be calculated as $N_{SA}/(N_{SA} + N_{s\_total})$.

Table S3 Volumetric CO chemisorption results of $Ir/MgAl_2O_4$ catalysts after pretreatment

Sample	Qty. adsorbed mmol/g	mol CO/total mol Ir [a]	mol CO/total mol Ir estimated from STEM [b]	Ir weight loading from synthesis and ICP measurement [c]	Ir weight loading from kinetic measurement [d]
Sample 0	0.0094	0.90	0.95	-	-
Sample 1	0.053	1.00	1.03	1%	1.33 %
Sample 2	0.073	1.40	1.24	1%	1.39 %
Sample 3	0.0025	0.96	1.54	0.05%	0.034%
Sample 5	0.010	0.20	1.67	1%	0.24%

[a] based on the Ir weight percent of each sample

[b] The (CO/total Ir) ratios were calculated using the number of surface sites for SA and NP from STEM (assuming all Ir is accessible) and 2CO per SA and 1CO per surface site on NP. For example, as an illustration if we have 50% SA and 50% NP of 0.8 nm in diameter, the (CO/total Ir) would be ($2 \times 0.5 + 1 \times 0.92 \times 0.5 = 1.46$) where 0.92 represent the fraction of surface sites in the 0.8 nm nanoparticles that can adsorb CO.

[c] Ir weight loading calculated based on the weight percentage of Ir added during incipient wetness impregnation experiment for sample 1,2 and 5. For sample 3 Ir weight loading was also confirmed by ICP-AES measurement of the filtered solution after wet impregnation.

[d] Ir weight loading calculated based on the total weight of Ir single atoms and Ir nanoparticles estimated from the fit of the kinetic measurements, i.e. $((n_{SA} + n_{NP}) \times MW_{Ir})/(\text{gram catalyst in the reactor})$.

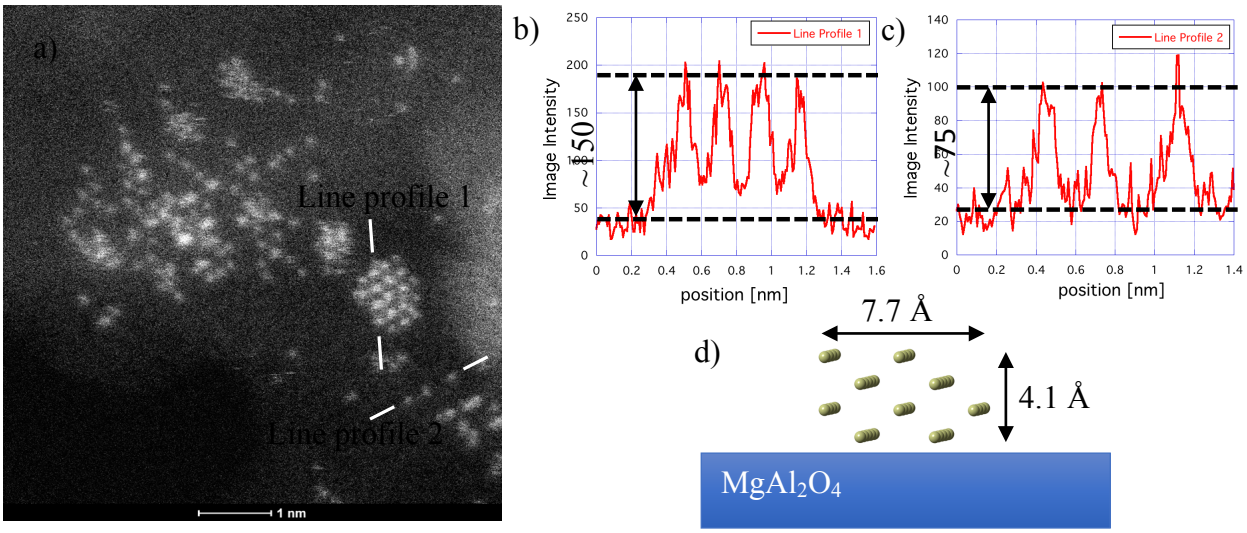

Fig. S1 STEM image and analysis showing an example of a hemispherical nanoparticle on the $MgAl_2O_4$ support (sample 2). The intensity measurements (line profiles in **(b)** and **(c)**) show that the nanoparticle is 2 atoms thick (2 rows of atoms directly above each other) and the nanoparticle is oriented in the [110] direction. The schematic of the nanoparticle in **(d)** (side view) shows that the nanoparticle thickness is ~half the diameter which suggests that the nanoparticle shape is hemispherical.

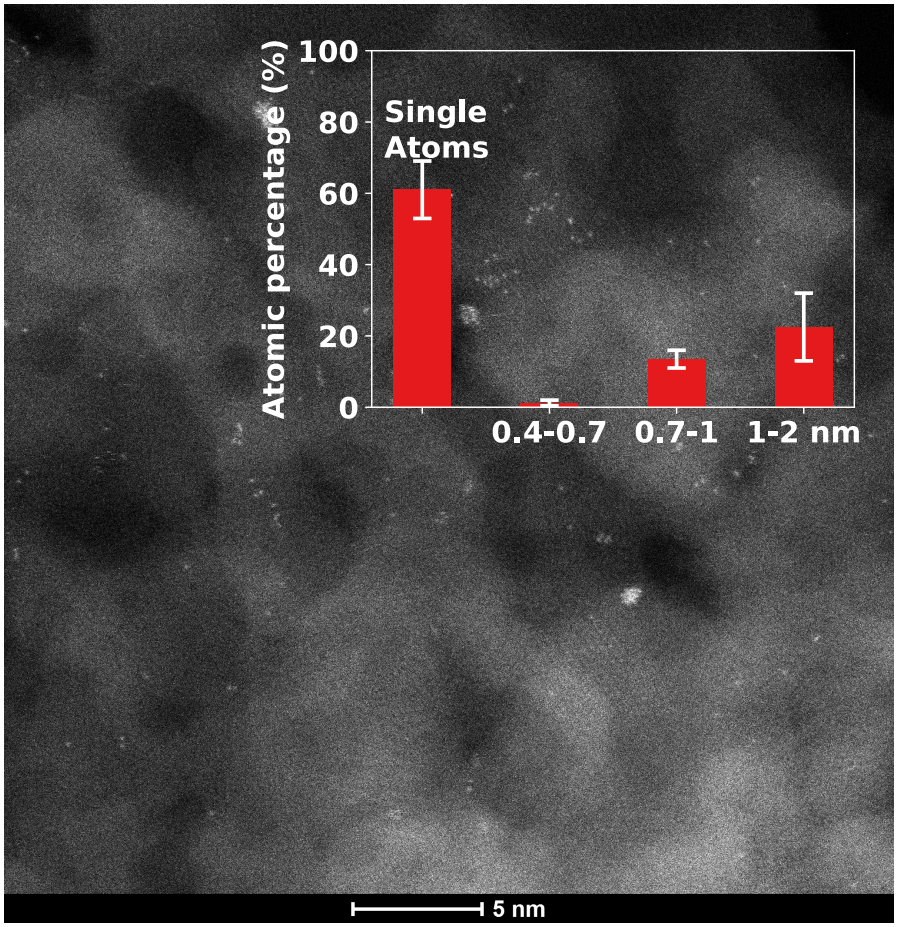

Fig. S2 STEM image and histogram of sample 3. Error bars were obtained by analysis (see SI Table S3 on page S4) of STEM images from 3 batches, two after reduction and one after reduction and CO oxidation.

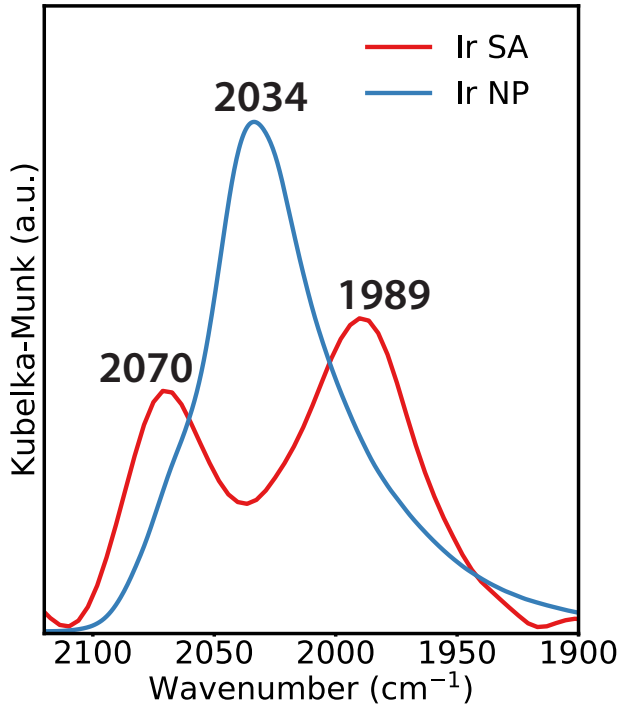

Fig. S3 In-situ infrared spectroscopy (FTIR) spectra in the ν_{CO} region characterizing $MgAl_2O_4$ supported 0.0025 wt.% Ir single atoms catalyst, sample 4 (red) and the 0.2 wt.% Ir nanoparticles catalyst, sample 0 (blue) with average particle size ~ 1 nm. The band intensities are normalized with the surface Ir in each sample (measured by chemisorption for sample 0 and assuming 100% Ir dispersion for sample 4).

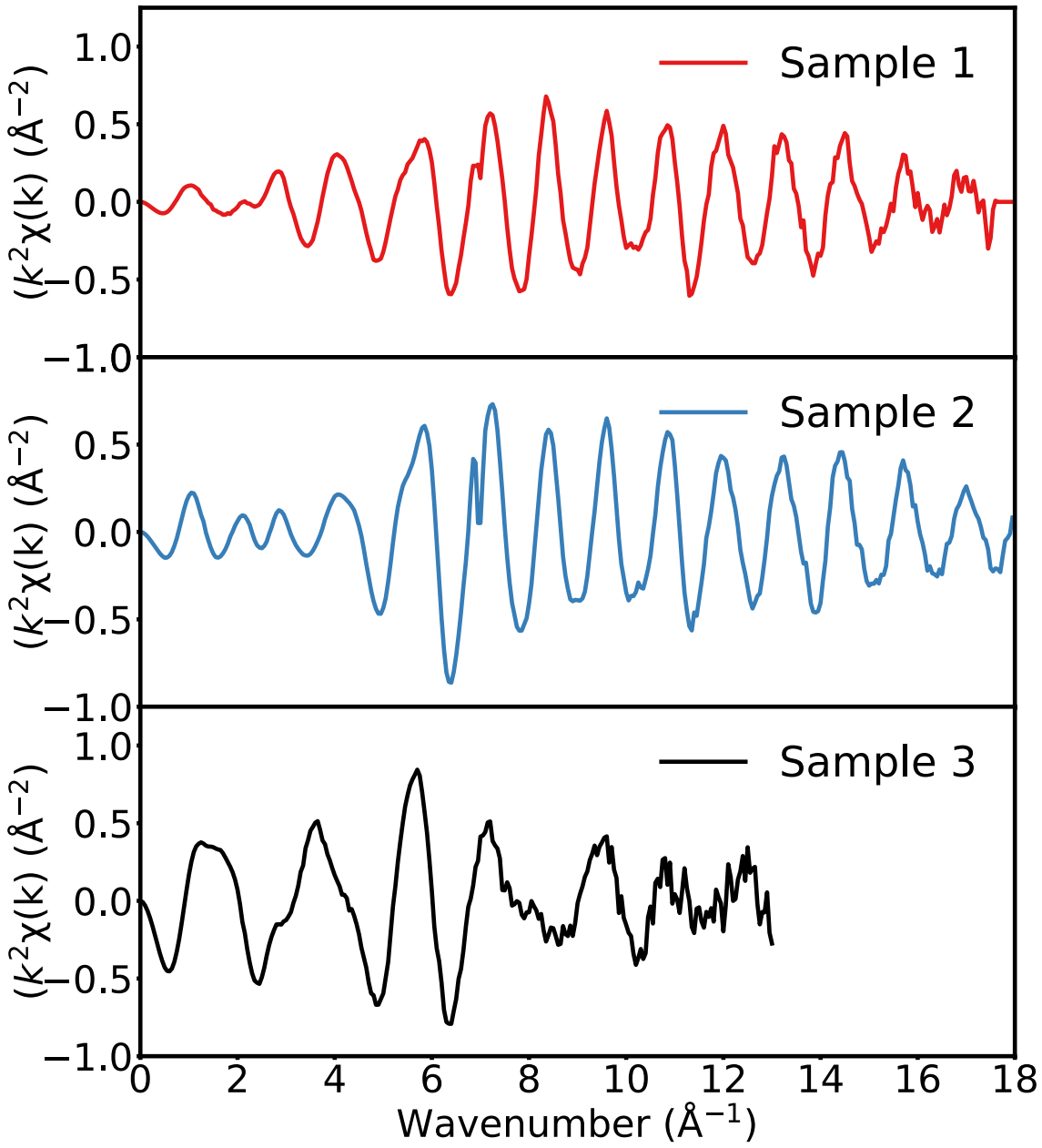

Fig. S4 k^2-weighted EXAFS data in k-space for samples 1-3.

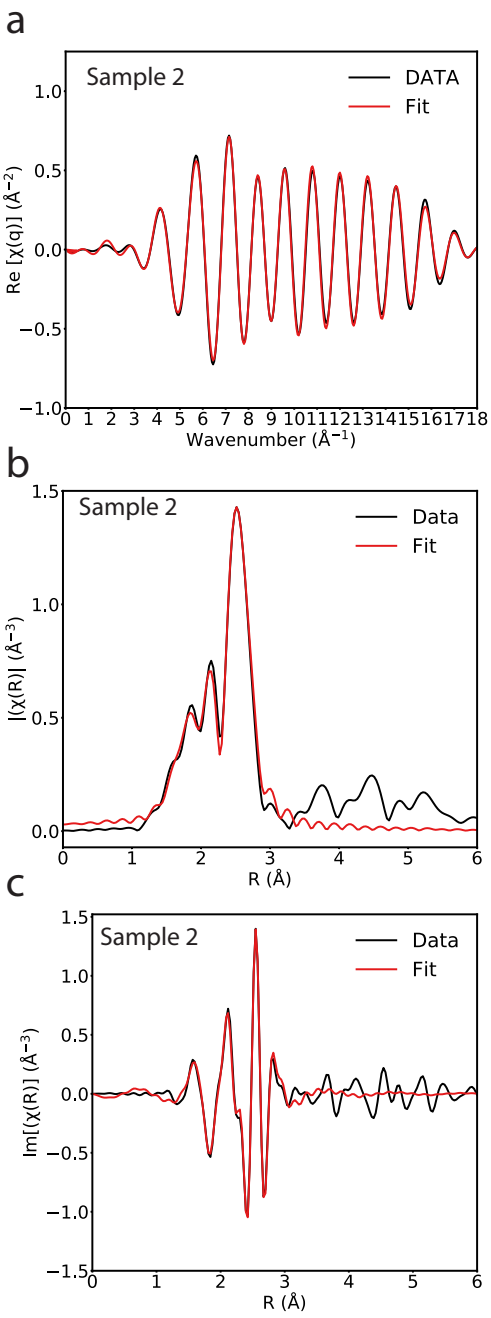

Fig. S5 Sample 2 Ir L_3-edge EXAFS spectra and fit in **(a)** q space and in r-space **(b)** magnitude and **(c)** imaginary part of the Fourier transformed k^2-weighted χ(k) data (Δk= 2.5-16 $Å^{-1}$). The r-range for the fit was 1.3-3.0 Å.

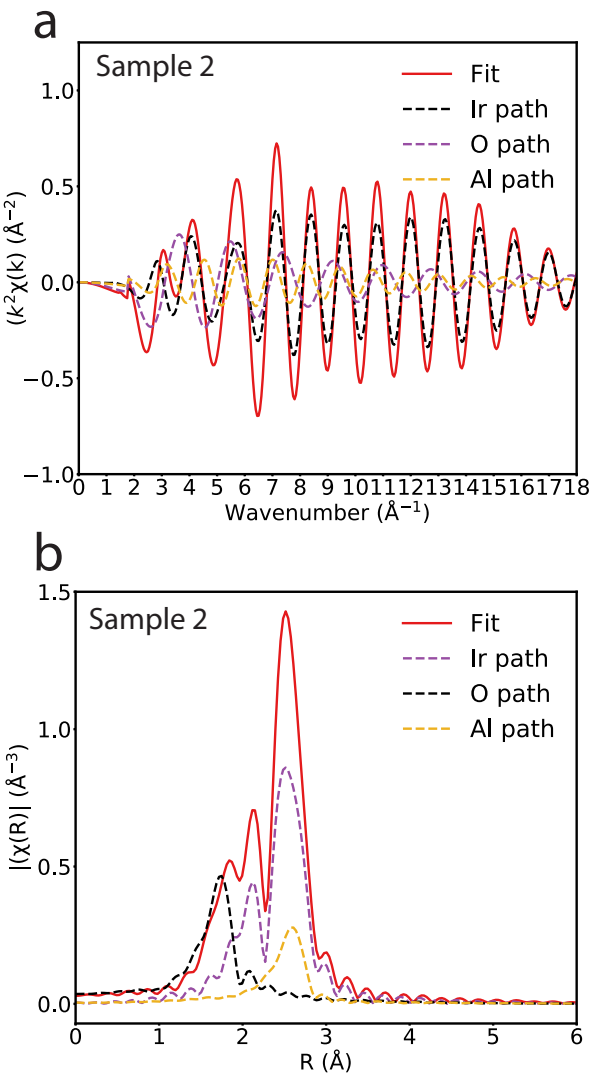

Fig. S6 EXAFS fit to sample 2. Contribution of different scattering paths. (Ir path = Ir-Ir; O path = Ir-O; Al path = Ir-Al) (**a)** q and **(b)** R space.

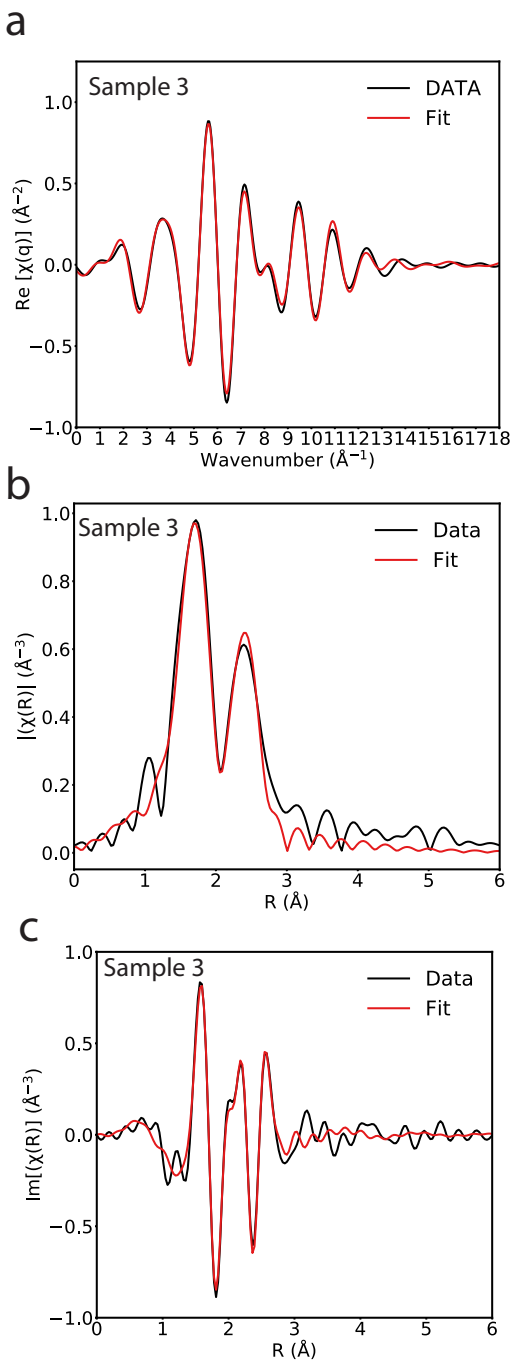

Fig. S7 Sample 3 Ir L_3-edge EXAFS spectra and fit in **(a)** q space and in r space **(b)** magnitude and **(c)** imaginary part of the Fourier transformed k^2-weighted χ(k) data (Δk= 2.5-12.5 Å^{-1}). The r-range for the fit was 1.3-3.0 Å.

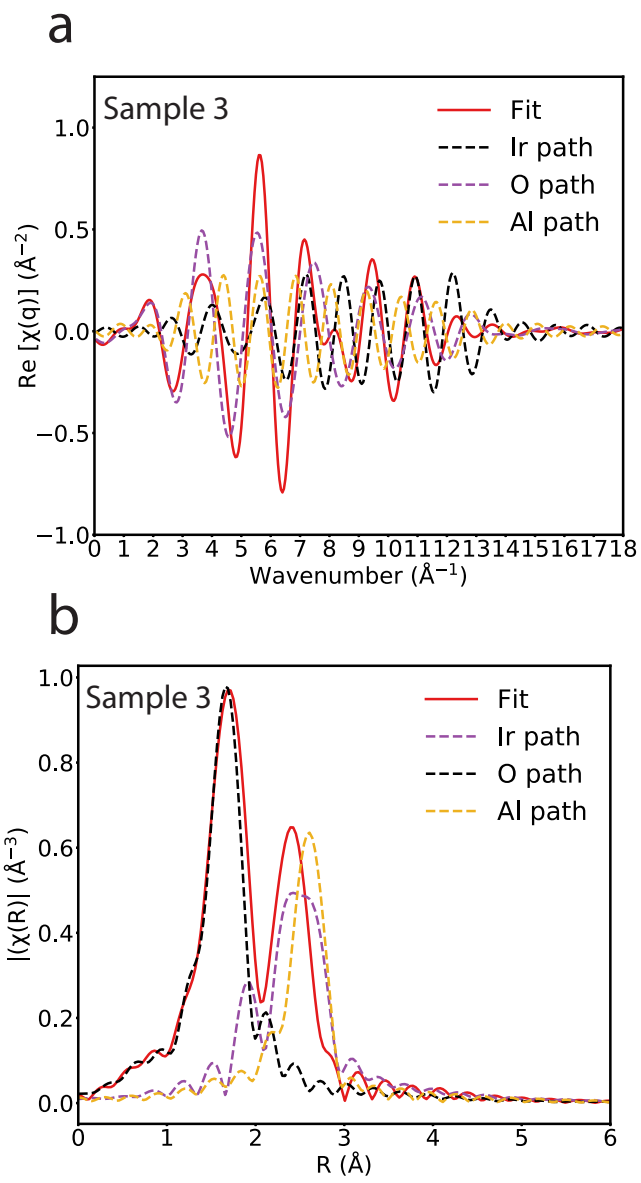

Fig. S8 EXAFS fit to sample 3. Contribution of different paths. **(a)** q and **(b)** R space.

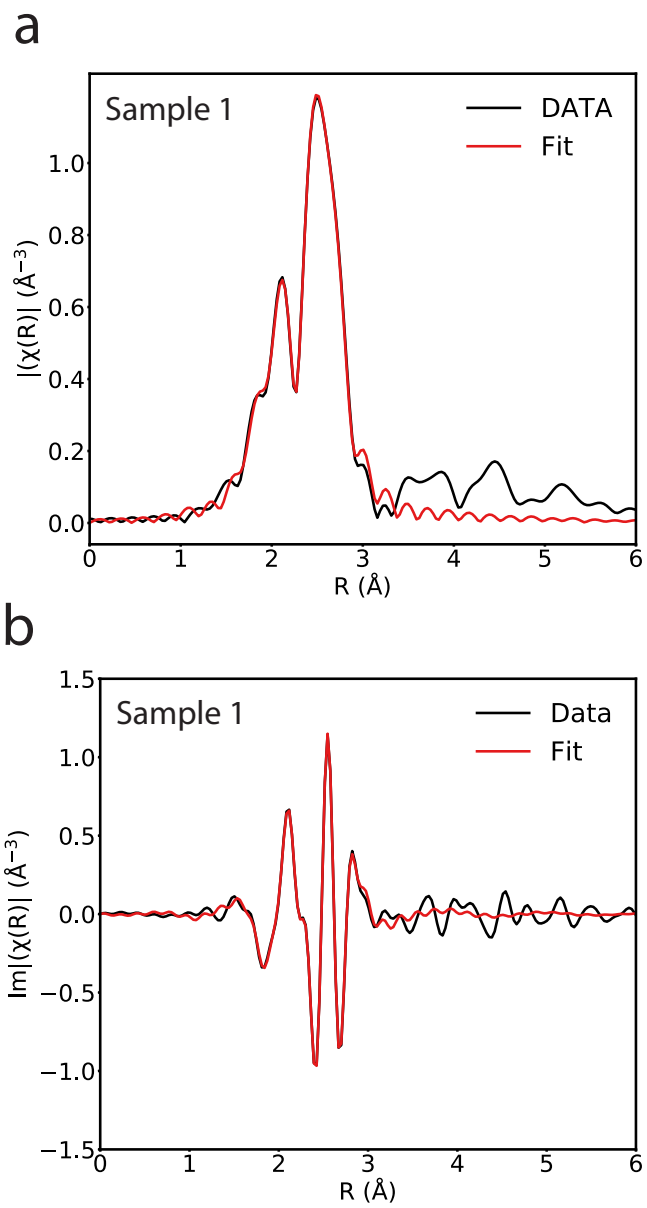

Fig. S9 Sample 1 Ir L_3-edge EXAFS spectra and fit in r-space. **(a)** magnitude and **(b)** imaginary part of the Fourier transformed k^2-weighted $\chi(k)$ data (Δk= 2.5-12 $Å^{-1}$) (Δk = 2.7-16 $Å^{-1}$). The r-range for the fit was 1.3-3.0 Å.

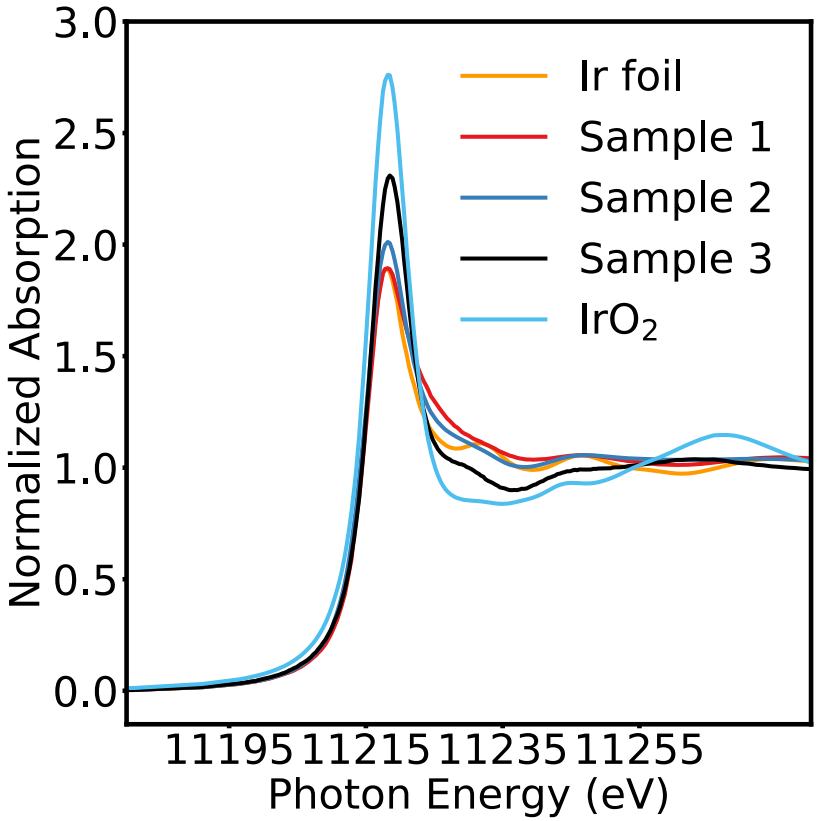

Fig. S10 X-ray absorption near edge (XANES) spectra of samples 1-3 with different ratio of single atoms and nanoparticles compared to Ir foil and IrO_2 standards.

An accurate estimation of the site fraction of single atoms and nanoparticles obtained by fitting the CO reaction order (Figure 4 in the manuscript) was feasible because of the large difference in reaction order on NP and single atoms, namely -1 and 1. To determine the sensitivity to the difference in the orders on SA and NP (e.g. for other systems) we also performed similar fitting with the O_2 reaction order which is not as different (compared to CO order) on SA and NP, namely 0 (sample 4) and 1 (sample 0, reported in earlier work from our group [4]) , respectively. P_{O_2} was varied between 2-14 kPa at two different P_{CO} (1 kPa and 0.2 kPa) to measure the O_2 order at 155 °C (Figure S11). The site fractions of single atoms and nanoparticles were obtained by minimizing RSS (equation 3) and the results are shown in Figure S12. The results were dependent on the CO partial pressure. At 1 kPa P_{CO}, the percentage of single atoms in samples 1-3 were 19%, 21% and 35%, while at 0.2 kPa P_{CO}, they were 31%, 37% and 62% respectively (Figure S12). The results show that while the accuracy of estimating the fraction of single atoms using the O_2 reaction order is lower than using the CO reaction order, the results are still in qualitative agreement with those obtained using the CO order and other techniques.

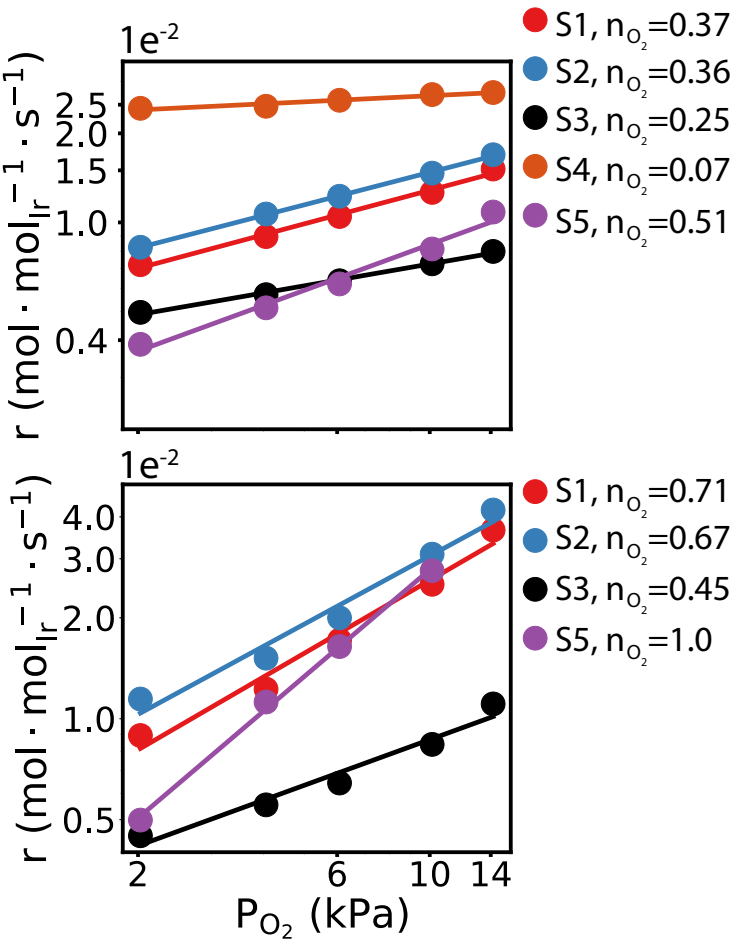

Fig. S11 Reaction O_2 order of samples 1, 2, 3 and 5 measured at 155 °C, with P_{O_2} between 2-14 kPa and P_{CO} at 1 kPa (top) and 0.2 kPa (bottom) respectively. Reaction rate of sample 1-5 were normalized with total mol of Ir during synthesis. At 1 kPa CO, the reaction order of O_2 of samples 1-4 decreased from 0.37 to 0.07 consistent with the increasing percentage of single atoms. At 0.2 kPa CO, the reaction order of O_2 of sample 1-3 decreased from 0.71 to 0.45 also consistent with the increasing percentage of single atoms. The lower orders measured for all the sample at 1 kPa P_{CO} compared with 0.2 kPa is due to the higher contribution of single atoms (+1 order in CO while NP have -1 order in CO). Reaction order of O_2 on sample 5 was 0.51 at 1 kPa CO and 1 at 0.2 kPa

CO, which is higher than sample 1 indicating that only a small percentage (<10 %) of the single atoms observed by STEM is on the surface (consistent with the results in Figure 5 in the manuscript).

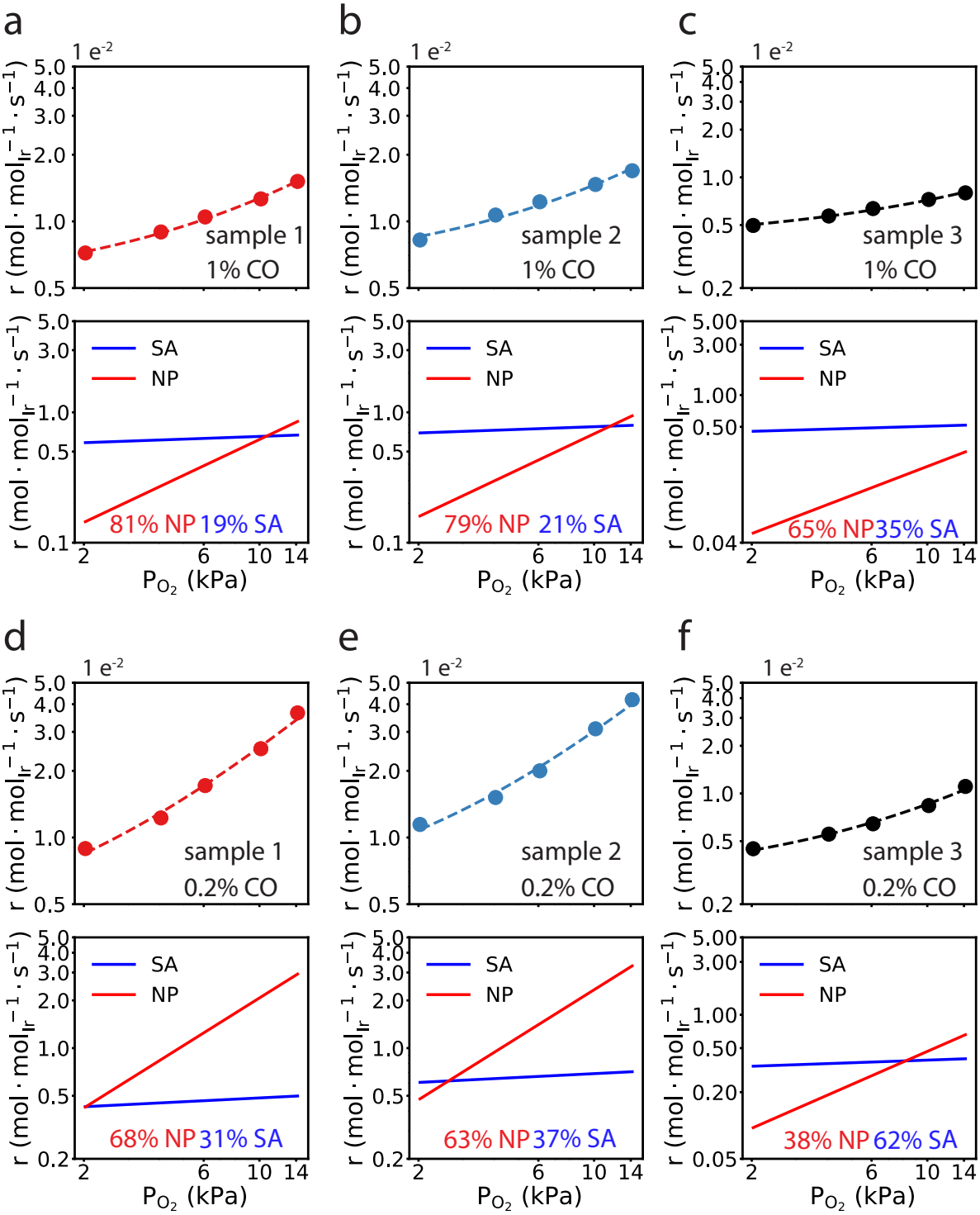
a
b
c
d
e
f
1 e-2
r (mol · mol$_{Ir}^{-1}$ · s^{-1})
sample 1
1% CO
sample 2
1% CO
sample 3
1% CO
sample 1
0.2% CO
sample 2
0.2% CO
sample 3
0.2% CO
SA
NP
81% NP 19% SA
79% NP 21% SA
65% NP35% SA
68% NP 31% SA
63% NP 37% SA
38% NP 62% SA
P$_{O_2}$ (kPa)

Fig. S12 Effect of O_2 partial pressure on reaction rate on sample 1-3. Sample 1-3 was measured with 2-14 kPa O_2, and 1 kPa CO **(a-c)** and 0.2 kPa CO **(d-f)** respectively at 155 °C. Log-log scale. All measured at 155 °C. Reaction rate of sample 1-3 was normalized with the total mol of Ir during synthesis. Reaction rate of samples 1-3 was fit with a linear combination of the activity of SA and the activity of NP. Experiments are shown as solid dots and fits are shown as dotted lines. At 1 % CO and 2-14 % O_2, activities were fitted with **(a)** 19% SA + 81% NP, **(b)** 21% SA + 72% NP **(c)** 35% SA + 65% NP, respectively. At 0.2 % CO and 2-14 % O_2, activities were fitted with **(d)** 31% SA + 68% NP, **(e)** 37% SA + 63% NP **(f)** 62% SA + 38% NP, respectively.

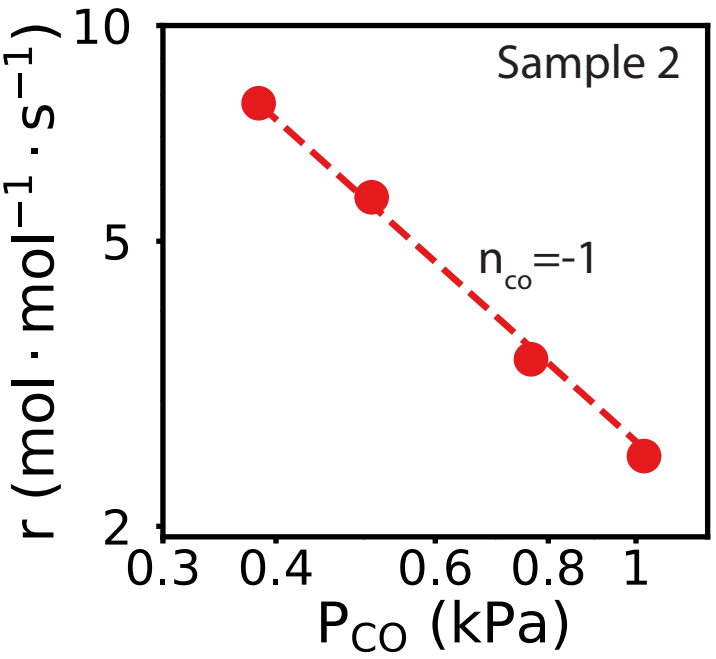

Fig. S13 Effect of CO partial pressure on reaction rate on sample 2. Measured at 155 °C, P_{O_2} = 50 kPa and P_{CO} at between 0.3-1 kPa. Reaction order of CO was measured as -1.

Appendix References

1. Van Hardeveld, R.; Hartog, F., The statistics of surface atoms and surface sites on metal crystals. *Surf. Sci.* **1969,** *15* (2), 189-230.

2. Mozaffari, S.; Li, W. H.; Thompson, C.; Ivanov, S.; Seifert, S.; Lee, B.; Kovarik, L.; Karim, A. M., Colloidal nanoparticle size control: experimental and kinetic modeling investigation of the ligand metal binding role in controlling the nucleation and growth kinetics. *Nanoscale* **2017,** *9* (36), 13772-13785.

3. An, K.; Somorjai, G. A., Size and shape control of metal nanoparticles for reaction selectivity in catalysis. *Chemcatchem* **2012,** *4* (10), 1512-1524.

4. Lu, Y.; Wang, J.; Yu, L.; Kovarik, L.; Zhang, X.; Hoffman, A. S.; Gallo, A.; Bare, S. R.; Sokaras, D.; Kroll, T.; Dagle, V.; Xin, H.; Karim, A. M., Identification of the active complex for CO oxidation over single-atom Ir-on-$MgAl_2O_4$ catalysts. *Nat. Catal.* **2019,** *2* (2), 149-156.

Chapter 4. Operando and Kinetic study of atomically dispersed Pt-on-CeO_2 catalysts for low-temperature CO oxidation

This manuscript is still in preparation.

Attribution:

Yubing Lu performed the characterizations (IR, calorimetry, and EXAFS) and catalytic tests, data analysis, and wrote the first draft of the paper. Deepak Kunwar performed the synthesis of Pt/CeO2 single-atom catalysts. Adam S. Hoffman, Alexey Boubnov and Simon R. Bare helped design the EXAFS and HERFD experiment and contributed to writing the XAS section. Adam S. Hoffman, Alexey Boubnov, Yubing Lu, Coogan Thompson performed the EXAFS experiments. Ayman M. Karim did the EXAFS analysis. Abhaya Datye directed the synthesis and helped the design of experiments. Karim conceived the idea and planned and directed the project. Yubing Lu and Ayman M. Karim co-wrote the paper. All the authors discussed the results and commented on the paper.

4.1. Abstract

Supported single-atom catalysts lead to more efficient use of noble metal atoms, and also provide opportunities for the design of catalysts with better activity and selectivity. CO oxidation on Pt single-atom catalysts has been reported on different supports. During CO oxidation, the Pt single

atoms are reported to be more or less active than their nanoparticle counterparts depending on the support, and the reaction mechanism is still unclear. in this work, we applied operando infrared spectroscopy, X-ray absorption fine structure (XAFS), calorimetry and kinetic measurement aiming to understand the CO oxidation reaction mechanism of atomically dispersed Pt/CeO_2 catalysts. Our XAFS result indicates that each Pt is bonded with 4 O and calorimetry showed that this $Pt(O)_4$ structure interacts weekly with both CO and O_2 at low temperature. When flowing CO and O_2 at 150 °C, CO could replace one of the lattice O to form $Pt(O)_3(CO)$. $Pt(O)_3(CO)$ structure is relatively stable in O_2 and N_2. However, when dosing CO, gas phase CO can react with one of the surface O in $Pt(O)_3(CO)$ structure to form $Pt(O)_2(CO)$ with an Eley-Rideal mechanism. The oxygen vacancy in this $Pt(O)_2(CO)$ vacancy can be filled with one lattice O to form $Pt(O)_3(CO)$ when flowing O_2 to complete the reaction cycle. This suggests that a CO spectator was involved during the whole reaction cycle. Though this spectator CO is stable in O_2, another CO could react with the surface lattice O to complete the reaction cycle.

4.2. Introduction

CO oxidation is an important reaction for emission control[1-3] and polymer electrolyte fuel cell application[4-6]. Pt is very active for such low-temperature oxidation reactions[7-9] and is widely used. However, on Pt single crystals and nanoparticles, Pt could be easily poisoned by CO during CO oxidation, and the activity is limited by the activation of O_2[10-13]. In catalytic converters, CO poisoning of catalysts leads to low conversion, especially at cold start temperature[14]. Pt/Pd supported on CeO_2 and Al_2O_3 are the commonly commercial used catalysts in the catalytic

converter[14-16]. To enhance the CO oxidation catalytic performance of Pt/Pd catalysts, better designed Pt/Pd catalysts are required.

Size and shape of the Pt particles have been proved to be essential for optimizing the catalyst activity. Cargnello et al.[12] showed that smaller particle size of Pt on CeO_2 leads to higher activity during CO oxidation because of the high activity at the Pt-CeO_2 interface. However, this size-dependence was not observed on Al_2O_3 supported Pt catalysts. Single-atom catalysts provided a new opportunity for further optimizing the catalytic performance of noble metal catalysts because of their unique geometric and electronic properties[17-24]. In 2011, Qiao et al.[25] synthesized atomically dispersed Pt/FeO_x catalysts and showed that Pt single atoms were slightly more active than their nanoparticle counterparts. Pt/Al_2O_3 single atoms were also shown to be more (or similar) active than Pt/Al_2O_3 nanoparticles for CO oxidation[26]. However, temperature programmed oxidation (TPO) on CO covered Pt single-atom catalysts on different supports (H-ZSM5, Al_2O_3, ZrO_2, SiO_2, TiO_2) indicates that Pt is not active during CO oxidation until a high temperature (>200 °C) because their band in infrared spectroscopy (> 2090 cm^{-1}) stays during TPO experiment[27]. Lu et al.[17] reported the reaction mechanism of CO oxidation on Ir single atoms, and showed that the strongly adsorbed CO was part of the active complex. This suggests that strongly adsorbed CO should not be an indicator of low activity. To solve the discrepancies when comparing the activity of Pt single atoms and Pt nanoparticles and understand the origin of activity on Pt single atoms, a better understanding of the detailed reaction mechanism and the active structure of Pt single atoms during CO oxidation is required.

Recent progress in stabilizing Pt single atoms paves the ways for mechanism studies. Zhang et al.[28] prepared stable single atoms on Al_2O_3 which can be maintained as atomically dispersed after

60 cycles of CO oxidation between 100 and 400 °C. Polyhedral and nanorods CeO_2 has been reported to be a very effective support for anchoring the platinum. Jones et al.[29] showed stable Pt single atoms on CeO_2 support could be prepared via atomic trapping where Pt with polyhedral CeO_2 was aged at 800 °C in air to ensure only the strongest bond stays. 3% Pt high-loading single atoms can be made through this atomic trapping method to form a stable Pt square planar structure[30]. In-situ infrared spectroscopy showed that the band assigned to the single atoms (centered at 2095 cm^{-1}) is stable in O_2 at 180 °C for Pt single-atom catalysts[29]. CO oxidation activity can be measured on Pt single-atom catalysts. However, the origin of activity could not be explained with the traditional Langmuir-Hinshelwood kinetic mechanism because the adsorbed CO is stable at 180 °C. To solve these discrepancies and further understand the reaction mechanism of Pt single atoms catalysts for CO oxidation, more detailed structural and kinetic studies are required.

In this work, we combined operando spectroscopy, micro-calorimetry and the reaction kinetic measurement to understand the structure and detailed reaction mechanism of the thermally stable Pt/CeO_2 single-atom catalysts for CO oxidation.

4.3. Methods

Catalyst preparation and pretreatment. Synthesis of different shapes of CeO_2 was performed using methods described in the literature[30]. High surface area ceria powder (obtained from Solvay, grade HSA 5) was used as support . Pt/CeO_2 catalysts (1 wt. %Pt, nominal) were prepared by incipient wetness impregnation using method. The pore volume of ceria (0.6 ml/g) was determined by first wetting the dry ceria powder with water. Impregnation of the platinum precursor was done

to fill the pores of ceria. The tetraamine platinum nitrate solution was loaded on ceria in multiple aliquots and dried at 110 °C for 4 hours until all the water evaporated in air after each impregnation. The samples were then calcined in a tube furnace with 100 ml/min of air for 10 h in air at 800 °C. The furnace temperature was ramped up at 1°C per minute.

Diffuse-reflectance infrared Fourier-transform spectroscopy (DRIFTS). DRIFTS was used to characterize the interaction of the supported Pt catalysts with CO, O_2 and the support. The *in-situ* DRIFTS experiments were performed using a Thermo Scientific IS-50R FT-IR equipped with an MCT/A detector. A spectral resolution of 4 cm^{-1} was used to collect spectra, which are reported in the Kubelka-Munk (KM) units. Approximately 50 mg sample (25-90 μm diameter particles) was loaded in the Harrick Praying Mantis high-temperature DRIFTS reaction chamber. The chamber was sealed and connected to a flow system with temperature control, and gases were flown through the sample at atmospheric pressure. Each reported spectrum is an average of 32 scans. The supported Ir samples were pretreated *in-situ* in the DRITS cell before collecting the spectra. The gas pretreatment procedure was the same as mentioned above. For in-situ pretreated catalyst, a spectrum under N_2 after the pretreatment was collected as the background.

X-ray absorption spectroscopy (XAS). The catalysts were characterized by *in-situ* XAS at the Pt L_3-edge (11564 eV) using an in-house built cell with a 4 mm ID glassy carbon tube[31]. The XAS measurements were performed at the Stanford Synchrotron Radiation Light Source (SSRL) at beamline 9-3 in fluorescence mode. Beamline 9-3 is a 16-pole, 2-Tesla wiggler side station with vertically collimating mirror for harmonic rejection and a cylindrically bend mirror for focusing. The photon energy was selected using a liquid-nitrogen-cooled, double-crystal Si (220) $\phi = 90°$

monochromator. Samples were scanned simultaneously in transmission and fluorescence detection modes using ion chambers (see above) and a 100-element solid-state Ge monolith detector (Canberra). A Pt standard (Pt foil) was scanned simultaneously with each sample for energy calibration. Step-scanning X-ray absorption spectra were measured from 11334 eV to 12554 eV, corresponding to photoelectron wave number k = 14.5 $Å^{-1}$. The catalysts were pretreated similar to before the catalytic measurements, then cooled to room temperature in pure H_2 flow (50 sccm) and the EXAFS spectra were collected at room temperature under pure H_2 flow. XANES and EXAFS data processing and analysis were performed using Athena and Artemis programs of the Demeter data analysis package[32-33]. For each catalyst, four scans were collected and merged after alignment. χ(k) was obtained by subtracting smooth atomic background from the normalized absorption coefficient using the AUTOBK code. The theoretical EXAFS signal was constructed using the FEFF6 code[34] and fitted to the data in *R*-space using the Artemis program.

Micro-calorimetry. Micro-calorimetry was performed on a Setaram SENSYS Evo DSC calorimeter with a self-built U-shape sample tube. The U-shape sample tube was connected to a Micromeritics 3Flex for the adsorption quantity measurement and temperature control. 70 mg catalyst was loaded in the U-shape reactor for each experiment. The gas pretreatment procedure was the same as mentioned above in a soaking mode with 760 mmHg O_2. After pretreatment samples were exposed to ultra-high vacuum (UHV) with pressure below 10^{-5} mmHg. For the first set of doses, adsorption heat of both chemisorption and physisorption CO/O_2 was measured. After the first set of doses, samples were exposed to ultra-high vacuum (unrestricted vacuum < 10^{-4} mmHg for 1hr) at 30 °C to remove the physisorbed CO/O_2. The second set of doses measured the

adsorption heat of the physisorbed CO/O_2. O_2 adsorption experiment was measured at 30 °C with pressure between 0-300 mm Hg for O_2 calorimetry and 0-20 mmHg for CO calorimetry.

CO oxidation kinetic measurements. CO oxidation kinetic measurements were performed under differential conditions (<4% conversion) in a conventional laboratory tubular plug flow reactor (7 mm ID quartz tube). Dilution experiments were performed according to Koros-Nowak test to determine the necessary dilution ratio for measurements under strict kinetic control without mass and heat transfer effects[35-37]. The catalysts (after intraparticle dilution) were pressed and sieved into a 106-250 μm diameter fraction. The dilution ratio test to eliminate transport limitations was performed on 1% Pt/Al_2O_3 catalyst using SiO_2 as the diluent. Intraparticle dilutions ratio of 1:40, 1:200 and 1:1000 showed no difference in activity under different CO and O_2 conditions between 145 °C and 170 °C, which indicates the measured catalytic activity was evaluated under kinetic control without transport artifacts. 1:10 dilution ratio with SiO_2 was applied for the 1% Pt/CeO_2 single-atom catalysts based on its activity. Each catalyst pretreatment was the same as mentioned above, and the total flow rate during pretreatment was kept at 50 sccm. The catalyst temperature was measured by a K-type thermocouple (OMEGA) attached at the center of the catalyst bed on the outside of the tube. After pretreatment, CO (5%, balance N_2, certified grade Airgas) was mixed with pure O_2 (99.999% Airgas) and He (99.999% Airgas, equipped with moisture/O_2 trap, Agilent OT3-2) at 35 °C to control the partial pressures of CO and O_2 (by varying their flowrates using Brooks mass flow controllers SLA5800 series). The CO gas line was equipped with a metal carbonyl purifier (Matheson, NanoChem Metal-X) to remove the trace amount of metal carbonyl and a molecular sieve 3A (8–12 mesh) trap to remove trace (ppm) levels of CO_2. No CO_2 was detected in the mass spectrometer with the CO or O_2 flowing during a blank test. The reactor was

heated from room temperature to the reaction temperature at 3 °C/min in 0.5 kPa CO and 10 kPa O_2 balanced with He. During the steady-state kinetic measurements, the conversion of CO was always below 4% by varying the total flow rate between 50-100 sccm. To investigate the effect of CO partial pressure on reaction rate, the partial pressure of O_2 was held constant at 10 kPa, and the partial pressure of CO was varied between 0.3 – 1.0 kPa. To investigate the effect of O_2 partial pressure, the CO partial pressure was held constant at 1.0 kPa, and the partial pressure of O_2 was varied between 2 – 14 kPa, then the measurements were repeated at the initial condition at 1 kPa CO partial pressure. We note that we rigorously monitored the catalyst stability by re-measuring the catalyst activity periodically throughout the experiment under the first condition measured. The activity was stable (< 10% deactivation) for each catalyst tested during the entire kinetic measurement. The composition of the effluent gases was measured by a gas chromatograph (Inficon Micro GC Fusion with two modules each with a separate carrier gas, injector, column and thermal conductivity detector (TCD). Column A: Rt-Molsieve 5A, 0.25 mm ID (10m) using Ar as the carrier gas. Column B: Rt-Q-Bond 0.25 mm ID (12m) using He as the carrier gas. The reaction rates were normalized by the total moles of Pt, assuming that all Pt is on the surface.

4.4. Results and Discussion

4.4.1. Synthesis and surface characterization using STEM

Pt/CeO_2 was prepared with atomic trapping method as reported earlier by Jones et al.[29] and Kunwar et al.[30] Majority of the sample was detected as atomically dispersed Pt atoms in high annular dark field –scanning transmission electron microscopy (HAADF-STEM)[29, 30].

4.4.2. Structural Characterization of Pt/CeO_2 single-atom catalysts

EXAFS was applied to characterize the structure of Pt/CeO_2 single-atom catalysts. To clean the surface and remove the weakly bonded species, the sample was pretreated in O_2 and then He at 400 °C. EXAFS was collected at 150 °C after cooling down in He. EXAFS results (Table 1) showed that Pt in average coordinated with 3.5 oxygen and this is consistent with the square planner structure where each Pt was bonded with 4 surface oxygen. The Pt-O bond distance was fitted as 2.02 Å. Pt was coordinated with 3 Ce on average, and the Pt-Ce bond distance is 3.11 Å. This is consistent with the square planar structure on a (111) step site[30].

Table 1. EXAFS parameters characterizing CeO_2 supported Pt single-atom catalysts after oxygen and He pretreatment at 400 °C.

	After oxidation
N_{Pt-O}	3.5 ± 0.4
N_{Pt-Ce}	3 ± 1.0
N_{Pt-O_long}	4 ± 1.2
R_{Pt-O} (Å)	2.02 ± 0.01
R_{Pt-Ce} (Å)	3.11 ± 0.03
R_{Pt-O_long} (Å)	3.56 ± 0.03

$\sigma^2_{Pt\text{-}O}$ (Å^2)	0.000 ± 0.001
$\sigma^2_{Pt\text{-}Ce}$ (Å^2)	0.004
$\sigma^2_{Pt\text{-}O\_long}$ (Å^2)	0.004
ΔE_0 Pt-O (eV)	12 ± 3

N, coordination number;

R distance between adsorber and backscatter atom;

σ^2, Debye-Waller factor to account for both thermal and structural disorders;

E_0, inner potential correction

4.4.3. In-situ and operando characterization using DRIFTS

The CO adsorbed on atomically dispersed Pt single atoms was reported to be relatively stable in O_2 after CO oxidation at 125 °C[29] and also 180 °C[38], and the DRIFTS spectra of Pt single atoms only decreased by <~10% after flowing O_2 for 10 min. We performed the stability test first at 150 °C on the same catalyst. After CO oxidation, when flowing O_2 after He stabilization, the CO on Pt single atoms maintained almost the same intensity (Figure 1a). This showed that after removing small proportion of weakly bonded CO (Figure S1), the CO bonded to Pt single atoms is stable under O_2 flow. CO has been reported [39] to have very low binding energy of 7 kJ/mol with $Pt(O)_4$ square spanner structure on CeO_2 (100) surface. This suggests that CO could not adsorb on $Pt(O)_4$ at the reaction temperature. Band located centered between 2095-2100 cm^{-1} in Figure 1 are assigned to the square planar $Pt(O)_3(CO)$ structure, where one CO replaced a lattice O in the

original $Pt(O)_4$ structure when flowing $CO+O_2$ at 150 °C. To test the stability and CO oxidation activities at different temperatures, DRIFTS was then measured from 150 to 250 °C in $CO + O_2$. Only one peak centered at ~2096 cm^{-1} was observed during this temperature range, which indicates the majority of Pt atoms stayed atomically dispersed. We note that a significant CO_2 peak (2361 and 2341 cm^{-1}) was observed at 150 °C (Figure 1b), which indicates that this catalyst is active for CO oxidation though TPO experiment in IR showed no decrease in the single atom band (2095-2100 cm^{-1}) at this temperature. The intensity of the Pt single atom band (2096 cm^{-1}) decreases with the increase of temperature, and the CO_2 peak increases, which showed that adsorbed CO can react with O_2 at temperatures above 150 °C.

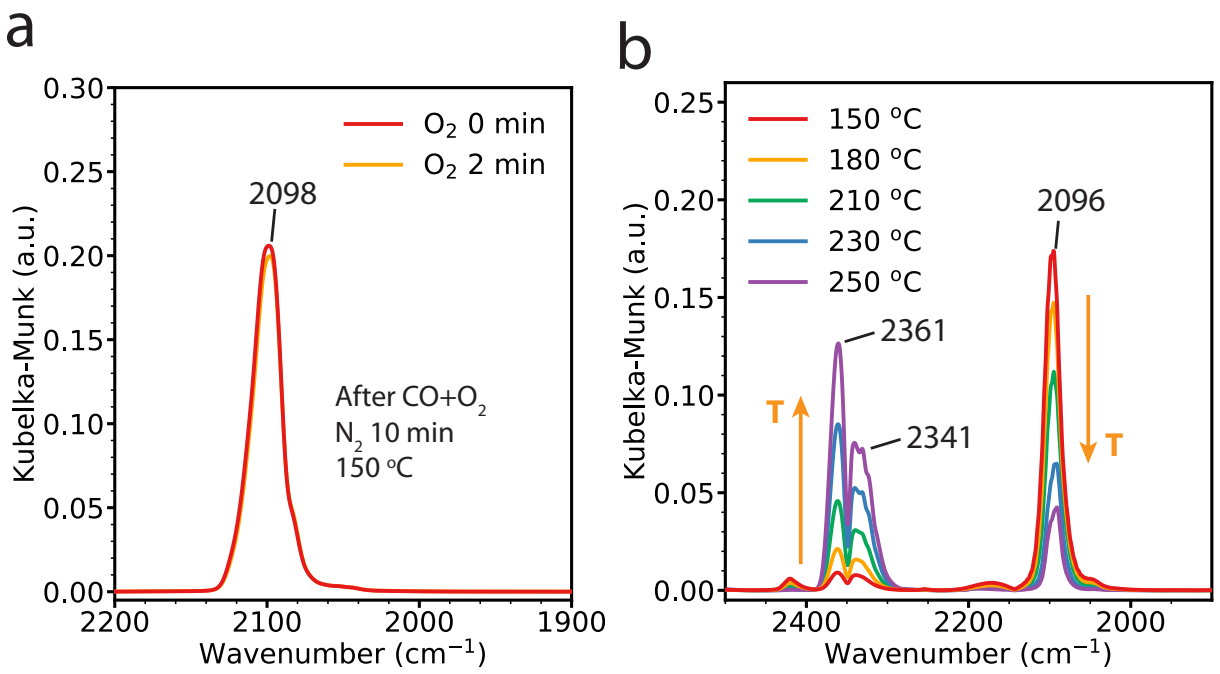

Figure 1. DRIFTS spectra in the υ_{CO} region characterizing the stability of the 1 wt.% Pt/CeO_2 single-atom catalysts under N_2 and O_2 at 150 °C and at different temperatures in $CO + O_2$. **(a)** DRIFTS Spectra was collected at different times in O_2 (50 sccm) after flowing 3 kPa CO and 2

kPa O_2 and then stabilized in He for 10 min. **(b)** DRIFTS spectra were collected at different temperatures between 150 °C and 250 °C in 3 kPa CO and 2 kPa O_2. CO_2 was observed at 150 °C, and the intensity of the CO_2 spectrum increased with temperature from 150 to 250 °C.

After testing the stability in O_2, the stability in CO was also tested on 1 wt.% Pt/CeO_2 single-atom catalysts. After CO oxidation at 150 °C, only one band was detected in DRIFTS centered between 2095-2100 cm^{-1} (Figure 2a, b, red). To minimize the possibility for structural change, a small concentration of CO (0.25%) was dosed into the chamber for 10 s (each dose). After 13 CO doses (Figure 2a, blue, Figure S2 for detailed changes), The intensity of the original 2095 cm^{-1} significantly decreased, and two new peaks at 2073 and 2038 cm^{-1} appeared. This indicates that part of the $Pt(O)_3(CO)$ species was replaced by new species with higher electron density on the metal center. When flowing O_2 after dosing CO, the intensity of the 2095 cm^{-1} increased to its original intensity, with small shoulder bands at lower wavenumbers. The DRIFTS spectrum changed back to its original position before dosing CO (Figure 2), and the isosbestic points present during CO dosing in both DRIFTS (Figure S2a) and XAFS (Figure 5a), which suggests that there is a reaction cycle in the process of dosing CO and flowing O_2. The shoulder bands at lower wavenumber (centered at 2038 cm^{-1}) can be assigned to Pt clusters, which suggest that small portion Pt agglomerates during CO dosing. After the above steps in Figure 2a, another set of longer CO doses (26 doses) were conducted (Figure 2b). After longer doses of CO, the 2095 cm^{-1} band was completely replaced by the lower frequency bands at 2073 and 2038 cm^{-1}. Then O_2 flowed through the sample, and the spectrum moved back to its original 2095 cm^{-1} with a shoulder band higher than the original shoulder band. The higher doses also presented a complete reaction cycle

between dosing CO (2095 cm^{-1}) and flowing O_2 (2073 cm^{-1}). Possible agglomeration was observed during CO dosing when there are no oxygen presents in the flow, which is understandable since CO could interact strongly and move with the metal atoms[40-41]. After the reaction cycle between CO and O_2, as shown in Figure 1a-b, CO and O_2 were introduced together to test the stability of the catalyst during these cycles. The spectrum in CO+O_2 after two cycles (Figure 2c, blue) contains one main band centered at 2099 cm^{-1}. When compared with the spectrum before two cycles (Figures 2c, red) there is only a slight increase in the lower frequency shoulder bands. This suggests after the reaction cycle between CO and O_2 when considering all Pt single atoms on the surface, the majority of the Pt stayed as atomically dispersed. With the reaction cycle between CO and O_2 observed in DRIFTS, we propose that $Pt(O)_3(CO)$ is the stable intermediate (υ_{CO} centered at ~2095 cm^{-1}) formed during CO+O_2 flow and it could react with a gas CO molecule to form $Pt(O)_2(CO)$ structure (υ_{CO} centered at 2073 cm^{-1}). The $Pt(O)_2(CO)$ could then react with O_2 to form $Pt(O)_2(CO)(O_2)$, and another CO react will the extra O in the adsorbed O_2 to form $Pt(O)_3(CO)$ and complete the reaction cycle.

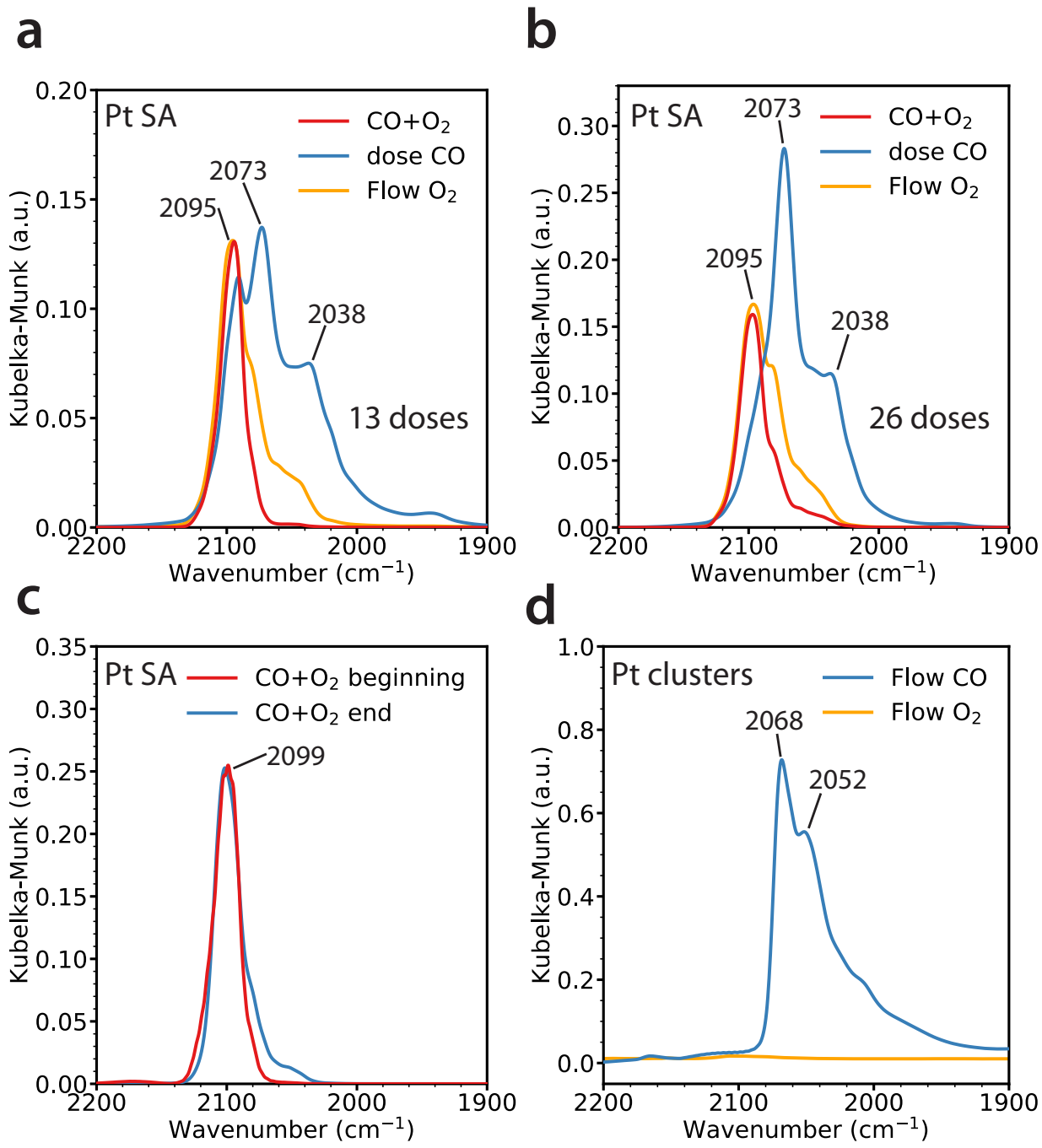

Figure 2. DRIFTS spectra in the υ_{CO} region characterizing 1 wt.% Pt/CeO_2 single atoms (Pt SA) when dosing CO, flowing O_2 and then CO+O_2; and the Pt clusters (reduced in CO at 300 °C) when flowing CO and O_2. **(a)** At 150 °C, 3% CO+ 2%O_2 flowed through the 1wt.% Pt/CeO_2 single-atom

catalysts until the DRIFTS are stable. Then the sample was flushed with N_2 for 2 min before collecting a spectrum (red spectrum). After that, 0.25 kPa CO was dosed on this catalysts with 0.1 kPa CO, 10 s for each dose and 10 s between doses. 13 doses in total before collecting the second spectrum in N_2 (blue spectrum). After the CO dosing, 1 kPa O_2 flowed through the sample followed by N_2 flush and spectrum (orange) was collected. **(b)** After steps in **(a)** (red spectrum), added 26 CO same doses (blue spectrum) and then flowed O_2. All at 150 °C.

4.4.4. Kinetic measurements

Kinect measurements were performed to further understand the reaction mechanism. As a reference sample, reaction kinetic was first performed on a sample contains mostly clusters (1% Pt/CeO_2 reduced in CO at 300 °C, see Methods for detailed pretreatment). The CO reduced clusters showed much higher activity which has been discussed. Reaction order of CO and O_2 on Pt clusters were measured as 0.08 and 0.22 respectively at 70 °C at O_2 rich condition (Figure S3). Cargnello et al. [12] measured similar reaction order on Pt/CeO_2 particles with average particle size 1.7 nm. The ~0 order in CO and O_2 on CeO_2 supported Pt clusters/particles is a result of the reaction between adsorbed CO on Pt and the O_2 provided by the ceria. CO and O_2 are adsorbed on different sites so that CO on the Pt is unable to suppress the activation of O_2[12]. For the 1 wt.% Pt/CeO_2 single-atom catalyst in this work, reaction order of CO was measured as 0.46 and reaction order of O_2 was measured as 0.01 at 150 °C with the same gas partial pressure as Pt clusters (Figure 3). The different reaction orders suggest that CeO_2 supported Pt single atoms follows a different reaction mechanism with CeO_2 supported Pt clusters. We also measured the CO order on Pt single atoms after dosing CO (26 doses). As shown in Figure S4, the reaction order of CO and activity

stays almost identical after CO dosing which suggests the Pt single atoms stay as atomically dispersed after CO dosing. The positive order in CO is consistent with the reaction mechanism observed in DRIFTS, where gas-phase CO react with the O on CeO_2 is the rate-limiting step. There is likely some contribution from Langmuir-Hinshelwood since the reaction order is not exactly +1 and kinetic measurement and DRIFTS results suggest that $Pt(O)_3(CO)$ is the stable intermediate where the adsorbed CO (2095-2100 cm-1) is a spectator species. CO could react with the surface O* in the $Pt(O)_3(CO)$ instead of O_2 react with the surface CO* in the $Pt(O)_3(CO)$.

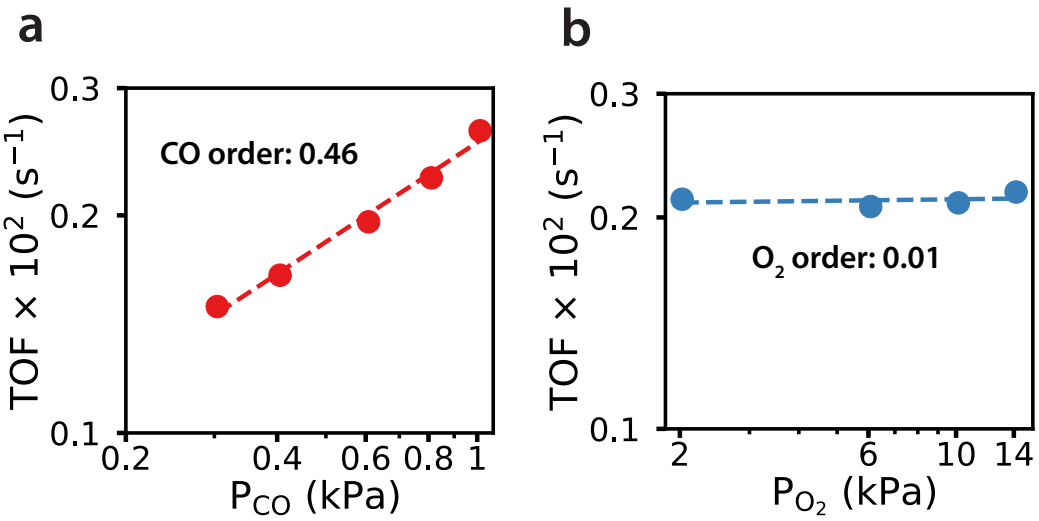

Figure 3. CO oxidation kinetic measurements (effect of CO and O_2 partial pressure on TOF) on 1 wt.% Pt/CeO_2 single-atom catalysts. Measured at 150 °C. P_{CO} = 0.3 -1 kPa and P_{O_2} = 10 kPa for CO order and P_{CO} = 1 kPa and P_{O_2} = 2-14 kPa for O_2 order.

4.4.5. Calorimetric study of the surface properties

Micro-calorimetry of CO and O_2 adsorption was performed at 30 °C on 1 wt.% Pt/CeO_2 single-atom catalysts after pretreatment. O_2 micro-calorimetry (Figure 4a) showed an initial heat of 15

kJ/mol at ~0 coverage and gradually decreased to ~0 kJ/mol at 0.15 mol O_2/mol Pt. This low adsorption heat suggests that O_2 bind very weakly, and confirmed the $Pt(O)_4$ structure which has been proven to be the most stable structure for Pt single atoms[39]. CO calorimetry showed an adsorption energy of 168 kJ/mol at ~0 coverage and gradually decreased to ~10 kJ/mol at ~0.15 mol CO/mol Pt. As a reference, the CO adsorption energy of Pt single atom on CeO_2 (100) facets with the $Pt(O)_4$ square planar structure was calculated as 7 k/mol[39]. The initial high adsorption energy suggests this sample contains $Pt(O)_4$ and a small proportion of $Pt(O)_3$. CO could and adsorb on the $Pt(O)_3$ to form $Pt(O)_3(CO)$ at room temperature. The low adsorption energy is related to the CO adsorption on $Pt(O)_4$, which is consistent with the calculated CO adsorption energy on $Pt(O)_4$ structure for Pt single atoms on CeO_2 (100).

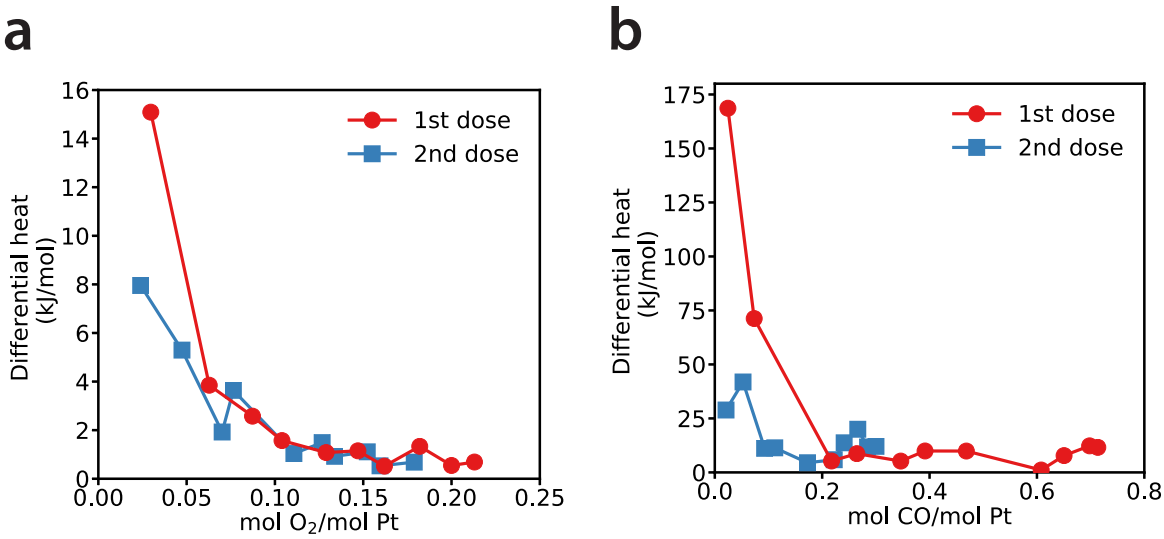

Figure 4. Micro-calorimetry of CO **(a)** and O_2 **(b)** adsorption on 1% Pt/CeO_2 single-atom catalysts at 30 °C in ultra-high vacuum condition. The first dose measured the heat of chemisorption and physisorption. The second dose measured the heat of physisorption.

4.4.6. Reaction mechanism and activation of Pt single atoms during CO dosing

Pt/CeO_2 single-atom catalyst showed a unique reaction mechanism as discussed in the previous section. Eley-Rideal and Mars Van-Krevelen mechanism are likely the most favorable pathways. To further understand the reaction mechanism and the structure, we conducted EXAFS under reaction conditions. We first dosed 13 and 26 doses of CO the same as the condition in IR (Figure 2). EXAFS and DRIFTS result indicates that not all Pt was accessible by CO after CO oxidation at 150 °C. This suggests that some of the Pt is bonded with less than 4 O or has one weakly bonded O initially, which can be accessed by CO when flowing CO and O_2 at 150 °C. When dosing CO at 150 °C for a larger dose (0.33 kPa CO balanced with He at 60 sccm, 40 s each dose and 40 doses in total for all 3 set of doses), in the DRIFTS (Figure 5b) the 2095 cm^{-1} band was further replaced by the lower frequency peaks centered at ~2072, ~2047, and ~2029 cm^{-1}. The 1st set of doses was similar to the doses in Figure 2b. The 2nd and two doses showed similar band intensity, and band shapes suggest that the species has been almost stabilized after the 2nd and 3rd doses. The XANES spectra of the 3 sets of CO doses are shown in Figure 5 a. The decrease of white line intensity during CO dosing suggests the Pt single atoms got reduced. We note that there are isosbestic points during CO dosing for both XANES (Figure 5a) and DRIFTS (Figure 5b and Figure S1a). The isosbestic points suggest that the majority of the Pt is still atomically dispersed because once agglomeration happens, different size of clusters is expected to be present and have different CO bands leading to a change in the center and asymmetry of the CO bands[13, 42]. EXAFS fitting of the sample after CO dosing and flow $CO+O_2$ after CO dosing are shown in Table 2. Pt-Pt coordination

could not be fitted for both after CO dosing and in $CO+O_2$, which suggests that the majority of Pt remains atomically dispersed even after large CO dosing. The Pt-C coordination was fitted as 1.1, and Pt-O coordination was fitted as 2.2. This indicates a $Pt(CO)(O)_2$ structure after CO dosing, where Pt was bonded with 1 CO and 2 O from the surface and one O vacancy present. After flowing $CO+O_2$ again, The Pt-C coordination was fitted as 1.2, and Pt-O coordination was fitted as 3.0. This indicates that after flowing $CO+O_2$, the O vacancy was filled by the gas phase O_2, and a $Pt(O)_3(CO)$ or $Pt(O)_2(CO)(O_2)$ structure was formed. The structure obtained from EXAFS under reaction condition is consistent with the proposed Eley-Rideal/Mars Van-Krevelen mechanism. When dosing CO, gas phase CO reacts with one of the surface O in the $Pt(O)_3(CO)$ structure to form $Pt(O)_2(CO)$ and creates a O vacancy. When flowing CO and O_2, the O vacancy will be filled and the stable intermediate $Pt(O)_3(O)$ will again dominate the surface. We note that compared with the CO_2 level when flowing $CO+O_2$ before CO dosing experiment, the CO_2 level after dosing increased by two orders of magnitude (Figure S5). This shows that after CO dosing the activity increased dramatically while most of the Pt stays as atomically dispersed. The increase of activity can be attributed to the slightly changing of local environment of Pt single atoms during CO dosing since CO could have a strong interaction with the noble metal center. The change of Pt position could affect the reducibility of the surface O atom and therefore affect the reaction barrier in the rate-limiting step, in this case, is the reaction between the gas phase CO and the surface O.

Table 2. EXAFS parameters characterizing CeO_2 supported Pt single-atom catalysts under reaction temperature when dosing CO and flowing $CO+O_2$.

	After CO dosing	**in $CO+O_2$**
$N_{Pt\text{-}C\ (CO)}$	1.1 ± 0.4	1.2 ± 0.3
$N_{Pt\text{-}O}$	2.2 ± 0.2	3.0 ± 0.6
$R_{Pt\text{-}C}$ (Å)	1.83 ± 0.02	1.83 ± 0.02
$R_{Pt\text{-}O}$ (Å)	2.01 ± 0.01	2.01 ± 0.01
$\sigma^2_{Pt\text{-}C}$ ($Å^2$)	0.000 ± 0.002	0.000 ± 0.002
$\sigma^2_{Pt\text{-}O}$ ($Å^2$)	0.000 ± 0.001	0.000 ± 0.001
ΔE_0 Pt-O (eV)	12 ± 6	11 ± 5

N, coordination number;

R distance between adsorber and backscatter atom;

σ^2, Debye-Waller factor to account for both thermal and structural disorders;

E_0, inner potential correction;

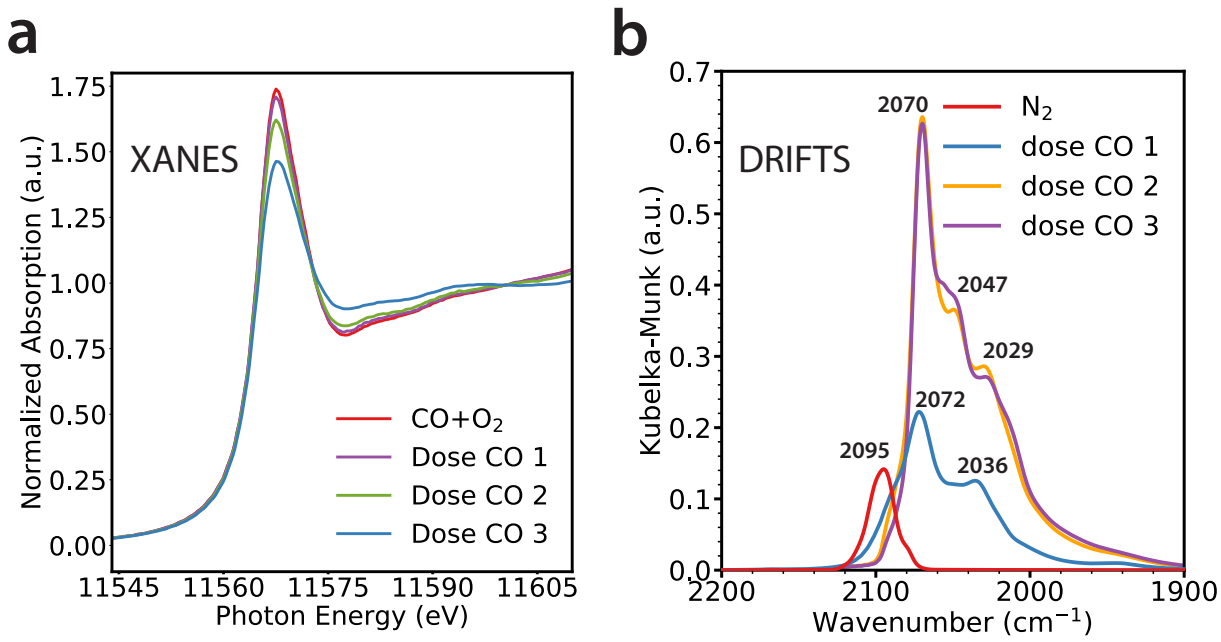

Figure 5. XANES and DRIFTS results of the Pt/CeO_2 catalysts when dosing large CO (~30 doses for each spectrum, with 10).

4.5. Conclusions

Pt single atoms were prepared with atomic trapping method. Infrared spectroscopy showed that most of the Pt single atoms are stable in O_2 and N_2 at the reaction temperature (150 °C). However, significant activity was measured in DRIFTS and catalytic performance test, so that the origin of activity could not be explained by Langmuir-Hinshelwood pathways where adsorbed CO react with the activated O_2 on the same Pt atom. EXAFS identified the surface structure after pretreatment as $Pt(O)_4$ square planar structure. Our operando DRIFTS and EXAFS results showed that while $Pt(O)_3(CO)$ structure is stable in O_2, gas phase CO could react with the surface O to form CO_2. The lattice O can be filled by O_2. Positive order in CO (~0.5) and 0 order in O_2 is consistent with the Mars Van-Krevelen /Eley-Rideal mechanism identified by operando DRIFTS

and EXAFS. We also noted that after CO dosing the reducibility of the surface O significantly increased and therefore the activity of CO oxidation dramatically increased. The adsorbed CO serves as a spectator at the low-temperature CO oxidation so that the TPO experiment is not a proper indicator of activity. For the future work, first–principle calculation can be applied to understand the more detailed reaction mechanism based on the proposed reaction mechanism in this work.

References

1. Kummer, J. T., Catalysts for automobile emission control. *Prog. Energy Combust. Sci.* **1980,** *6* (2), 177-199.
2. Song, Y. Y.; Grabow, L. C., Activity trends for catalytic CO and NO CO-oxidation at low temperature diesel emission conditions. *Industrial & Engineering Chemistry Research* **2018,** *57* (38), 12715-12725.
3. Khaminets, S. G.; Potapova, L. L.; Radkevich, B. Z.; Kochubei, D. I.; Egiazarov, Y. G., Effective platinum catalysts for low-temperature oxidation of CO. *Russ J Phys Chem a+* **2010,** *84* (4), 561-565.
4. Lin, J.; Qiao, B.; Li, L.; Guan, H.; Ruan, C.; Wang, A.; Zhang, W.; Wang, X.; Zhang, T., Remarkable effects of hydroxyl species on low-temperature CO (preferential) oxidation over Ir/Fe$(OH)_x$ catalyst. *Journal of Catalysis* **2014,** *319*, 142-149.
5. Baschuk, J. J.; Li, X. G., Carbon monoxide poisoning of proton exchange membrane fuel cells. *Int J Energ Res* **2001,** *25* (8), 695-713.

6. Rodrigues, A.; Amphlett, J. C.; Mann, R. F.; Peppley, B. A.; Roberge, P. R., Carbon monoxide poisoning of proton-exchange membrane fuel cells. *Iecec-97 - Proceedings of the Thirty-Second Intersociety Energy Conversion Engineering Conference, Vols 1-4* **1997**, 768-773.

7. Lou, Y.; Liu, J. Y., A highly active Pt-Fe/gamma-Al_2O_3 catalyst for preferential oxidation of CO in excess of H_2 with a wide operation temperature window. *Chemical Communications* **2017,** *53* (64), 9020-9023.

8. Yin, C. R.; Negreiros, F. R.; Barcaro, G.; Beniya, A.; Sementa, L.; Tyo, E. C.; Bartling, S.; Meiwes-Broer, K. H.; Seifert, S.; Hirata, H.; Isomura, N.; Nigam, S.; Majumder, C.; Watanabe, Y.; Fortunelli, A.; Vajda, S., Alumina-supported sub-nanometer Pt_{10} clusters: amorphization and role of the support material in a highly active CO oxidation catalyst. *Journal of Materials Chemistry A* **2017,** *5* (10), 4923-4931.

9. An, N. H.; Yuan, X. L.; Pan, B.; Li, Q. L.; Li, S. Y.; Zhang, W. X., Design of a highly active Pt/Al_2O_3 catalyst for low-temperature CO oxidation. *Rsc Adv* **2014,** *4* (72), 38250-38257.

10. Gao, F.; Wang, Y.; Cai, Y.; Goodman, D. W., CO Oxidation on Pt-group metals from ultrahigh vacuum to near atmospheric pressures. 2. palladium and platinum. *Journal of Physical Chemistry C* **2009,** *113* (1), 174-181.

11. Berlowitz, P. J.; Peden, C. H. F.; Goodman, D. W., Kinetics of CO oxidation on single-crystal Pd, Pt, and Ir. *Journal of Physical Chemistry* **1988,** *92* (18), 5213-5221.

12. Cargnello, M.; Doan-Nguyen, V. V. T.; Gordon, T. R.; Diaz, R. E.; Stach, E. A.; Gorte, R. J.; Fornasiero, P.; Murray, C. B., Control of metal nanocrystal size reveals metal-support interface role for ceria catalysts. *Science* **2013,** *341* (6147), 771-773.

13. Allian, A. D.; Takanabe, K.; Fujdala, K. L.; Hao, X.; Truex, T. J.; Cai, J.; Buda, C.; Neurock, M.; Iglesia, E., Chemisorption of CO and mechanism of CO oxidation on supported platinum nanoclusters. *J Am Chem Soc* **2011,** *133* (12), 4498-517.

14. Arvajova, A. B.; Brezina, J.; Pecinka, R.; Koci, P., Modeling of two-step CO oxidation light-off on Pt/gamma-Al_2O_3 in the presence of C_3H_6 and NO_x. *Appl Catal B-Environ* **2018,** *233*, 167-174.

15. Montini, T.; Melchionna, M.; Monai, M.; Fornasiero, P., Fundamentals and catalytic applications of CeO_2-based materials. *Chem. Rev.* **2016,** *116* (10), 5987-6041.

16. Yao, H. C.; Yao, Y. F. Y., Ceria in automotive exhaust catalysts .1. Oxygen storage. *Journal of Catalysis* **1984,** *86* (2), 254-265.

17. Lu, Y.; Wang, J.; Yu, L.; Kovarik, L.; Zhang, X.; Hoffman, A. S.; Gallo, A.; Bare, S. R.; Sokaras, D.; Kroll, T.; Dagle, V.; Xin, H.; Karim, A. M., Identification of the active complex for CO oxidation over single-atom Ir-on-$_{MgAl2O4}$ catalysts. *Nature Catalysis* **2019,** *2* (2), 149-156.

18. Yang, M.; Li, S.; Wang, Y.; Herron, J. A.; Xu, Y.; Allard, L. F.; Lee, S.; Huang, J.; Mavrikakis, M.; Flytzani-Stephanopoulos, M., Catalytically active Au-$O(OH)_x$-species stabilized by alkali ions on zeolites and mesoporous oxides. *Science* **2014,** *346* (6216), 1498-1501.

19. Yang, M.; Liu, J.; Lee, S.; Zugic, B.; Huang, J.; Allard, L. F.; Flytzani-Stephanopoulos, M., A Common single-site Pt(II)-O(OH)x- species stabilized by sodium on "active" and "inert" supports catalyzes the water-gas shift reaction. *J Am Chem Soc* **2015,** *137* (10), 3470-3.

20. Lu, J.; Serna, P.; Gates, B. C., Zeolite- and MgO-supported molecular iridium complexes: support and ligand effects in catalysis of ethene hydrogenation and H-D exchange in the conversion of H_2+D_2. *ACS Catalysis* **2011,** *1* (11), 1549-1561.

21. Cao, L.; Liu, W.; Luo, Q.; Yin, R.; Wang, B.; Weissenrieder, J.; Soldemo, M.; Yan, H.; Lin, Y.; Sun, Z.; Ma, C.; Zhang, W.; Chen, S.; Wang, H.; Guan, Q.; Yao, T.; Wei, S.; Yang, J.; Lu, J., Atomically dispersed iron hydroxide anchored on Pt for preferential oxidation of CO in H_2. *Nature* **2019,** *565* (7741), 631-635.

22. Cui, X.; Li, W.; Ryabchuk, P.; Junge, K.; Beller, M., Bridging homogeneous and heterogeneous catalysis by heterogeneous single-metal-site catalysts. *Nature Catalysis* **2018,** *1* (6), 385-397.

23. Shan, J.; Li, M.; Allard, L. F.; Lee, S.; Flytzani-Stephanopoulos, M., Mild oxidation of methane to methanol or acetic acid on supported isolated rhodium catalysts. *Nature* **2017,** *551* (7682), 605-608.

24. Choi, C. H.; Kim, M.; Kwon, H. C.; Cho, S. J.; Yun, S.; Kim, H. T.; Mayrhofer, K. J.; Kim, H.; Choi, M., Tuning selectivity of electrochemical reactions by atomically dispersed platinum catalyst. *Nature Communications* **2016,** *7*, 10922.

25. Qiao, B. T.; Wang, A. Q.; Li, L.; Lin, Q. Q.; Wei, H. S.; Liu, J. Y.; Zhang, T., Ferric oxide-supported pt subnano clusters for preferential oxidation of CO in H_2-rich gas at room temperature. *ACS Catalysis* **2014,** *4* (7), 2113-2117.

26. Moses-DeBusk, M.; Yoon, M.; Allard, L. F.; Mullins, D. R.; Wu, Z. L.; Yang, X. F.; Veith, G.; Stocks, G. M.; Narula, C. K., CO oxidation on supported single Pt atoms: Experimental and ab initio density functional studies of CO interaction with Pt atom on theta-$_{Al2O3}$(010) Surface. *Journal of the American Chemical Society* **2013,** *135* (34), 12634-12645.

27. Ding, K.; Gulec, A.; Johnson, A. M.; Schweitzer, N. M.; Stucky, G. D.; Marks, L. D.; Stair, P. C., Identification of active sites in CO oxidation and water-gas shift over supported Pt catalysts. *Science* **2015,** *350* (6257), 189-192.

28. Zhang, Z.; Zhu, Y.; Asakura, H.; Zhang, B.; Zhang, J.; Zhou, M.; Han, Y.; Tanaka, T.; Wang, A.; Zhang, T.; Yan, N., Thermally stable single atom Pt/m-Al_2O_3 for selective hydrogenation and CO oxidation. *Nature communications* **2017,** *8*, 16100.

29. Jones, J.; Xiong, H. F.; Delariva, A. T.; Peterson, E. J.; Pham, H.; Challa, S. R.; Qi, G. S.; Oh, S.; Wiebenga, M. H.; Hernandez, X. I. P.; Wang, Y.; Datye, A. K., Thermally stable single-atom platinum-on-ceria catalysts via atom trapping. *Science* **2016,** *353* (6295), 150-154.

30. Kunwar, D.; Zhou, S.; De La Riva, A.; Peterson, E.; Xiong, H.; Pereira Hernandez, X. I.; Purdy, S. C.; ter Veen, R.; Brongersma, H. H.; Miller, J. T.; Hashiguchi, H.; Kovarik, L.; Lin, S.; Guo, H.; Wang, Y.; Datye, A., Stabilizing high metal loadings of thermally stable platinum single atoms on an industrial catalyst support. *ACS Catalysis* **2019**.

31. Karim, A. M.; Howard, C.; Roberts, B.; Kovarik, L.; Zhang, L.; King, D. L.; Wang, Y., In situ X-ray absorption fine structure studies on the effect of pH on Pt electronic density during aqueous phase reforming of glycerol. *ACS Catalysis* **2012,** *2* (11), 2387-2394.

32. Ravel, B.; Newville, M., ATHENA, ARTEMIS, HEPHAESTUS: data analysis for X-ray absorption spectroscopy using IFEFFIT. *J Synchrotron Radiat* **2005,** *12*, 537-541.

33. Newville, M., IFEFFIT: interactive XAFS analysis and FEFF fitting. *J Synchrotron Radiat* **2001,** *8*, 322-324.

34. Zabinsky, S. I.; Rehr, J. J.; Ankudinov, A.; Albers, R. C.; Eller, M. J., Multiple-scattering calculations of x-ray-absorption spectra. *Physical Review B* **1995,** *52* (4), 2995-3009.

35. Bonet, F.; Grugeon, S.; Dupont, L.; Urbina, R. H.; Boudart, M.; Djega-Mariadassou, G., *Kinetics of Heterogeneous Catlytic Reactions*. Princeton University Press / Princeton, N.J.: 1984.

36. Koros, R. M.; Nowak, E. J., A diagnostic test of the kinetic regime in a packed bed reactor. *Chem. Eng. Sci.* **1967,** *22* (3), 470.

37. Madon, R. J.; Boudart, M., Experimental criterion for the absence of artifacts in the measurement of rates of heterogeneous catalytic reactions. *Ind Eng Chem Fund* **1982,** *21* (4), 438-447.

38. Nie, L.; Mei, D. H.; Xiong, H. F.; Peng, B.; Ken, Z. B.; Hernandez, X. I. P.; DeLariva, A.; Wang, M.; Engelhard, M. H.; Kovarik, L.; Datye, A. K.; Wang, Y., Activation of surface lattice oxygen in single-atom Pt/CeO_2 for low-temperature CO oxidation. *Science* **2017,** *358* (6369), 1419-+.

39. Bruix, A.; Lykhach, Y.; Matolinova, I.; Neitzel, A.; Skala, T.; Tsud, N.; Vorokhta, M.; Stetsovych, V.; Sevcikova, K.; Myslivecek, J.; Fiala, R.; Vaclavu, M.; Prince, K. C.; Bruyere, S.; Potin, V.; Illas, F.; Matolin, V.; Libuda, J.; Neyman, K. M., Maximum noble-metal efficiency in catalytic materials: atomically dispersed surface platinum. *Angew Chem Int Ed Engl* **2014,** *53* (39), 10525-30.

40. Kale, M. J.; Christopher, P., Utilizing quantitative in situ ftir spectroscopy to identify well-coordinated Pt atoms as the active site for CO Oxidation on Al_2O_3-supported Pt catalysts. *ACS Catalysis* **2016,** *6* (8), 5599-5609.

41. Wang, Y.-G.; Cantu, D. C.; Lee, M.-S.; Li, J.; Glezakou, V.-A.; Rousseau, R., CO Oxidation on Au/TiO_2: Condition-dependent active sites and mechanistic pathways. *Journal of the American Chemical Society* **2016**.

42. Baranova, E. A.; Bock, C.; Ilin, D.; Wang, D.; MacDougall, B., Infrared spectroscopy on size-controlled synthesized Pt-based nano-catalysts. *Surface Science* **2006,** *600* (17), 3502-3511.

Appendix C

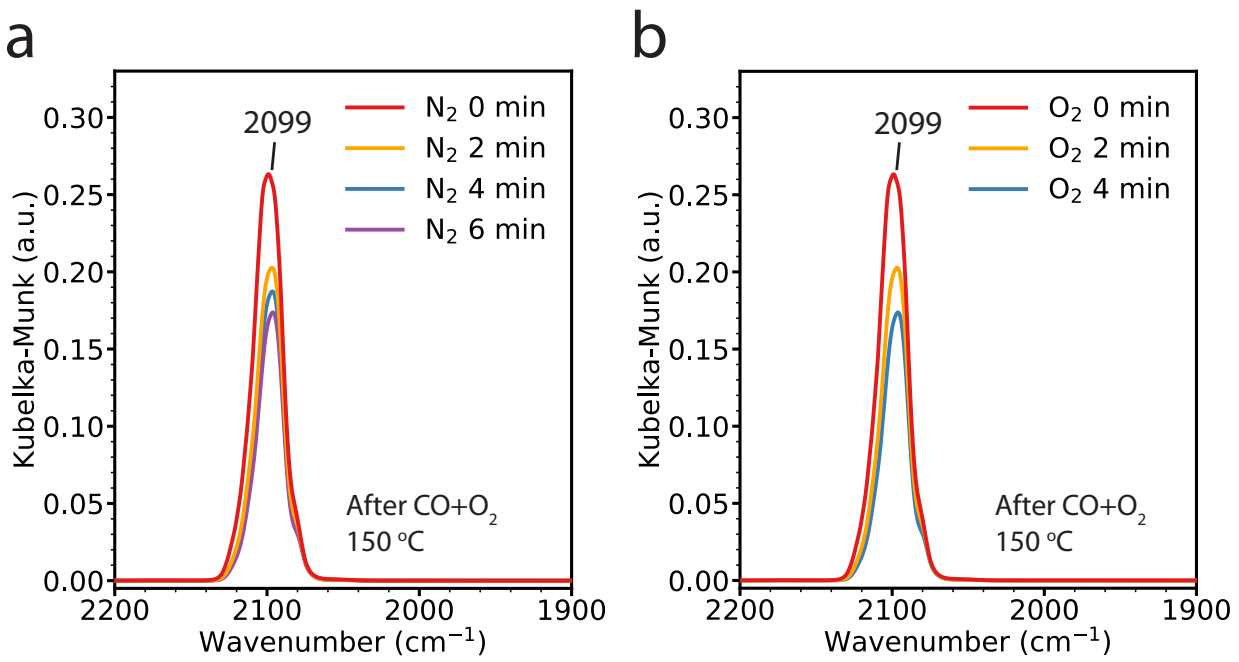

Figure S1. DRIFTS spectra in the υ_{CO} region characterizing the stability of the 1 wt.% Pt/CeO_2 single-atom catalysts under N_2 and O_2 at 150 °C and at different temperatures in CO + O_2. **(a)** DRIFTS Spectra was collected at different times in N_2 (100 sccm) after flowing 3 kPa CO and 2 kPa O_2. **(b)** DRIFTS Spectra was collected at different times in O_2 (100 sccm) after flowing 3 kPa CO and 2 kPa O_2.

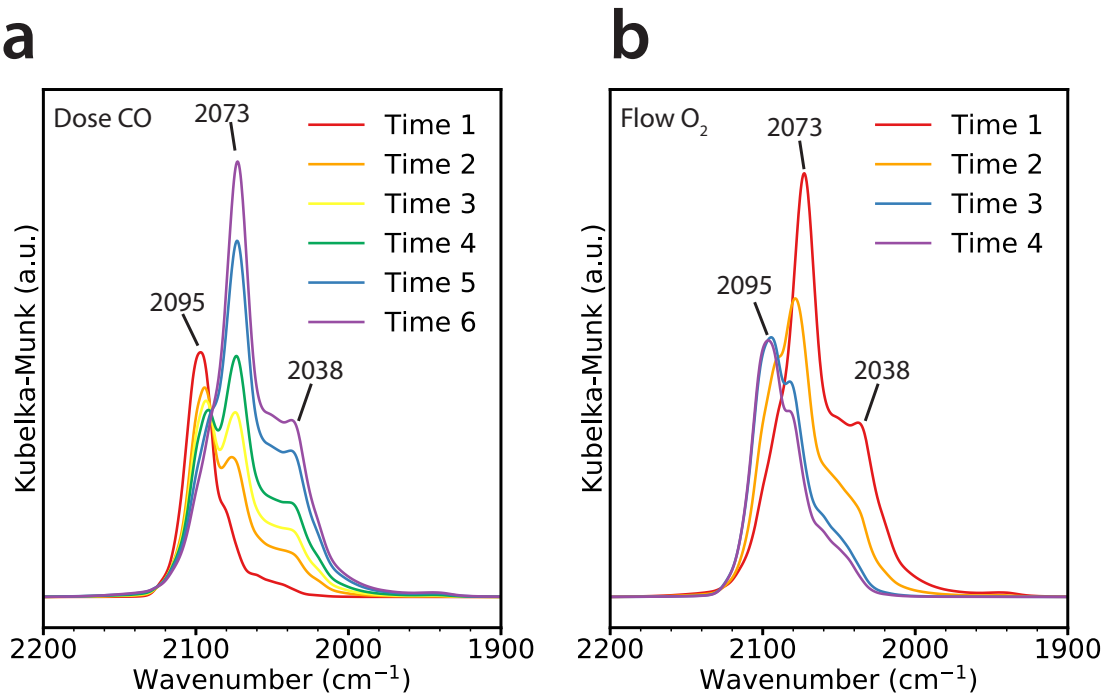

Figure S2. Change in DRIFTS spectra with time of 1 wt.% Pt/CeO_2 single-atom catalyst (a) initially after $CO+O_2$ at 150 °C and stable in He during dosing CO (0.25 kPa CO, balanced in He, 26 doses in total) at 150 °C (b) initially after dosing CO in (a) and flow O_2 (1 kPa, balanced in He) for 2 min.

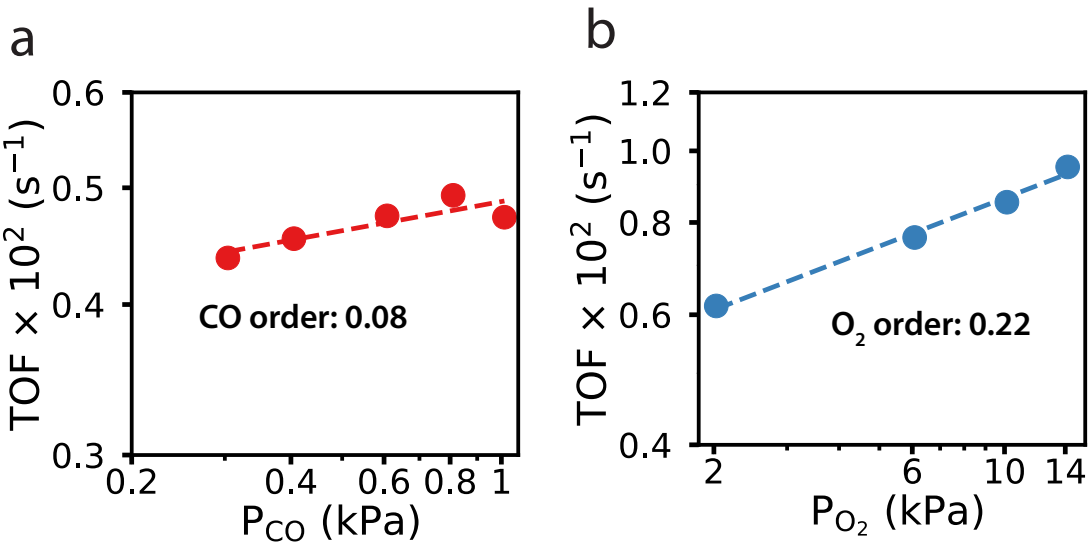

Figure S3. CO oxidation kinetic measurements (effect of CO and O_2 partial pressure on TOF) on 1% Pt/CeO_2 clusters catalysts (after reduction at 300 °C in CO). Measured at 70 °C. P_{CO} = 0.3 -1 kPa and P_{O_2} = 10 kPa for CO order and P_{CO} = 1 kPa and P_{O_2} = 2-14 kPa for O_2 order.

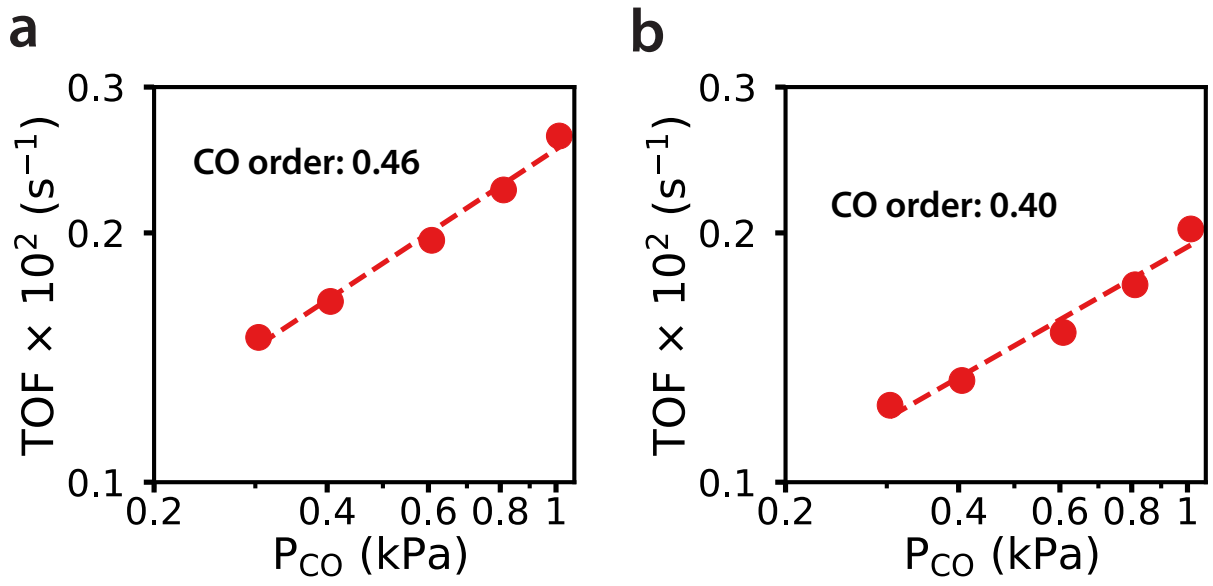

Figure S4. CO oxidation kinetic measurements (effect of CO partial pressure on TOF) on 1% Pt/CeO_2 single-atom catalysts before (a) and after (b) dosing CO (26 doses in total). All measured at 150 °C. P_{CO} = 0.3 -1 kPa and P_{O_2} = 10 kPa for CO order and P_{CO} = 1 kPa and P_{O_2} = 2-14 kPa for O_2 order.

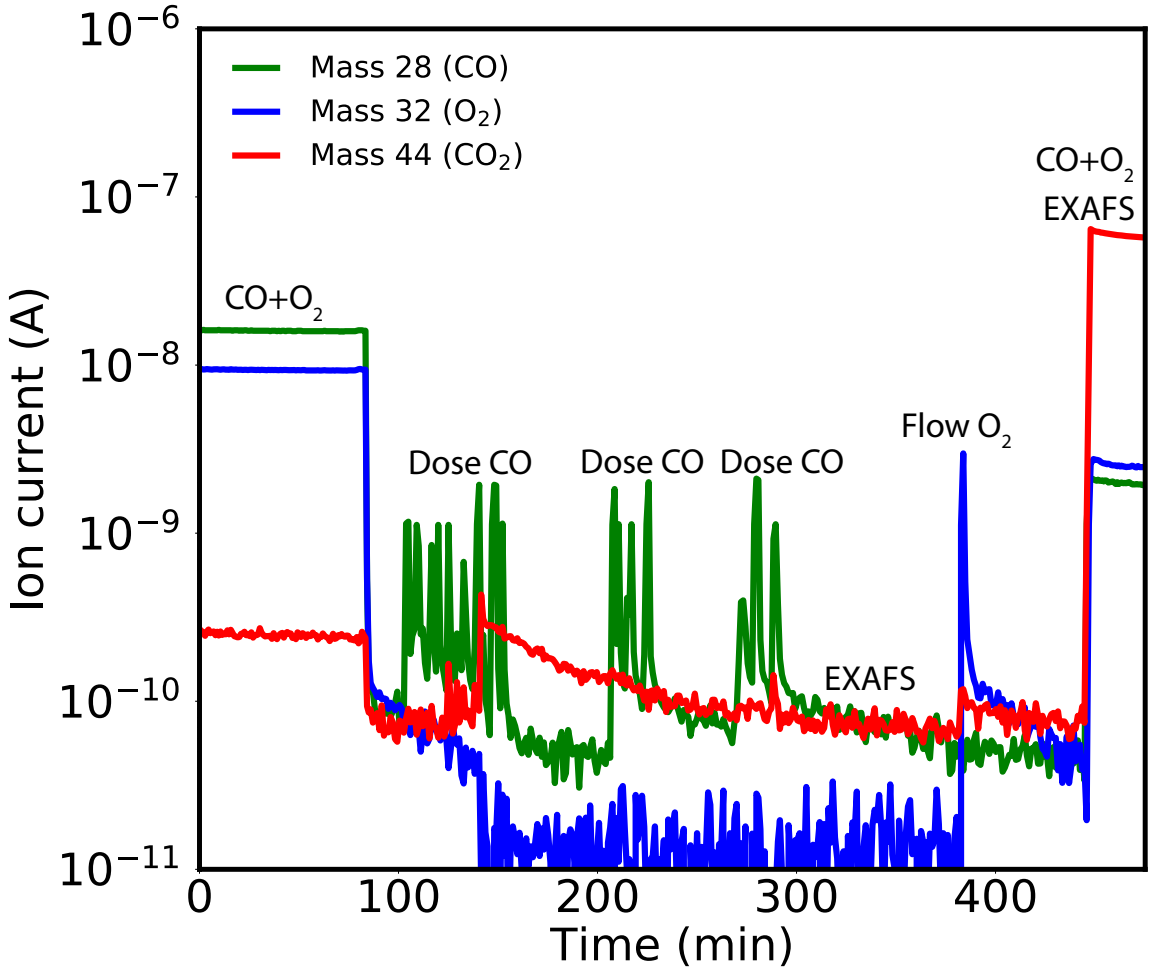

Figure S5. Mass spectroscopy results of the gas concentration after the reactor at 150 °C during EXAFS experiment. 3 kPa CO+2 kPa O_2 were introduced into the chamber at 150 °C. Then 3 sets of doses of CO (0.33 kPa CO balanced with He at 60 sccm, 40s each dose and 40 doses in total for all 3 set of doses) were introduced into the sample at 165 °C. After 3 sets of doses EXAFS experiment was conducted at 150 °C. Then 1 kPa O_2 (60 sccm) flowed through the sample at 150 °C. Then 3 kPa CO+2 kPa O_2 flowed through the sample again and EXAFS was collected under $CO+O_2$ flow.

Chapter 5. Structural and kinetic study of highly active subnanometer Ir clusters for low-temperature CO oxidation

This manuscript is in preparation.

Attribution:

Yubing Lu performed the synthesis, characterizations and catalytic tests, data analysis, and wrote the first draft of the paper. Adam S. Hoffman, Alexey Boubnov and Simon R. Bare helped design the EXAFS and HERFD experiment and contributed to writing the XAS section. Adam S. Hoffman, Alexey Boubnov, Yubing Lu, Chun-Te Kuo performed the EXAFS and HERFD experiments. Ayman M. Karim did the EXAFS analysis. Ayman M. Karim conceived the idea and planned and directed the project. Yubing Lu and Ayman M. Karim co-wrote the paper. All the authors discussed the results and commented on the paper.

5.1. Abstract

CO oxidation is one of the important reactions for catalytic converters and membrane electrolyte fuel cells. However, in catalytic converters noble catalysts are subject to the poisoning of CO especially at cold start temperature. Size and shape of particles have been shown to be essential to the catalytic performance. When the particle size is in the subnanometer regime, their electronic and geometric properties dramatically change. Therefore, their catalytic performance can also be very different from the large particles. In this study, we synthesized Ir subnanometer clusters with

size 0.6-0.8 nanometers. High CO oxidation activity was observed for the subnanometer clusters. In-situ high energy resolution fluorescence detected X-ray absorption near edge structure (HERFD-XANES) and infrared spectroscopy (IR) showed that CO and O_2 could co-adsorb on the subnanometer clusters without CO poisoning. CO and O_2 calorimetry was also performed to understand the adsorption energy of CO and O_2. Kinetic measurement showed that their reaction rates do not depend on the CO partial pressure, which can be explained by their unique adsorption behaviors of CO and O_2.

5.2. Introduction

Supported noble metal catalysts are extensively applied in industry and their catalytic performance is strongly affected by particle size and shape[1-3]. Extraordinary catalytic properties have been observed on supported noble metals with the size in the subnanometer regime[4-9]. We recently reported that Ir single atoms supported on $MgAl_2O_4$ showed higher activity than nanoparticles despite stronger CO adsorption due to a different mechanism (Eley-Rideal) on the single atoms[10]. Here we show that supported Ir subnanometer clusters are more active than both, single atoms and nanoparticles (> 1 nm). Unlike nanoparticles, CO is not the dominant species on the surface of subnanometer clusters. Despite a high CO adsorption energy on Ir subnanometer clusters, competitive adsorption of CO and O_2 was observed. Detailed kinetic and in-situ characterization measurements were performed to understand the reaction mechanisms and the origin of the high activity on the subnanometer clusters.

5.3. Methods

Synthesis and pretreatment. The 0.05 wt.% subnanometer clusters catalyst was prepared by wet impregnation. The $MgAl_2O_4$ support (Puralox MG 30, Sasol) was calcined at 500 °C for 4 hr before impregnation. 200 mL DI water was added to a Pyrex bottle and the pH was adjusted with nitric acid to 2.8. The Ir nitrate precursor (8.7 wt. % Ir, Furuya Metal CO. Ltd.) was added into the pH adjusted solution. The $MgAl_2O_4$ support was then added into the solution while stirring for 2 hr. The final pH of the solution was 9.5. The nominal Ir weight loading was 0.05%. After 2 hr of stirring, the solution was filtered out, and the solid sample was dried in air for 24 hr at room temperature. The sample was then dried at 80 ℃ and 100 °C before calcination at 500 °C for 4 hr. The Ir in the solution after filtration was measured by inductively coupled plasma atomic emission spectroscopy and no Ir was detected. The sample was pretreated in 20 kPa H_2 in situ (80 sccm total) for 2 hr and cooled down to room temperature in the same gas. Another 0.1 wt.% Ir/MgA_2O_4 subnanometer clusters were prepared by wet impregnation. Proper amount $Ir_4(CO)_{12}$ (Sigma Aldrich) precursor was dissolved in 16 mL of toluene (Sigma Aldrich) in a 20 ml vial while flowing N_2 at room temperature. Then the dissolved $Ir_4(CO)_{12}$ toluene solution was injected into another vial containing 5 g $MgAl_2O_4$ (Puralox MG 28, Sasol) under N_2 flow. The sample was then dried under N_2 flow at room temperature overnight to evaporate the toluene. No calcination was performed on this catalyst. The CO and acac ligands were removed in-situ by treatment in He at 400 °C and H_2 at 200 °C which led to the formation of subnanometer clusters as detailed below.

HERFD-XANES. HERFD-XANES measurements were collected at beamline 6-2 at the Stanford Synchrotron Radiation Light Source (SSRL). A liquid-nitrogen-cooled double-crystal Si(311) monochromator was equipped to select the energy of the incident beam with a flux of 3 x 10^{12} photons × s^{-1}. A Rowland circle spectrometer (radius 1 m) equipped with three spherically bent Si

(800) analyzers and a silicon drift detector was used to select the Ir L_α (9175 eV) emission line with a measured resolution of 1.3 eV. An iridium foil was scanned in the transmission mode for initial energy calibration.

Each sample (120 mg in mass, 25-90 microns) was loaded into a packed bed flow reactor. The in-situ packed bed reactor consists of a Be tube (Materion; PF-60 Grade) (OD 5 mm and ID 3.8 mm) connected to the gas line using graphite ferrules and heated by a stainless steel heating block equipped with four 100 W heating cartridges (Watlow). The in-situ reactor assembly was protected from oxidation by an air-free box with polyimide film X-rays windows and continuous He or N_2 flow. Two type-K thermocouples were used to monitor and control the heating block and the catalytic bed temperature. A portable gas delivery system equipped with 5 MFCs (Brooks - SLA5800) was used to control the gas flow. The composition of effluent gases was measured by an online quadrupole mass spectrometer (Hiden HPR20). Samples were pretreated the same as the previous section.

All HERFD-XANES spectra were measured within 2 min and three to six scans were averaged to improve signal-to-noise ratio. The analysis of the HERFD XANES data was carried out with the software ATHENA of the IFEFFIT package [42, 43]. The edge, determined by the first inflection point of the absorption edge of the Ir foil, was calibrated to the reported Ir L_3 energy, 11215 eV. This calibration was used to calibrate a known glitch in the monochromator observed in the I_0 signal of each scan. A least-squares Gaussian fit of the glitch, determined the error in the energy calibration of the samples to be 0.022 eV. Energy calibration was achieved by aligning the glitch in each scan to the glitch in the Ir foil reference scans. Three to six scans per sample were averaged with the averaged spectra being used for deglitching and normalization. The averaged spectrum was

processed by fitting a second-order polynomial to the pre-edge region and subtracting this from the entire spectrum. Edge energy was determined by the first derivative of the normalized absorbance. The data were normalized by dividing the absorption intensity by the height of the absorption edge.

Micro-calorimetry. Micro-calorimetry was performed on a Setaram SENSYS Evo DSC calorimeter with a self-built U-shape sample tube. The U-shape sample tube was connected to a Micromeritics 3Flex for the adsorption quantity measurement and temperature control. 70 mg catalyst was put in the U-shape reactor each time. The gas pretreatment procedure was the same as mentioned above in a soaking mode with 760 mmHg O_2. After pretreatment, samples were exposed to ultra-high vacuum (UHV) with pressure below $1e^{-5}$ mmHg. For the first set of doses, adsorption heat of both chemisorption and physisorption CO/O_2 was measured. After the first set of doses, samples were exposed to ultra-high vacuum (unrestricted vacuum <1 e^{-4} mmHg for 1hr) at 30 °C to remove the physisorbed CO/O_2. The second set of doses measured the adsorption heat of the physisorbed CO/O_2. O_2 adsorption experiment was measured at 30 °C with pressure between 0-300 mm Hg for O_2 calorimetry and 0-20 mmHg for CO calorimetry.

Scanning transmission electron microscopy. Aberration-corrected electron microscopy images for $Ir/MgAl_2O_4$ samples were taken on FEI TITAN 80-300 in STEM mode using a high angle annular dark field (HAADF) detector. The resolution is 0.1 nm, with the CEOS GmbH double-hexapole aberration corrector. To calculate the atomic percentage from multiple STEM images, the number of atoms per particle (N) was estimated with a spherical model [48]:

$$N = \frac{\pi D^3 \rho N_A}{6 M_w} \quad (1)$$

where D is the nanoparticle diameter, ρ is the bulk metal density, N_A is Avogadro's number, and Mw is the metal molecular weight.

5.4. Results

$MgAl_2O_4$ supported Ir subnanometer clusters catalysts were prepared with two different types of precursors. The first catalyst was prepared with inorganic precursor Ir nitrate and 0.05% Ir weight loading, and the second catalyst was prepared with organic precursor $Ir_4(CO)_{12}$ and 0.1% Ir weight loading (See Methods for details of synthesis). High angle annular dark field –scanning transmission electron microscopy (HAADF-STEM) was applied for the analysis of cluster size. The particle size was analyzed from multiple images, and the particle size distribution of two catalysts was summarized in Table 2 and the Histogram in Figures 1 and 2. The 0.05 wt.% Ir sample prepared with Ir nitrate has 28% single atoms, and the average particle size is ~0.7 nm. 0.1 wt.% Ir sample prepared with $Ir_4(CO)_{12}$ has 13% single atoms, and the average particle size is ~0.5-0.6 nm. The 0.1 wt.% sample prepared $Ir_4(CO)_{12}$ has a more uniform size distribution and smaller size on average compared with the 0.05 wt.% Ir sample prepared with Ir nitrate precursor.

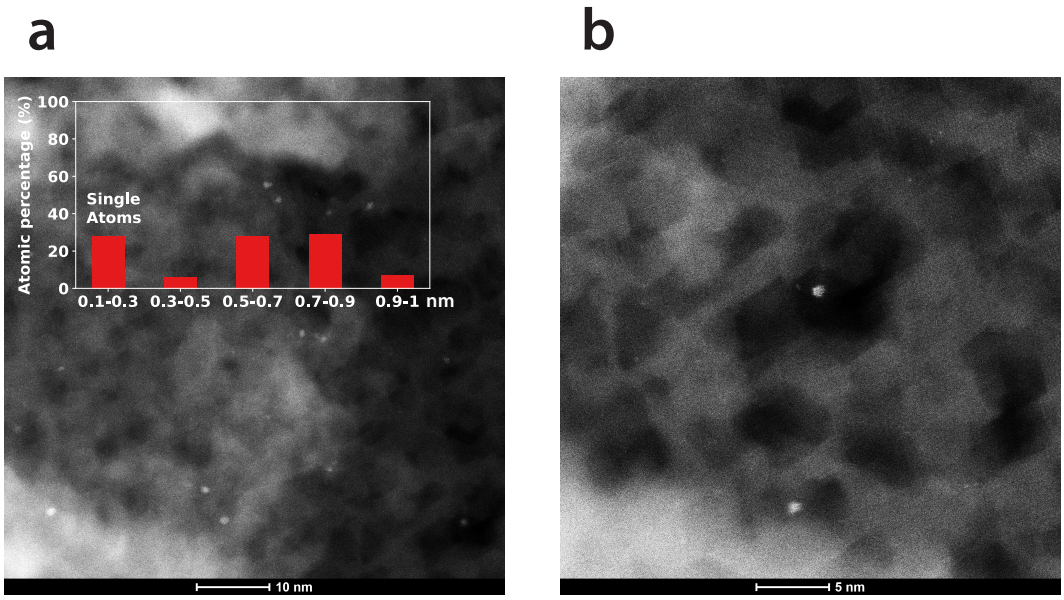

Figure 1. HAADF-STEM images of the 0.05 wt.% Ir supported on $MgAl_2O_4$ (prepared with Ir nitrate precursor). Histogram obtained from multiple images is shown in (a).

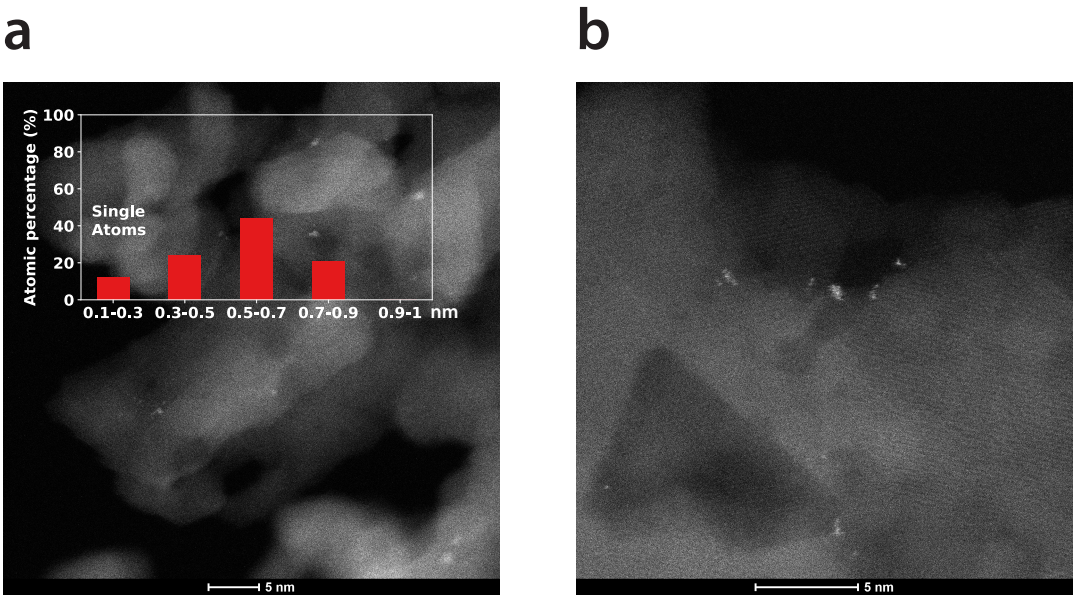

Figure 2. HAADF-STEM images of the 0.1 wt.% Ir (prepared with $Ir_4(CO)_{12}$ precursor) supported on $MgAl_2O_4$. Histogram obtained from multiple images is shown in (a).

Table 1. Size distribution of two subnanometer clusters samples prepared with different precursors.

Catalyst	0.1-0.3 nm	0.3-0.5 nm	0.5-0.7 nm	0.7-0.9 nm	0.9-1 nm
0.05 wt.%Ir ($Ir(NO_3)_2$ precursor)	28%	6%	28%	29%	7%
0.1 wt.%Ir ($Ir_4(CO)_{12}$ precursor)	13%	24%	44%	21%	0%

For low-temperature CO oxidation on Ir nanoparticles, nanoparticle surface is poisoned by CO, and O_2 activation becomes the rate limiting step. Thus negative order in CO was reported on Ir nanoparticles[11]. On Ir single atoms, a facile O_2 activation and an Eley-Rideal mechanism were reported by early work in our group which results in a positive order in CO[10]. In contrast to the negative order in CO on Ir nanoparticles (1-2 nm), and positive order on Ir single atoms [10], the Ir subnanometer clusters (~0.7 nm) showed ~0 order in CO and 0.4 order in O_2 (Figure 2). Moreover, during CO order measurement, the activity of Ir subnanometer clusters (~0.7 nm) was consistently higher than the single atoms and nanoparticles across most of the CO partial pressures measured. The activity of the single atoms reaches almost the same value at a higher partial pressure of 1 kPa as shown in Figure 3a, which was also observed when measuring the O_2 order at 1 kPa CO. The results indicate a different reaction mechanism on subnanometer clusters than on single atoms or nanoparticles. The high activity and ~0 order in CO and 0.4 in O_2 suggest that Ir subnanometer clusters are not fully covered by CO.

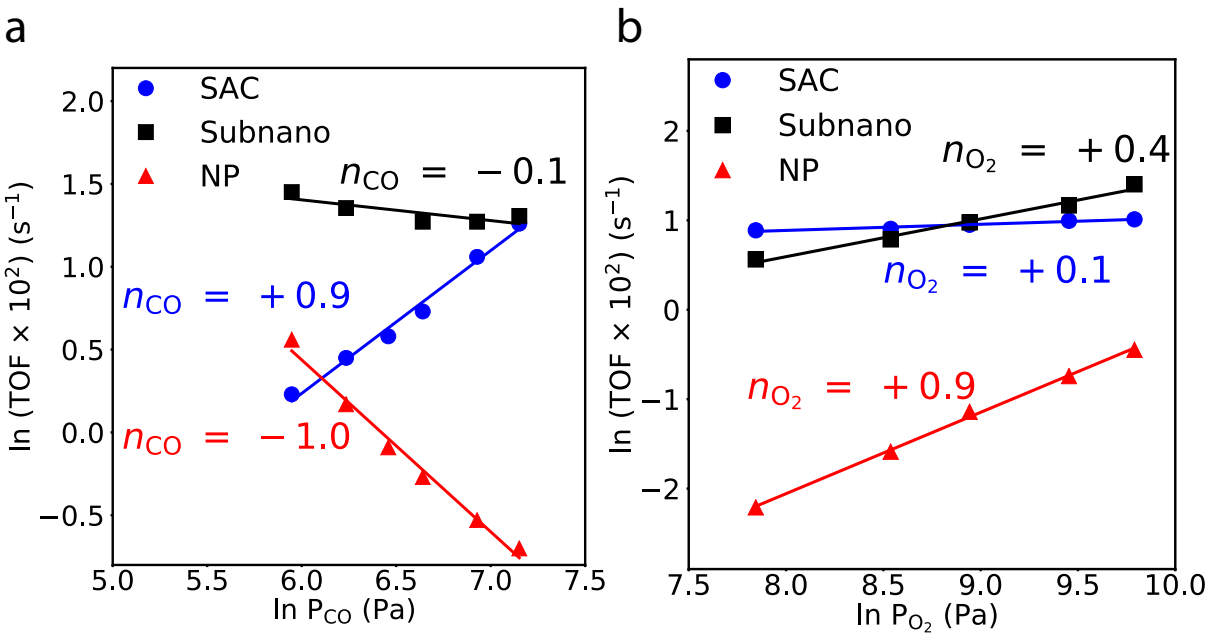

Figure 3. Effect of (a) CO partial and (b) O_2 pressure on turnover frequency (TOF) on $MgAl_2O_4$ supported Ir subnanometer clusters (0.05 wt.% Ir, prepared with Ir nitrate precursor, ~0.7 nm, black), single atoms (blue)[10] and Ir nanoparticles (1-2 nm, red)[10]. (a) O_2 partial pressure = 10 kPa, CO partial pressure = 0.3-1 kPa. Measured at 155 °C. (b) (a) O_2 partial pressure = 2-14 kPa, CO partial pressure = 1 kPa. Measured at 155 °C.

To understand the high activity and unique reaction kinetics, HERFD-XANES spectra were performed on both subnanometer clusters with different size and preparation methods. For the sample 0.05 wt.% Ir/$MgAl_2O_4$ prepared with Ir nitrate precursor, CO flowed through the sample at room temperature after pretreatment, and spectra were collected after flushed with He (Figure 4a, blue). When flowing O_2 on the CO covered sample at room temperature, a significant increase in white line intensity was observed (Figure 2a, blue) which indicates an increase in oxidation

states of Ir. CO2 was detected in the mass spectroscopy (Figure S1, a) when flowing O_2, which suggests that O_2 could react with the adsorbed CO, and then co-adsorb with the CO at room temperature. When flowing CO again after the oxygen step, a decrease in white line intensity was observed (Figure 4a, orange), but still higher than the original spectrum after flowing CO. A CO_2 spike was observed in the mass spectroscopy (Figure S1a). This suggests that CO could again replace some of the adsorbed O_2 by CO, or further adsorption of CO. Some CO could possibly react with adsorbed O to form CO2 as indicated by mass spectroscopy. This competitive co-adsorption of CO and O_2 could explain the high activity of CO oxidation on subnanometer clusters because CO is no longer the dominating species and the O_2 activation will have a lower barrier compared with nanoparticles. A similar experiment was done on the sample prepared with $Ir_4(CO)_{12}$ which has a smaller average cluster size as 0.5-0.6 nm. Similar increase and then decrease of white line intensity when flowing O_2 and CO respectively was observed. The increase of white line when flowing CO is more significant and the white line almost back to the original position after flowing CO again. CO_2 was observed during O_2 flow, but not the CO flow after O_2 (Figure S1b). This suggests that the competitive adsorption of CO and O_2 is more significant on this sample, which can be related to its smaller cluster size.

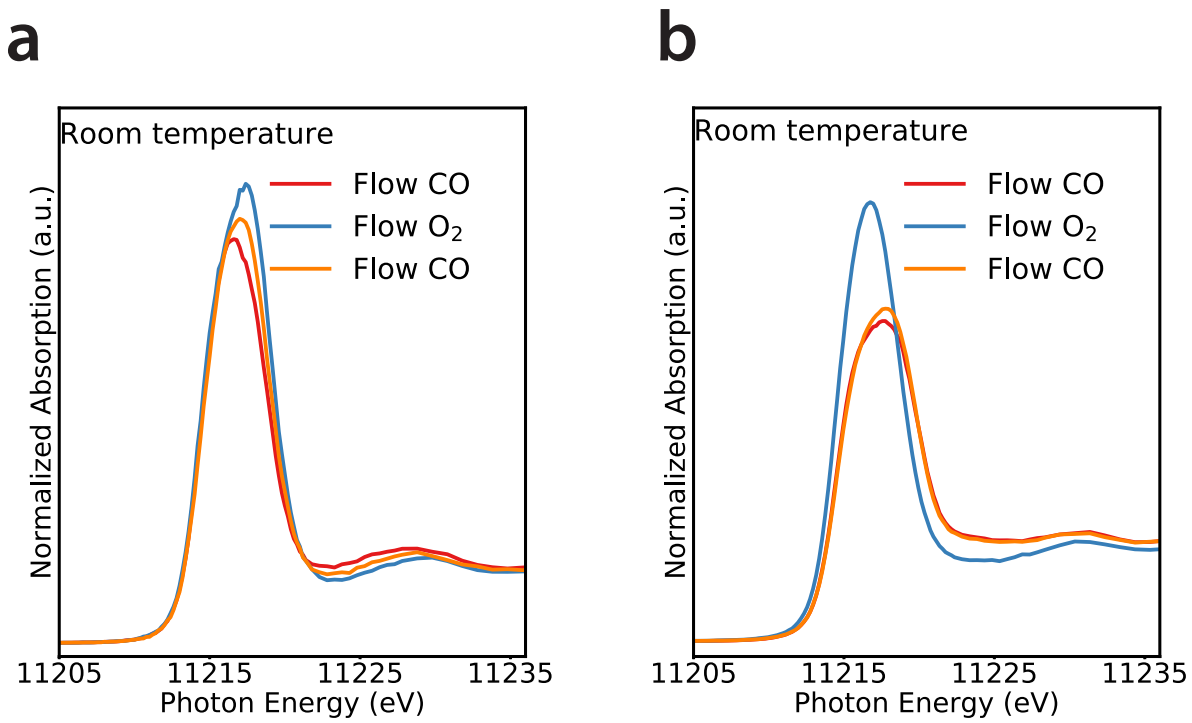

Figure 4. HERFD-XANES spectra of Ir subnanometer clusters (a) 0.05 wt.% Ir/$MgAl_2O_4$ prepared with Ir nitrate precursor; (b) 0.1 wt.%Ir/$MgAl_2O_4$ prepared with $Ir_4(CO)_{12}$ precursor.

CO micro-calorimetry results (Fig. 1b) showed that subnanometer clusters adsorb CO with binding energy of 203-210 kJ/mol (at low coverage, based on two measurements), which is much higher than the binding of CO on Ir nanoparticles (~150 kJ/mol at low CO coverage), and similar with the CO binding energy on Ir single atoms (~230 kJ/mol). On the other hand, the O_2 adsorption energy on the subnanometer clusters was also higher than nanoparticles (480-550 kJ/mol vs. ~330 kJ/mol at low coverage). The increase of binding energy of O_2 on subnanometer clusters (compared with the nanoparticles) is more significant than CO, which could facilitate the activation of O_2. This could further explain the high activity observed during CO oxidation.

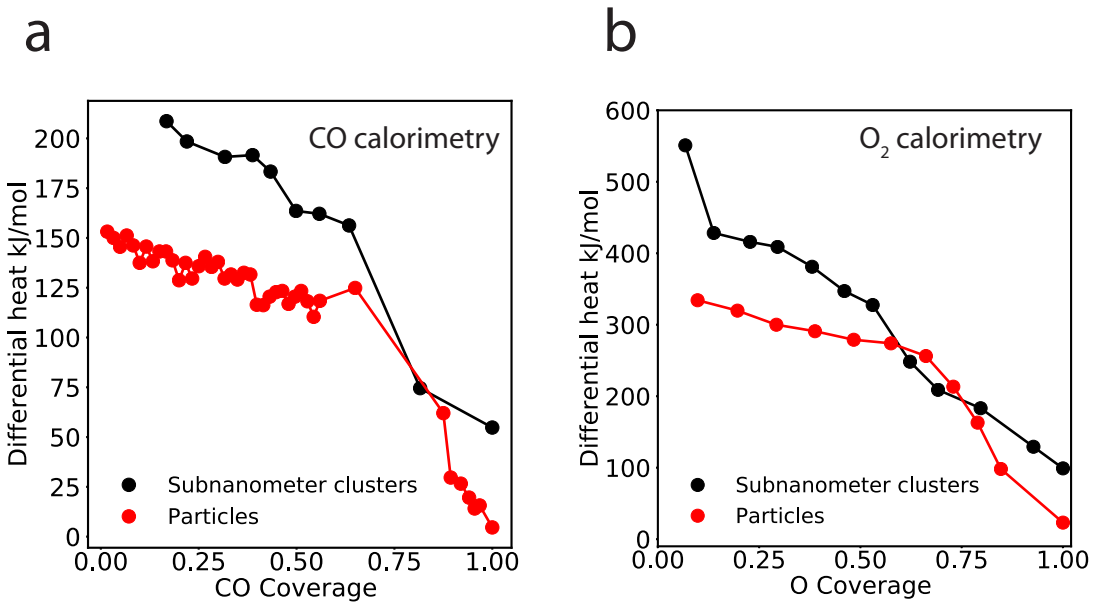

Figure 5. CO (a) and O_2 calorimetry of 0.05 wt. % $Ir/MgAl_2O_4$ prepared with Ir nitrate precursor. Measured at 30 ºC for both CO and O_2 calorimetry. CO and O_2 coverage were based on the ratio between adsorbed CO/O and the total surface CO/O. Total surface CO/O was calculated with the Ir loading and the volumetric chemisorption.

5.5. Conclusions

Two Ir subnanometer clusters samples were prepared with different clusters, one with an average cluster size 0.7 nm and one with average cluster size 0.5-0.6 nm. High activity was observed on these subnanometer clusters during CO oxidation (higher than both single atoms and nanoparticles at all conditions). In-situ HERFD-XANES suggests that O_2 could competitively co-adsorbed with CO, which suggests a lower reaction barrier on Ir subnanometer clusters. CO and O2 calorimetry showed that both CO and O_2 adsorbed stronger on subnanometer clusters (CO: ~230 kJ/mol, O2:

550 kJ/mol) than nanoparticles (CO: 150 kJ/mol, O2: 330 kJ/mol). The more significant increase in O_2 binding energy (1.7 times) than CO binding energy (1.5 times) could result in a lower reaction barrier of O_2 activation. Also, the different reaction mechanism as indicates in kinetic measurement could also be one of the reasons for the high activity on Ir subnanometer clusters.

References

1. Chen, Y.; Huo, M.; Chen, T.; Li, Q.; Sun, Z.; Song, L., The properties of Ir_n (n = 2-10) clusters and their nucleation on gamma-Al_2O_3 and MgO surfaces: from ab initio studies. *Physical chemistry chemical physics : PCCP* **2015,** *17* (3), 1680-7.

2. Li, L.; Gao, Y.; Li, H.; Zhao, Y.; Pei, Y.; Chen, Z.; Zeng, X. C., CO oxidation on TiO_2 (110) supported subnanometer gold clusters: size and shape effects. *J Am Chem Soc* **2013,** *135* (51), 19336-46.

3. Mao, K. K.; Li, L.; Zhang, W. H.; Pei, Y.; Zeng, X. C.; Wu, X. J.; Yang, J. L., A theoretical study of single-atom catalysis of CO oxidation using Au embedded 2d h-BN monolayer: a CO-promoted O_2 Activation. *Scientific Reports* **2014,** *4*.

4. Jones, J.; Xiong, H. F.; Delariva, A. T.; Peterson, E. J.; Pham, H.; Challa, S. R.; Qi, G. S.; Oh, S.; Wiebenga, M. H.; Hernandez, X. I. P.; Wang, Y.; Datye, A. K., Thermally stable single-atom platinum-on-ceria catalysts via atom trapping. *Science* **2016,** *353* (6295), 150-154.

5. Ding, K.; Gulec, A.; Johnson, A. M.; Schweitzer, N. M.; Stucky, G. D.; Marks, L. D.; Stair, P. C., Identification of active sites in CO oxidation and water-gas shift over supported Pt catalysts. *Science* **2015,** *350* (6257), 189-192.

6. Qiao, B.; Liu, J.; Wang, Y.-G.; Lin, Q.; Liu, X.; Wang, A.; Li, J.; Zhang, T.; Liu, J., Highly efficient catalysis of preferential oxidation of CO in H_2-Rich stream by gold single-atom catalysts. *ACS Catalysis* **2015,** *5* (11), 6249-6254.

7. Qiao, B. T.; Wang, A. Q.; Yang, X. F.; Allard, L. F.; Jiang, Z.; Cui, Y. T.; Liu, J. Y.; Li, J.; Zhang, T., Single-atom catalysis of CO oxidation using Pt_1/FeO_x. *Nature Chemistry* **2011,** *3* (8), 634-641.

8. Vajda, S.; Pellin, M. J.; Greeley, J. P.; Marshall, C. L.; Curtiss, L. A.; Ballentine, G. A.; Elam, J. W.; Catillon-Mucherie, S.; Redfern, P. C.; Mehmood, F.; Zapol, P., Subnanometre platinum clusters as highly active and selective catalysts for the oxidative dehydrogenation of propane. *Nature materials* **2009,** *8* (3), 213-6.

9. Li, Z. Y.; Yuan, Z.; Li, X. N.; Zhao, Y. X.; He, S. G., CO Oxidation Catalyzed by single gold atoms supported on aluminum oxide clusters. *Journal of the American Chemical Society* **2014,** *136* (40), 14307-14313.

10. Lu, Y.; Wang, J.; Yu, L.; Kovarik, L.; Zhang, X.; Hoffman, A. S.; Gallo, A.; Bare, S. R.; Sokaras, D.; Kroll, T.; Dagle, V.; Xin, H.; Karim, A. M., Identification of the active complex for CO oxidation over single-atom Ir-on-$MgAl_2O_4$ catalysts. *Nature Catalysis* **2019,** *2* (2), 149-156.

11. Berlowitz, P. J.; Peden, C. H. F.; Goodman, D. W., Kinetics of CO Oxidation on Single-Crystal Pd, Pt, and Ir. *Journal of Physical Chemistry* **1988,** *92* (18), 5213-5221.

Appendix D

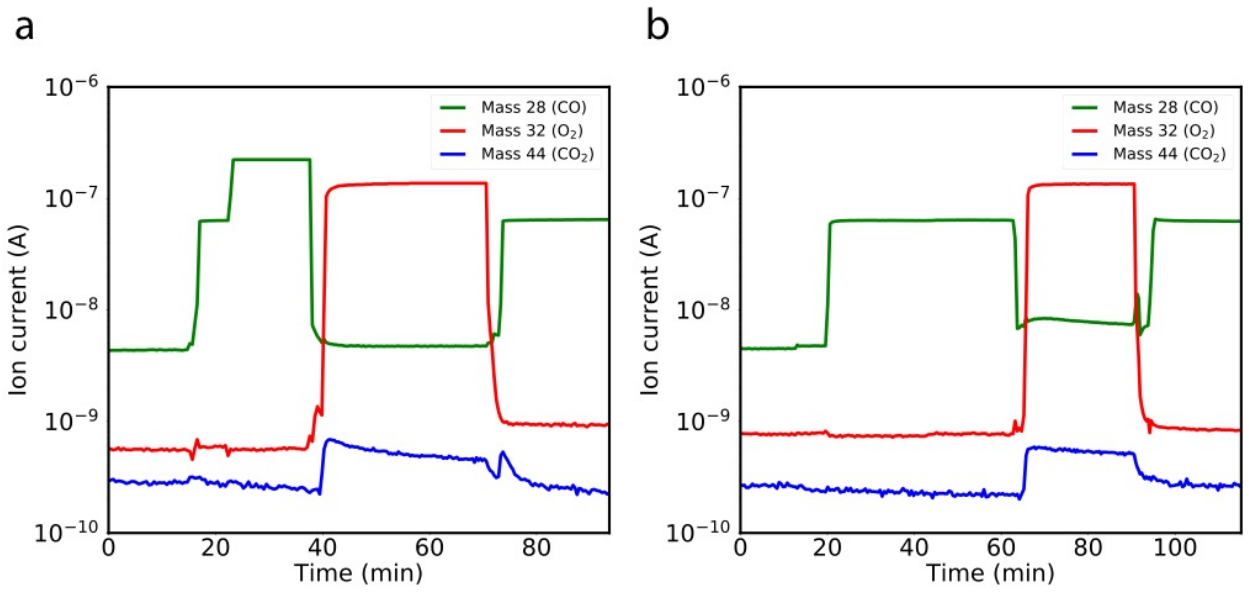

Figure S1. Mass spectroscopy results of the gas concentration after the reactor at 30 °C during EXAFS experiment on sample (a) 0.05 wt.% Ir/$MgAl_2O_4$ prepared with Ir nitrate precursor (b) 0.1 wt.% Ir/$MgAl_2O_4$ prepared $Ir_4(CO)_{12}$ precursor with 1 kPa CO (50 sccm). (a) Flowed 1 kPa and then 4 kPa CO, 4 kPa O_2, and 1kPa CO in sequence on 0.05 wt.% Ir/$MgAl_2O_4$ prepared with Ir nitrate precursor. (b) Flowed 1 kPa CO, 4 kPa O_2, and 1 kPa CO in sequence on 0.1 wt.% Ir/$MgAl_2O_4$ prepared $Ir_4(CO)_{12}$ precursor.

Chapter 6. Conclusions and future work

Supported single atoms and subnanometer clusters provide numerous opportunities for designing catalysts at the atomic scale. In this work, using in-situ and operando spectroscopy (FTIR, HERFD-XANES), HAADF-STEM, calorimetry and DFT calculations we studied the CO oxidation reaction mechanism of Ir and Pt single catalysts. For $MgAl_2O_4$ supported Ir single-atom catalyst, we show that Ir(CO) is the active complex and the formation of this Ir single-atom complex on $MgAl_2O_4$ promotes CO oxidation and the O_2 facile activation via an Eley-Rideal mechanism where Ir(CO)(O) is the resting state of the catalyst. For CeO_2 supported Pt single-atom catalyst, similar reaction behavior was observed. Infrared spectroscopy showed that most of the Pt single atoms are stable in O_2 and N_2 at the reaction temperature (150 °C). However, significant activity was measured during catalytic performance measurement. Operando DRIFTS, EXAFS and calorimetry results showed that though $Pt(O)_3(CO)$ structure is stable in O_2, gas phase CO could react with the surface O to form CO_2. The lattice O can be filled by O_2. One adsorbed CO present during the whole reaction cycle which acts as a ligand. Positive order in CO (~0.5) and 0 order in O_2 is consistent with the Mars Van-Krevelen and Eley-Rideal mechanism identified by operando DRIFTS and EXAFS.

With two different noble metal single-atom catalysts (Ir and Pt), our results show that detection of adsorbed CO on metal single atoms by infrared spectroscopy under reaction conditions or under O_2 flow does not necessarily indicate low activity for CO oxidation. The adsorbed CO serves as a spectator at the low-temperature CO oxidation so that TPO experiments is not a proper indicator of activity. For the future work, detailed kinetic study at different reaction conditions can be done

to further understand the reaction mechanism, and the first–principle calculation can be applied to understand the more detailed reaction mechanism based on the proposed reaction mechanism in this work.

Because of the unique reaction mechanism of CO oxidation on supported Ir (and Pt) single atoms, we identified kinetic measurements as a unique, facile and effective method to quantify the site distribution of iridium as single atoms and nanoparticles under reaction conditions. We show that the site fractions estimated from kinetic measurements on different catalysts are consistent with STEM, XAS, and FTIR. More importantly, CO oxidation measurements directly measures the surface sites, allowing the determination of the catalyst dispersion and whether single atoms are on the surface or in the sub-surface and this methodology is not limited to iridium and can potentially be used as a facile and sensitive tool for other reactions/metal catalysts to differentiate between two types of sites, provided they have different reaction orders.

To bridge the gap between the nanoparticles and single atoms and further understand the effect of nuclearity, two Ir subnanometer clusters samples were prepared and proved to be highly active during CO oxidation (higher than both single atoms and nanoparticles at all conditions). In-situ HERFD-XANES suggests that O_2 could competitively adsorb with CO, which suggests a lower reaction barrier on Ir subnanometer clusters. CO and O_2 calorimetry showed that both CO and O_2 adsorbed stronger on subnanometer clusters, and the difference in O_2 is more significant than CO. From Ir nanoparticles to Ir subnanometer clusters, a more significant increase in O_2 binding energy (480-550 kJ/mol on Ir subnanometer clusters and ~330 kJ/mol on Ir nanoparticle) than CO binding energy (203-230 kJ/mol on Ir subnanometer clusters and ~150 kJ/mol on Ir nanoparticles) could possibly explain the easier O_2 activation on Ir subnanometer clusters. Also, a different reaction

mechanism as suggested by the kinetic measurements could also be one of the reasons for the high activity on Ir subnanometer clusters.

This work studied the reaction mechanism of CO oxidation in the subnanometer regime with different sizes, from single atoms to subnanometer clusters, also with different metals: Pt and Ir. CO and O/O_2 co-adsorption on neighboring atoms was observed on Ir subnanometer clusters, and CO and O co-adsorption on the same atoms was observed on Ir single atoms. For both supported Pt and Ir single atoms catalysts, a strongly adsorbed ligand from adsorbate was observed during the whole reaction cycle, which dramatically changed the reaction pathways and the activation energy of O_2. This work highlights the importance of combining in-situ/operando spectroscopy, together with quantum chemical calculations, and kinetic measurements to identify the active complex, most stable intermediate (resting state) and reaction mechanism.

For future work, the effect of support can be further studied to decouple the effect of support from the effect of metal nuclearity and metal electronic properties. The metal surface interaction and metal adsorbate interaction can be further studied to understand how single atoms can be activated by tuning the electronic properties and the interaction with the support.